UNIVERSIDAD COMPLUTENSE DE MADRID

FACULTAD DE CIENCIAS FÍSICAS
DEPARTAMENTO DE FÍSICA ATÓMICA, MOLECULAR Y NUCLEAR

TESIS DOCTORAL

Positron range and prompt gamma modeling in PET imaging
Simulación de rango del positrón y emisiones gamma adicionales en PET

MEMORIA PARA OPTAR AL GRADO DE DOCTOR

PRESENTADA POR

Jacobo Cal González

Directores

José Manuel Udías Moinelo
Joaquín López Herraiz

Madrid, 2014

Departamento de Física Atómica, Molecular y Nuclear

UNIVERSIDAD COMPLUTENSE DE MADRID

TESIS DOCTORAL:

Positron range and prompt gamma modeling in PET imaging

Simulación de rango del positrón y emisiones gamma adicionales en PET

Realizada por:
Jacobo Cal González

Directores:
Dr. Jose Manuel Udías Moinelo
Dr. Joaquin López Herraiz

February 10, 2014

A mis padres y hermanos:
Por apoyarme siempre.

El misterio es la cosa más bonita que podemos experimentar.
Es la fuente de todo arte y ciencia verdaderos.

Albert Einstein

Agradecimientos

Te lo juro por Dios, Jimmy;
si sobrevivo a esto, voy a ponerme a bailar.

El último boy scout (1991)

Por fín: *habemus tesis!!* Tras varios años de mucho trabajo y esfuerzo, buenos y malos momentos, sudor, sangre y alguna que otra lágrima: ya tienes mi tesis en tus manos. Por supuesto sobra decir que esta tesis nunca hubiera sido posible sin la contribución de toda la gente que ha estado a mi lado durante estos últimos años. Por lo que puedo decir que esta tesis es también VUESTRA. Y como no, que mejor forma de empezar que agradeciendo a todos por vuestro apoyo durante esta etapa. Asi que, como diría Jack el Destripador, *vayamos por partes*:

Los inicios: Todo esto empezó hace ya seis años. Yo estaba en último año de licenciatura, había pensado en dedicarme a la Física Médica y hacer la oposición de Radiofísica Hospitalaria cuando terminase la carrera. Por esa misma época, me enteré de que en el grupo de física nuclear se ofrecían trabajos dirigidos sobre PET, y decidí probar a ver si me gustaba...y ahí me he quedado hasta ahora. En primer lugar debo agradecer a Jose Manuel: por confiar en mí desde el principio y por transmitirme su pasión por lo que hace. También tengo que agradecerle estar siempre disponible para resolver mis dudas y ayudarme en todo lo que he necesitado. A Joaquín, gracias por estar siempre dispuesto a echar una mano y por saber siempre como aportar luz en los momentos más oscuros. También gracias por acogerme en Boston y ayudarme en todo durante esos meses.

A Samuel, gracias por ser mi mentor durante los primeros meses y un modelo a seguir. Elena y Esther, muchas gracias a las dos por compartir todos estos años y por enseñarme a luchar y no darse nunca por vencido. A Borja y Rosa, gracias por ese verano que pasamos juntos: que fue mi primer verano en Madrid y que sin vosotros (y sin Elena, Esther y esas partidas de mus en el parque) hubiera sido muy duro.

También quiero agradecer a Bruno, Esteban (Tico), Khaled y a todos los compañeros de los cursos de doctorado por todo el tiempo que pasamos juntos y por ser todos grandes compañeros y amigos. Y a Pablo sus enseñazas de linux y anti-windows...ahora tienes un mini-yo al que enseñar, espero que no nos defraudes!

Y el tiempo pasó, y casi sin darme cuenta me fuí haciendo mayor, y pasé de ser un pipiolo que no sabía hacer la O con un canuto, a ser un casi doctor que todavía sigue sin saber casi nada (aunque si un poquito más que antes). Alguna gente se fue, y otra vino, y se fueron convirtiendo poco a poco en actores principales de esta historia: Paula y su maravillosa forma de ser. Vadym, un gran compañero de despacho que trae siempre (o casi siempre) comida muy rica. Mailyn, por ser tan maja y traernos un poco de la gracia cubana, y Edu, porque los químicos también molan. Vicky y su corre Sara Connor!! jeje. Richi: que aunque estes en Alemania no te olvidamos. Marie y su Foggtrann. De todos vosotros he aprendido muchísimas cosas y habeis sido (y sois) los mejores compañeros y amigos que uno pueda tener. Otra mucha gente ha pasado por el grupo y ha dejado su semilla, a ellos también les doy las gracias: Paloma, Miguelito, Joaquín Escayo, María Pinto, Marta, Diana, Raul, Irene, Rocio, Nuria y Jorge.

No solo de PET vive el hombre: Y por eso quiero también agradecer a Paloma, por su eficiencia con los papeleos y su buen humor. También Armando, por todos los cafés juntos y sus sabios consejos cuando más falta hacían. A Cristina, Raquel y Javi, por hacer las sobremesas más entretenidas. A Cesar por sus consejos y enseñanzas cuando todavía era un polluelo. También me gustaría agradecer a Jose María, Elvira, Joaquín Retamosa (que dejó una huella imborrable), Luis Mario, Martin, Henryk, Laura, Oscar y Juan Manuel.

Boston: Quiero también agradecer a toda la gente que conocí durante mis estancias en Boston, por hacer que fueran unas experiencias inolvidables. José Venegas and Steve Moore: thank you for giving me the opportunity of working with you and thanks to everyone in your groups. Thank you Elliott, Vanessa and Tilo, for being so nice with me, and thank you Mi-Ae and Morgan for the time we spent together. I also want to thank to all the people involved in the M+Vision Consortium, especially to: Eduardo, (dirty) Shivi, Germán, Nick, Vicente, Cristina Lois, Robert and Daryl.

Qué máis? Pues si, aún hay más: gracias a todos mis amigos y compañeros de la facultad y de Madrid. Gracias Esteban (Walter), Busta, Marta, Juan, Olga, Javi (perilla), Johanna, Irina y Natalia. Gracias por estar siempre ahí. Y Busta, para que no te quejes, ahí va la parte de la tesis escrita en Gallego: Tamén quero dar as grazas ós meus amigos de Lugo, por confiar sempre en min e facerme sentir orgulloso de vós. Grazas Luis, Alicia, Ruben, Tito, Bego, Iván, María, José, Emilio e Gonzalo.

Gracias también a ti, Susana, por aguantarme estos últimos meses, por la paciencia que has mostrado y por ser tan comprensiva conmigo.

No se vayan todavía, que aún hay más: No puedo terminar sin el agradecimiento más importante de todos: A MI FAMILIA. Doy gracias a mis padres (Carlos y Amparo) por la educación y cariño que me han dado. A mi madre y mis hermanos (Nuria, Paula, Carlos y Nacho) por confiar en mi y darme siempre ánimos, incluso cuando mas negro lo veía todo. También a Quique, Edu y Ángeles. A María, Santi, Elvi, y a mis trastos favoritos: Sabela y Noa. Y también a mis tíos, primos, y demás familiares por hacerme sentir orgulloso de la familia que tengo.

Y con esto, ahora sí: ponganse cómodos y disfruten leyendo la tesis que tienen entre sus manos. Y como decía Bruce Willis: *si sobrevivo a esto voy a ponerme a bailar....*

Contents

List of Figures

List of Tables

Summary

Introduction and objectives

Positron Emission Tomography (PET) [Cherry et al., 2003] is a molecular imaging technique that provides a 3D image of functional processes in the body in-vivo.

Since the first PET scanner was developed, positron emission tomography has been established in oncology, cardiology and neurology. With the extension of this technique from clinical to preclinical research, PET scanners for laboratory animals such as mice and rats, with sub-millimetric resolution, have been developed.

Alternatively, several new radionuclides have been proposed for PET imaging, and thousand of PET radiotracers, based on these radionuclides, have been developed.

The utilization of new positron emitter radionuclides for PET imaging raises several questions about their ability to provide images of good quality and to perform accurate quantification. This issue is even more significant when using high resolution scanners designed for the imaging of small animals. Two challenges arise with the use of these radionuclides: their large positron range, which compromise the achievable spatial resolution of the system [Levin and Hoffman, 1999]; and their emission of gamma rays in cascade with positrons, which complicates quantitative PET imaging.

In this thesis we tried to model, by using the Monte Carlo simulation tool developed by our group (PeneloPET, [España et al., 2009]), the effect of positron range and prompt gamma emissions in the image quality in PET. Later, we have used this modeling to correct PET images for positron range and prompt-gamma emissions effects. Further, a method for improving the quantification of PET images was implemented and evaluated in this thesis. In addition, we also modified our simulation tool in order to simulate and analyze triple coincidences in PET, as they have interesting potential applications.

Materials and methods

The algorithms developed in this thesis are not exclusive of any scanner in particular, they have been designed to be flexible and suitable both for preclinical and clinical PET systems. However, in this thesis we have taken advantage of the knowledge and access to real data of the preclinical Argus PET/CT scanner [Wang et al., 2006].

In this thesis we have chosen PeneloPET [España et al., 2009] as our PET simulation tool and PENELOPE [Baró et al., 1995] as the core (with all the physical processes) of our simulations.

PENELOPE is a code for the Monte Carlo simulation of coupled transport of electrons, positrons and photons. It is suitable for the range of energies between 100 eV and 1 GeV, and allows for complex materials and geometries definitions. Penelopet, on the other hand, is a Monte Carlo simulation tool for PET. The basic components of a PeneloPET simulation are detector geometry, materials definition, sources definition, non-active materials in the field-of-view of the scanner and electronic chain of detection. All these components are defined in the input files of the simulation. Different levels of output data are available for analysis, from sinogram and lines-of-response (LORs) histogramming to fully detailed list mode data [España et al., 2009].

The 3D-OSEM reconstruction algorithm used in this work was the FIRST reconstruction procedure. FIRST (Fast Iterative Reconstruction Software for (PET) tomography) is a fully 3D-OSEM reconstruction algorithm implemented by our group (GFN, Universidad Complutense Madrid) [Herraiz et al., 2006], which uses a compressed SRM that contains the resolution recovery properties of EM.

Results and conclusions

We used PeneloPET simulation tool [España et al., 2009] to model positron range for different radionuclides in several biological tissues. Positron range distributions for each radionuclide-tissue combination have been determined and PeneloPET estimations have been compared with previous results found in the literature. Our simulated results were consistent with previous literature, except for the case of [Champion and Le Loirec, 2007], which included Positronium formation in their model. In addition, different algorithms for correcting the effect of positron range in PET imaging have been developed and evaluated. These approaches improve significantly the quality of the reconstructed images, rendering range corrected images for medium-large range radionuclides practical and useful. Furthermore, the use of tissue-dependent and spatially variant positron range correction kernels yields artifact-free and better quality images when several tissues are present within the FOV.

We have modified the PeneloPET simulation tool in order to accurately simulate the decay cascades for some non-pure emitters of interest for PET imaging. We studied the image quality that may be achieved when acquiring with these non-conventional radionuclides and the effect of prompt-gamma emissions in the properties of the reconstructed images. We have seen that this effect is a smooth background in the image, which may be estimated by means of Monte Carlo simulations and introduced into the iterative reconstruction as a background contribution.

On the other hand, we have discussed the implementation and evaluation of the local projection algorithm (LPA) [Moore et al., 2012] to improve the quantification in small volumes of interest in PET images, by compensation for partial volume and spillover effects. We also evaluated the results obtained when the LPA estimations are incorporated into the reconstruction algorithm as a prior. This work was performed for pure (^{18}F) and non-pure emitters (^{68}Ga, ^{124}I), in the Argus PET/CT scanner [Wang et al., 2006]. We have seen that quantification was significantly improved by using LPA, which provided more accurate ratios of lesion-to-background activity concentration for hot and cold regions, both for pure and non-pure emitters. Further, using the activities estimated with the LPA during reconstruction improves the quantification within the volume of interest.

Finally, we implemented a framework to simulate and analyze triple coincidences in PET. We validated our simulation tool by comparison of our simulated estimations against experimental measurements performed in a modified prototype of the Argus PET/CT scanner [Wang et al., 2006], capable of acquire, store and analyze triple coincidence events. We found a good agreement between simulated and experimental results, with discrepancies below 10% in most cases. Inter detector scatter (IDS) events were significant (around 18% respect to standard double coincidences for the Argus scanner) in all the situations studied. This amount of IDS events can be used to increase the sensitivity of the scanner by the same ratio without affecting the resolution or contrast of the image [Lage et al., 2013]. The ratio between $\beta^+\gamma$ events and double coincidences was 2.5 % for ^{124}I in the Argus scanner. Once validated, we used our simulator to evaluate the sensitivity of triple-coincidence detection in two clinical scanners: the Siemens Biograph TPTV [Jakoby et al., 2009] and the GE Discovery-690 [Bettinardi et al., 2011]. For these scanners, we also found a significant amount of IDS events (10 and 17 % respectively), and a $\beta^+\gamma$ events ratio of 4% (using the proper energy window).

In summary, in this thesis we have modeled, using a new release of our PeneloPET code, positron range and prompt-gamma emissions for the most important radionuclides of interest for PET imaging. We also implemented a method to improve the quantification of small volumes of interest in PET images; and finally, we developed and validated a framework able to evaluate the sensitivity of triple-coincidence detection in different scenarios.

General overview and motivation of this thesis

Positron Emission Tomography (PET) [Ollinger and Fessler, 1997] is a molecular imaging technique to image biochemical or physiological processes in-vivo in the body. PET images can be acquired by registering the decay of radionuclides bound to molecules (radiotracers) with known biological properties [Bailey et al., 2005].

Since the first PET scanner was developed in the 1970s, positron emission tomography has been established in oncology, cardiology and neurology. With the extension of this technique from clinical to preclinical research, very high resolution PET scanners for laboratory animals such as mice and rats have been developed. Nowadays, it is possible to obtain PET images with submillimetric resolution and some preclinical PET scanners exhibit sensitivity in excess of 10% [Goertzen et al., 2012].

Alternatively, since the 1970s several new radionuclides such as ^{68}Ga, ^{82}Rb, ^{124}I, ^{94m}Tc, ^{76}Br or ^{86}Y have been proposed for PET imaging, and hundreds of PET radiotracers based on these radionuclides have been developed. The National Institute of Health (NIH) molecular imaging and contrast agent database [MICAD, 2013] lists almost 800 molecular imaging radiotracers with potential clinical and preclinical applications [Vallabhajosula et al., 2011].

Despite the availability of many PET radiotracers, FDG is, by far, the most widely used (90%) radiopharmaceutical for PET [Vallabhajosula et al., 2011]. Nevertheless, the information that the new PET radiopharmaceuticals could provide, would be highly useful for both clinicians and researchers.

The utilization of new positron emitter radionuclides for PET imaging raises several questions about their ability to provide images of good quality and accurate quantification. This issue is even more important when using high resolution scanners designed to image small animals. For such devices, the limit on the spatial resolution is dictated by the decay properties of the radionuclide and positron energy and consequent range, and careful analysis of spatial resolution, contrast and count recovery is mandatory [Laforest et al., 2002].

A challenge associated with the use of some of these positron-emitting radionuclides is that they may emit prompt gamma rays right after the beta decay, which complicates quantitative PET imaging. Other possible complications are the high energies of the emitted positrons, which results in large positron ranges, compromising the achievable spatial resolution of the system [Levin and Hoffman, 1999].

High-energy positrons and their long associated range in tissues, will exhibit reduced spatial resolution and count recovery in small volumes due to partial volume effects [Levin and Hoffman, 1999]. On the other hand, prompt-gamma rays emissions simultaneously with the positrons, will cause a high number of unwanted coincidences by their simultaneous detection with a 511 keV annihilation photon [Lubberink and Herzog, 2011].

It is known that realistic simulations of PET scanners allows for improving all the steps involved in the production of PET images, as for example: the design of the scanner and detectors, the computation of the system response matrix (SRM), the optimization of data acquisition and processing and data corrections [España et al., 2009]. In addition, with the use of Monte Carlo simulation tools [Zaidi, 1999] it is possible to model the effects of positron range and prompt gamma emissions, in order to use this modeling during reconstruction to obtain better images.

In this thesis we developed several approaches to remedy the above mentioned causes of degradation of PET image quality, inherent to the PET technique. To achieve this goal, the Monte Carlo simulation tool developed by our group (PeneloPET, [España et al., 2009]) has been extensively employed, in one side to study positron range and its effect on image quality, and, in the other hand, it has been extended so that it can be used to assess prompt gamma emissions from the less conventional PET radionuclides. Later, we have used this modeling to correct PET images for positron range and prompt-gamma emissions effects.

The knowledge gained from the PET physical processes can be employed during reconstruction to improve image quality. This can be combined with information complementary to the PET imaging process, such as for instance a high resolution image (CT or MRI) co-registered with the PET image. Algorithms aiming to combine the information from two modalities to improve PET images can be developed, and in this thesis we study in depth two of them, a CT-based positron range correction and the local projection approximation to improve quantification in PET images.

The algorithms developed in this thesis can be implemented to any conventional PET scanner. They have been designed to be flexible and suitable both for preclinical and clinical PET systems. However, in this thesis we have taken advantage of the knowledge and access to real data collected by a specific system available at the Medical Imaging Laboratory (Laboratorio de Imagen Médica, LIM) of Hospital General Universitario Gregorio Marañón (Madrid), the Argus PET/CT preclinical scanner [Wang et al., 2006].

The objectives of this thesis can be summarized as follows:

- To obtain positron range distributions for new radionuclides in various human tissues, employing PeneloPET. To validate our simulations by comparison of PeneloPET predictions against other results found in the literature, both for simulations and for experimental measurements.

- To develop positron range correction prescriptions in 3D PET imaging, in order to obtain PET images for medium and large range radionuclides rivaling in spatial resolution to the ones reconstructed with the standard short-range ^{18}F radionuclide.

- To implement and validate $\beta^+\gamma$ decay cascades in our simulation tool, characterizing the prompt-gamma emissions for several radionuclides of interest and studying the quantitative properties of PET imaging with these radionuclides.

- To implement and evaluate a method to improve the quantification in small volumes of interest in PET images, both for pure and non-pure emitters.
- To include in our simulation tool the possibility of simulate and analyze triple coincidences. To validate this tool in order to study triple coincidences in many different PET scanners with several radionuclides of interest.

Thesis outline

This thesis is organized as follows:

- In chapters 1 and 2 we present a theoretical introduction (chapter 1) and the description of the materials and methods employed in this thesis (chapter 2). In chapter 1 the basics concepts of PET imaging are introduced: physics of PET, image reconstruction and corrections, scanner performance parameters and Monte Carlo simulation methods. In chapter 2 we explained the argus PET/CT scanner [Wang et al., 2006], where the algorithms developed in this thesis have been evaluated, PeneloPET [España et al., 2009] and the FIRST reconstruction procedure [Herraiz et al., 2006].
- Chapters 3 and 4 present the modeling of positron range and prompt-gamma emissions for different radionuclides, as well as the effect in PET image quality of these parameters. The validation of the estimations obtained with our simulation tool is also presented in these chapters.
- In chapter 5 we discuss the implementation of different algorithms to correct for positron range in 3D PET image reconstruction. We also evaluate the performance of these algorithms in different situations.
- Chapter 6 presents the implementation and evaluation of either post-reconstruction or during reconstruction methods to improve the quantification of PET images in small volumes of interest which employ complementary high resolution information obtained from a different image modality to PET. These algorithms have been tested both for PET imaging with standard pure emitters and with non-pure radionuclides. We also tested the performance of these methods in combination with positron range correction, for radionuclides with emission of high energy positrons.
- Finally, in chapter 7 we implement and validate a framework to simulate and analyze triple coincidences in PET. Using this framework we evaluate the amount of triple coincidences detected in different PET scanners with several radionuclides.
- At the end of this manuscript we present the general conclusions of the thesis and the publications and conference proceedings derived from this work.

Chapter 1

Theoretical background

1.1 Physics of PET

Positron Emission Tomography (PET) [Cherry et al., 2003] is a functional imaging technique that produces a three-dimensional image of functional processes in the body. The system detects pairs of gamma rays emitted by a positron-emitting radionuclide, which is introduced into the body on a biologically active molecule. This ability to visualize physiological function, combined with anatomic images using for example Computed Tomography (CT) or Magnetic Resonance Imaging (MRI), provides the best available information on tumor staging and diagnostic of other diseases [MacManus et al., 2009].

PET technique is based on the annihilation coincidence detection of the two collinear 511 keV γ rays resulting from the mutual annihilation of a positron with an electron. Positron-electron annihilation occurs most likely at the end of the positron range, when the positron has dissipated all of its kinetic energy and both the positron and electron are essentially at rest [Zanzonico, 2004]. The two emitted γ rays are registered in coincidence by a par of detectors of the scanner defining a Line of Response (LOR) along which the positron annihilation took place. The information stored in every LOR is assembled and employed to reconstruct an image of the activity distribution inside the patient (figure 1.1).

1.1.1 β^+ decay and positron annihilation

Beta particles are fast electrons or positrons produced in the decay of neutrons or protons in neutron or proton rich nuclei [Krane, 1987]. Here we consider the β^+ decay, where in a proton rich nuclei, a positron (e^+) and a neutrino (ν_e) are emitted after the transformation of a proton (p^+) into a neutron (n) via the process:

$$p^+ \rightarrow n + e^+ + \nu_e \tag{1.1}$$

This β^+ process cannot happen to free protons, due to energy constrains, but it is possible in nuclei when it is energetically favorable [Powsner and Powsner, 2006] and it can be described as:

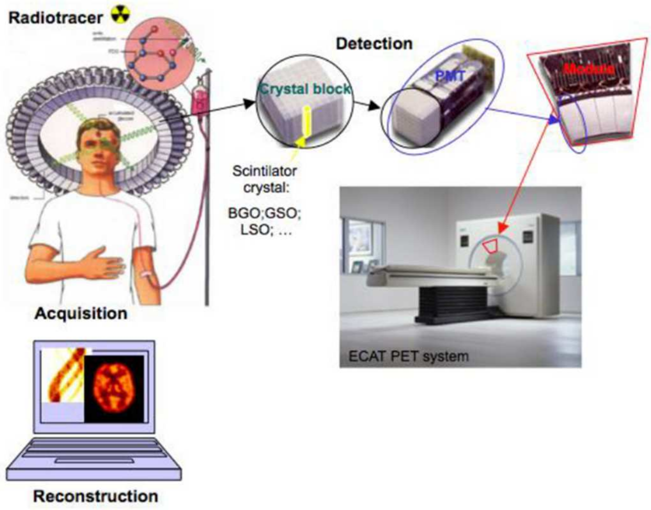

Figure 1.1: Schematic view of a PET scanner (from [Ter-Pogossian, 1982]).

$$\mathrm{X}_N^Z \rightarrow \mathrm{X}_{N+1}^{Z-1} + e^+ + \nu_e \tag{1.2}$$

where X_N^Z represents a father nucleus with Z protons and N neutrons, X_{N+1}^{Z-1} is the daughter nucleus and e^+ and ν_e are the emitted positron and neutrino respectively.

Note that some proton rich nuclei may decay, instead of β^+ mode, by the electron capture process (EC), in which the nucleus absorbs an inner atomic electron, thereby changing a nuclear proton to a neutron and causing the emission of a neutrino (ν_e). The branching ratio (BR) for a particular decay mode is defined as the ratio of the number of atoms decaying by that decay mode to the number decaying in total.

A basic characteristic of the β^+ decay processes is the continuous energy spectra of the β^+ particles. This happens because the available energy in the decay is shared between the β^+ particle and the ν_e. A typical energy spectra for the positrons emitted in a β^+ decay is shown in figure 1.2.

After being emitted in a β^+ decay process, the positron will travel thought the biological media where it was emitted. The most relevant interactions of positrons at these energies within this media are: elastic scattering, inelastic collisions, Bremsstrahlung emission and positron annihilation, either in flight or at rest. The dominant energy loss mechanisms for positrons with intermediate and low energies are inelastic collisions. When the positron reaches thermal velocities (a few eV), it either annihilates directly with an electron into two gammas, or first form an intermediate state called Positronium, in the singlet or triplet state [Berko and Hereford, 1956], [Patro and Sen, 1971], [Westbrook et al., 1987].

The distance between the emission and annihilation point is known as *positron range*, and it is one of the main limiting factors to the spatial resolution of PET scanners [Derenzo, 1979], [Levin and Hoffman, 1999], [Champion and Le Loirec, 2007],[Cal-Gonzalez et al., 2009].

As the majority of annihilations occur with both positron and electron at thermal energies,

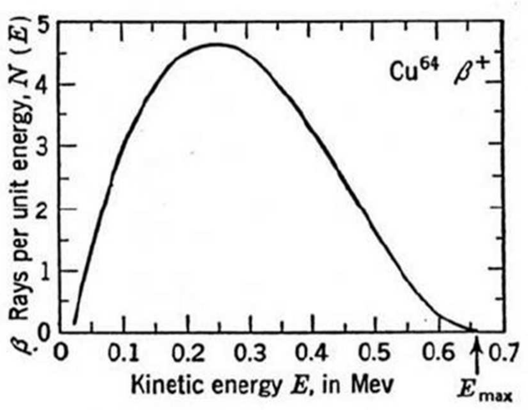

Figure 1.2: Experimental β^+ spectrum obtained from decaying ^{64}Cu. (from [Krane, 1987]).

momentum conservation laws implies that the two annihilation photons are emitted with a relative angle of approximately 180 ° [DeBenedetti et al., 1950], that is, the two emitted photons will be collinear. However, as the momentum (P) of the positron might be not strictly equal to zero, there will be a slight deviation from collinearity, which is given by [Erdman, 1955]:

$$\Delta\varphi = \frac{P}{m_e c} \tag{1.3}$$

where $\Delta\varphi$ is the angular spread (FWHM) of the annihilation photons in reference to 180 °. [DeBenedetti et al., 1950] measured $\Delta\varphi = 0.4\,°$ - $0.5\,°$. This non-collinearity of the photon pair is another limiting factor of spatial resolution in PET [Herraiz et al., 2007].

Figure 1.3 shows a schematic representation of positron range and non-collinearity.

1.1.2 Interactions of γ radiation with matter

For the energy range of interest in PET (from several keV to MeV), the most probably interaction processes of a γ photon with the matter (either the patient or the detectors) are: photoelectric absorption (τ), Compton or Rayleigh scatter (σ) and pair production (only for energies of few MeV, κ). The overall absorption coefficient (μ) results from the sum of these three individual absorption coefficients [Knoll, 2000]:

$$\mu = \tau + \sigma + \kappa \tag{1.4}$$

Thus, the overall absorption can be described by:

$$I = I_0 e^{-\mu x} \tag{1.5}$$

Where I_0 is the incident intensity and I is the intensity after crossing a distance x of material. Here we briefly summarize the main characteristics of these processes:

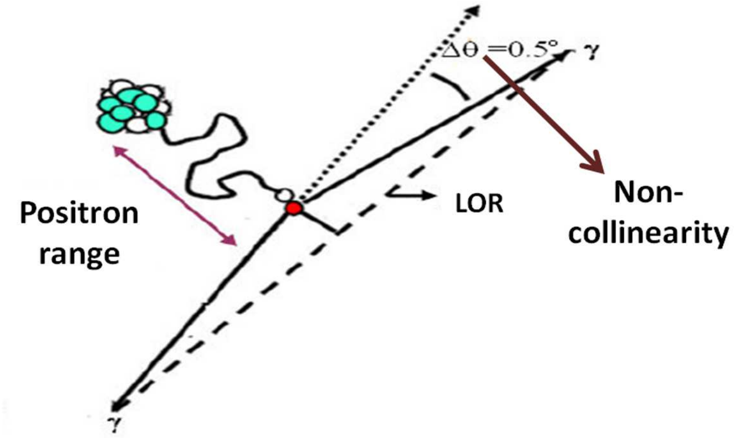

Figure 1.3: Scheme represents the definition of positron range and non-collinearity. From its emission, the positron follows an erratic path until the annihilation process. Non-collinearity is independent of radionuclide, and it is due to the fact that the annihilation does not take place exactly at rest.

Photoelectric absorption: In the photoelectric absorption process, a photon undergoes an interaction with an absorber atom in which the photon completely dissapears. In its place, a photoelectron is ejected by the atom from one of its bound shells. This photoelectron is emitted with an energy [Knoll, 2000]:

$$E_{e^-} = h\nu - E_b \tag{1.6}$$

where E_b represents the binding energy of the photoelectron in its shell. For γ rays of relatively low energy (up to 100 keV), the photoelectric absorption is the predominant mode of interaction (see figures 1.4 and 1.5). This process is also enhanced for absorber materials of high atomic number Z. The probability of photoelectric absorption can be well described by the expression [Knoll, 2000]:

$$\tau \approx constant \cdot \frac{Z^n}{E_\gamma^{3.5}} \tag{1.7}$$

where the exponent n varies between 4 and 5.

PET detectors are designed to have a high photoelectric cross section at 511 keV.

Compton scattering: In this process the γ ray is deflected through and angle θ with respect to its original direction after interacting with an electron in the absorbing material. It is often the predominant interaction mechanism for gamma-rays with the typical energies of radioisotope sources. The photon transfers a portion of its energy to the electron, and the energy transferred to the electron depends on the scattering angle θ and can vary from zero to a large fraction of the initial γ ray energy. The expression that relates the energy transfer and the scattering angle is [Knoll, 2000]:

$$h\nu' = \frac{h\nu}{1 + \frac{h\nu}{m_0c^2}(1 - cos\theta)} \tag{1.8}$$

where m_0c^2 is the rest-mass energy of the electron (511 keV). For small scattering angles θ, very little energy is transferred, and some of the initial energy is always retained by the incident photon, for all angles θ. The angular distribution of scattered gamma rays is predicted by the *Klein-Nishina formula* [Knoll, 2000].

Pair production: If the gamma-ray energy exceeds the rest-mass energy of an electron-positron pair (1.022 MeV), the process of pair production is energetically possible. However, the probability of this interaction is very low until the gamma-ray energy approaches several MeV, so this process is predominant to high energy photons. In this process, the gamma-ray is replaced by an electron-positron pair in the electric field of a nucleus.

A plot of the attenuation coefficients for the different processes described above is shown in figure 1.4 and the relative importance of these three processes for different absorber materials and γ ray energies is depicted in figures 1.4 and 1.5.

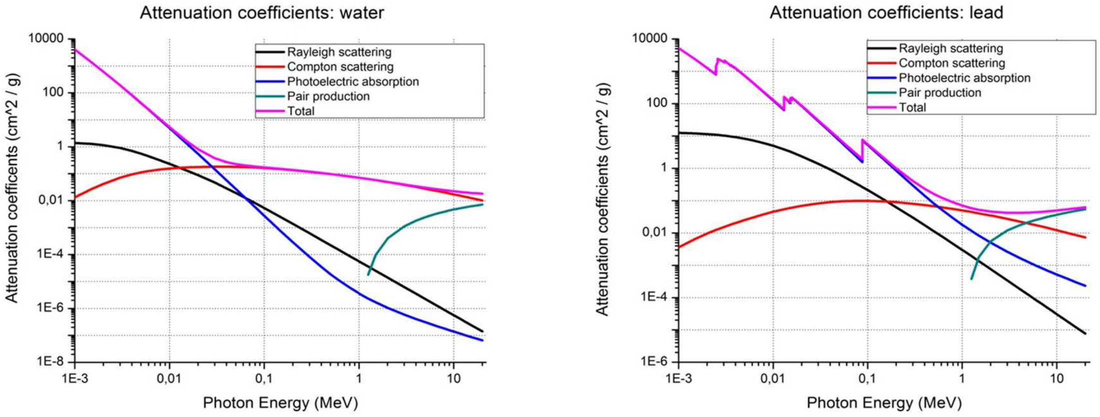

Figure 1.4: Attenuation coefficients for the interactions of photons in water (low Z material, left) and lead (high Z, right). The figure includes photoelectric absorption, Rayleigh and Compton scattering, pair production and the total attenuation coefficient. The main contribution to the total cross section at 511 keV for low Z media is due to Compton scattering, while for high Z media it is shared between Compton scattering and photoelectric absorption. Source: NIST XCOM database [NIST, 2012].

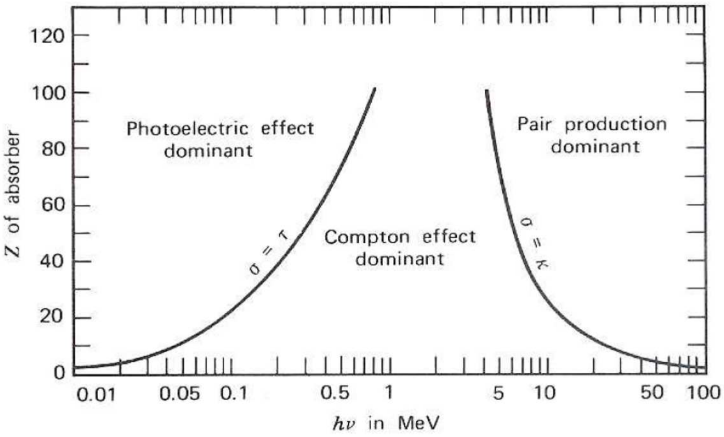

Figure 1.5: Relative importance of the three major types of γ ray interactions. The lines show the values of Z and hν for which the two neighboring effects are the same (from [Evans, 1972]).

1.1.3 PET radionuclides

There are just a few radionuclides that have the adequate chemical and physical properties which make them suitable for *in vivo* biochemical and physiological studies [Raichle, 1983]. The main requisites that a radioisotope suitable for PET imaging are: it must be easy to incorporate into molecules that participate in metabolic processes, it must have a relatively short half-live to reduce significantly the radiation dose to the patient and to the people handling the radionuclides. Most of the positron-emitting radionuclides are produced by using a cyclotron [Bailey et al., 2005], [Valk et al., 2003]; the more used are: ^{18}F, ^{11}C, ^{13}N and ^{15}O. The trade off of these radionuclides is the need for a dedicated cyclotron in the vicinity of the PET facility. In addition, there are other radionuclides, like ^{68}Ga and ^{82}Rb, that are obtained from generators, which contain relatively long-life mother radionuclides. Other radionuclides of potential use in PET are for example: ^{124}I, ^{64}Cu, ^{86}Y, ^{76}Br or ^{94m}Tc. For a complete discussion of this point we suggest to see *chapter 4* of this thesis and [Bailey et al., 2005]. In table 1.1 a list of potentially useful positron-emitting radionuclides is presented.

Many radio-pharmaceuticals have been used for PET imaging; however, only a few are routinely utilized for clinical purposes. Almost all of them are labeled with one of the common positron emitters named above. Of them, ^{18}F is preferred most, since it has a relatively longer half life that allows its supply to remote places. In all cases, a suitable synthesis method is adopted to provide a stable product with good labeling yield, high specific activity, high purity, and most importantly, high in vivo tissue selectivity. Some examples of radio-tracers are shown in table 1.2, together with their typical clinical and research applications.

The largest area of clinical use of PET is in oncology. The most widely used tracer in oncology is ^{18}F-fluoro-deoxy-glucose (^{18}F-FDG), a glucose uptake tracer. This is of interest in oncology because proliferating cancer cells have a higher than average rate of glucose metabolism [Warburg, 1931]. ^{11}C-methionine is also used in oncology, where it acts as a marker for protein synthesis.

Radionuclide	**Half life**	**Production device**	**β^+ branching ratio (%)**
^{18}F	109.8 min	Cyclotron	96.7
^{11}C	20.5 min	Cyclotron	99.8
^{13}N	10.0 min	Cyclotron	99.8
^{15}O	2.0 min	Cyclotron	99.9
^{68}Ga	67.7 min	Generator (from ^{68}Ge)	89.1
^{82}Rb	1.3 min	Generator (from ^{82}Sr)	95.4
^{124}I	4.2 days	Cyclotron	22.7
^{64}Cu	12.8 hours	Cyclotron	17.6
^{76}Br	16.2 hours	Cyclotron	55.0
^{94m}Tc	52.0 min	Cyclotron	70.2
^{86}Y	14.7 hours	Cyclotron	31.9

Table 1.1: Potentially useful positron-emitting radionuclides (adapted from [Bailey et al., 2005]).

PET has also applications in cardiology, where ^{13}N-NH3 is used as a tracer for myocardial perfusion [Marshall et al., 1983]. In addition, PET has been used in a range of conditions in neurology, and in particular in severe focal epilepsy.

It is not the scope of this thesis to describe with detail the synthesis of PET radiopharmaceuticals, for detailed descriptions we suggest the reader to see references [Saha, 2005], [Vallabhajosula et al., 2011], [Wiebe, 2004] and [Nanni et al., 2010].

radionuclide	**Tracer compound**	**Physiological process or function**	**Typical application**	**Reference**
^{18}F	Fluoro-deoxy-glucose (FDG)	glucose metabolism	oncology, neurology and cardiology	[Hoh, 2007]
^{18}F	[^{18}F]Fluoride ion	bone metabolism	oncology	[Hawkins et al., 1992]
^{18}F	[^{18}F]FMISO, [^{18}F]FAZA,[^{18}F]FETA	tumor hypoxia	oncology - response to radiotherapy	[Koh et al., 1995]
^{18}F	[^{18}F]FHBG	gene therapy	gene expression	[Jacobs et al., 2005]
^{11}C	[^{11}C]Choline	choline metabolism	oncology	[Reske et al., 2006]
^{11}C	[^{11}C]Methionine	protein synthesis	oncology	[Hellman et al., 1994]
^{11}C	[^{11}C]Flumazenil	benzodiazepine receptor antagonist	neurology	[Burdette et al., 1995]
^{13}N	[^{13}N]Ammonia	blood perfusion	myocardial perfusion	[Kuhle et al., 1992]
^{15}O	[^{15}O]Carbon Dioxide	blood perfusion	brain activation estudies	[Kanno et al., 1984]
^{15}O	[^{15}O]Water	blood perfusion	brain activation estudies	[Huang et al., 1983]
^{68}Ga	^{68}Ga-DOTATOC, ^{68}Ga-DOTATATE, ^{68}Ga-DOTANOC	receptor binding SSRT	neuroendocrine tumors	[Rufini et al., 2007]
^{82}Rb	^{82}Rb-rubidium chloride	blood perfusion	myocardial perfusion	[Alvarez-Diez et al., 1999]
^{124}I	[^{124}I]MIBG, [^{124}I]IAZA, [^{124}I]IAZG	tumor hypoxia	oncology - response to radiotherapy	[Koehler et al., 2010]

Table 1.2: Examples of existing radio-tracers and their applications.

1.2 Detector design and acquisition protocols

Detection of γ radiation is a very common technique in experimental nuclear physics, actually the knowledge in this field has been adapted to the specific requirements of PET. Essentially, a γ detection system is a block of material where the gamma photon interact, and the γ energy is transformed to a measurable electrical signal.

1.2.1 PET Detectors

The most commonly used detector systems in PET are based on scintillator detectors, because they are fast, have high stopping power and low electronic noise [Knoll, 2000]. A scintillation detector consist of a crystal that produces scintillation light after the interaction with radiation and a photodetector that converts the scintillation light into a electrical signal [Wernick and Aarsvold, 2004], [Melcher, 2000], which will be processed by the electronic system.

Scintillation detectors

An scintillator detector emits light (photons in visible energy range) when it is excited by radiation of higher energy. There are several scintillating materials in use nowadays. They can be classified into organic or inorganic scintillators, in solid, liquid or gaseous forms. For PET applications, inorganic scintillators in solid form are mainly chosen, due to their greater stopping power needed for a high sensitivity. They also have some of the highest light outputs (number of photons emitted per unit of deposited energy), which are usually related to better energy resolution.

The time structure of the light emitted by scintillators can be described by [Ljungberg et al., 1998]:

$$N(t) = N_0 \frac{e^{-t/\tau_{fall}} - e^{-t/\tau_{rise}}}{\tau_{fall} - \tau_{rise}} \tag{1.9}$$

Where N(t) is the number of photons emitted by the scintillator at time *t*, N_0 is the total number of photons emitted, and τ_{fall} and τ_{rise} are fall and rise time constants of the scintillator. The time response of the crystal must be as fast as possible, in order to avoid coincidences of uncorrelated photons and pile-up of consecutive pulses.

Other important factor for PET detectors is the energy resolution. This is the extent to which the detector can distinguish two close lying energies. In general, the energy resolution can be measured by sending a monoenergetic photon beam into the detector and observing the resulting spectrum. The resolution is usually given in terms of *full width half maximum* (FWHM) of the peak. In general, the resolution is a function of the energy deposited in the detector.

PET systems also need to have the best possible spatial resolution. For that purpose, most systems use segmented scintillators to minimize the uncertainty in the interaction position [Casey and Nutt, 1986]. Scanners with blocks made of continuous crystal are less frequently used for high resolution PET scanners [Joung et al., 2001], [Lerche et al., 2005]. Table 1.3 list some of the properties of the most common used scintillators in PET scanners. In addition to these scintillators, new ones continue to be developed. Many of the newer scintillators are based on cerium doping of lanthanide and transition metal elements, as for example: LuAP:Ce, $CeBr_3$, $LuBO_3$:Ce, and others based on lead (Pb), tungsten (W) and gadolinium (Gd).

One possible drawback of Luthetium-based scintillators (such as LSO, LYSO or LuAP) is the intrinsic radioactivity in these scintillator crystals due to the presence of ^{176}Lu, which decays by β^- emission followed by one or more prompt gamma-ray emissions. This leads to intrinsic counts that can influence the image when scanning low levels of activity [Goertzen et al., 2007, Rodrigues et al., 2007, Yamamoto et al., 2005].

	NaI	**BGO**	**GSO**	**LSO**	**LYSO**	**LaBr$_3$**	**BaF$_2$**	**LuAP**
Composition	NaI:Tl	$Bi_4Ge_3O_{12}$	Gd_2SiO_5:Ce	Lu_2SiO_5:Ce	$(LuY)_2SiO_5$:Ce	$LaBr_3$:Ce	BaF_2	LuAP:Ce
Density (g / cm^3)	6.7	7.1	6.7	7.4	7.1	5.3	4.9	8.3
Effective atomic number	51	74	59	66	60	47	54	65
Attenuation coefficient (cm^{-1})	0.34	0.92	0.62	0.87	0.86	0.47	0.44	0.90
Refractive index	1.85	2.15	1.85	1.82	1.81	1.88	-	1.95
Light yield (%NaI:Tl)	100	15	41	75	80	160	5	16
Wavelength for max. emission (nm)	410	480	430	420	420	370	220	365
Decay constant (ns)	230	300	56	40	41	25	0.8	18
Hygroscopic	Yes	No	No	No	No	No	Slight	No

Table 1.3: Physical properties of some scintillators used in PET detectors (from [Levellen, 2008]).

Photodetectors

The photodetectors used in scintillation detectors for PET can be divided in two categories: the photomultiplier tubes (PMTs) and the semiconductor based photosensors: where we can find the avalanche photo-diodes (APDs) and the more recently developed silicon photomultipliers (SiPMs) [España et al., 2010],[Schaart et al., 2009].

Photomultiplier tubes (PMTs) (figure 1.6) represent the oldest and most common technique to measure and detect low levels of scintillator light. They consist of a vacuum enclosure within a thin photocathode layer at the entrance window. The electrons produced in the photocathode are directed by the focusing electrode towards the electron multiplier, where they are multiplied by means of secondary emission. The electron multiplier consist of several electrodes, called dynodes. Each dynode is held at a more positive voltage than the previous one. As the electrons move from the photocathode to the first dynode they are accelerated by the electric field, and after striking this dynode, more low energy electrons are emitted and these are accelerated toward the second dynode. Finally the electrons reach the anode where the accumulation of charge results in a sharp current pulse indicating the arrival of one photon at the photocathode. In summary, the PMT gives an electric pulse with an amplitude proportional to the number of scintillation photons that reaches the photocathode, which is proportional to the energy deposited. The gain is defined as the total number of electrons that arrive to the anode for the production of a single electron in the photocathode. Gains from 10^5 to 10^8 can be reached with these devices. Photomultiplier tubes typically require a power voltage of 1000 to 2000 volts for proper operation. Voltages are distributed to the dynodes by a resistive voltage divider.

As spatial resolution is a key parameter in PET, scintillation arrays must be coupled to a PMT that is able of localize the point where the light has entered the device. For this purpose, position sensitive photomultipliers (PS-PMT) were developed. These devices have an array of anodes where the collected charge is distributed, the distribution of charge among different anodes can be used to calculate the incident light position [Anger, 1969].

One significant drawback of PMTs is their extreme sensitivity to magnetic fields, which makes them unsuitable for use in combination with Magnetic Resonance scanners (MR), which use static and homogeneous magnetic fields higher than 1 T and radio-frequency pulses. Even very weak magnetic field can have an effect on PMT signals due to the deflection of the electron

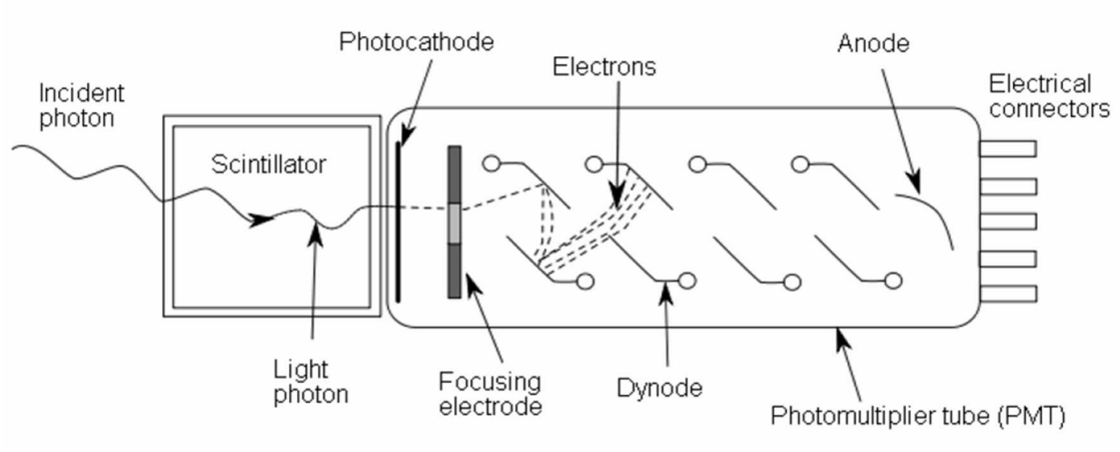

Figure 1.6: Principle of operation of a photomultiplier tube (from [Knoll, 2000]).

trajectories between the photocathode and dynodes (figure 1.6). As shown by [Peng, 2006], significant variations of the gain and energy resolution of PMT-based detectors are observed as soon as the magnetic field is increased above 10 mT, and the ability to decode crystals in a array with PMT-based detectors is rapidly lost as soon as the magnetic field becomes significant [Vaquero et al., 2012].

Solid-state detectors have several inherent advantages over PMTs (table 1.4): high quantum efficiency, compact and flexible shape that can be adapted to individual crystals, ruggedness, demonstrated insensitivity to magnetic fields up to at least 9.4 T and potentially inexpensive mass production.

Avalanche photodiodes (APDs) are semiconductor devices with a low-field depleted region where visible or near-UV photons can create hole-electron pairs by photoelectric effect. In contrast to PMT-based amplification, the amplification process in APD is affected by an excess statistical noise factor that increases with the gain [Webb et al., 1974]. APDs exist as small discrete devices [Lecomte et al., 1985] or as monolithic arrays [Pichler et al., 2004], which can be used for individual or multiplexed crystal readouts. APDs typically have a maximum size limited to about 1 cm^2, due to the difficulty of manufacturing large-area semiconductor devices. The low-noise, fast front-end electronics required for processing signals from individual APD pixels represents a serious burden to the large-scale implementation of this technology in PET systems.

Silicon Photomultipliers (SiPMs) consists of a densely packed matrix of small APD cells biased to be operated above avalanche breakdown in the so-called Geiger mode. All cells are connected in parallel via individual quenching resistors, which are needed to recharge a cell after a breakdown discharge. The Geiger-mode operation yields a high gain (10^5 - 10^6), and the multi-cell structure can provide a proportional output for moderate photon flux by summing all cells that have been activated. These new devices have many attractive properties for implementing in detector designs in PET (table 1.4): gain similar to PMTs that avoids the need for a low-noise electronic front-end, fast response, lower bias (<100 V) and standard MOS semiconductor production process with low fabrication costs. However, SiPMs also have some characteristics that makes their practical use more difficult than expected, as for example: non-linear response, low photon detection efficiency, after-pulsing due to optical crosstalk between cells, high dark current and strong temperature and bias dependence of the gain [Lecomte, 2009].

	PMT	**APD**	**SiPM**
Active area (mm^2)	1- 2000 cm^2	1 - 100 mm^2	1 -10 mm^2
Gain	10^5 - 10^6	10^2	10^5 - 10^6
Dynamic range	10^6	10^4	10^3
Excess noise factor	0.1 - 0.2	>2	1.1 - 1.2
Rise time (ns)	<1	2 - 3	1
Time jitter (ns FWHM)	0.3	>1	0.1
Dark current	<0.1 nA/cm^2	1 - 10 nA/mm^2	0.1 - 1 MHz/mm^2
Photon Detection Efficiency at 420 nm (%)	25	60 - 80	< 40
After-pulsing	Yes	No	Yes
Bias-voltage (V)	1000 - 2000	100 - 1500	< 100
Power consumption	100 mW/ch	10 $\mu W/mm^2$	< 50 $\mu W/mm^2$
Temperature coefficient	< 1 $\%/^oC$	2 -3 $\%/^oC$	3 - 5 $\%/^oC$
Bias coefficient	< 1 $\%/V$	10 $\%/V$	100 $\%/V$
Magnetic susceptibility	Very high (mT)	No (up to 9.4 T)	No (up to 15 T)

Table 1.4: Characteristics of photodetectors for PET (from [Lecomte, 2009]).

Electronics

When a photon reaches a scintillation detector, the electrical pulse generated by the photosensor is used to generate a timing signal and energy/position information. Timing information is obtained by passing the pulse through a constant fraction discriminator (CFD), which generates a digital pulse when the signal reaches a constant fraction of the peak pulse height. This pulse is then used in the coincidence circuit [Knoll, 2000]. The events triggered in a detector are fed into coincidence units that test whether each event is close enough in time to other events from other detectors, so that they can be considered as coincidence events. The time resolution achievable by the scanner is the result of a convolution of the time resolution of the scintillator, photodetector and electronics. It is usually of the order of a few nanoseconds or hundred of picoseconds [Knoll, 2000].

Once pulses have passed all discriminators, the amplitude of the signal, which contain the energy information for the event, must be obtained. All output lines of the PS-PMT that have been triggered are integrated to obtain the total charge for the energy calculation and the position of interaction. This is usually performed by electronic modules that integrate the charge of each output line and convert the resulting integrated charge into a digital number (ADC conversion), that is transmitted and stored in a PC [Lewellen et al., 2001]. Usually there is a lower energy-level discriminator (LLD) and an upper energy-level discriminator (ULD) which may be used to reject pulses below or above particular values.

1.2.2 Data acquisition

The end goal of PET studies is to produce an image, from which quantitative information can be derived. In this section we will discuss the process of collecting data and several possibilities for performing such collection, such as 2D and 3D acquisition modes. We will also discuss strategies for data storage, such as list mode data, LOR histograms or sinograms.

Classification of detected events in PET

Event detection in PET relies on electronic collimation. A event is regarded as valid if: two photons are detected within a predefined time window, the subsequent line-of-response (LOR) formed between them is within a valid acceptance angle of the tomograph, and the energy deposited in the crystal by both photons is within the selected energy window. Such coincident events are referred to as *prompt* event.

However, a number of registered *prompt* events are, in fact, unwanted events as one or both of the photons could have been scattered, or the coincidence is the result of the accidental detection of two photons from unrelated positron annihilations. The detected events in PET can be grouped into the following categories (figure 1.7):

- *Single events:* a single event is a photon counted by a detector. A PET scanner typically converts between 1% and 10% of single events into coincidence events.
- *True coincidence:* is a event that derives from a single positron-electron annihilation. The two photons reach detectors on opposing sides of the tomograph without interacting with the surrounding atoms and are recorded within the energy and time coincidence windows.
- *Random coincidence:* occurs when two nuclei decay at approximately the same time, and two photons coming from different annihilation processes are counted within the timing window and then considered as coincidence event. The number of *random* events is clearly related to the number of disintegrations per second (see *section 1.3.3*).
- *Multiple events:* three (or more) events coming from the same of from different annihilation processes are detected within the coincidence timing window. Due to the ambiguity in deciding which pair of events arises from the same annihilation, these events are generally disregarded or not used appropriately in common PET acquisitions.
- *Scattered events:* when one or both of the photons from one annihilation detected within the coincidence timing window have undergone a Compton interaction. The consequence of counting a scattered event is that the line-of-response (LOR) assigned to the event is uncorrelated with the origin of the annihilation event.

The *prompt* count rate is given by the sum of the *true* + *random* + *scattered* event rates, as all of these events have satisfied the pulse height energy criteria for further processing. The corrections employed for *random* and *scattered* events are discussed in *section 1.3.3.*

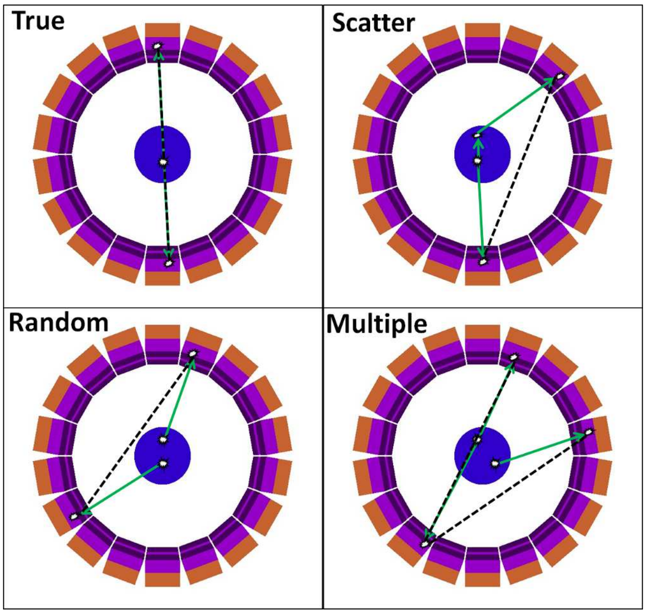

Figure 1.7: The various coincidence events that can be recorded in PET are shown. The line-of-response for each coincidence event is indicated by a dashed line.

2D and 3D acquisition modes

Septal rings can be used to prevent photons coming out of the detector ring plane from reaching the detectors. This improves resolution by reducing the amount of *scattered* and *random* events from photons originating outside the plane of one ring of crystals. The sensitivity of the scanner is reduced, however, because a significant fraction of true coincidence events are rejected. Removal of the septa increases sensitivity and may decrease resolution if effective scatter and random corrections are not used. Scans obtained with the septa in place are called two-dimensional (2D) scans. Scans without septa are called three-dimensional (3D).

The difference between 2D and a 3D acquisitions is: in a 2D acquisition data are collected for LORs that are within the same transaxial plane (each ring can be treated separately). In a 3D acquisition mode, in addition to transaxial planes, data are also acquired for LORs connecting detector elements in different rings: within oblique LORs, corresponding to polar angles different from zero (see figure 1.8). Thus, 3D mode contains all the information of a 2D acquisition, plus the information coming from the oblique LORs [Bailey et al., 2005], [Fahey, 2002]. Therefore, recently the 2D acquisition is not use in the clinical PET scanners. One of the 3D mode dilemma is the huge size of the data collected, hence methods of reduction of the size of data collected in 3D mode are employed.

Sorting of the data acquired

List mode: One way to store the measured coincidences for further processing is to write the information from prompt events in order of occurrence in the acquisition system. An event packet

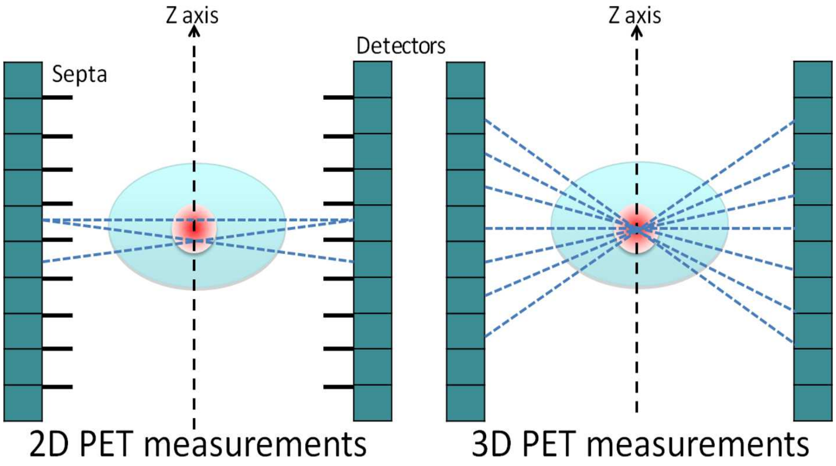

Figure 1.8: Comparison of fully 3-D and 2-D PET measurements. In 2-D mode, scanner only collects direct and cross planes (organized into direct planes). In fully 3-D mode, scanner collects all, or most, oblique planes.

may include: crystal number, photon energy, positioning, etc. In addition, gantry information (as for example count rate and time information) as well as external data (gating and patient motion information) can be inserted into the list mode file [Byme, 2001], [Parra and Barrett, 1998].

The event packets stored are processed afterwards and eventually transformed into sinogram data sets or LORs histograms [Kadrmas, 2004], while the timing information is analyzed so that the data can be split into different time frames.

LOR histograms: Storing the coincidences for each LOR corresponds to the LOR histogram way of organizing the data. The main advantage of the LOR histogram format is to take full benefit of the nominal spatial resolution of the scanner.

This sorting of the data acquired is the one employed in the FIRST [Herraiz et al., 2006] reconstruction procedure for the Argus PET/CT scanner [Wang et al., 2006] (for more details see sections 1 and 3 in *chapter 2*).

Sinograms: Considering the 2D case, a projection is defined as the number of counts in a set of parallel LORs at a specific angle ϕ [Bailey et al., 2005]:

$$P(s,\phi) = \int_{-\infty}^{\infty} f(x,y)dy_r \tag{1.10}$$

This is known as the *Radon Transform* of $f(x,y)$, which is a two-dimensional representation of the activity distribution. s is the radial coordinate and y_r is the transversal direction coordinate of the line defined by (s,ϕ). Projections from all angles can be arranged in a matrix. Because a point source will be represented by a sine curve in this matrix representation (figure 1.9), the matrix is called *sinogram* [Bailey et al., 2005].

Sinograms consist of a histogram representing the number of counts in each (s, ϕ) bin. They are the basic ingredient of most of the image reconstruction algorithms [Bendriem and Townsend, 1998], because they have good mathematical properties [Fahey, 2002].

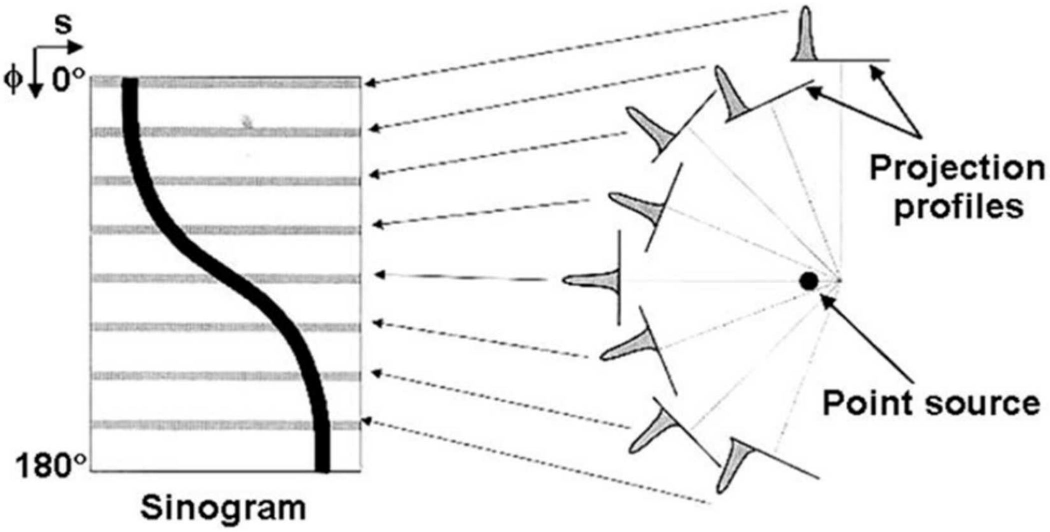

Figure 1.9: The projections of a point source at different angles are represented with a sine curve in a sinogram representation of the data acquired (from [Bailey et al., 2005]).

Michelogram and axial mashing

The Michelogram is a way of dealing with the axial sampling of PET data, devised by C. Michel [Bendriem and Townsend, 1998]. It is used to illustrate and classify the amount of axial data combined. A Michelogram is a grid with two axes, each one with a number of unitary marks equal to the number of rings in the scanner (see figure 1.10). Each point in the grid of the Michelogram corresponds to one sinogram between two rings. On the other hand, it is possible to reduce the size of the 3D mode data, combining several LORs adjacent in the axial direction. This process is called axial mashing and it is a common compression method used in PET scanners. The Michelogram is a good representation tool for axial meshing.

Figure 1.10 shows three different Michelograms corresponding to three different types of acquisitions. The Michelogram in figure 1.10a represents a 2D acquisition, coincidences are allowed just for LORs inside each transaxial plane, so points are along the diagonal. Figure 1.10b is for a 3D acquisition with no restrictions, that is, any ring can be in coincidence with any other. Finally, the Michelogram in figure 1.10c corresponds to a 3D acquisition with mash, a group of planes with the same axial position and neighboring values of ring differences mashed upon one single plane. Thick lines connecting points in the sinogram describe the mashing data that are reassigned to the points in the thin lines. Indeed, this strategy leads to bands, or segments, in the sinogram. The *span* determines the number of axial LORs which will be combined together. Here, the *span* is the sum of the numbers of combined LORs in odd and even planes, that is, 5 (2+3) in this example (points connected by lines in figure 1.10c). The *maximum ring difference* (MRD) defines the maximum allowed ring difference. Data acquired between two rings, where their ring difference exceeds the MRD are discarded [Fahey, 2002].

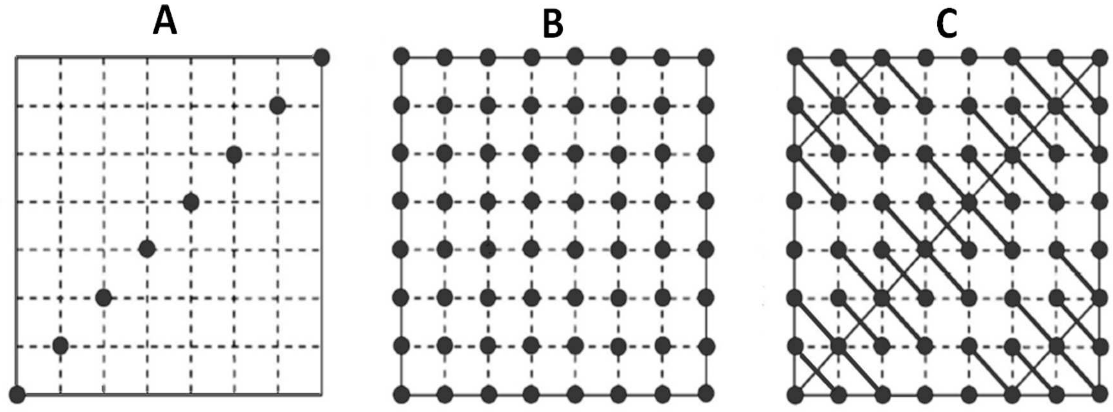

Figure 1.10: Three examples of Michelograms for a 8-ring scanner corresponding to three different acquisitions: 2D acquisition (a), 3D acquisition without mashing (b), and 3D acquisition with mash (c), where the span is 5 (2 + 3) and MRD is 7 (8-1) (Adapted from [Fahey, 2002]).

Data rebinning

Typically, 3D reconstruction algorithms are substantially more complicated and time consuming than 2D methods. Several methods have been developed for rebinning 3D data such that they can be reconstructed with 2D algorithms.

A rebinning algorithm is defined as an algorithm which sorts (rebins) the 3D data into a stack of ordinary 2D data sets, where for each transaxial slice the 2D data are organized as a sinogram. These rebinned data are equivalent geometrically to data collected in the conventional 2-D mode and can therefore be reconstructed by applying the conventional 2D reconstruction algorithms to each slice separately. Thus, rebinning decomposes the 3D reconstruction problem into a set of independent 2D Radon transforms. Provided the rebinning procedure itself is efficient, reconstruction becomes almost as fast as in the 2D mode, while retaining the increased sensitivity of 3D acquisition because the complete set of 3D LORs are used in the reconstruction.

Mainly two approaches are used nowadays in clinical routine: single slice rebinning (SSRB) [Daube-Witherspoon and Muehllehner, 1987] and Fourier rebinning (FORE) [Defrise et al., 1997].

Single slice rebinning (SSRB): This approximate algorithm is based on the assumption that each measured oblique LOR only traverses a single transaxial section within the support of the tracer distribution [Daube-Witherspoon and Muehllehner, 1987]. Then each oblique LOR can be converted into a LOR belonging to the transaxial plane halfway to the planes containing the extremities of the original LOR. This method works well along the central axis of the scanner, but steadily becomes worse with increasing radial distance. The rebinned sinograms are defined by [Bailey et al., 2005]:

$$P_{ssrb}(s,\phi,z) = \frac{1}{2\theta_{max}(s,z)} \int_{-\theta_{max}}^{\theta_{max}} P_s(s,\phi,\zeta = z,\theta)d\theta \tag{1.11}$$

$$\theta_{max}(s,z) = arctan\left(\frac{min[z, L - z]}{\sqrt{R_d^2 - s^2}}\right) \tag{1.12}$$

Where θ_{max} is the maximum axial aperture for a LOR at a distance s from the axis in slice z, R$_d$ is the scanner radius and L the number of transaxial sections sampled. An inspection of the assumption SSRB is based on restricts the use of this algorithm for activity distributions that are spanned within a short radial distance from the scanner axis, as well as for LORs corresponding to small values of θ. For realistic distributions these conditions may not be met and the accuracy of this algorithm is limited. The main advantage of SSRB is its simplicity.

Fourier rebinning (FORE): In FORE algorithm, rebinning is performed by applying the 2D Fourier method to each oblique sinogram in the frequency domain [Defrise et al., 1997]. This method is more accurate than the SSRB method because of the more accurate estimation of the source axial location, and extends the range of 3D PET studies that can be processed using rebinning algorithms [Herraiz, 2008]. The FORE algorithm provides a fast transformation from 3D data to 2D data based on a second-order Taylor series approximation of the 3D Fourier transformation of the data. Rebinning is based on the relation between the Fourier transforms of oblique and direct sinograms [Bailey et al., 2005]. It is given by:

$$P_{fore}(\nu, k, z, 0) = P_s(\nu, k, \zeta = z + k\tan\theta/(2\pi\nu), \theta) \tag{1.13}$$

Where k is the azimuthal Fourier index. The FORE method slightly amplifies the statistical noise, compared to SSRB, but results in significantly less azimuthal distortion.

1.3 Reconstruction algorithms and data corrections

The basic role of image reconstruction is to convert the counts at projections measured at many different angles around the object, into a image that quantitatively reflects the distribution of positron-emitting nuclei. There are two basic approaches to image reconstruction. One approach is analytic and the other is statistic-iterative [Zanzonico and Heller, 2007, Reader and Zaidi, 2007, Alessio and Kinahan, 2006]. Analytic reconstruction methods offer a direct mathematical solution for the problem of image reconstruction based on the inverse Radon transform [Alessio and Kinahan, 2006]. Iterative methods are based on a more accurate description of the imaging process, resulting in a more complicated mathematical solution requiring multiple steps to achieve an image. The iterative methods model the data collection process in a PET scanner and search for, though a serie of iterations, the image that is most consistent with the measured data [Alessio and Kinahan, 2006].

On the other hand, the projected data acquired is affected by a number of factors, namely variations in detector efficiencies, photon attenuation, random coincidences, scattered coincidences, dead time, and parallax error. Quantitative measurements and images free from artifacts require some corrections to the acquired data before, during and after reconstruction.

This section contains a short overview of the image reconstruction algorithms most used in PET among with some of the corrections that are usually applied to PET acquisitions.

1.3.1 Analytic image reconstruction

The central-section theorem: The central-section theorem, also known as the central-slice or Fourier-slice theorem, states that: *the Fourier transform of a one-dimensional projection is equivalent to a section, or profile, at the same angle through the center of the two-dimensional Fourier transform of the object* [Kak and Slaney, 1988]. Figure 1.11 shows a schematic description of this theorem, where $\mathcal{F}_1\{p(s,\phi)\}$ is the one-dimensional Fourier transform of a projection, $\mathcal{F}_2\{f(x,y)\}$ is the two-dimensional Fourier transform of the image and ν_x is the Fourier space conjugate of x. The central-section theorem indicates that if we know $P(\nu_s,\phi)$ at all angles $0 \leq \phi < \pi$, then we can fill in all values for $F(\nu_x,\nu_y)$.

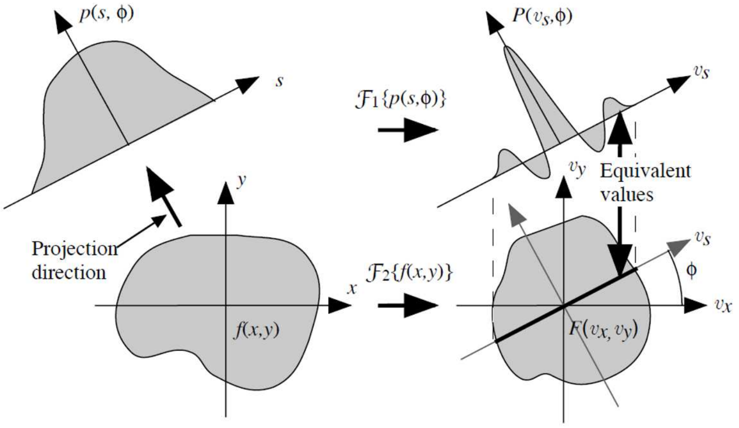

Figure 1.11: Pictorial illustration of the two-dimensional central-section theorem [Alessio and Kinahan, 2006].

Backprojection: An essential step in image reconstruction is backprojection, which is the adjoint to forward projection process that forms the projections of the object. It can be described as placing a value of $p(s,\phi)$ back into an image array along the appropriate LOR, placing a constant value into all elements along the LOR [Henkin et al., 2006]. One may assume that straight backprojection of all the collected projections will return the image, but this is not the case, due to the oversampling in the center of the Fourier transform. This oversampling needs to be re-weighted, or filtered, in order to have equal contributions throughout the field of view.

Reconstruction by backprojection-filtering: After backprojection, the oversampling in the center of Fourier space needs to be filtered in order to have equal sampling throughout the Fourier space. This filtering usually is performed using a cone filter ($\nu = \sqrt{\nu_x^2 + \nu_y^2}$). This cone filter accentuates values at the edge of the Fourier space and de-accentuates values at the center [Alessio and Kinahan, 2006]:

$$F(\nu_x, \nu_y) = \nu \cdot B(\nu_x, \nu_y) \tag{1.14}$$

where $B(\nu_x, \nu_y)$ is the 2-D Fourier transform of the backprojected image and $F(\nu_x, \nu_y)$ is the 2-D Fourier transform of the backprojection-filtered image. The final step is the inverse Fourier transform of $F(\nu_x, \nu_y)$ to obtain the image $f(x, y)$.This method is known as the backprojection-filtering (BPF) image reconstruction method, and is summarized in [Alessio and Kinahan, 2006]. A disadvantage of this approach is that the function $b(x, y)$ has a larger support than $f(x, y)$ due to the convolution with the filter term, which results in gradually decaying values outside the support of $f(x, y)$. This disadvantage can be avoided interchanging the filtering and back-projection steps, in the commonly known filtered-backprojection (FBP) method.

Reconstruction by filtered-backprojection: The filtered-backprojection (FBP) reconstruction method is probably the most well-known standard method for reconstruction which applies the concept of backprojection and filtering explained before. Within FBP, the general expression employed to calculate the source distribution from projection data is [Herman, 1980]:

$$f(x, y) = \int_0^\pi \mathcal{F}_1^{-1}\{|\nu_s| \mathcal{F}_1\{p(s, \phi)\}\} d\phi \tag{1.15}$$

The filtered projection can be regarded as a pre-correction for the oversampling of the Fourier transform of $f(x, y)$. The one-dimensional *ramp* filter, $|\nu_s|$, is a section through the rotationally symmetric two-dimensional cone filter. An advantage of the FBP method is that the ramp filter is applied to each measured projection, and we only need to backproject the filtered projections for $|s|$ less than the radius of the field of view.

Other recent alternatives for implementing FBP have been proposed. These alternatives are based on the Hilbert Transform, which has advantages for truncated sinograms [Defrise et al., 2006, Clackdoyle et al., 2004].

Regularization: The inverse problem of image reconstruction is ill-posed,and its solution, is unstable in the sense that a small perturbation of the data can lead to large changes of the estimate of $f(x, y)$. As photon detection is a stochastic process, some form of regularization is required to constrain the solution space to physically acceptable values. The most common form of regularizing the image reconstruction is by smoothing (removing high-frequency noise). With the FBP algorithm, this can be written as [Alessio and Kinahan, 2006]:

$$f(x, y) = \int_0^\pi \mathcal{F}_1^{-1}\{W(\nu_s)|\nu_s| \mathcal{F}_1\{p(s, \phi)\}\} d\phi \tag{1.16}$$

where $W(\nu_s)$ is the smoothing function, that can take any shape that is deemed most advantageous based on the image SNR, or other considerations. A very common function is the Hamming function [Bendriem and Townsend, 1998].

Analytic 3D image reconstruction

There are two important differences between two and three-dimensional image reconstruction from X-ray transforms: spatially-varying scanner response and data redundancy. In fully-3D mode, the scanner is more sensitive at the center of the field of view. This causes a spatial variance, which complicates the use of analytical reconstruction techniques. On the positive side, 3D data contains redundancies because of the fact that only a single slice of data is required to reconstruct an image.

3D Reprojection Algorithm (3DRP): A common method of restoring spatial invariance to measured 3D X-ray projection data is the 3D reprojection algorithm [Kinahan and Rogers, 1989]. In this method, unmeasured regions of projections are estimated by numerically forward-projecting through an initial estimate of the image. This initial estimate is formed by reconstructing an image using only the direct planes with 2D FBP for each transversal plane [Defrise and Kinahan, 1998].

Another option to reconstruct 3D data using the 2D-FBP method is to first rebin the 3D data into 2D transaxial slices, as discussed in *section 1.2.2*.

1.3.2 Iterative image reconstruction

Iterative methods offer improvements over the analytical approach because they can account for the noise structure of the data and can use a more realistic model of the system (resolution recovery). These more realistic approaches are often solved with methods that successively improve, or iterate, an estimate of the unknown image. This iterative process results in a potentially more accurate estimate than analytical methods, paying the cost of greater computational demands. In the following a short introduction to iterative methods will be presented, references [Leahy and Qi, 2000] and [Natterer and Wübbeling, 2001] offer more detailed discussions.

All iterative methods contain five basic components, which are going to be described in the following:

The first component is *a model of the image.* This is usually a discretization of the image into N distinct voxels. Other models have been proposed, such as spherical elements (blobs) [Matej and Lewitt, 1996] in a hexagonal grid, with overlapping boundaries. Blobs are computationally expensive, but its use can be justified when the maximum resolution achievable may be compromised by the image discretization method [Cabello et al., 2012, Isola et al., 2008].

The second basic component is a *system model* that relates the image to the data. An element A_{ij} of the system model, characterizes the imaging system and represents the probability that an emission from an image element j is detected in projection i. Therefore:

$$\bar{p}_i = \sum_{j=1}^{N} A_{ij} f_j \tag{1.17}$$

where $\bar{p}_i$ is the estimation of the i^{th} projection and f_j is the activity in voxel j as ilustrated in figure 1.12.

The third component is a *model of the data*, which in statistical methods describes the statistical relationship between the measured and the expected value of the measurements. Photon detections are Poisson distributed so, in the majority of methods, a Poisson model is used.

The forth basic component is the *governing principle* that defines the best image. The most common principle for iterative reconstruction is the Maximum Likelihood approach, where the probability relationship is a likelihood function of the object f, in this approach we must choose an estimate of the object $\hat{f}$ that provides the greatest the value of the probability relationship (cost function).

The final component of all iterative methods is an *algorithm* that optimizes the cost function, that is, finds the best image estimate.

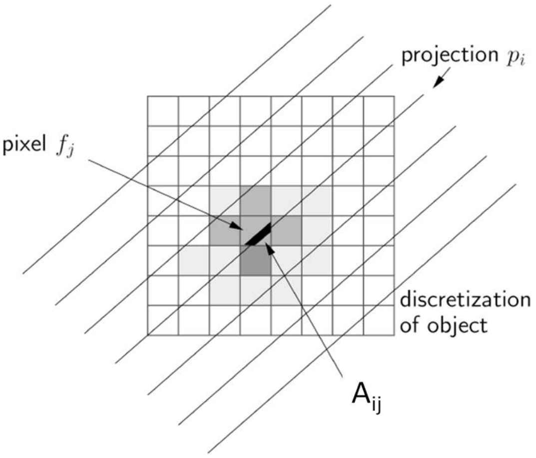

Figure 1.12: Illustration of a single element of the system model matrix A_{ij} (adapted from [Alessio and Kinahan, 2006]).

Maximum Likelihood - Expectation Maximization

The Expectation Maximization (EM) algorithm [Dempster et al., 1977] offers a numerical method for determining a Maximum Likelihood Estimate (MLE). Since its introduction to the field of image reconstruction in 1982 by Shepp and Vardi [Shepp and Vardi, 1982], remains the basis for the most popular statistical reconstruction methods.

The EM-ML algorithm can be written as [Alessio and Kinahan, 2006]:

$$f_j^{(n+1)} = \frac{\hat{f}_j^{(n)}}{\sum_{i'} A_{i'j}} \sum_i A_{ij} \frac{p_i}{\sum_k A_{ik} \hat{f}_k^{(n)}} \tag{1.18}$$

where $f_j^{(n+1)}$ is the next estimate of voxel j based on the current estimate $\hat{f}_k^{(n)}$. The accuracy of the system model is extremely important for the quality of the images resulting from the reconstruction method. Figure 1.13 shows a schematic view of how this algorithm works. The first step (1) forward projects an initial image guess (usually the entire image set to a constant value) into the projection domain. Then, (2) these projections are compared with the measured projections. This forms a multiplicative correction factor for each projection, which is backprojected (3) into image domain to obtain a correction factor for the initial image estimate. This correction factor is multiplied by the current image (4) and divided by a weighting term (based on the system model). The new image estimate is re-entered in the algorithm as the next image.

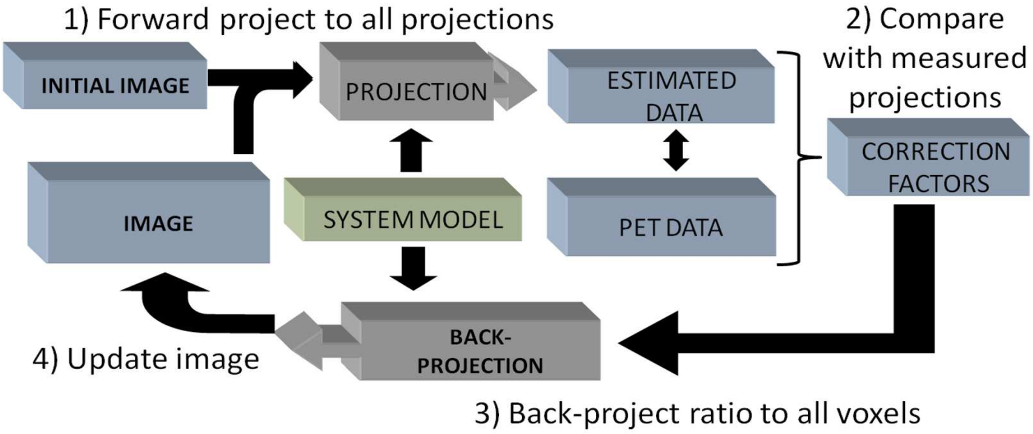

Figure 1.13: Flow diagram of the maximum likelihood-expectation maximization algorithm.

Usually, iterative algorithms based on ML statistical models assume that the data being reconstructed retain Poisson statistics [Shepp and Vardi, 1982]. However, to preserve the Poisson statistical nature of data, it is usually necessary to avoid pre-corrections to the data [Qi et al., 1998]. therefore, corrections for randoms, scatter and other effects should be incorporated into the reconstruction procedure itself, rather than being applied as pre-corrections to the data.

Other alternatives to EM-ML reconstruction algorithm are the iterative image space reconstruction algorithm (ISRA) [Daube-Witherspoon and Muehllehner, 1986], which assume that the statistical nature of data is Gaussian; or the algebraic reconstruction techniques (ART, SIRT or SART, [Kak and Slaney, 1988]).

Ordered Subsets Expectation Maximization

A serious disadvantage of the EM procedure is its slow convergence [Lewitt et al., 1994]. Typically, hundreds of image updates are required. This is due to the fact that the image is updated only after a full iteration is finished, that is, when all the LORs have been projected and back projected at least once.

Ordered Subsets Expectation Maximization (OSEM) was introduced by [Hudson and Larkin, 1994] to reduce reconstruction time of conventional ML-EM. This slight modification of ML-EM uses subsets of the entire data set for each image update in the form:

$$f_j^{(n+1)} = \frac{\hat{f}_j^{(n)}}{\sum_{i' \in S_b} A_{i'j}} \sum_{i \in S_b} A_{ij} \frac{p_i}{\sum_k A_{ik} \hat{f}_k^{(n)}} \tag{1.19}$$

where the backprojection steps sum over only the projections in subset S_b of a total of B subsets. Therefore, the image is updated after each sub-iteration and one complete iteration consist of B image updates. If there is only one subset (B=1), OSEM is equivalent to the ML-EM algorithm.

Bayesian / Penalized Methods

According to the literature, EM methods have another important drawback: noisy images are obtained from over-iterated reconstructions, and this is usually attributed to either the fact that there is no stopping rule in this kind of iterative reconstruction [Johnson87] or to the statistical (noisy) nature of the detection process and reconstruction method [Bettinardi et al., 2002], [Biemond et al., 1990]. Several techniques have been proposed to address the noisy nature of the data: filtering the image either after completion of the reconstruction, during iterations or between them [Slijpen and Beekman, 1999], removal of noise from the data using wavelet based methods [Mair et al., 1996] or smoothing the image with Gaussian kernels (Sieves method) [Snyder et al., 1987], [Liow and Strother, 1991].

Bayesian methods try to improve the quality of the reconstructed image by taking advantage of prior knowledge of the image [Wang and Qi, 2012]. This information is known a priori and is often incorporated into a maximum a posteriori (MAP) objective function [Green, 1990], the typical assumption being that due to the inherent finite resolution of the system the reconstructed image should not have abrupt edges. Thus, MAP methods usually apply a penalty function to those voxels which differ too much from their neighbors. [Qi and Leahy, 2006] provided a good review of MAP regularization.

1.3.3 Data corrections

Quantitative and artifact-free images require applying several corrections to the acquired data, before, during and after reconstruction. This section introduces some of the corrections that are commonly applied to PET acquisitions.

Decay

During a study, the tracer activity decreases due to decay of the radionuclide. Therefore it is necessary to scale the acquired data by a decay correction factor, D_i, which can be calculated as follows [Bailey et al., 2005]:

The number of counts measured during the acquisition is:

$$N = \int_{t_i}^{t_i+\Delta t_i} A(t)dt = \int_{t_i}^{t_i+\Delta t_i} A_0 e^{-\lambda t_i} dt = \frac{A_0}{\lambda} e^{-\lambda t_i}(1 - e^{-\lambda \Delta t_i}) \tag{1.20}$$

where Δt_i is the duration of the frame, A_0 the initial activity and λ the decay constant. If A_i is the mean tracer activity during frame i, we can also write:

$$N = A_i \Delta t_i \qquad A_0 = A_i \cdot D_i \tag{1.21}$$

where D_i is the decay correction factor:

$$D_i = \frac{\Delta t_i \lambda e^{-\lambda t_i}}{1 - e^{-\lambda \Delta t_i}} \tag{1.22}$$

Note that the decay correction factor is only a scale factor for each frame, which can be applied to the images after reconstruction. Decay correction is specially important in dynamic quantitative PET studies.

Attenuation

Annihilation photons in PET are subject to attenuation as they travel through the patient. As consequence, the number of detected photons in each LOR will be reduced. However, if the material properties of the object are known, the measurement along each line of response can be corrected by this attenuation effect [Huang et al., 1979].

The attenuation probability depends exponentially on the attenuation coefficient (μ) of the crossed material and the length traveled inside it. As both photons travel in opposite directions, and the probability of a emission being attenuated is the product the probability of each photon being attenuated, the attenuation does not depend on the point along the LOR where the emission occurred. Therefore, if the distance traveled by one photon is x and the total length of the LOR in the material is D, the number of non-attenuated coincidences is given by:

$$N = N_0 e^{-\mu x} e^{-\mu(D-x)} = N_0 e^{-\mu D} \tag{1.23}$$

This is also true when the source is positioned outside the body. Therefore, the problem of correcting for photon attenuation in the body is equivalent to the determination of the probability of attenuation of all sources lying along every LOR [Bailey et al., 2005].

Different methods to correct for attenuation have been proposed in the literature. In early 2D-PET scanners, the most common approach has been to use a long-lived positron emitter, such as ^{68}Ge - ^{68}Ga, and measure the annihilation photons in coincidence as they pass through the body from an external source (see figure 1.14 a). A transmission scan usually takes 2 - 10 minutes to acquire and may be performed before of after the PET tracer is administered. In scanners with only 3D acquisition mode, the transmission scan explained before is impractical; this is because in 3D the near detector is exposed to an extremely high photon flux arising from the transmission source. An alternative approach was suggested by [Derenzo et al., 1975], in this approach data are acquired with the far detector in singles rather than coincidence mode [deKemp and Nahmias, 1995], [Karp et al., 1995] (figure 1.14 b). Finally, and with the advent of dual modality PET/CT scanners, there has been considerable effort put into developing methods to make use of CT data for PET attenuation correction (figure 1.14 c). The potential advantages of this approach arise because the statistical quality and spatial resolution of CT data is far superior to transmission data conventionally used in PET. The most widely used method nowadays is the hybrid method (proposed by [Kinahan et al., 1998]). Following this procedure, the PET attenuation image is estimated by first using a threshold to separate out the bone component and the soft tissues of the CT image, and then using separate scaling factors for the bone and non-bone component.

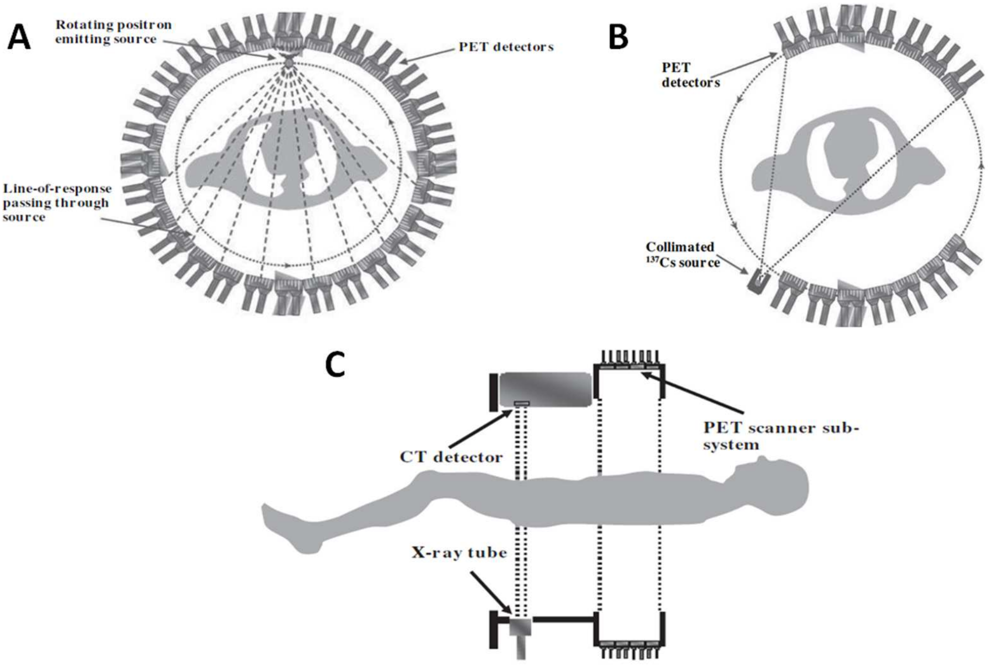

Figure 1.14: Methods of acquiring transmission data for attenuation correction in PET: (a) coincidence measurements using a rotating positron-emitting source, (b) singles measurements and (c) X-ray CT measurements performed on a PET/CT scanner. (Adapted from [Bailey et al., 2005]).

Scatter

When a positron annihilates in the body, there is a reasonable chance that one or both of the annihilation photons will scatter in the body, before being detected, or in the detector itself. Since the coincidence LOR formed after an scattering event is no longer aligned with the annihilation point, such events will degrade the quality of PET images (loss of contrast and quantitative accuracy [Saha, 2010]). The proportion of accepted coincidences which have undergone scattering prior to detection is known as *scatter fraction*, and its magnitude depends on the size and density of scattering media, geometry of PET scanner and the geometry of the energy acceptance window. There are several characteristics of scattered coincidences which can be used to estimate their distribution and potentially correct for it [Bailey et al., 2005]:

- LORs recorded outside the object boundaries can only be explained by scatter in the object, assuming that random coincidences have been subtracted.
- The distribution of scatter counts is very smooth.
- The region of the coincidence energy spectrum below the photopeak has a large contribution from scattered events.

- Scattered coincidences that fall within the photopeak window are mainly due to photons that have scattered only once.

These characteristics have given rise to a wide variety of approaches for estimating and correcting scattered coincidences in PET data. Among them, the more extensively used are: multiple energy window technique or Dual Energy Window (DEW), convolution method, projection profile examination immediately outside the body and simulation methods, as for example the Single Scatter Simulation (SSS) method [Watson, 2000]. The review by [Zaidi, 2006] provides an extensive account on the influence of scatter in patient imaging and methods to correct for it.

Random coincidences

Random coincidences appear when two uncorrelated photons, from two different decays, are detected in coincidence within the timing window. The most evident consequence of random events on a reconstructed image is the introduction of a relatively uniform background which reduces contrast and distorts the relationship between image intensity and activity of the object [Bailey et al., 2005].

The number of random coincidences can be reduced by choosing the scanner geometry so that the FOV for single events is reduced or by reducing the time coincidence window of the system. The background introduced by random coincidences can also be reduced by estimating the number of random counts on each LOR and taking this estimation into account during the reconstruction. The number of random coincidences on a LOR can be estimated using [Cooke et al., 1984]:

$$R_{ij} = 2\tau r_i r_j \tag{1.24}$$

where r_i and r_j are the uncorrelated singles rates on detectors i and j respectively [Oliver and Rafecas, 2008] and τ is the time coincidence window of the system.

Another way of estimating random coincidences employs a delayed coincidence channel. In this scheme, timing signals from one detector are delayed by a time greater than the time coincidence window, and all detected coincidences in this detector will be unrelated, giving a estimation of the number of random coincidences in the prompt signal. This estimation is then subtracted from the number of prompt coincidences [Knoll, 2000] or incorporated into the iterative reconstruction algorithm.

Partial volume and spillover effects

Related with the limited spatial resolution of the PET system, we find the partial volume effect (PVE), which will affect the quantification of PET images, specially for small lesions [Soret et al., 2007]. The PVE refers to 2 distinct phenomena that make intensity values in images differ from what they ideally should be.

The first effect is the 3D image blurring introduced by the limited spatial resolution of the imaging system. This resulting 3D blurring causes spillover between regions, as illustrated in

2 dimensions in figure 1.15A, although the effect is actually 3D. Because of the finite spatial resolution, the image of a small source is a larger but dimmer source.

The second phenomenon causing PVE is image sampling. In PET, the radio-tracer distribution is usually sampled on a voxel grid. Obviously, the contours of the voxels do not match the actual contours of the tracer distribution. Most voxels therefore include different types of tissues. This phenomenon is usually called the tissue fraction effect.

The impact of PVE depends on several factors, as for example: lesion size and shape, surrounding tissues, spatial resolution in the reconstructed images, image sampling and measurement method [Soret et al., 2007]. A large number of methods to correct for PVE have been proposed in the literature, for detailed discussions on this issue we suggest the reader to consult references [Soret et al., 2007, Erlandsson et al., 2012] and *chapter 6* of this thesis.

Other cause of quantitative inaccuracy, closely related to PVE, is the spillover effect (see figure 1.15B). The count spillover phenomenon causes counts to be blurred from inside a structure of interest to outside (spill-out), or from outside to inside (spill-in). These count spillover contributions arise primarily from the limited spatial resolution of nuclear medicine imaging systems, as well as from photon scatter or prompt γ emissions (in non-pure emitters) that are not adequately corrected during reconstruction.

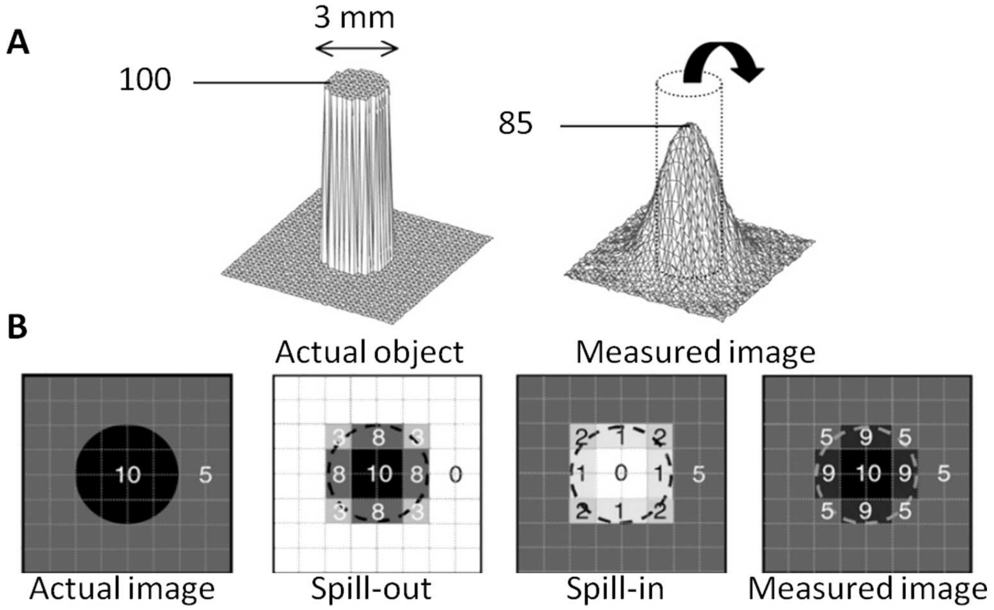

Figure 1.15: A: Illustration of partial volume effect - Circular source of uniform activity in non radioactive background yields measured image in which part of signal emanating from source is seen outside it. B: Spillover - The measured image of the activity distribution results from mixture of spilling-out and spilling-in (adapted from [Soret et al., 2007]).

Normalization

Because of variations in the gain of PMTs, inaccuracies/tolerances in detector block building, physical variation of scintillator efficiency [Bailey et al., 2005], etc., detection sensitivity of a detector pair varies from pair to pair, resulting in non-uniform count rates along, in principle equivalent, detector pairs. Information on these variations is required for the reconstruction of quantitative and artifact free images. The method of correcting these variations is often known as normalization [Badawi and Marsden, 1999], [Hoffman et al., 1989].

Normalization is frequently accomplished by exposing all detector pairs to a uniform activity concentration and distribution to grant the same exposure of all LORs. Normalization factors are calculated for each pair by dividing the average of counts of all equivalent LORs by the individual detector pair count [Bailey et al., 2005], [Cherry et al., 2003]. This process is known as direct normalization. The main problem of this method is that it requires accumulation of a large number of counts in order to achieve an acceptable statistical accuracy for each LOR.

A different approach is to split normalization into different components and treat each one of them separately: this is the so-called *component-based model* for normalization. The normalization is factored into detector efficiency and spatial distortion correction, intrinsic detector efficiency, geometric factors, crystal interference, dead time factors, etc. [Badawi and Marsden, 1999], [Badawi et al., 2000].

Dead time

PET detectors have a limited maximum number of events per second that can be detected and processed. This is caused by the time response of the crystal, the electronics speed, and the delay produced in the data cable and hard disk. If a event is detected while a previous one is being processed, it can be lost.

The parameter that characterizes the counting behavior of the system at high event rates is known as dead-time [Knoll, 2000]. The fractional dead-time of a system at a given count-rate is defined as the ratio of the measured count-rate and the count-rate that would have been obtained if the system behaved in a linear manner [Casey et al., 1995].

Dead-time correction schemes are usually constructed measuring the live-time (1-fractional deadtime) for each subsystem. If this is not possible, an analytic model incorporating knowledge of the system architecture is constructed, and fitted to data from decaying source experiments [Vicente et al., 2013]. The decay correction scheme then consists of applying a set of measured and modeled correction factors to the data acquired.

Dead time models usually treat system dead time as being separable into two components, described as paralyzable and non-paralyzable [Knoll, 2000]. The paralyzable [Knoll, 2000] model describes the situation where the system is unable to process events for a fixed amount of time τ after the detection of an event. Therefore, if an event arrives while the system is busy due to a preceding event, the system remains dead for a further τ seconds from the time of arrival of the second event. The relationship between the measured event rate m, the actual event rate n, and the dead time resulting from a single event is given by:

$$m = ne^{-n\tau} \tag{1.25}$$

In the non-paralyzable case, the system is again rendered dead for a time τ after each event, but while the system is dead, further events have no effect. For this model, the relationship between m, n and τ is given by [Knoll, 2000]:

$$m = \frac{n}{1 - n\tau} \tag{1.26}$$

Pile-up

Pulse pile-up occurs when a photon deposit energy in the detector crystal while the signal from the previous event is still being integrated. Pile-up events cause two types of errors in PET data: the first one occurs when the pile-up event provides a large enough signal to fall outside the energy window and the event is lost. The second error type is event interaction point miss-positioning. This will cause loss of resolution and contrast in the image [Badawi and Marsden, 1999], [Vicente et al., 2007].

Note that, pile-up, when causing loss of counts, can be considered as an ingredient of a general dead-time concept. Such is the case that it is often found in the literature that both dead-time and pile-up effects are referred to simply as dead-time [Vicente, 2012].

Several methods for characterizing the count rates of a PET scanner and data losses due to pile-up and dead-time effects have been proposed [Hoffman et al., 1983, Stearns et al., 1985, Mazoyer et al., 1985, Yamamoto et al., 1986, Eriksson et al., 1994]. These correction methods are usually based on a combination of analytical models that describe the individual electronics components and empirical data derived from phantom scans.

Using dead-time and pile-up recovery, it is also possible that a event with low energy is recovered after the pile-up correction [Vicente et al., 2013].

1.4 Performance evaluation of PET scanners

In this section, the main parameters that characterize a PET scanner performance are discussed.

Energy resolution

Energy resolution is the precision with which the system can measure the energy of incident photons. Energy resolution is usually measured by histograming the energy of each event acquired and plotting the number of events versus the energy measured. Good energy resolution helps to exclude scattered events from the acquisition, which in turns enhances contrast and reduces background in the image [Levin et al., 2006]. Primary causes for the degradation of the energy resolution are random statistical variations, as for example: variations in the number of scintillation light photons produced per keV of energy deposited in the crystal, variations in the number of photoelectrons emitted from the photocathode, or variations in the electron multiplication stage (dynodes) of the PMT [Bailey et al., 2005].

Timing resolution

We define the time resolution of a detector as the minimum time interval between two subsequent photon events in order for these to be recorded as separate events [Knoll, 2000]. In PET, time resolution is typically measured for pairs of detectors that detect many annihilation photon events and is defined as the full width at half maximum (FWHM) of the distribution of time difference between the two detectors, over a large number of coincidence events [Spanoudaki and Levin, 2010].

Obtaining good timing resolution of a PET scanner is a challenging goal because it involves detection of correlated photons that will arrive to the detectors with time differences of a few hundreds of picoseconds. The size of the time coincidence window should be chosen taking into account the timing resolution of the scanner. Since random coincidences are proportional to the coincidence time window, a narrow window helps reducing their occurrence. Hence, for PET imaging, fast scintillators and electronic systems with good timing resolutions are desirable, in order to obtain good timing resolution and therefore reduce the number of random coincidences.

Other scenario where good timing resolution is essential is in clinical Time of Flight (ToF) PET scanners [Moses, 2003]. The time-of-flight (TOF) is the time difference between detection of the two photons produced by the positron annihilation. High resolution measurement of this time difference would allow to determine the precise location at which the annihilation occurred [Abushab, 2013]. Typical time resolutions achieved by non ToF-PET systems lie within the ns range. In the case of ToF-PET, however, such magnitudes are insufficient in order for ToF information to have a benefit over a conventional PET acquisition. The existing commercially available ToF-PET imaging systems [Jakoby et al., 2009, Bettinardi et al., 2011] can achieve time resolutions in the range of 500 ps allowing for a Gaussian weighted localization with a FWHM of 7.5 cm along each LoR [Spanoudaki and Levin, 2010].

Spatial resolution

The spatial resolution of a PET scanner represents the minimum distance (in the image) between two point sources that allows them to be disentangled [Bailey et al., 2005]. Spatial resolution is usually characterized by imaging a point source or a line source and measuring the corresponding full width half maximum (FWHM) of the image of these sources. A Gaussian function is often used as an approximation to this profile. Spatial resolution is usually measured along several directions, in the transaxial plane as well as along the axial direction, as the sampling is not necessarily the same in some PET systems. There are many factors that influence the resolution of a PET reconstruction [Bailey et al., 2005]:

- Positron range after radionuclide decay (*section 1.1.1*).
- Non-collinearity of the annihilation photons due to residual momentum of the positron (*section 1.1.1*).
- Distance between detectors.
- Width of the detectors.

- Stopping power of the scintillation detector.
- Incident angle of the photon reaching the detector.
- Depth of interaction of the photon in the detector.
- Number of angular samples.
- Reconstruction parameters (matrix size, reconstruction filter, etc).

Including all these factors, the best spatial resolution of a PET system can be expressed as [Saha, 2005]:

$$FWHM = 1.2\sqrt{\left(\frac{d}{2}\right)^2 + b^2 + (0.0022D)^2 + r^2 + p^2} \tag{1.27}$$

Where the first factor *(d/2)* is due to the finite dimension of the scintillator pixel elements (of pitch d), b is due to the identification of the pixel where the interaction occurs that may be affected by a certain *coding error*, r indicates the *positron range* contribution, p is due to the *parallax error* and the factor 0.0022 D is given by the *non collinearity* effect. D is the distance between two opposite detectors. The multiplicative factor depends of the used reconstruction algorithm and it is about 1.2 for the analytical *Filtered Back Projection (FBP)* algorithm.

Sensitivity

The sensitivity of a PET scanner quantifies the ability of a scanner to detect the coincident photons emitted from inside the FOV of the scanner. It is mainly determined by the geometry of the scanner and by the stopping power of the detectors for 511 keV photons [Bailey et al., 2005]. The scanner geometry defines the fraction of the total solid angle covered by detectors. The stopping efficiency of a PET detector is related to the type of detector used. The stopping power of the detector is dependent upon the density and Z_{eff} of the crystal used. A high stopping power, which allows for shorter crystals, is desirable for the reduction of parallax error in the images [Bailey et al., 2005].

Scatter fraction

The scatter fraction is defined as the fraction of coincidences recorded in the energy window which have suffered scatter, in either one or two events of the coincidence pairs [Bailey et al., 2005]. Scattered events decrease image contrast in PET images and cause errors in the reconstructed radioactivity distribution.

Scatter can arise from three sources:

- Scattering within the object containing the radionuclide. This is the main scatter source in human imaging [Cherry et al., 2003].
- Scatter at the detector elements.
- Scattering off the gantry components and surrounding equipment, such as side shields.

Count rate performance

Count rate performance refers to the finite time it takes the system to process detected photons. The most common method employed in PET for count rate and dead time determinations is to use a source of a relatively short-lived radionuclide in a multi-frame dynamic acquisition protocol and record a number of frames of data of suitable short duration, over a number of half-lives of the source. Usually a cylinder containing a solution of ^{18}F in water is used. From this, count rates are estimated for true, random, scatter and multiple coincidence events. An example of the count rates achieved for a preclinical PET scanner in is shown in figure 1.16.

The Noise Equivalent Count Rate (NEC) [Strother et al., 1990] is an indicator of the number of useful events that the system can acquire for a given activity level. It is a performance curve suitable to compare count rate performance of different scanners or of the same scanner operating at different conditions [NEMA-NU-2, 2007], [NEMA-NU-4, 2008]. As it is defined in the standard performance comparison methodology, one could say that the NECR represents the count rate which would have result in the same SNR in the image if the data would be free of scatter and random events [Bailey et al., 2005]. The NEC rate has been presented in several approximately equivalent ways, for instance it is defined in [NEMA-NU-2, 2007] as:

$$NEC = \frac{T^2}{T+S+R} \tag{1.28}$$

where T is the true coincidence count rate, S is the count rate of scatter coincidences and R is the count rate of random coincidences. The NEC has been shown to be proportional to the square of the Signal to Noise Ratio (SNR) [Strother et al., 1990], where the signal refers to the true events and the noise to the combined statistical fluctuations from all types of events.

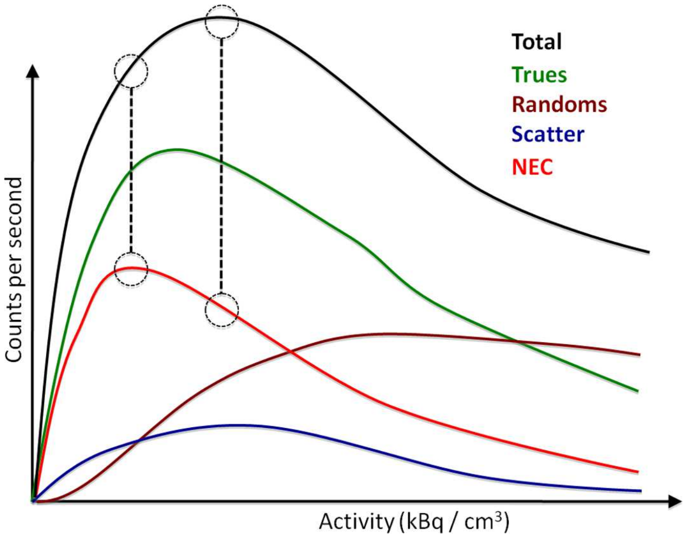

Figure 1.16: Count rate curves for true, random and scatter coincidences, and the NEC curve derived.

Image quality

Because of the complex interplay of different aspects of system performance, it is desirable to be able to compare the image quality of different preclinical or clinical imaging systems for a standardized imaging situation. In order to achieve this aim, a set of measurements have to be carried out on a given phantom (the NEMA IQ phantom [NEMA-NU-4, 2008] for preclinical systems) with different regions simulating a whole-body study.

Several figures of merit may be evaluated in order to determine the image quality of a given scanning system (see [NEMA-NU-4, 2008] for preclinical scanners and [NEMA-NU-2, 2007] for clinical systems):

- **Spatial resolution:** As it was previously described, is the minimum distance (in the image) between two point sources that allows them to be disentangled.
- **Recovery coefficients (RC):** They can be defined as the measured activity concentration divided by the actual activity concentration
- **Noise in the image:** Also defined as percentage standard deviation (%STD). Standard deviation divided by mean multiplied by 100%.
- **Signal to noise ratio (SNR):** Relation between the mean activity in the uniform region (background) and the standard deviation in this region.
- **Spill-over ratio (SOR):** The activity concentration in cold regions relative to the mean activity concentration in the hot background

Contrast recovery coefficients (RC) measured in hot regions are indicative of the resolution and sensitivity of the system. Noise in the uniform region (background) is used to calculate the signal to noise ratio (SNR), while the uniformity in this uniform region is a measure of the accuracy of attenuation and scatter corrections, which can be also obtained from contrast measurements in cold regions.

1.5 Multimodality imaging

Among the existing functional imaging techniques, Positron Emission Tomography (PET) is an extremely sensitive method for quantitative investigation of events at molecular level and has proved to be one of the most powerful methodologies in vivo. Nevertheless, PET reveals the physiology rather than the anatomy. The lack of anatomical information in PET images is a major limitation of PET only studies, and consequently, it has been recognized that for maximizing the potential of PET this technique needs to be combined with an anatomical imaging modality, such as X-ray Computed Tomography (CT) or Magnetic Resonance Imaging (MRI).

In this thesis we will focus in the PET/CT systems, since they are the most common systems present in the market.

1.5.1 PET/CT scanners

A PET/CT system is usually comprised of a PET and a CT scanners, joined together on the same axial axis and with a common patient bed. An important issue in a PET/CT system is the relative positions of the two systems, and then of the two fields of view that should be overlapped during image processing to obtain fused PET/CT images [Townsend et al., 2003]. For the modern systems, the reported maximum displacement error is about 0.5 mm.

PET and CT components in a integrated PET/CT are usually both top end performance scanners so as to be able to produce high quality images in each modality. The CT part of a PET /CT can be also used as a diagnostic tool (higher mAs, contrast media). In addition, PET/CT systems are usually equipped with the gated acquisition modality.

The combination of PET and CT gives much more information with respect to the separate use of the two instruments. The main advantage resides in the possibility to fuse the morphological information obtained from the CT with the functional information from PET. Further advantages of the PET/CT combination are: the possibility to use CT information to correct PET data, to define the region of interest for the calculation of Standardized Uptake Values (SUV) or the correction of partial volume effect. On the other hand, the PET image completes the morphological information of a CT acting like a "metabolic" contrast agent, which is very important for example in the definition of the treatment planning in radiotherapy [Ciernik et al., 2003].

1.5.2 PET/MRI scanners

Even though CT has certain advantages in clinical and pre-clinical imaging, a very attractive alternative to PET/CT is to combine PET with Magnetic Resonance Imaging (MRI), since the repertoire of MRI examinations is highly complementary to PET. MRI reveals structure and functions through the interaction of a strong magnetic field with the protons present in the tissues. The wide variety of imaging sequences, along with better soft-tissue contrast compared with X-ray CT, makes MRI an important diagnostic tool. In addition, MRI does not use ionizing radiation, that is another important advantage compared with CT.

The combination of PET and MRI is still a great challenge for molecular imaging technology [Zaidi and Del Guerra, 2011]. Conventional PET systems use PMTs to detect the scintillation light. However, the PMTs are very sensitive to magnetic fields and, therefore, cannot be operated inside a MRI system. One possible approach to overcome this handicap is to place the PMTs outside the MRI system, connecting them to the scintillator by means of light-guides [Christensen et al., 1999]. However, the need to bring the scintillation light outside of the magnetic field puts stringent topological constraints, limiting the axial field of view what is possible to cover. Other alternative approaches make use of the potential of solid state photo-detectors, such as APDs or SiPMs (see *section 1.2.1*) [Judenhofer et al., 2008], [Degenhardt et al., 2009], [España et al., 2010].

1.6 Monte Carlo simulations

The Monte Carlo methods consist of a very broad area of science, in which many processes, physical systems and phenomena are simulated by statistical methods employing random numbers. Nowadays, Monte Carlo methods are widely used to solve complex physical and mathematical problems [James, 1980], [Kalos and Whitlock, 1986], particularly those involving multiple independent variables where more conventional numerical methods would demand formidable amounts of memory and computer time.

Due to the stochastic nature of radiation emission and detection processes, the Monte Carlo method is particularly interesting for medical physics in areas such as radiotherapy, radiation protection and nuclear medicine [Andreo, 1991]. In fact, this simulation technique is nowadays an essential research tool in nuclear medicine to study the response of imaging systems, predicting the performance of new detectors and optimizing their design [Zaidi, 1999]. In addition, Monte Carlo data is currently essential for the development, validation and comparative evaluation of image reconstruction techniques and for the assessment of correction methods such as photon attenuation and scattering.

The general idea of Monte Carlo analysis is to create a model which is as similar as possible to the real system of interest, and to create interactions within that system based on known probabilities of occurrence, with random sampling of the probability density functions (pdfs). Figure 1.17 illustrates the idea of Monte Carlo or statistical simulation applied to an imaging system.

The main components of a Monte Carlo simulation method are [Zaidi, 1999], [Zaidi and Sgouros, 2003]:

- Probability density functions (pdf's): the physical system must be described by a set of pdf's.
- Random number generator: a source of random numbers uniformly distributed on the unit interval must be available.
- Sampling rule: a prescription for sampling from the specified pdf's.
- Scoring of the outcomes of the simulation.
- Error estimation: an estimate of the statistical error as a function of the number of trials.
- Variance reduction techniques: methods for reducing the statistical error, in order to reduce the computational time for the simulation.
- Parallelization and vectorization algorithms to allow Monte Carlo methods to be implemented efficiently on advanced computer technologies.

Random numbers generators

A key component of a Monte Carlo calculation is the numerical sampling of random variables with specified pdf's. In general, random-sampling algorithms are based on the use of random numbers

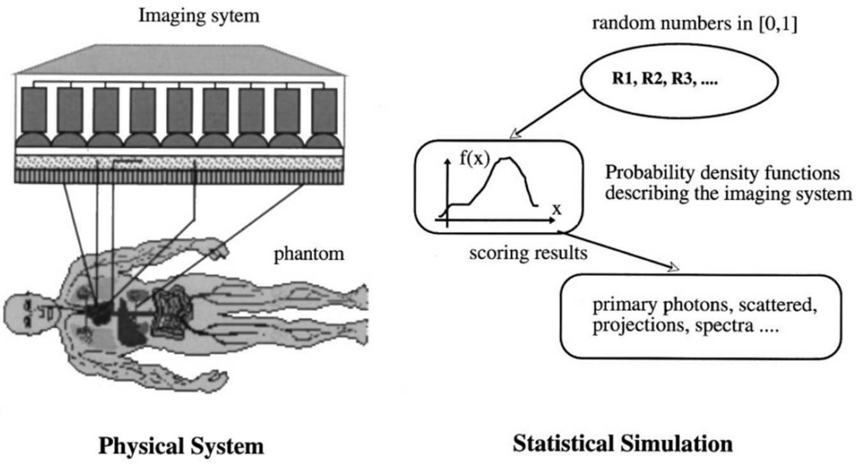

Figure 1.17: Principles of Monte Carlo simulation of an imaging system (adapted from [Zaidi, 1999]).

ξ uniformly distributed in the interval (0,1). Among the "good" random-number generators currently available, the simplest ones are the so-called multiplicative congruential generators [Press, 1992]. A popular example of this kind of generator is:

$$R_n = 7^5 \cdot R_{n-1}(mod 2^{31} - 1), \qquad \xi_n = \frac{R_n}{231 - 1} \tag{1.29}$$

This generator produces a sequence of random numbers ξ_n uniformly distributed in (0,1) from a given "seed" R_0 ($< 2^{31} - 1$). Actually, the generated sequence is not truly random, because it is obtained from a deterministic algorithm, and the term *pseudo-random* would be more appropriate. In any case it is very unlikely that the subtle correlations between the values in the sequence have an appreciable effect on the simulation results.

The probability density function (pdf) of a continuous variable x ($p(x)$) is the function that contains the probability for x taking a specific value. This function must be positive and normalized to unity in a range of values (x_{min}, x_{max}) [Ljungberg et al., 1998]:

$$p(x) \geq 0, \qquad \int_{x_{min}}^{x_{max}} p(x)dx = 1 \tag{1.30}$$

The cumulative distribution function (cdf) of a variable x is the function that contains the probability that the value of the random variable falls within a particular interval $[x_{min}, x]$. It is therefore a non-decreasing function from $P(x_{min}) = 0$ to $P(x_{max}) = 1$ [Ljungberg et al., 1998]:

$$P(x) = \int_{x_{min}}^{x} p(x')dx' = 1 \tag{1.31}$$

Different techniques to generate random values of a variable x, distributed in the interval

(x_{min}, x_{max}) according to a given pdf can be found in [Andreo, 1991], [Ljungberg et al., 1998], [Zaidi, 1999], [Zaidi and Sgouros, 2003] and [Salvat et al., 2008].

Variance reduction methods

A direct (analog sampling) Monte Carlo simulation using true probability functions may require an unacceptably long time to produce statistically relevant results. It is thus desirable to bias the sampling (non-analogue sampling) by introducing different types of importance sampling and other variance reduction techniques to improve the computational efficiency of the Monte Carlo method [Zubal and Harell, 1992]. The results obtained by non-analogue simulation are, however, biased by the variance reduction technique and a correction for this is required. A particle history weight, W, is introduced, which describes the probability of the particle following the current path. This weight is calculated for each particle history, and used in the calculation of the results. [Bielajew and Rogers, 1989] divided variance reduction techniques into three categories: those that concern photon transport only (interaction forcing, Russian roulette or particle splitting), those that concern electron transport only (electron range rejection) and other more general methods (correlated sampling or use of geometry symmetry). A detailed description of these variance reduction methods can be found in [Bielajew and Rogers, 1989], [Zaidi, 1999] and [Zaidi and Sgouros, 2003].

1.6.1 Monte Carlo techniques in Nuclear Medicine

Several Monte Carlo computer codes for the simulation of radiation transport are available in the public domain.

Accurate and versatile generally-aimed simulation packages, such as EGS4 [Rogers, 1984], MCNP [Briesmeister, 1993], PENELOPE [Baró et al., 1995] and Geant4 [Agostinelli, 2003] have been made available. The latter packages require a lot of expertise in order to model emission tomography configurations. Further, SimSET [Harrison et al., 1993], GATE [Jan et al., 2004], Eidolon [Zaidi, 1999], PETSIM [Thomson et al., 1992], PeneloPET [España et al., 2009] and GAMOS [Arce et al., 2008] are powerful simulation codes for specific applications in PET and SPECT. Nowadays, SimSET and GATE are probably the most extensively used [Du et al., 2002], [Lazaro et al., 2004],[Barret et al., 2005]. Table 1.5 shows the principal features of these Monte Carlo codes.

	Voxelized att/act distrib.	Positron range/ Non-collinearity	Pixelated detectors	Randoms	Validated
PETSIM	No	Yes	Yes	Yes	No
GATE	Yes	Yes	Yes	Yes	Yes
Eidolon	Yes	Yes	Yes	No	No
SimSET	Yes	Yes	No	No	Yes
PeneloPET	No / Yes	Yes	Yes	Yes	Yes

Table 1.5: Main features of PET Monte Carlo codes

Chapter 2

Materials and tools

In this chapter we will describe the tools employed to carry out the goals proposed in this thesis. In *section 2.1* we describe the Argus PET/CT preclinical scanner, which is the scanner where the methods studied in the thesis have been tested. In addition, *section 2.2* presents the main features of the Monte Carlo simulation tools employed in this thesis. Finally, the 3D-OSEM reconstruction algorithm used in this work is described in *section 2.3*.

2.1 Argus PET/CT preclinical scanner

The Argus small-animal PET/CT scanner (Sedecal) (table 2.1), formerly eXplore Vista/CT (General Electric) [Wang et al., 2006] consists of 36 PMT detector modules, each one coupled to a dual layer array (phoswich) of 13 × 13 cerium - doped lutetium - yttrium orthosilicate (LYSO) and cerium - doped gadolinium orthosilicate (GSO) scintillation crystals. The GSO layer is optically coupled to a Hamamatsu R8520-C12 position-sensitive photomultiplier (PS-PMT). Each pixel crystal has a cross section of $1.45 \times 1.45\ mm^2$ separated by white reflector of 0.1 mm thick. The resulting pitch size is 1.55 mm and the length of LYSO and GSO layers is 7 and 8 mm respectively. The 36 modules are arranged in two rings of 18 modules each, with a diameter of 11.8 cm.

Each ring is comprised of 18 of these modules, and each module is in coincidence with 14 opposing modules (seven in its own ring and seven in the other ring). This configuration provides a transaxial Field of View (FOV) of 67 mm and axial FOV of 48 mm.

Argus PET system acquires coincidence events in 3D using a data acquisition system based on charge integrating ADC modules (A & D Precision, MA) and a custom coincidence logic controller, all of them connected to the main signal processor using high-speed Ethernet links.

The Argus PET/CT model integrates, in addition to the PET system, a fully functional CT. The CT is composed of a micro-focus X-ray tube and a digital flat panel detector (flat panel CMOS technology with a micro-columnar CsI:Tl scintillator plate) on a rotary gantry.

Item	Parameter	Description or value
Detector modules	Type of module	Dual layer phoswich (front: LYSO, back: GSO)
	Phoswich elements dimensions (LYSO)	1.45 × 1.45 × 7 mm^3
	Phoswich elements dimensions (GSO)	1.45 × 1.45 × 8 mm^3
	Light decay time	LYSO: 40 ns, GSO: 60 ns
	Phoswich element arrays	13 × 13 (outside dimensions: 20 × 20 mm^2
	Phoswich pitch	1.55 mm
	Phototubes	Hamamatsu R8520-C12
System	Number of detector modules	36 (2 rings of 18)
	Number of phoswich elements	6084 (13 × 13 × 36
	Total number of crystals	12168
	Ring diameter	11.8 cm
	Gantry aperture	8.0 cm
	Effective transaxial field of view	6.8 cm
	Normalization or transmission source	^{68}Gaannulus
	Overall dimensions	121 cm wide × 151 cm high × 82 cm deep
	Estimated gantry weight	∼ 200 kg
	Power	120 V alternating current, < 20 A
Datasets	Acquisition mode	3D only
	Total number of Lines of Response (LOR)	28.8 million
	Number of 2D sinograms (direct)	61
	2D sinogram size	175 spatial samples × 128 angles
	2D dataset size	5.2 Megabytes

Table 2.1: Main characteristics of the PET sub-system for the Argus PET / CT preclinical scanner (from [Wang et al., 2006]).

2.1.1 Depth of Interaction (DOI) Detectors

For research studies in biomedical sciences, small animal PET scanners, such as the Argus PET/CT, must be highly sensitive and must have high sensitivity. In order to satisfy the high sensitivity requirement, the scanner should contain long crystals in the radial direction and have a large solid angle. However, parallax error increases with larger crystals.

Depth of interaction (DOI) detectors are one way of achieving high sensitivity without being affected by parallax [Seidel et al., 1999] errors. Many types of DOI detectors have been proposed: a phoswich-type detector using the difference of scintillation decay time of the materials that form the scintillator layers [Seidel et al., 1999], a multiple layer detector with insertions between crystals producing a shift in a two-dimensional projection of the collected light on the PMT [Murayama et al., 1998], a detector that uses the signal ratio of two photo detectors coupled at both ends of crystal elements [Braem et al., 2004], among many other methods.

In the Argus scanner the DOI or parallax-correcting capability is implemented by dual-scintillator phosphor sandwich (phoswich) detector modules [Wang et al., 2006], as depicted in figure 2.1.

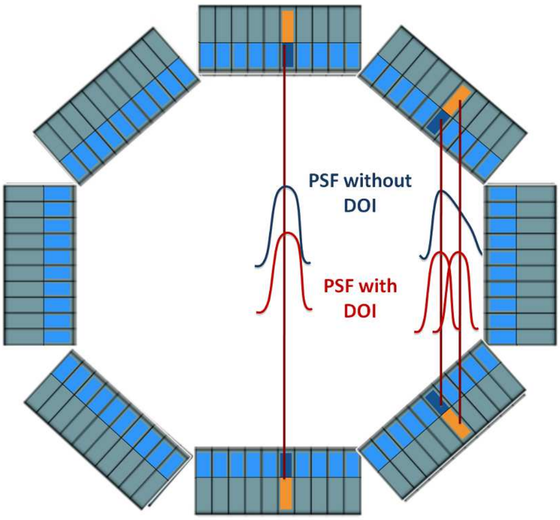

Figure 2.1: Schematic view of the phoswich detector modules with DOI capability. In blue we represent the Point Spread Function (PSF) obtained without using DOI and in red the PSF with DOI. Note that, for simplicity, the number of detectors in the picture do not correspond to the actual number of detectors in the Argus scanner.

2.2 Monte Carlo simulation

In this thesis we have chosen PeneloPET [España et al., 2009] as our PET simulation tool and PENELOPE [Baró et al., 1995] as the core (with all the physical processes) of our simulations. Although our simulation tool is less generally aimed than Geant4 or GATE simulation codes, it suits well PET needs and it is fast, robust and provides accurate results for the transport of photons, electrons and positrons thought matter.

2.2.1 PENELOPE

PENELOPE is a code for the Monte Carlo simulation of coupled transport of electrons, positrons and photons. It is suitable for the range of energies between 100 eV and 1 GeV, and allows for complex materials and geometries definitions. Due to its accuracy and flexibility, PENELOPE is being broadly employed, with numerous applications in the fields of nuclear and medical physics [Sempau and Andreo, 2006], [Panettieri et al., 2007].

PENELOPE consist of a package of subroutines invoked by a main program, which controls the evolution of the stories of particle counters and accumulates the magnitudes of interest for each specific application. These subroutines are written in the Fortran77 programming language, and are distributed by the Nuclear Energy Agency - Organization for Economic Co-operation and Development (NEA - OECD).

The simulation of electrons and positrons includes the following types of interactions:

- Hard elastic collision ($\theta > \theta_c$).

- Hard inelastic collision ($\theta > \theta_c$).
- Hard Bremsstrahlung emission.
- Delta interaction.
- Artificially soft event ($\theta < \theta_c$).
- Inner-Shell impact ionization.
- Annihilation (only for positrons).
- Auxiliary (user defined) interaction: that is, an additional mechanism that may be defined by the user, for example, to simulate photo-nuclear interactions.

On the other hand, the simulation of photons includes the following interactions:

- Coherent scattering (Rayleigh).
- Incoherent scattering (Compton).
- Photoelectric absorption.
- Electron - Positron pair production.
- Delta interaction.
- Auxiliary (user defined) interaction.

Each interaction can lead to secondary particles which can be later tracked and simulated. For further information regarding the physics included in these interaction mechanisms, the reader is referred to [Salvat et al., 2008].

The use of PENELOPE requires to prepare a main program which will be responsible for calling the PENELOPE subroutines and for storing the information about the particles simulated. The main program should provide PENELOPE with the information about the geometry and materials, and also other parameters such as type of particle, energy, position and direction of movement of the particle to be simulated. Through appropriate use of these tools the user can create a simulation environment to carry out the desired studies.

2.2.2 PeneloPET

PeneloPET is a Monte Carlo simulation tool for PET. The PENELOPE package (previously described) is used to simulate the physics of the interaction and transport of radiation though matter. The application makes use of PENELOPE subroutines and other new subroutines that deal with the remaining emission and detection processes.

We have chosen the PeneloPET code in our simulation studies, instead of another simulation tool, because it was developed by our group (GFN, Universidad Complutense de Madrid, [España et al., 2009]) and in consequence we have a better knowledge on it, which means a clear benefit whether modifications are required in order to fit our needs in the different studies to be performed. On the other hand, PeneloPET is an easy to use simulation tool, it allows for realistic simulations of complex systems, including high detail in physics and electronics of the scanner. In summary, because of its versatility, speed and easy-to-analyze outputs, PeneloPET is a powerful tool for scanner design, system response calculations, development of correction methods and many other applications [España et al., 2009], [España, 2009].

The basic components of a PeneloPET simulation are detector geometry, materials definition, sources definition, non-active materials in the field-of-view of the scanner and electronic chain of detection. All these components are defined in the input files of the simulation. Different levels of output data are available for analysis, from sinogram and lines-of-response (LORs) histogramming to fully detailed list mode data. A detailed description of the input and output data of PeneloPET is included in [España et al., 2009], [España, 2009] and [Vicente, 2012].

The PeneloPET package consist of two main modules. The first one deals with the PENELOPE simulations and the level of detail chosen for these, and takes care of the information about scanner detectors and materials, source and decay. This module includes the routines involved in the distribution of isotopes and emission of particles generated in the decay processes, as well as their interactions.

The second module post-processes the decay and interaction data generated by the first module. It takes into account the Anger logic for positioning the interaction inside the crystal array, detector pile-up, energy resolution in the scintillator and aspects of the electronics, such as coincidence time window, dead time, time resolution and integration time. No PENELOPE routines are involved in this second module.

In order to run the simulations on clusters of computers, a simple and portable Python script is provided with the code. After configuring PeneloPET for the execution of the desired setup in a single CPU, the Python script launches the simulation on the number of CPUs desired, with different random seeds, and takes care of the initial activities and the acquisition time for each sub-process, in order to simulate the same number of events in each CPU. In this way, the simulation time may be reduced proportionally to the number of CPUs employed.

The agreement between PeneloPET simulations and the experimental results obtained in real scanners confirms PeneloPET as a powerful tool for PET research and development, as well as for quality assessment of PET images [España et al., 2009], [España, 2009]. Although the examples and studies presented in this thesis deal with preclinical scanners, PeneloPET is also capable of simulating clinical PET scanners [Abushab et al., 2011, Abushab, 2013].

PeneloPET can be obtained under request from the authors. The reader interested can visit: http://nuclear.fis.ucm.es/penelopet for details.

PeneloPET input files

Four input files have to be prepared by the user prior to the simulation. The first input file (*main.inp*) contains the general parameters of the acquisition, as for example the acquisition protocol and acquisition time. It also enables the simulation of secondary particles, if desired, and controls whether positron range and non-collinearity are taken into account. This file contains also information about scanner rotation, energy and coincidence time windows, dead time, output format and type of study. The scanner definition (number of rings and detectors, number of crystals and layers per detector, etc) is included in the *scanner.inp* file. Non-radioactive materials other than the detectors are defined in the *object.inp* file. Finally, the radioactive source is defined separately in the *source.inp* file, which contains source geometry and information about activity and isotope.

Typical materials for crystals, shielding and phantoms are predefined in PeneloPET and, if necessary, new materials can be created in a straightforward way. The visualization tools built in PENELOPE (gview2d, gview3d) are also available in PeneloPET to display and test the geometries to be simulated. Figure 2.2 shows the geometry, visualized with the gview3d program, for the Argus PET/CT scanner described in the previous section.

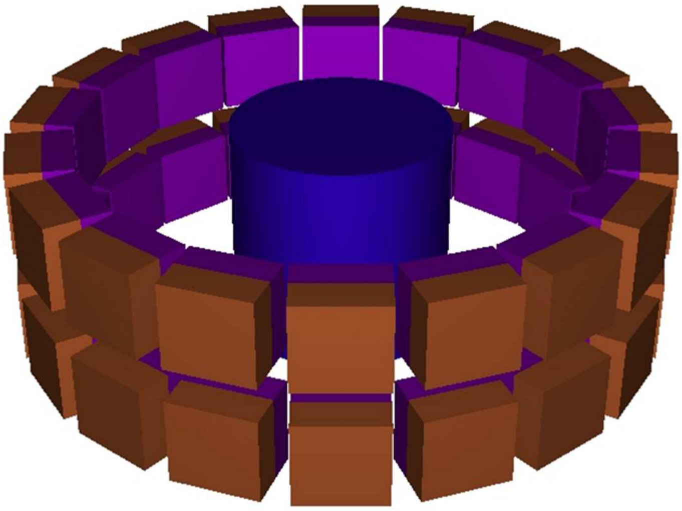

Figure 2.2: View of the sedecal Argus PET/CT scanner [Wang et al., 2006] obtained with the gview3d visualization tool. A water cylinder centered in the FOV can be also observed.

PeneloPET output files

Output files generated by PeneloPET can offer three different levels of detail. At the highest level, all the information about each interaction is recorded. At the second level, just the single events and the information needed for their analysis is recorded. Finally, at the lowest level of detail, only coincidence events are recorded in a compact LIST mode. Information about pile-up, scatter, random and self-coincidence events obtained from the simulation is also available in a final summary report of the simulation.

PeneloPET also generates several output histograms that may help to understand the results of the simulations; as for instance sinogram projections, LOR histograms, single and coincidence maps and energy spectrum.

2.3 Iterative image reconstruction: FIRST

There is a strong demand for fast and accurate reconstruction procedures for high resolution and sensitivity PET scanners, as for example the Argus PET /CT scanner (see *section 2.1*). Since spatial resolutions in the range of 1 mm are required, these kind of scanners employ detectors with many small crystals, thus leading to a very large number of lines of response (LORs), defined by every possible pair of crystals. Moreover, 3D acquisitions (and reconstructions) are mandatory due to sensitivity requirements.

To reconstruct high-resolution images in 3D-PET, iterative methods, such as OSEM, are superior to analytical reconstruction algorithms. Although their high computational cost is still a drawback [Johnson et al., 1997, Herraiz et al., 2006], the performance of modern computers can make iterative image reconstruction fast enough and able of dealing with the large number of probability coefficients of the system response matrix.

As it was discussed in *chapter 1 (section 1.3.2)*, one of the key advantages of iterative reconstructions is the ability to incorporate accurate models of the PET acquisition process through the use of the system response matrix (SRM). However, SRM for 3D systems are of the order of several billions of elements, which imposes serious demands for statistical iterative methods in terms of the time required to complete the reconstruction procedure and the computer memory needed for the storage of the SRM.

FIRST (Fast Iterative Reconstruction Software for (PET) tomography) is a fully 3D-OSEM non sinogram-based reconstruction algorithm implemented by our group (GFN, Universidad Complutense Madrid) [Herraiz et al., 2006], which uses a compressed SRM that contains the resolution recovery properties of EM.

2.3.1 System Response Matrix (SRM)

The SRM is composed of all the $V \times L$ probability elements $A(i,j), i = 1, ..., L$ and $j = 1, ..., V$, representing the probability of detecting an event coming from voxel $V(j)$ at LOR $L(i)$. This matrix depends on factors such as the physics of beta decay, attenuation and scatter in the source volume, solid angle subtended from voxel to detector element and intrinsic detector response characteristics.

For the Argus PET/CT scanner studied in this thesis (see *section 3.1* and [Wang et al., 2006]) the number of LORs is over 2.8×10^7 (see table 2.1, *section 3.1*). At a nominal image resolution of $175 \times 175 \times 62$ voxels (that is near 1.9 million of voxels), the number of elements in the SRM (number of LORs × number of voxels) is of the order of 5×10^{13}. Storing all these elements of the SRM would require more than 10 Tb [Rafecas et al., 2004]. This storage requirement exceeds the resources of an ordinary workstation. Then it is mandatory to disregard all redundant elements and to perform approximations in order to be able to store the SRM within the amount of RAM available in ordinary workstations.

In the FIRST software, three techniques have been used to achieve this goal: removal of null or almost-null elements (matrix sparseness), intensive use of system symmetries and compression of the resulting SRM employing quasi-symmetries [Herraiz et al., 2006].

Matrix sparseness

Every detector pair might receive coincidence counts only from a relatively small portion of the FOV. Therefore, most elements of the SRM will be null and only the non-zero elements should be stored. The voxels connected to a given LOR (voxels from which the positron decay can produce with non-negligible probability a valid coincidence count in the detectors that define the LOR) constitute the so-called channel of response (CHOR) [Michel et al., 2000] for that LOR. In the FIRST reconstruction procedure, we consider a voxel not connected to a LOR if the probability that a positron emitted from this voxel yields a count in the corresponding LOR is smaller than 1-thousandth of the maximum value for all the voxels connected to the given LOR. Using this criteria, the number of non-zero elements in the SRM for the Argus scanner is only a 0.2% of the total. However, storing these non-zero elements (floats, 4 bytes per element) will require about 600 Gb of disk space, which is still to high for the current RAM amount of industry-standard computers.

System symmetries and quasi-symmetries

An additional reduction factor of approximately 40 in the number of non-null SRM elements can be achieved by assuming that exact axial (translation and reflection) and in-plane symmetries exist [Johnson and Sofer, 1999]. The symmetries that might be used to reduce the size of the SRM are:

- Z-translation symmetry, due to the fact that voxels in the same relative position of the CHOR and belonging to parallel CHORs should have equal values (figure 2.3).
- Z-reflection symmetry (figure 2.3). Using both parallel and reflection Z-symmetries, the number of elements to be stored is reduced considerably,
- Reflection symmetry among blocks in the XY plane. Using this symmetry, the number of pairs of detectors that have CHORs with different values is reduced by a factor of 3.

Finally, additional reduction of the SRM can be obtained by using additional non-exact symmetries, or *quasi-symmetries*. If we allow for relatively small differences between *quasi-symmetric* elements of the SRM, we cab group certain LORs into sets of the same quasi-symmetry class. The differences between the elements of the SRM for LORs belonging to a given class should be much smaller than between LORs belonging to different classes. This procedure is illustrated in figure 2.4, where LORs 1-3 are parallel or almost parallel to the crystals and thus the probability values along these three CHORs should be very similar. Analogously, LORs 4-6 have a large LOR-crystal angle, similar for the three of them.

Quasi-symmetry classes can be obtained, for instance, by grouping together LORs from crystals with different, but very close, LOR-crystal orientations. The differences among the elements of the same quasi-symmetry class are about 5-10%, depending of the amount of compression desired.

The processes described above lead to a compression of the SRM to 30-150 Mb, depending of the degree of quasi-symmetry assumed. Besides, the elements of the SRM are stored as cubic spline profiles and matched to voxel size during reconstruction. In this way, the advantages

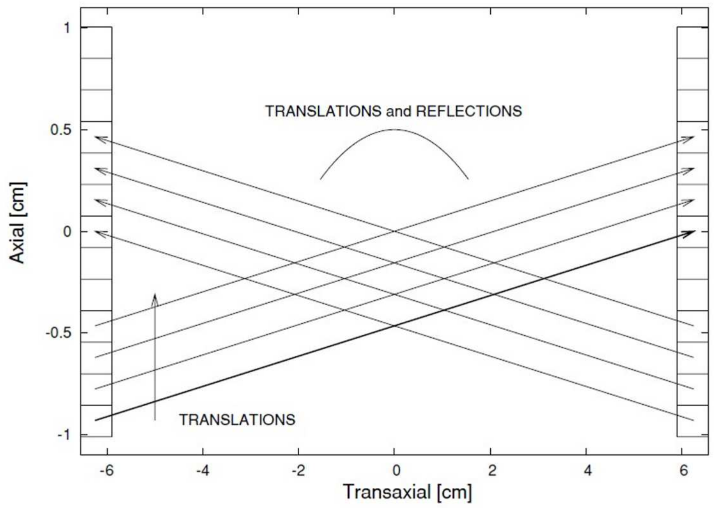

Figure 2.3: Schematic drawing of an Argus small animal PET scanner detector pair, showing the (exact) translation and reflection symmetries employed in the FIRST reconstruction procedure. All the elements of the SRM belonging to parallel LORs are, by symmetry, equivalent (from [Herraiz et al., 2006]).

of on-the-fly calculation and of fully stored SRM are combined. The on-the-fly part of the calculation (matching the profile functions to voxel size) of the SRM accounts for 10-30% of the reconstruction time, depending on the number of voxels chosen.

Monte Carlo calculation of the SRM

Given the fact that the compressed SRM fits in RAM, it does not need to be computed during reconstruction, nor read from disk once loaded in memory at the beginning of the reconstruction. Thus,the SRM can be computed using a very realistic model and stored once and for all. Monte Carlo (MC) methods are,in principle, well suited to provide realistic estimates of SRM elements. In our case, we use or PeneloPET MC code,which includes scatter and incomplete collection of energy in the scintillator crystals, positron range and non-collinearity effects. Positron range is dependent on the emission energy of the isotope and on the annihilation media. In order to incorporate its effect in the SRM, in our simulations the range is computed assuming that ^{18}F is the positron emitter and water as annihilation media. Positron range for other isotopes and tissues can be modeled by introducing an additional blurring during the reconstruction procedure (see *chapter 5*). We also include the scatter of gamma photons when they reach the scintillator crystals.

A large number of simulated events are accumulated until the statistical uncertainty is below 5% at the center of a typical LOR. The calculation of the SRM requires around one week of computing time in a cluster composed of 12 industry-standard workstations.

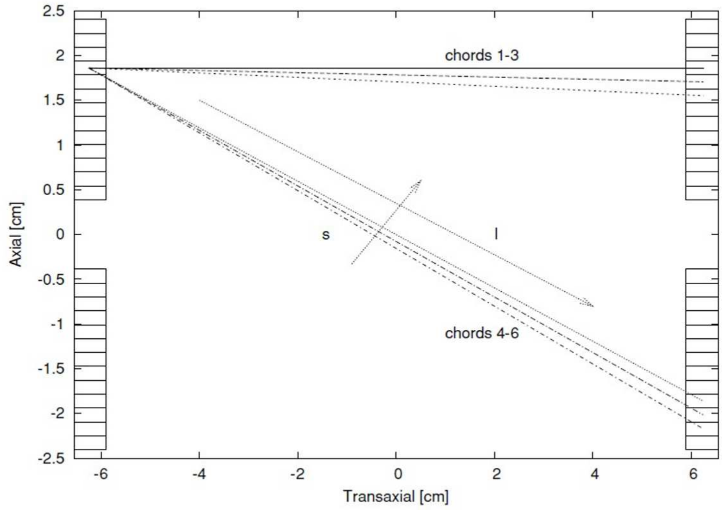

Figure 2.4: Schematic representation of several lines of response (LOR) considered for the discussion on quasi-symmetries. Three LORs (numbered 1-3 from top to bottom) with a small relative LOR-crystal angle and three (numbered 4-6, also from top to bottom) with large relative LOR-crystal angle are depicted. l and s are the coordinates along the LOR direction and normal to it, respectively (from [Herraiz et al., 2006])

2.3.2 FIRST

In order to address the issue of the noisy nature of the data, an OSEM algorithm that includes the possibility of Maximum A Priori (MAP) by means of a generalized one-step late MAP-OSEM algorithm has been implemented. This MAP-OSEM algorithm is similar to the one described in [Lewitt and Matej, 2003, Kadrmas, 2004], and is given by:

$$x_j^{n,s+1} = x_j^{n,s} \left[\frac{\sum\limits_{i \in Subset(S)} A_{ij} \dfrac{y_i}{(R_i^n + S_i)}}{\sum\limits_{i \in Subset(S)} A_{ij}(1 + P_{j,n})} \right] \tag{2.1}$$

Where x_j is the activity of voxel j ($j = 1$, maximum voxel number V), $x_j^{n,s}$ is the expected value of voxel j at iteration n and subiteration S, $A_{i,j}$ is the SRM of the system, that is: the probability that a photon emitted from voxel j is detected at LOR i, y_i is the projection from the object measured at LOR i (experimental data), S_i is the object scatter and random coincidences at LOR i, $P_{j,n}$ is the penalty value at voxel j and iteration n, and R_i^n is the projection estimated for the image reconstructed at iteration n:

$$R_i^n = \sum_{j=1}^{Maxvoxel} A_{ij} x_j^n \tag{2.2}$$

This MAP-OSEM algorithm can be considered as a generalization of the MLEM. It incorporates a penalty MAP function which can be chosen in different ways (Stayman and Fessler 2001, Yu and Fessler 2002, Nuyts and Fessler 2003), and scatter and random counts estimates that may require additional modeling of these processes. OSEM reconstruction without MAP regularization is obtained by setting the penalty function to zero.

In summary, FIRST is a fully 3D-OSEM or 3D-MAP-OSEM non-sinogram-based reconstruction algorithm, which use a compressed SRM that contains the resolution recovery properties of EM. The full SRM can be stored in less than 150 MB of storage, obtaining reconstructed images indistinguishable from the ones obtained without compression. The use of the compressed SRM allowed for a reconstruction with a more realistic response of the system.The calculation of the realistic SRM was performed using a MC model of the scanner which incorporates physical effects such as positron range, non-collinearity and scatter in the scintillator material. The SRM is computed only once, and stored in compressed form so that the reconstruction program could keep it in dynamic memory.

MPI and GPU implementations of the FIRST algorithm

In addition, the FIRST reconstruction procedure can include the usage of the Message Passing Interface (MPI) protocol [Gropp et al., 1999] to launch parallel task on the available CPUs (or CPU cores) in a cluster of computers. The parallel version of the FIRST sofware is designed to run in clusters of several CPUs in a master / slave configuration, characterized by the use of a master process and several (usually as many as the number of available CPUs) slave processes. The master distributes the job among the slaves and continuously balances the workload to achieve the best performance taking into account differences in individual speed or workload on each CPU. The slave processes perform the CPU intensive calculations, such as the forward and backward projections.

A potential acceleration of the reconstruction procedure might be achieved by using massive parallelization of the main time consuming parts of the code (forward and backward projections) in Graphics Processing Units (GPU) [Jones and Yao, 2004, Hong et al., 2007]. GFIRST is an adaptation of FIRST to use the efficient computing capabilities of GPUs developed by our group [Herraiz et al., 2011a]. The code is implemented in CUDA [NVIDIA, 2010], an application programming interface (API), which allows writing programs in C language with extensions to execute part of them (CUDA kernels) on the GPU. Since forward and backward projections take up most of the reconstruction time, only these two steps are implemented as CUDA kernels called from the main reconstruction C code, running in the CPU.

Chapter 3

Positron range modeling

3.1 Introduction and motivation

One of the most important sources of resolution degradation in PET imaging is the positron range, particularly for certain radionuclides and materials. The degree of image blurring depends on the positron kinetic energy, since larger energies lead to longer paths before annihilation. Positron range also depends on the surrounding tissue type in such a way that in those tissues with lower electron density positron ranges are larger. In this chapter we will study the positron range blurring effect for the most common used PET radioisotopes (^{18}F, ^{11}C, ^{13}N, ^{15}O, ^{68}Ga and ^{82}Rb) in different biological media (cortical bone, soft bone, skin, muscle striated, brain, water, adipose tissue and lung).

The blurring effect of the positron range may be described as a contribution to the system Point Spread Function (PSF) [Derenzo, 1986], [Haber et al., 1990]. Recent studies have proposed the use of space-variant PSF functions [Rapisarda et al., 2010] to obtain optimal range-corrected PET images [Bai et al., 2003, 2005, Fu and Qi, 2010, Cal-González et al., 2011b]. In order to develop accurate positron range correction techniques it is essential to properly characterize the positron range, both with simulation and experimental studies. Positron range correction in image reconstruction is of particular importance when dealing with small-animal PET studies or when radioisotopes with large positron range are involved.

Early experimental efforts [Phelps et al., 1975, Cho et al., 1975, Hoffman et al., 1976] to measure positron range in water for medically important positron emitters were of limited accuracy because the resolution of the detector was comparable to the positron range. [Derenzo, 1979] measured annihilation point spread distributions in low-density polyurethane foam, where positron range is significantly larger. Positron range distribution data were deconvoluted, fitted to an empirical function, and finally scaled to water equivalent values using range-energy relations derived for electrons [Katz and Penfold, 1952]. There are several potential difficulties inherent to this approach [Levin and Hoffman, 1999], such as the need to extrapolate range results from polyurethane to water or the possible loss of information due to the deconvolution. [Palmer and Brownell, 1992] evaluated annihilation density distributions for certain positron emitters through calculations based on beta-decay energy spectra combined with an empirical range formula, assuming that positrons behave diffusively. More recently, several authors have studied the reduction of positron range in presence of a magnetic field [Wirrwar et al., 1997, Herzog et al., 2010]. According to [Soultanidis et al., 2011] and [Kraus et al., 2012], positron range is unaffected or just slightly enlarged along the direction of the magnetic field, thus producing an anisotropic distribution of annihilations.

The difficulties involved in the experimental measurements of positron range support the widespread use of Monte Carlo simulations [Levin and Hoffman, 1999, Harrison et al., 1999, Champion and Le Loirec, 2006, 2007, Le Loirec and Champion, 2007a,b,c]. Most of these studies use water as a reference medium for positron interaction. The exclusive use of water-based data may be misleading since positron range depends on density and atomic composition of the tissue [Sánchez-Crespo et al., 2004, Alessio and MacDonald, 2009, Lehnert et al., 2011, Jødal et al., 2012]. An accurate assessment of the consequences of positron range in PET imaging requires a specific model for each tissue type.

The correction of positron range effects in PET image reconstruction is becoming mandatory in the light of the increasing use of high-energy positron emitters in clinical PET imaging and the excellent spatial resolution of modern pre-clinical PET scanners, even sub-millimetric for some small-animal systems. Some studies have addressed the question of how accurately the positron range should be known to obtain good range-corrected PET images (see chapter 4 of this thesis and [Cal-González et al., 2011b]). It was found that differences of about 10% in the average positron range of the profiles employed to correct the reconstruction with respect to the profiles employed during the simulation of the acquisition, translate into detectable changes in image quality. This raises the question of whether positron range profiles are known with such accuracy for the radioisotopes and materials of current interest for PET imaging. A first review of the available positron range data in the literature, either from simulations or from experiments, reveals discrepancies larger than 20% in many cases [Levin and Hoffman, 1999, Champion and Le Loirec, 2007]. However, as pointed by [Cal-González et al., 2010], different authors chose different ways of representing range profiles, which precludes a straightforward comparison.

Thus, the goals of the work presented in this chapter are the following [Cal-González et al., 2013a]:

- To obtain positron range distributions for the most common PET isotopes in various human tissues, employing the PeneloPET simulation tool.
- To develop a general framework and a tool to convert from any of the multiple ways employed in the literature to show positron range into another. Using this framework, we make a general comparison of PeneloPET predictions for positron range for the available experimental data and also for simulations from other authors.

3.2 Monte Carlo simulation

We have chosen PENELOPE (2008 version, with the standard simulation parameters, as recommended in [Salvat et al., 2008]) to simulate positron trajectories. Many Monte Carlo codes employ multiple dispersion models for the transport of electrons and positrons, which allow for the global simulation of a large number of interactions in a condensed form. This condensed history methodology may cause a loss of accuracy when facing media boundary. PENELOPE, on the other side, considers in detail the transport of electrons and positrons, interaction by interaction, which makes it particularly suited to simulate positron range, eventually even across media boundaries. PENELOPE has been shown to produce good results up to distances below one millimeter [Muñoz et al., 2005]. Positron interactions and subsequent annihilation simulated with PENELOPE have been included in PeneloPET [España et al., 2009]. PeneloPET is built on top of PENELOPE and provides a simple framework to simulate PET scanners. PeneloPET is freely available and can be obtained under request (see http://nuclear.fis.ucm.es/penelopet).

3.2.1 Energy spectra

When a positron is generated in a decay process, it has a kinetic energy that depends on the energy shared with the neutrino created in the same process. This yields a continuum energy spectrum distribution whose theoretical grounds are well-known, both for allowed or super allowed transitions as well as for forbidden decays, and the energy spectrum can be computed with accuracy [Gove and Martin, 1971], including the Coulomb correction factor [Wu and Moskowski, 1966]. For allowed decays, the theoretical energy distribution [Fermi, 1934] has the form:

$$N(E)dE = gF(Z,E)pE(E_{max} - E^2)dE \tag{3.1}$$

Where g is a constant, E is the positron kinetic energy and p is the corresponding momentum, in units of mc^2 and mc, respectively. E_{max} corresponds to the maximum kinetic positron energy. Table 3.1 reports E_{max} for the isotopes considered, along with the decay mode, the parent half life, the mean kinetic positron energy E_{mean}, and the intensity for each positron and gamma ray emitted in the decay. Note that in this table an intensity of 100% corresponds to the emission of one particle (photon or positron in β^+ decay) per decay. In the case of annihilation photons, one can have up to two photons emitted per decay, that is, 200% intensity.

Radionuclides	^{18}**F**	^{11}**C**	^{13}**N**	^{15}**O**	^{68}**Ga**	^{82}**Rb**
Decay mode	β^+	β^+	β^+	β^+	β^+	β^+
Branching ratio	96.7%	99.8%	99.8%	99.9%	89.1%	95.4%
Parent Nucleus	^{18}F	^{11}C	^{13}N	^{15}O	^{68}Ga	^{82}Rb
Parent J^π **/ Daughter** J^π	$1^+/0^+$	$3/2^+/3/2^-$	$1/2^-/1/2^-$	$1/2^-/1/2^-$	$1^+/0^+, 2^+$	$1^+/0^+, 2^+$
Type of transition	Allowed	Allowed	Allowed	Allowed	Allowed	Allowed
Parent $T_{1/2}$ **(min)**	109.8	20.4	10.0	2.0	67.7	1.3
Daughter nucleus	^{18}O	^{11}B	^{13}C	^{15}N	^{68}Zn	^{82}Kr
E_{max} **(keV)**	633.5	960.2	1198.5	1732.0	821.8 / 1899.1	2601 / 3378
E_{mean} **(keV)**	249.8	385.6	491.8	735.3	352.6 / 836.0	1168 / 1535
Intensity of positrons (%)	97%	99.8%	99.8%	99.9%	1.2% / 87.9%	13% / 82%
Intensity of annihilation photons (%)	193.5%	199.5%	199.6%	199.8%	178.3%	190.9%

Table 3.1: Decay mode, half life, maximum and mean kinetic energies (E_{max} and E_{mean} respectively), and intensity of the annihilation photons emitted by the radioisotopes considered in this work (from [NNDC, 2011])

$F(Z,E)$ is the Fermi function which takes into account the effect of the nuclear Coulomb field in the electron or positron emitted. In positron range simulation, this latter Coulomb correction factor is often either neglected or just treated within a non relativistic approach (see, for instance, [Levin and Hoffman, 1999]). PeneloPET uses the exact expression for the Coulomb correction factor [Fermi, 1934], which, albeit relatively close to one for light nuclei and positron emission, it may significantly distort the beta spectrum for medium to heavy nuclei, particularly in the case of electron emission [España et al., 2009]. The energy spectra simulated for the radioisotopes of interest are shown in figure 3.1.

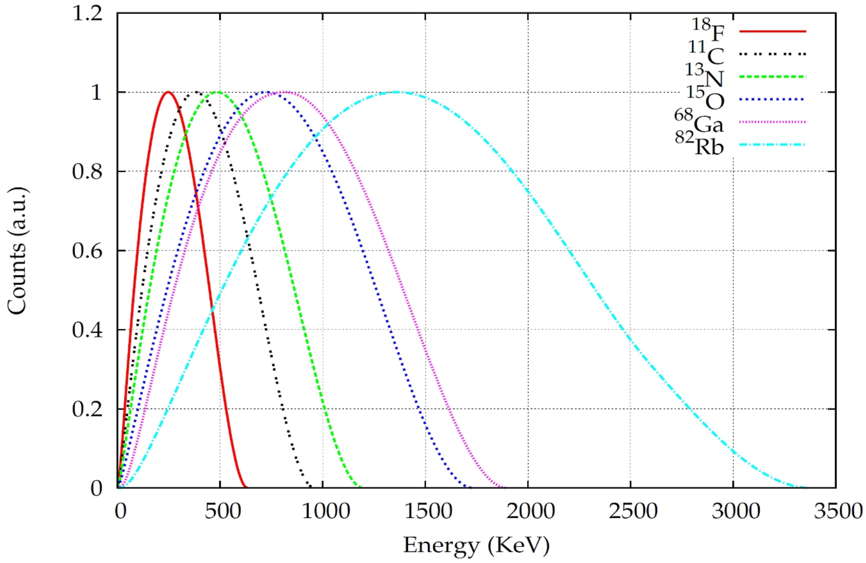

Figure 3.1: Simulated energy spectra for the radioisotopes considered in this work. The distributions are obtained with peneloPET following Eq. 3.1, and were normalized to the same value at the maximum.

3.2.2 Electron and positron interactions and transport mechanism

The possible interactions of electrons and positrons within a medium of interest for positron range estimates are: elastic scattering, inelastic collisions and Bremsstrahlung emission; positrons can also undergo annihilation, either in flight or at rest. The dominant energy loss mechanisms for electrons and positrons with intermediate and low energies are inelastic collisions. For a detailed description of the way PENELOPE deals with inelastic collisions of electrons and positrons, see [Salvat and Fernández-Varea, 1992] and [Fernández-Varea et al., 1993]. For the simulation of electron and positron transport mechanisms, PENELOPE implements a *mixed* simulation scheme [Andreo and Brahme, 1984], which combines the detailed simulation of hard events with condensed simulation of soft events [Fernández-Varea et al., 1993, Baró et al., 1995, Bielajew and Salvat, 2001].

3.2.3 Positron annihilation

When the positron reaches thermal velocities (a few eV), it either annihilates directly with an electron into two gamma rays, or first forms positronium (Ps) in the singlet ($^1S_0$, para-positronium, p-Ps) or triplet ($^3S_1$, ortho-positronium, o-Ps) states [Berko and Hereford, 1956]. Para-positronium decays only into two photons, while ortho-positronium decays into three [Harpen, 2004]. The fraction of positrons forming positronium is known as the Ps yield. Using the technique of Positron Age-Momentum-Correlation (AMOC), [Castellaz et al., 2002] have measured Ps yields in a variety of liquids for an external 4 MeV positron beam. The Ps yield in water was found to be 38% and in other liquids (organic solvents) it can be as high as 70% in spite of positron recoil effects at the liquid surface. It seems reasonable to expect the yield from lower energy sources embedded in tissue to be higher than the 38% found by Castellaz et al in water, thanks to the lack of surface and the lower instance of in-flight annihilation. In fact, [Champion and Le Loirec, 2007] estimated values of Ps yield of about 83% in water, independent on the isotope considered. Owing to the fact that positronium is a neutral particle and does not interact electromagnetically; the effect of Ps formation in the annihilation process will be a higher positron range. The subsequent positronium drift could be estimated from its residual momentum and effective half-life, as it has been described by [Brawley et al., 2010a,b].

Once formed, p-Ps is observed to decay in liquids with its vacuum lifetime, 125 ps [Asai et al., 1995]. The observed lifetime of o-Ps in liquids is considerably shorter than its vacuum value due to pick-off effect, where a second electron with opposed spin reacts with the positron in the o-Ps atom resulting in two photon annihilation. The observed lifetime of o-Ps in water is 1800 ps, shorter than the vacuum lifetime of 140 ns [Westbrook et al., 1989], but much longer than p-Ps lifetime, thus we may conclude that most annihilations in tissue result in two-gamma ray emissions despite the larger amount (3:1) of o-Ps initially formed [Harpen, 2004].

Although positronium formation may be an important factor in positron range, in PeneloPET, as in the majority of other Monte Carlo codes, such as EGS4, Geant4, etc; positron annihilation is described as an in flight process and formation of positronium is not considered. To the best of our knowledge, only in [Champion and Le Loirec, 2006, 2007, Le Loirec and Champion, 2007a,b,c] was Ps formation considered. When considering the effect of Ps in positron range, one must address Ps formation rates estimations inside tissues.

3.3 Positron range modeling

For a given positron emitting point source, the distribution of $3D$ Cartesian coordinates (x, y, z) of the annihilation events provides the $3D$ annihilation Point Spread Function (*aPSF*). A model for *aPSF* was proposed by [Palmer and Brownell, 1992, Palmer et al., 2005]. In those works, the *aPSF* for mono-energetic positrons (with energy $E_0 < 4MeV$) in isotropic media was represented by a three-dimensional Gaussian function, and later the *aPSF* for each isotope is computed weighting the mono-energetic distributions with the energy spectra of the positrons emitted by the isotope.

Other authors compute $1D$ distribution from the *aPSF*. For instance, the projection onto one direction ($aPSF_{sin}$), has been often employed. This distribution can be readily transformed into sinogram representation [Blanco, 2006].This $1D$ distribution is given by the expression:

$$aPSF_{sin}(x) = \int_{-\infty}^{\infty} dz \int_{-\infty}^{\infty} aPSF(x, y, z) dy \tag{3.2}$$

A different $1D$ distribution can be formed by considering the profile, across the maximum, of the $aPSF$ projected in a plane ($aPSF_{img}$). It is given by:

$$aPSF_{img}(x) = \int_{Y_m-\Delta y}^{Y_m+\Delta y} dy \int_{-\infty}^{\infty} aPSF(x, y, z) dz \tag{3.3}$$

where Y_m is the location of the maximum of the distribution projected onto the plane and Δy is the sampling interval on y. The schematic procedure to obtain these $1D$ distributions from the $3D$ $aPSF$ is depicted in figure 3.2.

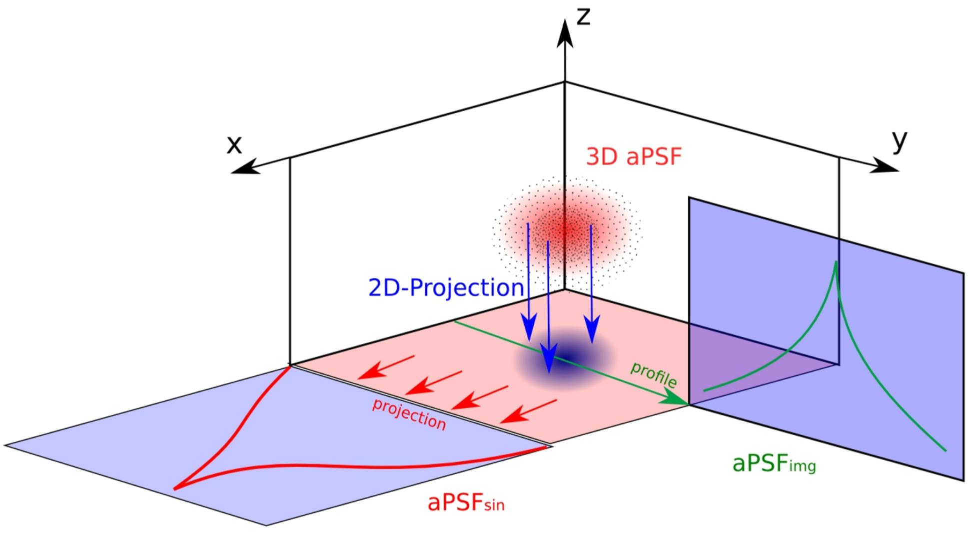

Figure 3.2: Schematic procedure to obtain $aPSF_{sin}$ and $aPSF_{img}$ from the original $3D$ $aPSF$

These $1D$ positron range distributions can be fitted to a sum of two exponential functions [Derenzo, 1979]:

$$P(x) = Ce^{-k_1 x} + (1 - C)e^{-k_2 x}; \qquad x \geq 0, k_1 >> k_2 \tag{3.4}$$

Figure 3.3 sketches $aPSF_{sin}$ for a ^{18}F point source in water. We can consider three different regions in the curve. For $x \to 0$, the distribution is determined by the k_1 coefficient. One has to take into account that in this limit the behavior of the distribution depends strongly on the bin size chosen, thus k_1 should not be employed to compare to other results available in the literature. At intermediate values of x, the behavior of the distribution is determined by k_2, that is a meaningful parameter to compare $1D$ distributions from different authors. Finally, for large x, comparable to the maximum positron range, the $1D$ distribution is no longer well represented by a sum of two exponential functions, as it does not fall to zero for large distances, contrarily to actual positron range distributions.

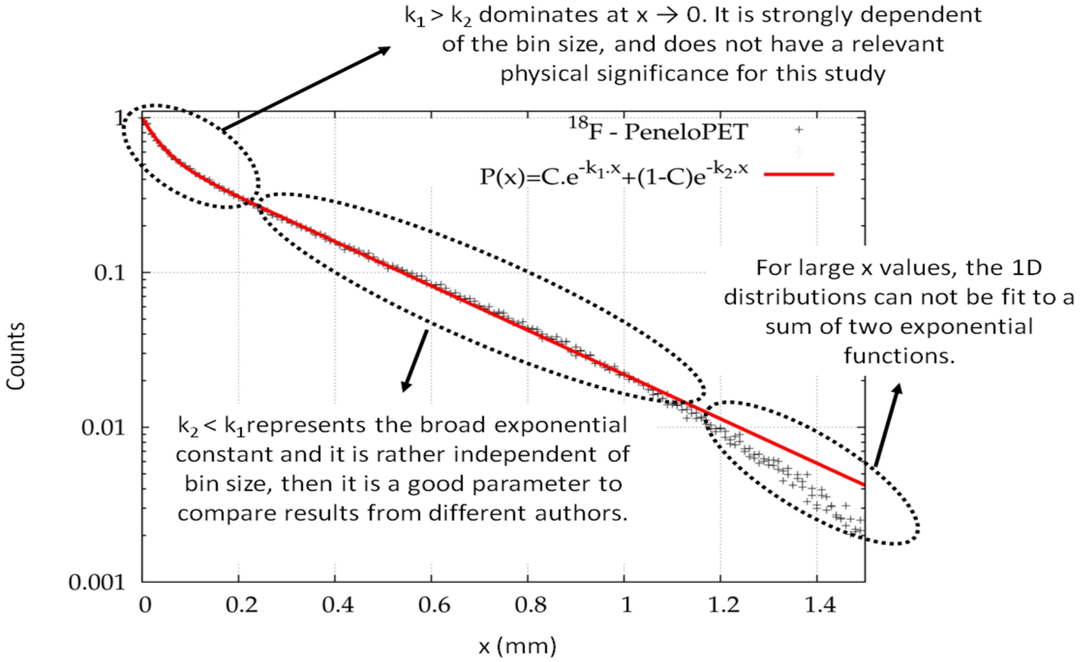

Figure 3.3: $aPSF_{sin}$ obtained from a PeneloPET simulation of ^{18}F in water and two exponential fit proposed by [Derenzo, 1979]

In a homogeneous media, $aPSF(x, y, z)$ must be spherically symmetric for a point source. Thus it can be represented as $aPSF(r)$. Therefore, $3D$ radial histograms can be also obtained for the positron annihilation distribution.

$$g_{3D}(r) = 4\pi \int_r^{r+dr} r'^2 aPSF(r')dr'; \qquad G_{3D}(r) = \frac{\int_0^r g_{3D}(r')dr'}{\int_0^\infty g_{3D}(r')dr'} \tag{3.5}$$

$g_{3D}(r)$ in equation 3.5 represents the number of annihilations at a given radial distance. The $3D$ cumulative distribution $G_{3D}(r)$ (in equation 3.5) can also be obtained from $aPSF(r)$.

From the projection of $aPSF(r)$ in the XY plane, we can obtain the $2D$ radial distributions $g_{2D}(r)$ and $G_{2D}(r)$. These radial distributions can be computed with the following expressions:

$$g_{2D}(r) = 2\pi \int_r^{r+dr} r' aPSF(r')dr'; \qquad G_{2D}(r) = \frac{\int_0^r g_{2D}(r')dr'}{\int_0^\infty g_{2D}(r')dr'} \tag{3.6}$$

PeneloPET was used to simulate the positron range of ^{18}F, ^{11}C, ^{13}N, ^{15}O, ^{68}Ga and ^{82}Rb in the following tissues: cortical bone, B-100 bone equivalent plastic, skin, striated muscle, brain, water, adipose tissue and lung. Table 3.2 shows the physical properties of these tissues, whose compositions were obtained from [ICRP, 1975, ICRU, 1989] databases. From these compositions, the relative electron densities of the different tissues have been calculated with the following expression [Schneider et al., 1996]:

$$\rho_e = \frac{\rho N_g}{\rho^{water} N_g^{water}} \tag{3.7}$$

where ρ is the density of the tissue and N_g is the number of electrons per unit volume of tissue, given by:

$$N_g = \sum_i N_{g,i} = N_A \sum_i \frac{w_i Z_i}{A_i} \tag{3.8}$$

where N_A is Avogadro's number, Z_i and A_i are the atomic number and atomic weight of the i^{th} element and w_i is its proportion by weight.

Tissue	**Effective Z**	**Density** (gcm^{-3})	N_g ($10^{23}e^{-}cm^{-3}$)	**Electronic density** (relative to water)
Cortical bone	5.29	1.85	4.42	1.64
B-100 bone eq. plastic	4.17	1.45	4.52	1.31
Skin	3.41	1.10	4.85	1.07
Striated muscle	3.44	1.04	4.89	1.02
Brain	3.30	1.03	4.95	1.02
Water	3.33	1.00	4.99	1.00
Adipose tissue	2.99	0.92	4.89	0.90
Lung	3.46	0.30	4.89	0.29

Table 3.2: Physical properties for the tissues studied in this work

For each isotope/material combination investigated, more than five million positron histories were generated. $aPSF_{sin}(x), aPSF_{img}(x), g_{3D/2D}(r)$ and $G_{3D/2D}(r)$ distribution profiles were histogrammed with a bin size of 10 μm.

3.4 Methods to compare positron range estimations

In this section we will present the different procedures employed to compare the positron range distributions obtained with PeneloPET with the results obtained by other authors.

3.4.1 Comparison using a genetic algorithm

As many different ways of presenting positron range results are adopted in the literature, in order to produce meaningful comparison of our simulations to previous results, and among previous results themselves, we have developed a tool able of transforming a given positron range distribution into any other [Cal-González et al., 2011a, 2013a]. We chose as canonical distribution the radial $3D$ distribution $g_{3D}(r)$. In this work we employed the following analytical expression for $g_{3D}(r)$:

$$g_{3D}(r) \approx C \left[(ar+1) \left(1 - \frac{r}{r_0} \right)^n - \frac{\epsilon}{r^n} \right] \tag{3.9}$$

for $r < r_0$, and zero otherwise. a, r_0, n and $\epsilon(\epsilon << 1)$ are fitting parameters, which a genetic algorithm [Fernández-Ramirez et al., 2008] will modify to adjust g_{3D} to data on whatever other quantity that can be derived from g_{3D} (when needed, the relationships among different positron range distributions, equations R1 - R6 [Poularikas, 2000], are employed). C is a constant employed to scale g_{3D} to the data. In this work we present results scaled to a maximum value of one. By means of the genetic algorithm and the transformations among different profile expressions, results for range profile are employed to fit equation 3.9. Using g_{3D} as canonical range distribution is convenient, but other distributions could be employed as well.

$$\begin{aligned}
g_{3D}(r) &= 4\pi r^2 aPSF_{3D}(r) && R1\\
aPSF_{sin}(r) &= -\int_0^r \frac{1}{2r'} g_{3D}(r')dr' && R2\\
G_{3D}(r) &= \frac{\int_0^r g_{3D}(r')dr'}{\int_0^\infty g_{3D}(r')dr'} && R3\\
aPSF_{img}(r) &= \int_\delta^\infty \frac{1}{4\pi r'(r'^2-\delta^2)^{1/2}} g_{3D}(r')dr' && R4\\
g_{2D}(r) &= 2\pi r aPSF_{img}(r) && R5\\
G_{2D}(r) &= \frac{\int_0^r g_{2D}(r')dr'}{\int_0^\infty g_{2D}(r')dr'} && R6
\end{aligned}$$

The analytical expression proposed in 3.9 has two parts. The first one represents the shape of the $g_{3D}(r)$ distribution for r not close to 0, while the second term, diverging at the origin, was added in order to give flexibility to fit to data when $r \to 0$. One has to recall that actually the divergence near the origin displayed by Eq. 3.9 poses no special problem as long as the integral of Eq. 3.9 on any volume enclosing the origin, no matter how small, remains finite. This functional form makes it possible to fit projected profiles whose behavior near the origin may depend on non physical parameters, such as binning size. On the other hand, r_0 has a clear physical meaning: it represents the maximum positron range. Compared for instance to expression 3.4 previously mentioned and often employed in the literature, Eq. 3.9 shows the expected behavior at large r.

As mentioned above, a genetic algorithm was used to fit $g_{3D}(r)$. The algorithm begins producing individuals with initial random values of the parameters, representing many possibilities for $g_{3D}(r)$. If needed, by means of relations [R1] - [R6], positron range distributions expressed in any of the usual ways found in the literature are obtained for each individual. The difference of the positron range distribution with the one taken as a reference is evaluated in terms of χ^2 (see Figure 3.4), that is employed as the fitness value for each individual. Individuals with small fitness are replaced by new ones. Evolution proceeds until a stable minimum χ^2 is obtained. This fitting procedure has proven to be very robust, and allows to obtain $g_{3D}(r)$ from positron range data expressed in any of the commonly found ways. Figure 3.4 shows a schematic diagram of the procedure employed. The genetic algorithm was running using 200 generations of 400 individuals each. This requires a few seconds on a modern personal computer. We found that the genetic algorithm produced adequate best fit parameters for all the profiles after single shot execution, without the need to prepare initial estimates of the parameters.

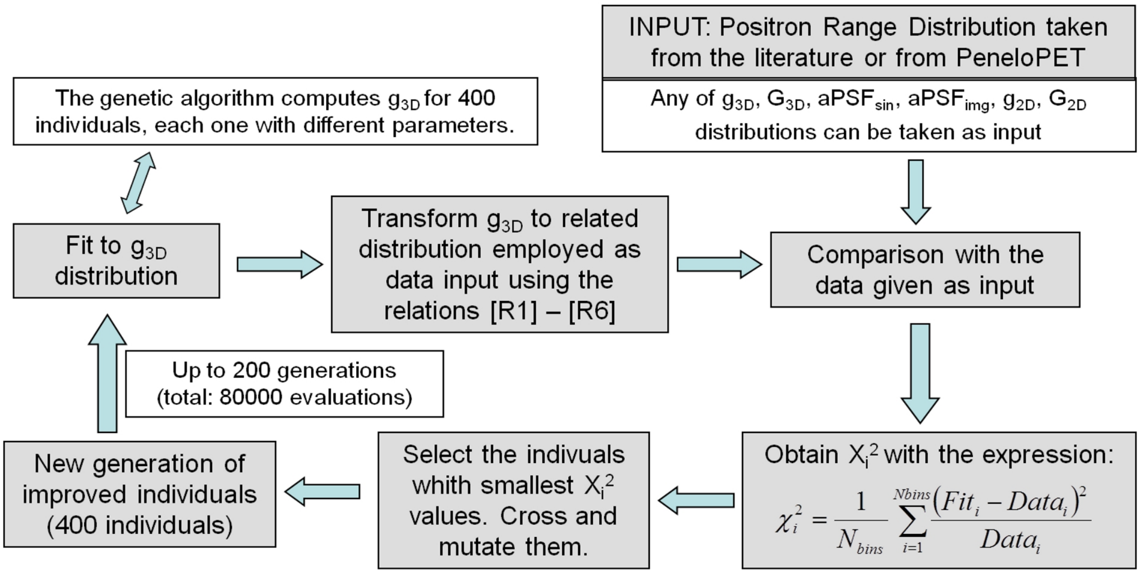

Figure 3.4: Procedure to fit positron range distributions.

3.4.2 Comparison of mean and maximum range values

We report (see tables 3.5 and 3.6, *section 3.6.3*) a comparison for PeneloPET to the available literature concerning mean and maximum positron ranges in water, R_{mean} and R_{max}, respectively. On the simulation side, we consider [Champion and Le Loirec, 2007, Partridge et al., 2006, Bailey et al., 2003], who reported R_{mean} values varying from $\sim$ 0.6 mm for ^{18}F to $\sim$ 7.5 mm for ^{82}Rb. Concerning the maximum penetration of positrons in water, R_{max}, we compare PeneloPET results with [Champion and Le Loirec, 2007]. On the experimental side, [Cho et al., 1975] have measured range distributions for several nuclides. Additionally, we have also compared to positron range measurements taken from [Derenzo, 1979]. We compare also with semi empirical expressions for the mean and maximum ranges. We consider the results of [Katz and Penfold, 1952], reviewed in [Evans, 1972]. In his book, Evans estimates the mean positron range with the following semi empirical expression:

$$R_{mean}(cm) \approx \frac{0.108\left[E_{\beta}^{max}(MeV)\right]^{1.14}}{\rho(g/cm^3} \tag{3.10}$$

The maximum positron range, also called extrapolated range, is very similar to the extrapolated range of electrons (see [Evans, 1972]), and it can be estimated from the following semi empirical relationships:

$$R_{max}(cm) \approx \frac{412\left[E_{\beta}^{max}(MeV)\right]^{n}}{\rho(mg/cm^{3}};\qquad 0.01 \leq E \leq 2.5MeV \tag{3.11}$$

$$R_{max}(cm) \approx \frac{530E_{\beta}^{max}(MeV) - 106}{\rho(mg/cm^{3}};\qquad 2.5 \leq E \leq 20MeV \tag{3.12}$$

With: $n = 1.265 - 0.0954 \ln E_{\beta}^{max}(MeV)$

3.5 Simulated positron range distributions

This section shows positron range distributions for the isotope-material combinations considered in this work.

3.5.1 Planar projection of annihilation positions

Figure 3.5 shows a two-dimensional scatter plot of positron annihilation points for different isotopes in water. Figure 3.6 shows the corresponding figure for ^{18}F in cortical bone, B-100 bone equivalent plastic, water and lung.

In figure 3.5 one can see how the distribution increases size with the energy of the β^{+} emitter. For instance, ^{18}F gives a region where annihilations take place of about 0.2 cm in diameter. For other isotopes with larger emission energy, for instance ^{82}Rb, this diameter is larger than 1 cm. Figure 3.6 shows the dependence of the diameter of the region with significant annihilations on the material in which positrons emitted by ^{18}F propagate and annihilate. In this case one can see how spatial extension of positron annihilation points decreases with the density of the material. For example, for cortical bone (density 1.85 $g.cm^{-3}$) the diameter of the region where annihilations take place is smaller than 0.1 cm, while for lung (density 0.30 $g.cm^{-3}$) this diameter is about 0.5 cm.

3.5.2 1D positron range distributions

As we have already said, in order to obtain the $1D$ and $3D$ positron range distributions, more than five million positron histories were generated for each isotope/material. The bin size was 10 μm. We can estimate the expected error in the parameters of the simulated positron range distributions from the variance of the Monte Carlo simulation. For instance, the expected error for the radial position at which 0.1% of the particles survive is less than 0.1% for short-range isotopes (as ^{18}F or ^{11}C) in water, less than 1% for large-range isotopes (as ^{68}Ga or ^{82}Rb) in water, and less than 2% for long range isotopes in soft tissues, such as lung.

Figure 3.7 (left) shows $aPSF_{sin}$ distributions for different isotopes placed in water. Figure 3.7 (right) shows the same distributions for ^{18}F placed in different materials. Table 3.3 shows the values obtained for k_2 parameters for the $aPSF_{sin}$ distributions and the isotopes studied in this work in the following materials: cortical bone, soft bone (B100 bone-equivalent plastic), water and lung.

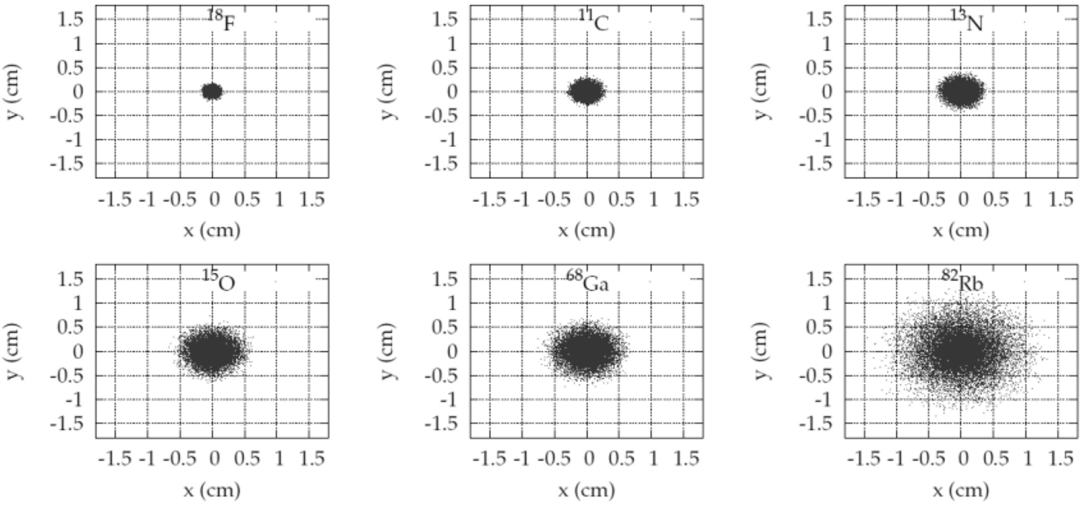

Figure 3.5: Distribution of annihilation points (projected in the 2D-plane) for 10^5 trajectories originating from a point source in water. Isotopes considered are ^{18}F, ^{11}C, ^{13}N, ^{15}O, ^{68}Ga and ^{82}Rb.

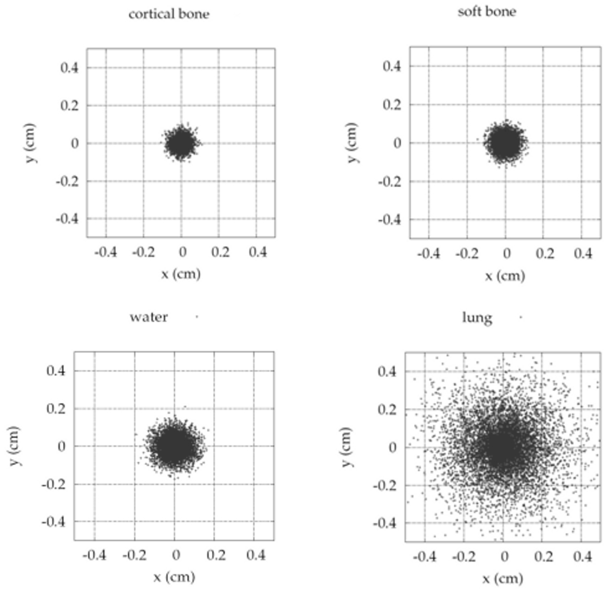

Figure 3.6: Distribution of annihilation points (projected in the 2D-plane) for 10^5 trajectories originating from a ^{18}F point source in cortical bone, B-100 bone-equivalent plastic, water and lung.

As expected, $aPSF_{sin}$ spans a larger spatial range for increasing energies of the positron and smaller spatial range for larger densities of the material in which the positron propagates and annihilates.

	Cortical bone	**Soft bone**	**Water**	**Lung**
Radionuclide	k_2 (mm^{-1})	k_2 (mm^{-1})	k_2 (mm^{-1})	k_2 (mm^{-1})
^{18}**F**	6.06	4.69	3.27	0.98
^{11}**C**	3.29	2.54	1.79	0.53
^{13}**N**	2.42	1.83	1.30	0.39
^{15}**O**	1.43	1.10	0.77	0.23
^{68}**Ga**	1.24	0.95	0.67	0.20
^{82}**Rb**	0.59	0.45	0.31	0.10

Table 3.3: k_2 resulting from the fit to the positive x region of the $aPSF_{sin}$ distributions for each isotope in the following materials: cortical bone, soft bone, water and lung.

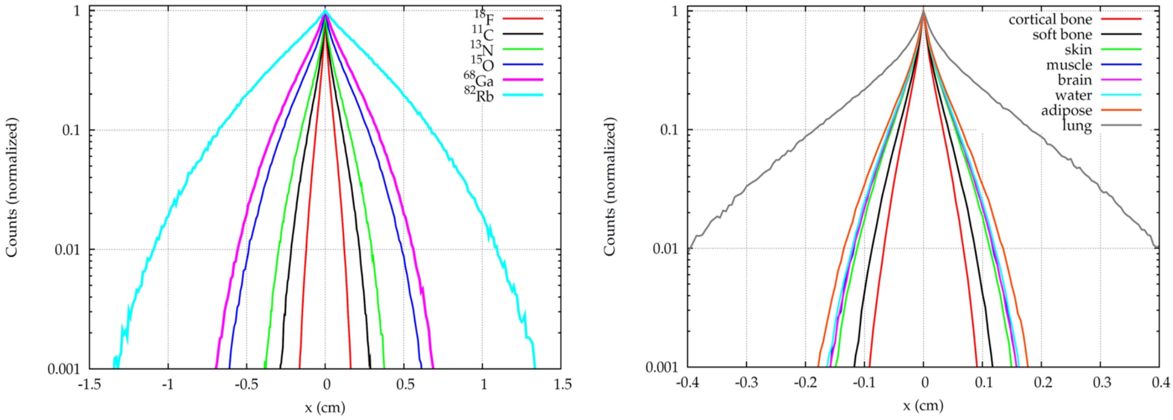

Figure 3.7: Left: $aPSF_{sin}$ distributions for ^{18}F, ^{11}C, ^{13}N, ^{15}O, ^{68}Ga and ^{82}Rb emitters in water. Right: $aPSF_{sin}$ distributions for ^{18}F emitter in different materials.

3.5.3 3D positron range distributions

Radial histograms weighted by the total number of annihilations at a given radial distance [$g_{3D}(r)$] and 3D cumulative distribution $G_{3D}(r)$ are studied in this section. Figure 3.8 shows $g_{3D}(r)$ for different isotopes placed in water (left) and $g_{3D}(r)$ for ^{18}F placed in different materials (right). Equivalent plots are presented for $G_{3D}(r)$ in figure 3.9.

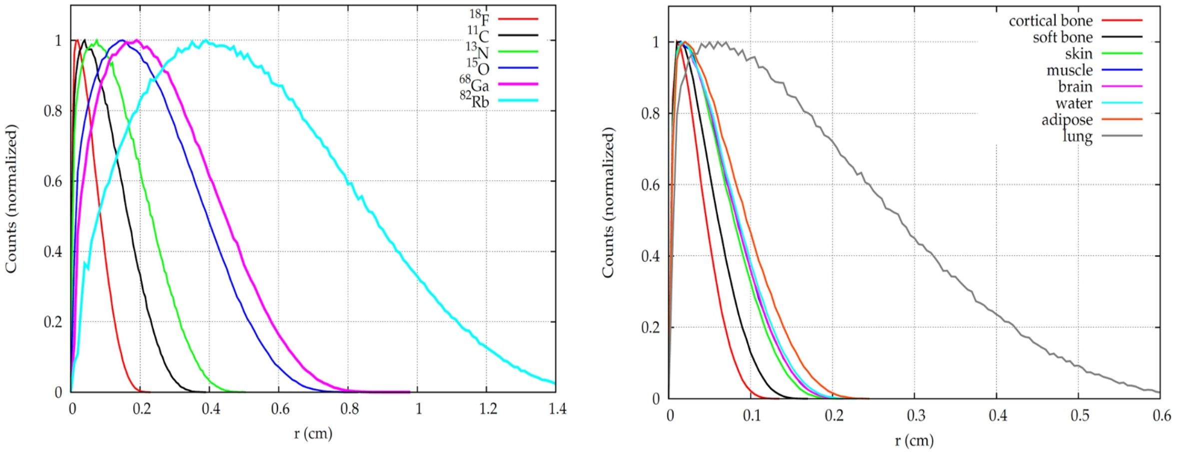

Figure 3.8: Left: $g_{3D}(r)$ distributions for ^{18}F, ^{11}C, ^{13}N, ^{15}O, ^{68}Ga and ^{82}Rb point sources in water. Right: $g_{3D}(r)$ distributions for a ^{18}F point source in different materials

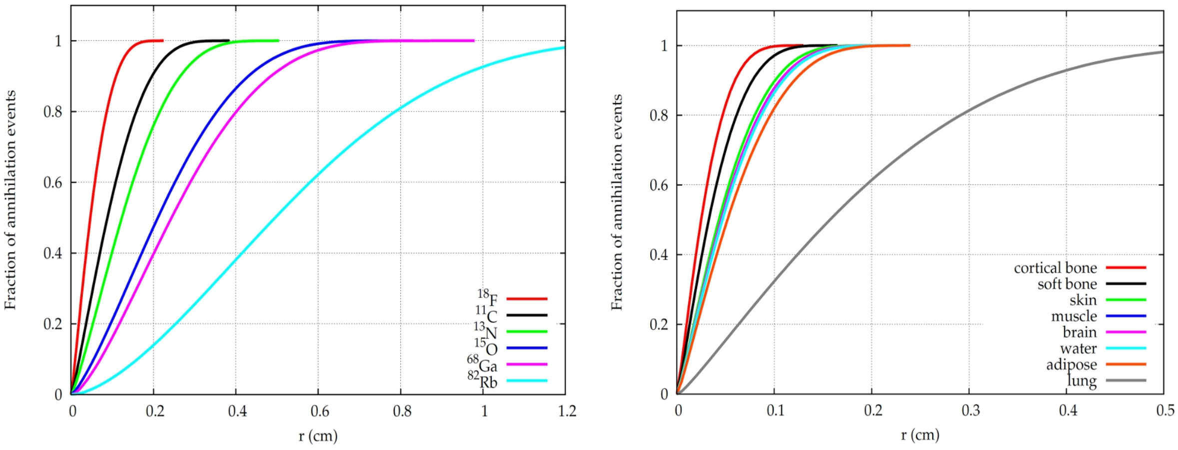

Figure 3.9: Left: $G_{3D}(r)$ distributions for ^{18}F, ^{11}C, ^{13}N, ^{15}O, ^{68}Ga and ^{82}Rb point sources in water. Right: $G_{3D}(r)$ distributions for a ^{18}F point source in different materials

3.6 Comparison with previous estimations and measured data

A comparison of PeneloPET results and other studies of positron range, either theoretical, simulated or experimental, presented in the literature is shown in this section. Wherever some observable for an author was not available, the genetic algorithm was employed to reconstruct $g_{3D}(r)$ and from it, the other observables were derived.

3.6.1 1D distributions

We will first consider k_2 from the two-exponentials fit to $aPSF_{sin}$ given in table 3.4. Figure 3.10 (left) shows the dependence of k_2 with the maximum β^+ energy for the radionuclides covered in this work. We find discrepancies with other results in the literature below 20%, in the majority of cases. The dependence of k_2 on the density for a given radionuclide (^{18}F in this case) is shown in figure 3.10 (right).

Looking at figure 3.10, we note that PeneloPET estimations are in good agreement with the results of other authors, except for Champion's results, which under-estimate k_2 values compared to all other curves. This can be attributed to the consideration of positronium formation by [Champion and Le Loirec, 2007], while it is not included in all other calculations.

On the right side of the figure we can see that the dependence of k_2 on the density of the propagation media is almost linear.

	Water
Radionuclide	k_2 (mm^{-1})
^{18}**F**	**3.27** / 2.79$^{(1)}$ / 3.1$^{(2)}$ / 3.94$^{(4)}$ / 3.38$^{(5)}$
^{11}**C**	**1.79** / 1.49$^{(1)}$ / 1.8$^{(2)}$ / 2.19$^{(3)}$ / 1.78$^{(5)}$
^{13}**N**	**1.30** / 1.07$^{(1)}$ / 1.4$^{(2)}$ / 1.31$^{(5)}$
^{15}**O**	**0.77** / 0.60$^{(1)}$ / 0.90$^{(2)}$ / 0.77$^{(5)}$
^{68}**Ga**	**0.67** / 0.49$^{(1)}$ / 0.87$^{(3)}$ / 0.87$^{(4)}$ / 0.65$^{(5)}$
^{82}**Rb**	**0.31** / 0.22$^{(1)}$ / 0.33$^{(3)}$ / 0.39$^{(4)}$ / 0.30$^{(5)}$

Table 3.4: Comparison of the k_2 parameters resulting from the two-exponential fit for $aPSF_{sin}$ of PeneloPET (in bold) and the ones of [Champion and Le Loirec, 2007] (1), [Levin and Hoffman, 1999] (2), [Derenzo, 1979] (3), [Haber et al., 1990] (4) and [Blanco, 2006] (5) for several radionuclides in water.

3.6.2 2D and 3D cumulative distributions

In this section we compare $G_{2D}(r)$ and $G_{3D}(r)$ distributions to the experimental results of [Derenzo, 1979] and with the simulations of [Blanco, 2006, Champion and Le Loirec, 2007]. Figure 3.11 shows these comparisons, for $G_{3D}(r)$ (left) and $G_{2D}(r)$ (right). As it was the case for k_2, PeneloPET results are relatively close to GEANT4 ones (they are within 12% of each other) and to the experimental ones (only available in the literature for the $2D$ cumulative distribution, shown in the right part of the figure), again with differences of the order of 10%, while Champion's results depart from the ones obtained in this work by more than 25%.

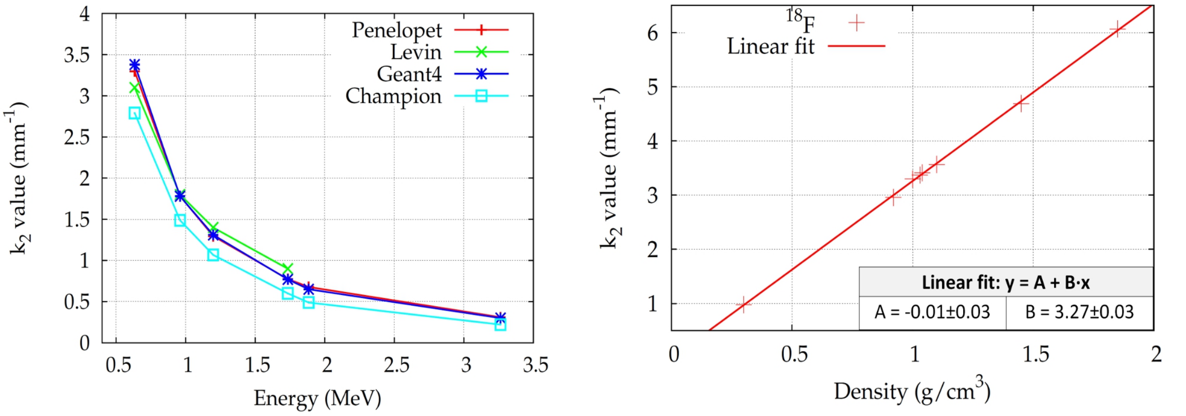

Figure 3.10: Left: dependence of k_2 with the maximum energy of the positron spectrum for each radionuclide. PeneloPET results are compared with results obtained by [Blanco, 2006, Levin and Hoffman, 1999, Derenzo, 1979, Champion and Le Loirec, 2007]. Right: dependence of k_2 with the density of the media, for ^{18}F.

3.6.3 Comparison of R_{mean} and R_{max} values

Mean positron range values were computed with PeneloPET for different media and compared to GATE results [Lehnert et al., 2011] and predictions of expression 3.10, reported by [Evans, 1972]. This comparison is displayed in table 3.5. Table 3.6 shows mean and maximum positron ranges in water, R_{mean} and R_{max} respectively.

3.6.4 Comparison of range distributions using a genetic algorithm

In the previous section we limited our comparison to observables actually quoted in the literature. Here we will use the genetic algorithm described before, to make a comparison of other observables related to positron range.

Fit of $g_{3D}(r)$ distribution

First, we examine how well the genetic algorithm is able of reproducing $g_{3D}(r)$ in a test case with simulated data from PeneloPET. Figure 3.12 shows the $g_{3D}(r)$ obtained from the algorithm, when it is fed with $aPSF_{sin}$ or G_{3D} distributions from the PeneloPET simulation of a ^{68}Ga point source in water. In a similar fashion, Figure 3.13 shows the $g_{3D}(r)$ distribution recovered from the algorithm, using as input g_{3D}, $aPSF_{sin}$ or G_{3D} distributions. In all cases, the $g_{3D}(r)$ distribution directly obtained from the simulation is also plotted. These figures show that the analytical expression for $g_{3D}(r)$ we propose fits very well the PeneloPET simulations.

Table 3.7 presents the resulting parameters of the fit of PeneloPET $g_{3D}(r)$ to eq. 3.9, for the different radionuclides considered in this work, annihilating in water. The expected error, resulting from the fit, in these parameters is less than 5% in all cases. It is important to keep in mind that r_0 parameter in table 3.7 represents the maximum range of positrons. A comparison

		R_{mean} (mm)			R_{max} (mm)	
Radionuclide	**Material**	**PeneloPET**	**GATE**	**Eq. 3.10**	**PeneloPET**	**Eq. 3.11**
^{18}F	Cortical bone	0.32	0.25 (-21.9%)	0.35 (9.3%)	1.28	1.24 (-3.2%)
	Water	0.57	0.48 (-15.8%)	0.64 (12.3%)	2.16	2.27 (4.8%)
	Lung	1.85	1.86 (0.5%)	2.14 (15.7%)	7.49	7.56 (0.9%)
^{11}C	Cortical bone	0.55	0.48 (-12.7%)	0.56 (1.8%)	2.18	2.12 (-2.8%)
	Water	1.02	0.92 (-9.8%)	1.03 (1.0%)	3.67	3.91 (6.1%)
	Lung	3.35	3.61 (7.8%)	3.45 (3.0%)	12.4	13.0 (4.6%)
^{13}N	Cortical bone	0.75	-	0.72 (-4.0%)	2.82	2.79 (-1.1%)
	Water	1.40	1.30 (-7.1%)	1.32 (-5.7%)	4.88	5.16 (5.4%)
	Lung	4.61	-	4.43 (-3.9%)	16.1	17.2 (6.4%)
^{15}O	Cortical bone	1.26	1.16 (-7.9%)	1.09 (-13.5%)	4.46	4.34 (-2.8%)
	Water	2.34	2.21 (-5.6%)	2.01 (-14.1%)	7.92	8.02 (1.2%)
	Lung	7.70	8.51 (10.5%)	6.73 (-12.6%)	24.7	26.7 (7.5%)
^{68}Ga	Cortical bone	1.44	-	1.20 (-16.7%)	4.89	4.78 (-2.3%)
	Water	2.69	-	2.24 (-16.7%)	9.06	8.84 (-2.5%)
	Lung	8.86	-	7.41 (-16.4%)	27.1	29.5 (8.1%)
^{82}Rb	Cortical bone	3.00	-	2.25 (-25.0%)	9.11	8.72 (-4.5%)
	Water	5.33	-	4.29 (-19.5%)	16.5	16.1 (-2.5%)
	Lung	17.6	-	13.9 (-21.0%)	52.0	53.8 (3.3%)

Table 3.5: Comparison of PeneloPET, GATE and semiempirical estimates from Eq. 3.10 for R_{mean}. Within parentheses are shown the deviations with respect to PeneloPET.

	R_{mean} in water(mm)				R_{max} in water (mm)		
Radionuclide	**PeneloPET**	**Other simulations**	**Eq. 3.10**	**Experiments**	**PeneloPET**	**Other simulations**	**Eq. 3.11**
^{18}F	0.57	0.66[1] / 0.6[2] / 0.6[3]	0.64[4]	0.54[5] / 0.9[6]	2.16	2.63[1]	2.27[4]
^{11}C	1.02	1.13[1] / 1.1[2] / 1.1[3]	1.03[4]	0.92[5] / 1.095[6]	3.67	4.54[1]	3.91[4]
^{13}N	1.40	1.73[1] / 1.5[2] / 1.5[3]	1.32[4]	1.39[6]	4.88	5.75[1]	5.16[4]
^{15}O	2.34	2.96[1] / 2.5[2] / 2.5[3]	2.01[4]	1.785[6]	7.92	9.13[1]	8.02[4]
^{68}Ga	2.69	3.56[1] / 2.9[2]	2.24[4]	2.8[5] / 1.975[6]	9.06	10.3[1]	8.84[4]
^{82}Rb	5.33	7.49[1] / 5.9[2]	4.29[4]	6.1[5] / 2.9[6]	16.5	18.6[1]	16.1[4]

Table 3.6: PeneloPET results for R_{mean} in water compared to [Champion and Le Loirec, 2007] (1), [Partridge et al., 2006] (2) and [Bailey et al., 2003] (3) and for R_{max}, compared to [Champion and Le Loirec, 2007] (1). The table also shows semi-empirical estimates from [Evans, 1972] (4) and measurements from [Derenzo et al., 1993] (5) and from [Cho et al., 1975] (6).

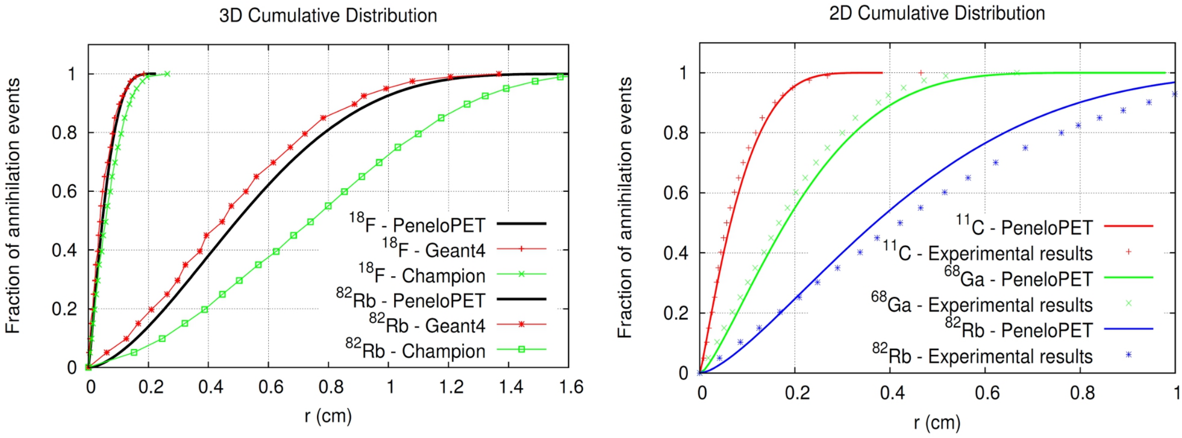

Figure 3.11: Left: $3D$ cumulative distributions obtained with PeneloPET, GEANT4 [Blanco, 2006] and [Champion and Le Loirec, 2007] simulations, for ^{18}F and ^{82}Rb radionuclides in water. Right: $2D$ cumulative distributions for PeneloPET simulations compared to [Derenzo, 1979] experimental results, for ^{11}C, ^{68}Ga and ^{82}Rb radionuclides in water.

of r_0 to the maximum range derived from PeneloPET simulations is included in the table. On the other hand, r_i is obtained using the following expression for ϵ in expression 3.9: $\epsilon = 0.01 \cdot r_i^n$.

Radionuclide	**a** (mm^{-1})	r_0 / R_{max} **(mm)**	**n**	r_i **(mm)**
^{18}**F**	2.60	2.39 / 2.16	4.04	0.051
^{11}**C**	1.48	3.80 / 3.67	3.16	0.21
^{13}**N**	1.46	4.95 / 4.88	3.04	0.29
^{15}**O**	1.15	7.90 / 7.92	3.09	0.36
^{68}**Ga**	2.41	8.98 / 9.06	3.27	0.20
^{82}**Rb**	7.13	16.6 / 16.5	3.11	0.41

Table 3.7: Parameters of the fit to the g3D distribution of PeneloPET to Eq. 3.9, for $5 \cdot 10^6$ positrons annihilating in water.

Comparison to range distributions from other authors

We compare PeneloPET positron range distributions with the ones presented by [Alessio and MacDonald, 2009, Derenzo, 1979, Champion and Le Loirec, 2007, Levin and Hoffman, 1999]. In their paper, [Alessio and MacDonald, 2009] computed directly the g_{3D} distributions for ^{18}F, ^{11}C, ^{13}N and ^{82}Rb radionuclides annihilating in water. [Derenzo, 1979] calculated the $aPSF_{img}$ and G_{2D} distributions for ^{11}C, ^{68}Ga and ^{82}Rb radionuclides in water. [Champion and Le Loirec, 2007] computed the g_{3D}, G_{3D} and $aPSF_{sin}$ distributions for ^{18}F, ^{11}C, ^{13}N, ^{15}O, ^{68}Ga and ^{82}Rb radionuclides, also in water. Finally, [Levin and Hoffman, 1999] obtained $aPSF_{sin}$ distributions for ^{18}F, ^{11}C, ^{13}N and ^{15}O radionuclides.

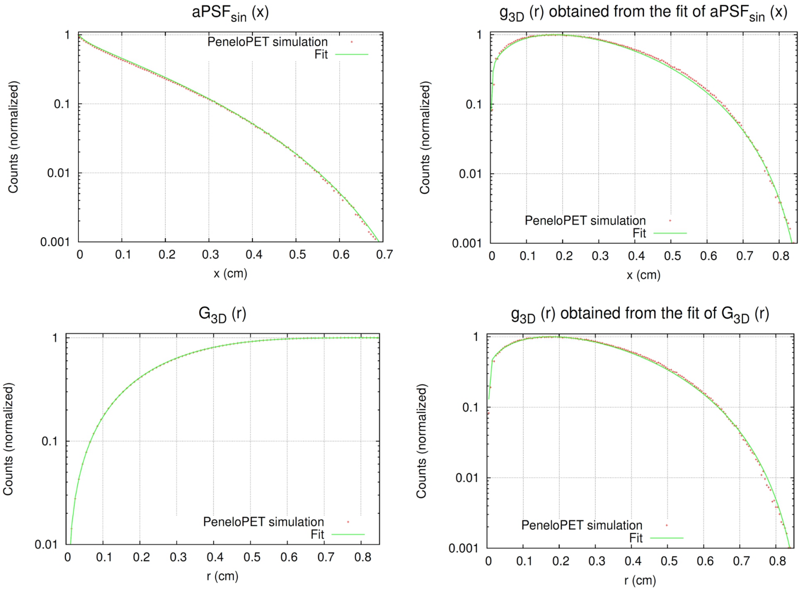

Figure 3.12: Left: $aPSF_{sin}$ (top) and G_{3D} (bottom) distributions obtained from the genetic algorithm. Right: $g_{3D}(r)$ the genetic algorithm recovers to fit the $aPSF_{sin}$ (top) and to the G_{3D} (bottom) distributions shown in the left part of the figure. In all cases for ^{68}Ga in water. The comparison with the direct result of PeneloPET simulation is shown.

Figure 3.14 shows $aPSF_{sin}(x)$ for ^{11}C, ^{13}N, ^{68}Ga and ^{82}Rb point sources in water. Figures 3.15 and 3.16 show the same plots for $g_{3D}(r)$ and $G_{3D}(r)$ distributions. Alessio's [Alessio and MacDonald, 2009] and Champion's [Champion and Le Loirec, 2007] results were obtained taking the g_{3D} distribution from their published figures. On the other hand, Levin's [Levin and Hoffman, 1999] results were obtained from the published $aPSF_{sin}$ distributions. Finally, Derenzo's [Derenzo, 1979] results were obtained from the published G_{2D} distributions.

Looking at figures 3.14, 3.15 and 3.16, one can observe sizeable differences for g_{3D} and $aPSF_{sin}$ distributions from different authors. On the other hand, G_{3D} distributions show smaller differences. Most distributions are within 10% of each other, except, the ones from [Champion and Le Loirec, 2007]. Champions results are also the ones farthest away from Derenzo's data.

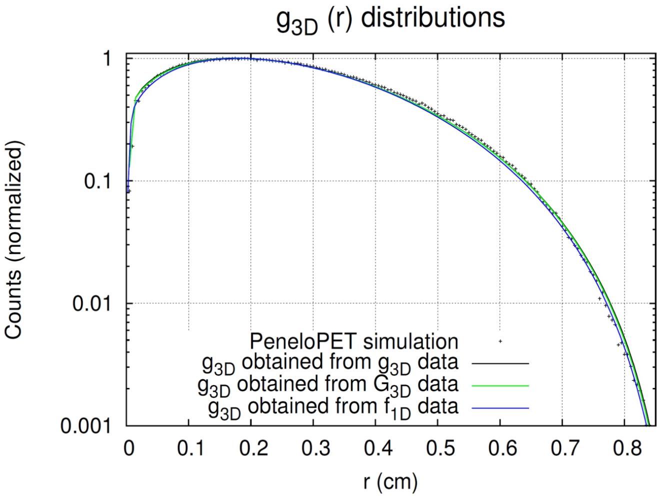

Figure 3.13: $g_{3D}(r)$ given by PeneloPET and the ones recovered with the genetic algorithm fiting Eq. 3.9 using as input g_{3D}, $aPSF_{sin}$ or G_{3D}. For ^{68}Ga in water.

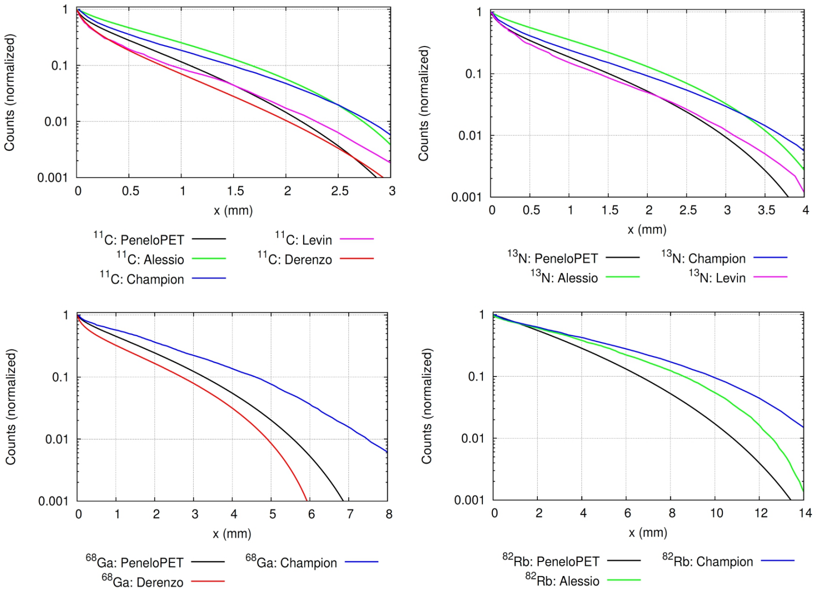

Figure 3.14: Comparison of PeneloPET results with the ones from other authors (Alessio - green, Champion - blue, Levin - pink and Derenzo - red), obtained using the genetic algorithm, for the $aPSF_{sin}(x)$ distributions of ^{11}C, ^{13}N, ^{68}Ga and ^{82}Rb radionuclides annihilating in water.

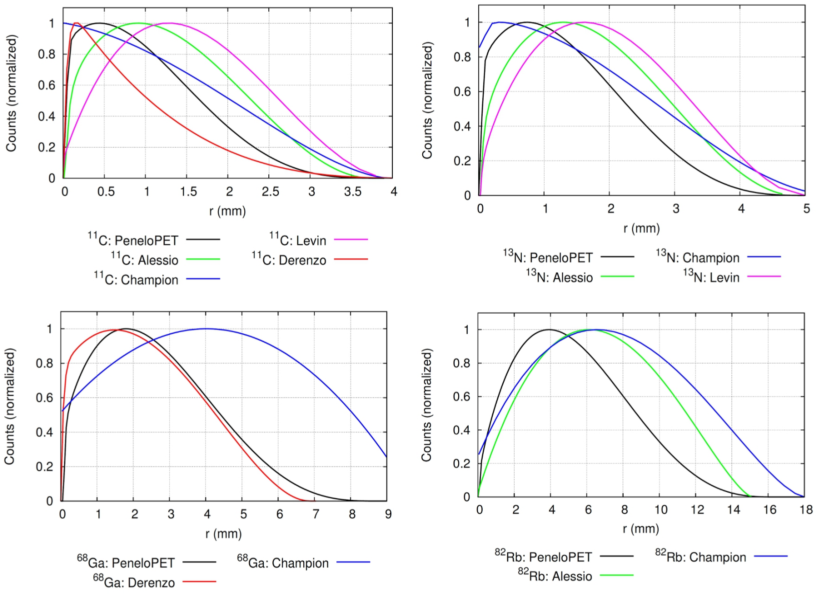

Figure 3.15: Comparison of PeneloPET results with the ones from other authors for the $3D$ angular integrated radial distributions $[g_{3D}(r)]$.

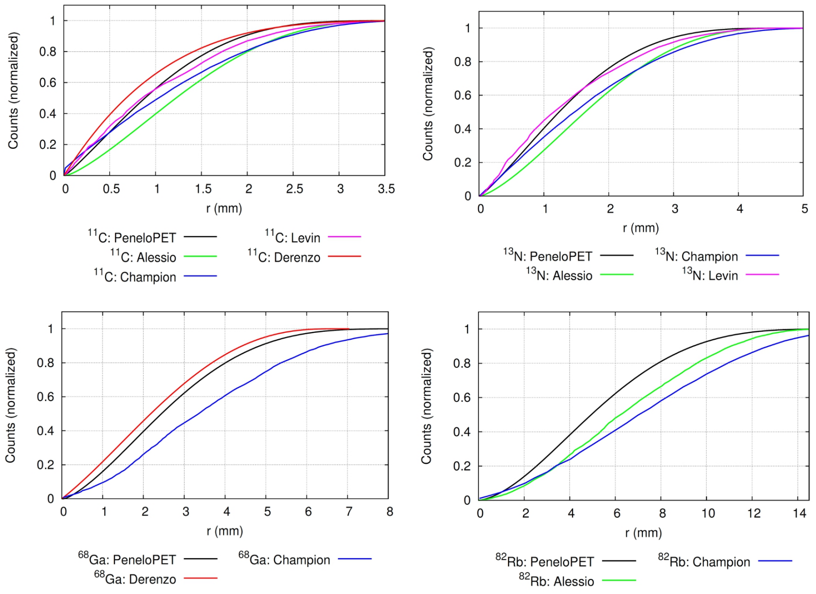

Figure 3.16: Comparison of PeneloPET results with the ones from other authors for the $3D$ accumulated range distributions $[G_{3D}(r)]$.

3.7 Discussion

In this work we derived positron range distributions for different settings, and compared them to existing results in the literature. There is a significant diversity in the way different authors present the results, for instance, using $1D$ projection of the positrons annihilation coordinates ($aPSF_{sin}$ and $aPSF_{img}$), angular integrated radial distributions (g_{3D} and g_{2D}), or accumulated range distributions (G_{3D} and G_{2D}).

It is known that differences of 10% in the mean and maximum positron range values lead to visible differences in range-corrected images (see *chapter 5* of this thesis and [Cal-González et al., 2011b]). Although our estimations obtained with PeneloPET are in agreement with other works and with experimental measurements, there is a clear need for improved experimental results, in order to disentangle the role of positronium formation. Actually, calculations that take this phenomenon into account [Champion and Le Loirec, 2007] clearly depart from most other results.

In our work we used a new procedure based on genetic algorithms to compare our results with others available in the literature. We fitted the g_{3D} distribution to an expression with 3 free parameters (a fourth parameter is fixed by the profile normalization condition used in the positron range model). The parameter r_0 fits the maximum range, n fits the slope at the end of the profile, and a determines the slope at intermediate distances (Eq. 3.9). This fitting function outperforms the two exponential sum proposed by [Derenzo, 1979] for the $aPSF_{sin}$, which fails for large x values. Other authors [Champion and Le Loirec, 2007, Lehnert et al., 2011] proposed a Gaussian fit for g_{3D}, with only 3 parameters. However, PeneloPET results show that these functions depart from the Gaussian shape for large r values. More recently, [Jødal et al., 2012] proposed a non Gaussian fit that seems to perform similarly to ours. However, their fit does not include any parameter explicitly related to maximum positron range.

As expected, g_{3D} and $aPSF_{sin}$ distributions tend to be more different for several authors and approaches, while $3D$ cumulative distributions (G_{3D}) are more stable. G_{3D} represents the fraction of positrons annihilated within a sphere or radius r and it seems to be more robust to compare results available in the literature.

We also compared the mean and maximum positron ranges in water obtained with PeneloPET with those previously available in the literature (tables 3.5 and 3.6). Regarding the mean range R_{mean}, a relatively good agreement is observed between our results and other simulated or semi-empirical estimates, with discrepancies ranging from 7% for ^{18}F to 18% for ^{82}Rb. However, the differences with the results of [Champion and Le Loirec, 2007] are larger, up to 40%. Further, they are larger for larger positron range radionuclides. These discrepancies are likely due to the fact that Positronium formation is included in Champion's results, in contrast with our calculations and most other results that do not consider it.

Regarding to experimental data, PeneloPET predictions are in disagreement with the R_{mean} values measured by [Cho et al., 1975] by more than 50% for ^{18}F, but they are in relatively good agreement with the data provided by [Derenzo, 1979]. The discrepancies observed between our results and some experimental data are likely due to the limited accuracy achievable in the experimental procedures, since the detector resolution was comparable to the positron range for the lowest range radionuclides, such as ^{18}F.

Regarding the maximum range, R_{max}, PeneloPET predictions are consistent with those obtained from Evans' empirical relationships [Evans, 1972], while the discrepancies with

[Champion and Le Loirec, 2007] are again substantial.

Table 3.5 shows the comparison of R_{mean} values obtained for different media with the results obtained with GATE simulations and the theoretical predictions given by the expression in Eq. 3.10. Although PeneloPET and GATE results are in good agreement, with discrepancies smaller than 10% in almost all cases, larger relative differences can be observed for the higher range radionuclides: ^{15}O, ^{68}Ga, and ^{82}Rb.

Positronium (Ps) formation deserves a deeper discussion. As mentioned above, the results of the work that considered Ps formation [Champion and Le Loirec, 2007] depart from all the other ones, which are otherwise in relatively good agreement with each other. This is somehow understandable since Ps formation is expected to have a clear impact on the positron range, especially for formation probabilities larger than 80%, such as the ones used in [Champion and Le Loirec, 2007]. However, these results, that include Ps effects, do not match the experimental results of [Derenzo, 1979] while it is unclear for the experimental values reported by [Cho et al., 1975], which are in turn very different from the Derenzo's ones for the larger range radionuclides.

It is noteworthy that the improvement of the physical model by considering Ps formation seems to worsen the agreement with experiments, especially for larger range radionuclides. This may be due to different Ps formation probabilities for different materials. While [Champion and Le Loirec, 2007] values were extracted from simulations in water, [Derenzo, 1979] experiment was performed in low density polyurethane foam. Ps formation probabilities might be very different in liquid water than in the foam. In consequence, while the inclusion of Ps effects in a simulation may be relatively straightforward, we must realize that accuracy can only be achieved by knowing the formation probabilities for most body tissues, or at least for bone, water and lung.

In summary, to complete the model and to achieve a thorough description of the phenomena involved, accurate experimental measurements of positron range in relevant biological tissues and Ps formation (as well as Ps lifetimes) are warranted.

3.8 Conclusions

In this work we used PeneloPET to generate Monte Carlo simulations of positron range for different radionuclides in different media. $aPSF_{sin}$, $aPSF_{img}$, g_{3D}, g_{2D}, G_{3D} and G_{2D} distributions for each combination radionuclide/material were determined and PeneloPET predictions were compared with values from previous literature. To this end, we also propose the use of a new framework based on a genetic algorithm that fits the radial, angle integrated, $g_{3D}(r)$ distribution of the annihilation points, to any distribution chosen as reference.

Our results were consistent with previous literature, except for the case of [Champion and Le Loirec, 2007], which included positronium formation in their model. Insufficient experimental data are available to properly assess the importance of positronium formation. Therefore, more accurate experimental results for positron range, especially on newer radionuclides and in biological tissues are needed in order to correct for range effects, especially in pre-clinical image reconstruction.

Chapter 4

Simulation of non-pure PET radionuclides

4.1 Introduction

In last chapter we have studied positron range distributions for some common radionuclides in PET imaging.

The most widely used radionuclide and imaging agent is of course ^{18}F-fluorodeoxyglucose (^{18}F-FDG) which is used clinically for staging and evaluation of cancer therapy for a wide variety of cancer types. ^{11}C radionuclide may be used as ^{11}C-choline in oncology or as ^{11}C-methionine for the delineation and measurement of the metabolic activity of brain tumors [Lilja and Bergstrom, 1985]. ^{13}N has many applications in cardiac PET imaging by labeling ammonia molecules for PET myocardial perfusion imaging and ^{15}O may be used also for cardiac PET imaging by labeling water molecules [Bailey et al., 2005].

On the other hand, non cyclotron-based radioisotopes, such as ^{68}Ga [Hoffend et al., 2005, Breeman and Verbruggen, 2007] and ^{82}Rb [Yoshinaga et al., 2006], might be used in a center without a cyclotron facility and have many potential applications in PET imaging. ^{68}Ga has been used to label blood constituents, proteins, peptides and antibodies [Bailey et al., 2005]. On the other hand, ^{82}Rb has been used to study myocardial perfusion and blood flow [Herrero et al., 1992].

All these radionuclides share several properties in common, which facilitate their use in PET imaging:

- Short half-life which allow for short dynamical studies.
- Their decays are allowed, with high branching ratio for β^+ decay (higher than 90%).
- Pure or almost pure emission of positrons (very low amount of extra γ photons emitted among with the annihilation photons).

In this chapter we will study the feasibility of PET imaging with several radionuclides which do not meet the above criteria [Laforest and Liu, 2008, Liu and Laforest, 2009], such as ^{124}I

[Pentlow et al., 1991, Herzog et al., 2002, Belov et al., 2011], ^{76}Br [Dupont et al., 1999, Lövqvist et al., 1999, Lubberink et al., 2002], ^{94m}Tc [Barker et al., 2001] and ^{86}Y [Herzog et al., 1993, Walrand et al., 2003].

These radionuclides are being investigated for novel diagnostic or internal radiotherapy strategies. The generally longer half-life of these non-conventional radioactive nuclides enables the biological processes to be studied over a longer time and allow for distribution of the radioisotope to other imaging centers. However, these radioactive nuclides have usually higher positron emission energies than ^{18}F and emit cascade γ photons following the positron emission or the electron capture [Laforest et al., 2002]. As we have seen in previous chapter, the longer positron range due to higher positron energies results in resolution degradation in PET. In addition, the cascade γ photons will produce photon coincident detections that are spatially uncorrelated, resulting in the background in the emission sinograms which will affect the quantitative accuracy. The cascade γ rays also increase the single event rate of the PET scanner producing additional random coincidences and may lead to inaccurate dead time correction.

^{124}I is one of the most promising new radioisotopes for PET imaging [Belov et al., 2011]. Among the currently available positron emitters suitable for imaging with PET, ^{124}I has the longest physical half-life of 4.2 days (see table 1.1). Combined with the well-investigated behavior of iodine as a label in vivo, this makes ^{124}I a very appealing label for quantitative pharmacokinetics studies. However, two major features of the radioactive decay of ^{124}I have to be accounted for. One is the high energy and therefore long range of the emitted positrons, and the other is a high fraction of non-positron decays accompanied by single photon emission in the same energy window with the annihilation photons: 60.5% of all decays result in a 602 keV photon, and half of the positron producing decays contain such photon in the same cascade.

Other promising radionuclide for PET imaging is ^{94m}Tc, which can potentially be used as a substitute in the typical ^{99m}Tc-labeled single-photon-emitting radio-pharmaceuticals [Bailey et al., 2005, Barker et al., 2001].

The other radionuclides which will be studied in this chapter are ^{76}Br and ^{86}Y. ^{76}Br has been suggested for labeling of antibodies [Lövqvist et al., 1997] and of bromodeoxyuridine, a DNA synthesis tracer which has a specific uptake in fast dividing cells such as in tumours [Bergström et al., 1998, Gardelle et al., 2001]. It has a half-life of 16.2 hours and the branching ratio for cascades with β^+ decay is about 55%. On the other hand, the radionuclide ^{86}Y, which may be used for the in vivo determination of the biodistribution and dosimetry of therapeutic pharmaceuticals labelled with yttrium-90 [Lövqvist et al., 2001, Schneider et al., 2009], has a half-life of 14.7 hours and decays by positron emission with a branching ratio of 32%. As an indication of the complexity of the decay scheme of these radionuclides, the mean number of γ photons (excluding the annihilation photons) per decay for ^{76}Br and ^{86}Y is respectively 1.35 and 2.55. This means that, in average, there will be multiple possibilities to create coincidence pairs from the simultaneous detection of γ photons for each decay event (not only with the annihilation photons). This has the consequence of that the PET camera will not be able to distinguish the true coincidence pairs (those coming from a real annihilation event) for the spurious coincidence events (those fortuitous in which at least one of the singles come from a extra γ emitted in the same or another decay). Thus, images will be contaminated with these spurious counts, and will lose qualitative and quantitative accuracy.

The aim of this chapter is to characterize these radionuclides for quantitative PET imaging and study the effect of the loss of resolution from the positron range, especially in small animal PET imaging where most of novel imaging agent research is performed.

To this end, we will perform the following studies, using our Monte Carlo simulation tool:

- Evaluation of positron range distributions for the non-conventional radionuclides: ^{124}I, ^{76}Br, ^{94m}Tc and ^{86}Y
- From simulated acquisitions of a NEMA NU-4 2008 IQ Phantom [NEMA-NU-4, 2008] filled with each of these radionuclides or with ^{18}F or ^{68}Ga (as reference), we will evaluate:
  - Evolution with the activity of true, random, scatter and positron-gamma coincidences.
  - Background in the image due to spurious coincidences in non-pure emitters.
  - Recovery coefficients for the five capillaries of the phantom and quantification in the hot and cold regions.

4.2 Methods

4.2.1 Prompt-γ simulations with PeneloPET

An accurate modeling of the decay cascades of several radionuclides of interest (^{68}Ga, ^{82}Rb, ^{124}I, ^{76}Br, ^{86}Y and ^{94m}Tc) was included in PeneloPET code, using data obtained from nuclear databases [NNDC, 2011]. The new simulation samples the decay scheme of the radionuclide, and generates tracks for each cascade, with the corresponding probability for them. In this modeling, only cascades with a branching ratio (number of times that a certain decay mode occurs per disintegration) greater than 1% were considered. In the same way, we only considered gamma emissions with a branching ratio greater than 1%.

In figure 4.1 we show the new format (with information about the decay cascades) for the PeneloPET input file **isotope.inp** [España et al., 2009] for ^{68}Ga radionuclide. As illustration, we also included in the figure the simplified decay scheme for this radionuclide, with the cascades included in the simulation, that is, those with a branching ratio greater than 2%. The complete decay scheme can be found in [NNDC, 2011].

With the new format of the **isotope.inp** file, each isotope definition includes one first line with the numeration ID, half life in seconds, atomic mass and name of the radionuclide. Then, for each cascade one new line must be added. This line must include the word *CC* (tag for new decay cascade), the fraction of occurrence for this decay cascade and the type of transition (0 for allowed and 1 for forbidden decays). Next, each emitted particle within a given decay cascade should include its information in a different line including type of particle (B+, B- or G for positron, electron or photon respectively), maximum emission energy and fraction of emission occurrence per decay cascade.

For example, in ^{68}Ga we found four different decay cascades with probability higher or similar to 2%. First cascade is the decay β^+ to the ground state of the daughter nucleus, with the emission of a positron (with maximum energy of 1899 keV), and a probability of 87.9%. Other three decay cascades are included: one β^+ with 1.2% probability and two CE cascades,

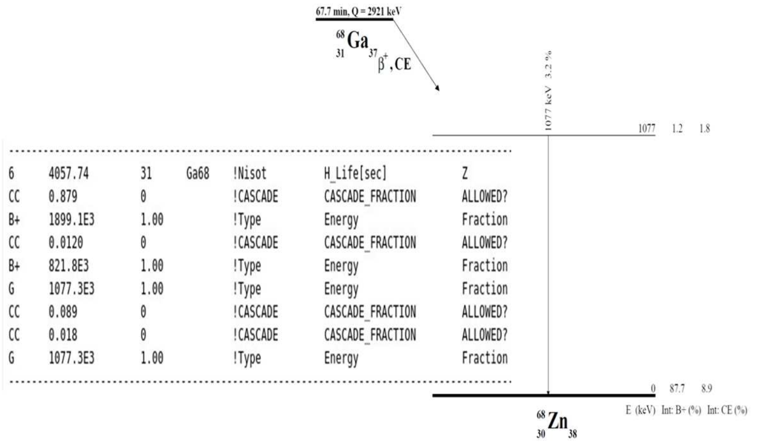

```
-----------------------------------------------------------------------------------------
6     4057.74     31      Ga68    !Nisot       H_Life[sec]        Z
CC    0.879       0               !CASCADE     CASCADE_FRACTION   ALLOWED?
B+    1899.1E3    1.00            !Type        Energy             Fraction
CC    0.0120      0               !CASCADE     CASCADE_FRACTION   ALLOWED?
B+    821.8E3     1.00            !Type        Energy             Fraction
G     1077.3E3    1.00            !Type        Energy             Fraction
CC    0.089       0               !CASCADE     CASCADE_FRACTION   ALLOWED?
CC    0.018       0               !CASCADE     CASCADE_FRACTION   ALLOWED?
G     1077.3E3    1.00            !Type        Energy             Fraction
-----------------------------------------------------------------------------------------
```

Figure 4.1: Left: Example of the new format of the isotope.inp file for ^{68}Ga, with the description of decay cascades included. Right: Simplified decay scheme obtained for this radionuclide including cascades with branching ratio greater than 1%.

with probabilities 8.9% and 1.8% respectively. In addition, one γ emission (1077 keV and 1.8% emission intensity) is included in the simulation.

The half-life of the intermediate excited states in the daughter nuclei, being always inferior to 100 ps, was neglected. This short half-life is about one order of magnitude lower than the typical timing resolution of conventional PET scanners. Therefore, in these simulations, the prompt γ rays are emitted simultaneously with the positron emission. It is common in the considered radionuclides that most of the decays succeed without the emission of a positron, in a process known as Electron Capture decay (EC). In cases with cascades of 2 or more γ rays (coming from a EC decay in most of the cases), these photons may be detected in coincidence, because the half life of the excited states are short in comparison with the usual timing resolution of a PET scanner. These not-correlated gamma emissions may result in spurious coincidences, which will increase the background in the image, reducing the contrast and accuracy of the image.

4.2.2 Decay schemes, β^+ and γ emissions for non-conventional radionuclides

In this section we study in detail the characteristic emissions for the radionuclides (^{124}I, ^{76}Br, ^{94m}Tc and ^{86}Y) which will be included in the analysis performed in this chapter. As we previously mentioned, only decay cascades with a branching ratio higher than 1% were considered in our simulations.

Figure 4.2 shows the simplified decay schemes used in our simulations, for ^{124}I (left) and ^{94m}Tc radionuclides. ^{124}I has a half-life of 4.2 days, and decays by positron emission (β^+), with a branching ratio of 23%, or by Electron Capture (EC), with a probability of 77%. On the other hand, the γ ray abundance exceeds 90% per disintegration. 6 levels of the daughter nucleus are populated with decay probabilities higher than 2% and 6 different γ rays are emitted with a branching ratio greater than 1%. ^{94m}Tc has a half-life of 52 minutes, and decays by β^+ or CE with a probability of 70% or 30% respectively. It decays to 4 levels of the daughter nucleus with a branching ratio higher than the above mentioned 2% and 5 γ photons are emitted with branching ratio higher than 1%, and therefore considered in our simulation framework. Detailed levels schemes for ^{124}I and ^{94m}Tc can be found in [Katakura and Wu, 2008] and [Abriola and Sonzogni, 2006] respectively.

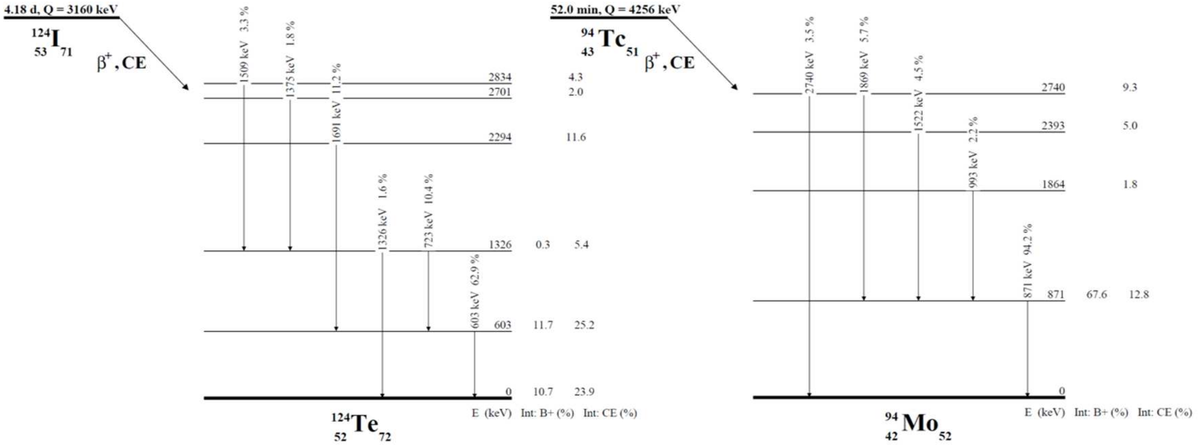

Figure 4.2: Left: Decay scheme considered in our simulations for ^{124}I radionuclide. Right: Decay scheme for ^{94m}Tc

In addition, figure 4.3 presents the simplified levels scheme used in our simulations, for ^{76}Br radionuclide. It has a half-life of 16.2 h and, as in the case of ^{124}I and ^{94m}Tc, decays by positron emission or by EC. The branching ratio for cascades with β^+ decay is about 55%, while the branching ratio for cascades with EC is about 45%. Note that only decays with probability higher than 2% have been considered in our simulations. For this radioisotope, 9 levels of the daughter nucleus are populated with decay probabilities higher than 2% and 10 different gamma rays are emitted with a branching ratio greater than 2%. A detailed decay scheme can be found in [Singh, 1995].

Finally, the decay scheme for ^{86}Y, which has a half-life of 14.7 h and decays by β^+ (32%) or by EC (68%), is depicted in figure 4.4. It has a very complex decay scheme with 20 β^+ decay lines and 28 EC lines, resulting in a large quantity of cascade emissions (a Monte Carlo study of the cascade emissions for this radionuclide was already performed by [Zhu and El Fakhri, 2009]). The complete decay scheme can be found in [Singh, 2001]. In this work we modeled only the major gamma lines with energy between 30 and 2000 keV and intensity higher than 1%. Fifteen different levels of the daughter nucleus are populated with decay probabilities higher than 2% and 26 gamma rays are emitted with the characteristics described above.

Other important characteristic of the decay of non-conventional radionuclides is the existence of several decay cascades, with emission of one positron. The energy of the positron emitted will be dependent on the decay cascade in which the disintegration of the father nucleus took place. A detailed modeling of these emissions must be taken into account in order to estimate the positron range blurring for these radionuclides. Table 4.1 shows the positron emission energies (in keV) and their corresponding intensities (in %) for the non-conventional radionuclides considered in this work.

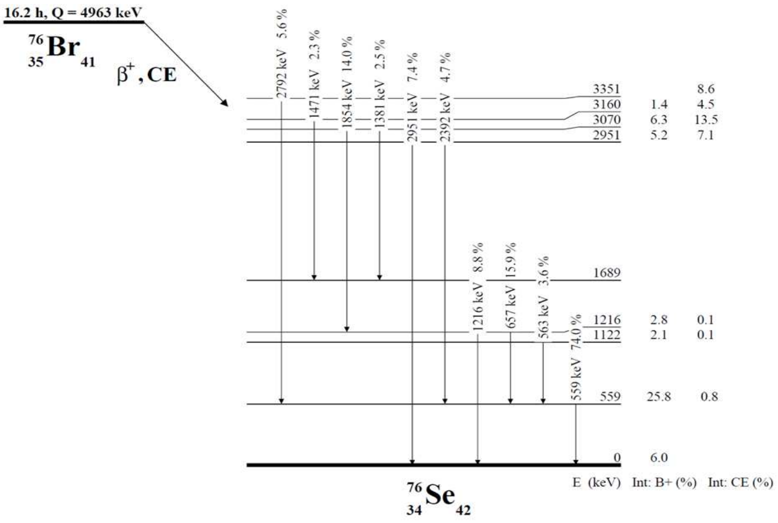

Figure 4.3: Decay scheme considered in our simulations for ^{76}Br radionuclide.

radionuclide	**Positrons emitted:** E_{max} **(keV) / Intensity (%)**								
^{18}**F**	633 / 96.7								
^{82}**Rb**	3378 / 81.8	2601 / 13.1							
^{124}**I**	2138 / 10.7	1535 / 11.7							
^{94m}**Tc**	2439 / 67.6								
^{76}**Br**	3941 / 6.0	3382 / 25.8	2819 / 2.1	2725 / 2.8	2153 / 1.0	1271 / 1.2	990 / 5.2	871 / 6.3	781 / 1.4
^{86}**Y**	3141 / 2.0	1988 / 3.6	1736 / 1.7	1545 / 5.6	1221 / 11.9	1162 / 1.3	1033 / 1.9	900 / 1.1	

Table 4.1: Positron emissions considered in our simulations for the non-conventional radionuclides. ^{18}F and ^{68}Ga are included as reference.

As we can see in table 4.1, for ^{94m}Tc radionuclide only one decay cascade (with 67% probability) involve positron emission, ^{124}I has two decays cascades with positron emission, of energies 1535 (decay to first excited level) and 2138 (decay to ground level) keV respectively. On the other hand, ^{76}Br and ^{86}Y have 9 and 8 decay cascades with positron emission and probability higher than 1%.

Table 4.2 shows the energy distribution of prompt γ emissions in coincidence and not in coincidence with the 511 keV annihilation photons, for the radionuclides studied in this chapter, as well as for other non-pure emitter which will be also studied in *chapter 7* of this thesis (simulation of triple coincidences): ^{22}Na, ^{68}Ga, and ^{82}Rb. In this table we can see the percentage of γ photons emitted by these radionuclides, in coincidence and not in coincidence, below the energy window usually employed in PET studies ($<$ 400 keV), in the energy window (400 - 650 keV) and above the energy window ($>$650 keV).

Note that the amount of spurious coincidences in PET will be given by the fraction between prompt γ photons emitted in coincidence with the emission of a positron and the annihilation γ photons emitted per decay. For example, in the case of ^{124}I radionuclide, although the number of prompt γs emitted in coincidence with the annihilation photons is not so high (12% per decay in the coincidence window), as the branching ratio for decay with emission of a positron (and in

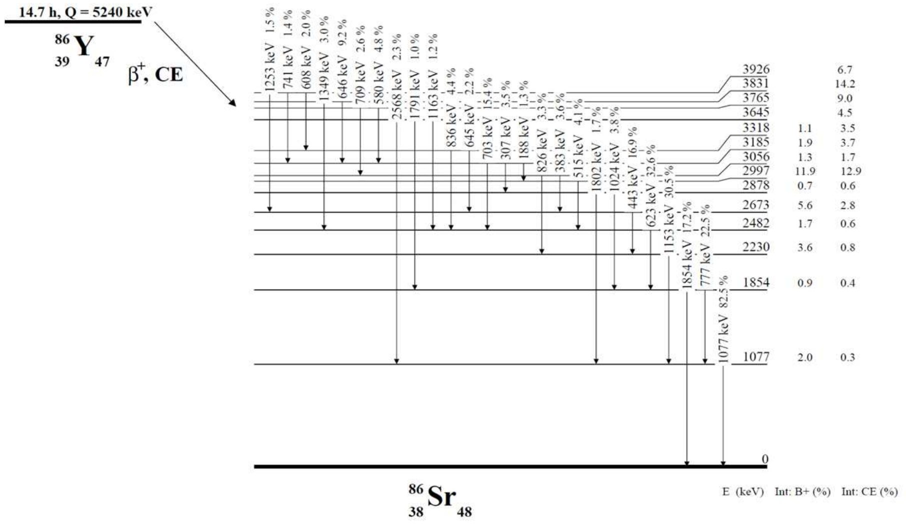

Figure 4.4: Decay scheme considered in our simulations for ^{86}Y radionuclide.

				γ emissions: In coinc. / Not in coinc. (% per decay)			
radionuclide	**Ratio β^+ (%)**	**CE (%)**	**Annih. γ (% per decay)**	**$<$ 400 keV**	**400 - 650 keV**	**$>$ 650 keV**	**Total**
^{22}Na	90.4	9.6	180.8	0.0 / 0.0	0.0 / 0.0	90.4 / 9.5	90.4 / 9.5
^{68}Ga	88.9	11.1	177.8	0.0 / 0.0	0.0 / 0.0	1.2 / 2.2	1.2 / 2.2
^{82}Rb	95.4	4.6	190.9	0.0 / 0.0	0.0 / 0.0	13.1 / 2.6	13.1 / 2.6
^{94m}Tc	70.2	29.8	140.3	0.0 / 0.0	0.0 / 0.0	70.2 / 37.1	70.2 / 37.1
^{124}I	22.7	77.3	45.0	0.0 / 0.0	11.9 / 43.0	0.5 / 27.7	12.4 / 70.7
^{76}Br	55.0	45.0	109.0	0.0 / 0.0	71.8 / 2.4	34.8 / 25.6	106.6 / 28.0
^{86}Y	31.9	68.1	64.0	3.2 / 5.0	37.9 / 33.9	133.3 / 61.0	174.4 / 99.9

Table 4.2: Energy distribution of prompt gamma emissions for several radionuclides of interest. For each energy window, the percent abundance of emitted γ rays per decay (in coincidence and not in coincidence with the annihilation photons) is presented.

consequence the intensity of annihilation photons) is also low (22.7%); the effect of these prompt γ_s emitted (and the amount of spurious coincidences) will be relatively large. On the other hand, the amount of γ photons emitted not in coincidence with the annihilation photons will increase the number of random coincidences for a given activity.

4.2.3 Positron range for non-conventional radionuclides

The simulation of the positron range for the non-conventional radionuclides was performed using the same framework described in **chapter 3**. However, there are several factors which we need to take into account in order to perform an accurate positron range simulation for the non-standard radionuclides:

- The complex decay scheme for most of these radionuclides, with several decay cascades involving positron emission. We will obtain one energy spectra for each positron emitted, which we have to normalize by the branching ratio of this positron emission.

- Most of these radionuclides have non-allowed β^+ decays, with different shape of the energy spectrum [Daniel, 1968].

A forbidden β^+ decay is the one does not take place in the allowed approximation (see *section 3.2.1* in **chapter 3**), but in a higher order approximation. The first forbidden β^+ decay, which is the one we will find in the decay cascades considered for these radionuclides, may be defined by the selection rules: $\Delta I = 0,\ 1$ or 2 with parity change. Generally speaking, the shape of the energy spectrum for a forbidden β^+ decay may be defined by a correction factor to be applied to the allowed energy spectrum [Daniel, 1968]:

$$S_n = \sum_J S_n^{(J)} \tag{4.1}$$

Where the subscript n refers to the degree of approximation (n = 0: allowed, n = 1: first forbidden, etc.), and J refers to the total angular momentum carried away by the two leptons (positron and neutrino in a β^+ decay).

In the case of first-forbidden decay, we have:

$$S_1 = S_1^{(0)} + S_1^{(1)} + S_1^{(2)} \tag{4.2}$$

In a particular transition, one or two of the $S_1^{(i)}$ elements may be discarded.

A particular class of forbidden transitions are the *unique* transitions, where a unique angular momentum $J = n + 1$ contributes to the shape of the energy spectrum. For these kind of transitions, the correction factor that must be applied is:

$$S_1^{(2)} = p^2 + q^2 \tag{4.3}$$

Where p and q are the momentum of the positron and the neutrino respectively.

In the case of non-unique transitions, the definition of the correction factor is more complex. Usually the spectral shapes are fitted with the formula:

$$S_1 = Cte[1 + aE + \frac{b}{E} + cE^2] \tag{4.4}$$

Where a, b and c might be obtained by fitting the theoretical spectra to experimental data.

In this work, the simulation of positron range for ^{94m}Tc (allowed), ^{124}I, ^{76}Br and ^{86}Y (first-forbidden) radioisotopes was carried out by using the PeneloPET code, modified to take into account the decay cascades and the non-allowed transitions for these radionuclides. We have simulated one million of decays from a point source placed at the center of the Field Of View (FOV), in water media. Projection into one direction $aPSF_{sin}(x)$, radial $g_{3D}(r)$ and cumulative $G_{3D}(r)$ positron range distributions were obtained. As most of forbidden transitions for these radionuclides are unique, and the difference in shape of energy spectra for unique and non-unique transitions is relatively small; we will only consider the correction factor from 4.3 in our simulation of forbidden decay cascades.

For radionuclides with only one or two positron emissions with similar energy (as for example: ^{94m}Tc or ^{124}I, see table 4.1), the $g_{3D}(r)$ range distribution may be modeled, as in the allowed radionuclides, using the analytic expression in Eq. 3.9. On the other hand, in the case of multiple positron-emitting radionuclides (as for example ^{76}Br and ^{86}Y), the expression 3.9 does not fit well the $g_{3D}(r)$ range distribution, due to the fact that there are many positron emissions with different energies and similar probabilities, and the shape of $g_{3D}(r)$ is different than in cases with only one or two positron emissions with similar energies. For the multiple positron-emitting radionuclides, we modeled the $g_{3D}(r)$ distribution using the following expression:

$$g_{3D}(r) \approx C \left[A_1 \cdot r \cdot e^{-\frac{(r-B_1)^2}{C_1}} + A_2 \cdot e^{-\frac{(r-B_2)^2}{C_2}} \right] \left[1 - \left(\frac{r}{r_0} \right)^2 \right] \tag{4.5}$$

For $r < r_0$, and zero otherwise. A_1, B_1, C_1, A_2, B_2, C_2, r_0 and n are the fitting parameters. This expression has three parts: first member (Gaussian function multiplied by r) represents the contribution to range of positrons emitted at low energies, the second member (Gaussian function) represents the contribution of high energy cascades. Finally, in the third part of the equation, the r_0 fitting parameter, as in Eq. 3.9, represents the maximum positron range.

4.2.4 Simulated acquisitions

In order to evaluate the feasibility of obtaining PET images using these non-conventional radionuclides, we have carried out simulations of an Image Quality (IQ) phantom (according to [NEMA-NU-4, 2008] protocol) filled with ^{124}I or ^{76}Br. Acquisitions with ^{18}F (short range and no additional emissions) and ^{68}Ga (medium-large range and no additional emissions) have also been simulated, as reference. The IQ phantom is described in **appendix 1** of this thesis and in [NEMA-NU-4, 2008].

From these simulated acquisitions, we have evaluated:

- Evolution of coincidences with the activity: We have measured the evolution of each type of coincidence (number of trues, randoms and positron-gamma coincidences) with the activity of the acquisition, for ^{124}I, ^{94m}Tc, ^{76}Br and ^{86}Y. These studies were carried out by means of short simulations (of about 1 second) of the IQ phantom.

- Noise (%): We measured the noise by drawing a 22.5 mm diameter (75% of active diameter) and 10 mm long cylindrical Volume Of Interest (VOI), within the uniform region of the phantom. Mean value and standard deviation (in %) were measured for each simulated acquisition.

- Background (%): The background was estimated by drawing a cylindrical VOI (4 mm diameter and 12 mm long) centered in the capillaries region. The mean value in counts / voxel within this VOI is compared against the mean value obtained in the uniform region (the ratio background / uniform is presented in percentage).

- Quantification in hot and cold regions: We measured ratios hot / uniform and cold /uniform for each simulated acquisition. To carry out this purpose, we drawn cylindrical VOI inside the HOT and COLD regions (8 mm diameter and 8 mm long), and we compared the mean value of counts / voxel within these VOIs against the mean value measured in the uniform region.

- We also compared the activity profiles thought the 2 and 3 mm capillaries and thought the hot and cold regions of the IQ phantom.

The simulations performed to study the image quality were set in order to have around 100 million counts in each IQ image. The radionuclides simulated have been ^{18}F, ^{68}Ga, ^{124}I and ^{76}Br. ^{18}F and ^{68}Ga have been used as reference (short and medium large positron range with no additional γ emissions, respectively). In table 4.3 we show the parameters chosen for the simulated acquisitions for each radionuclide.

The image reconstruction was performed by using the FIRST reconstruction algorithm [Herraiz et al., 2006], with 1 iteration and 100 subsets. The reconstructed images were saved to disk each 20 image updates.

Radionuclide	Initial activity (MBq)	Half life	β^+ branching ratio (%)	ACQ time (s)	Coincidences ($\times 10^6$)
^{18}F	24.3	109.8 min	96.7	290	101.1
^{68}Ga	24.3	67.7 min	88.9	320	101.5
^{124}I	24.3	4.2 days	22.7	940	101.8
^{76}Br	24.3	16.2 hours	55.0	440	100.2

Table 4.3: Parameters for the simulated acquisitions of the IQ phantom.

4.3 Results

In this section we present the results obtained from the simulations carried out for the non-conventional radionuclides studied in this thesis.

First we studied the positron range distributions for ^{18}F, ^{82}Rb, ^{124}I, ^{94m}Tc, ^{76}Br and ^{86}Y radionuclides, as well as the comparison of energy spectra for allowed and non-allowed β^+ decays. Then, the evaluation of the statistics for each type of coincidence with the activity is presented for ^{18}F, ^{124}I, ^{94m}Tc, ^{76}Br and ^{86}Y. Finally, we show the results obtained from the evaluation of image quality in the IQ phantom filled with ^{18}F, ^{68}Ga, ^{124}I and ^{76}Br.

4.3.1 Positron range distributions

In this section we study the positron range distributions for the radionuclides considered in this work.

First, we evaluated the effect of taking into account forbidden decay cascades in the energy spectra of emitted positrons and, in consequence, in the positron range distributions. In this work we centered just in 1^{st} forbidden decays, due to the fact of the most of the decay cascades in these radionuclides are of this type. Figure 4.5 shows the energy spectra (left) and the $g_{3D}(r)$ range distribution obtained for ^{124}I radionuclide, using the allowed approximation and considering 1^{st} forbidden decays for the cascades of this radionuclide.

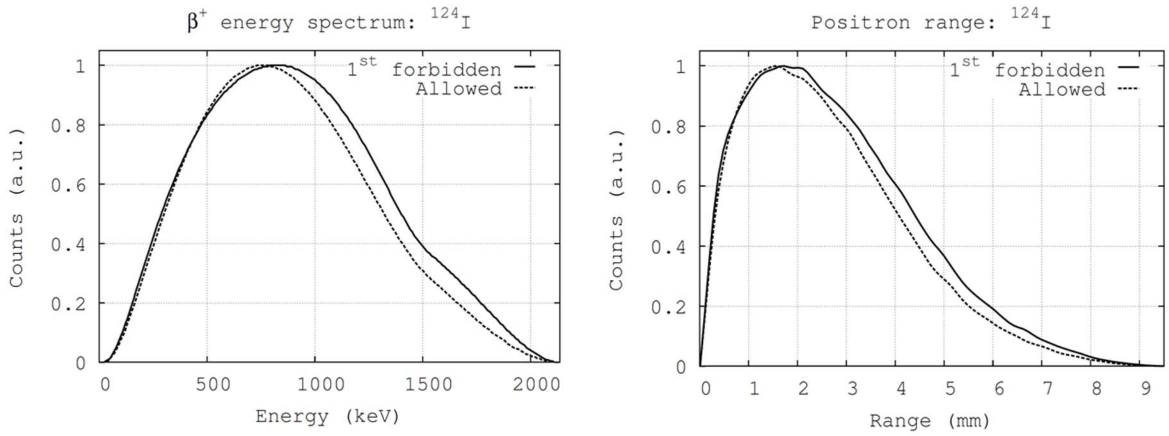

Figure 4.5: Shape of energy spectra (left) and $g_{3D}(r)$ range distribution for ^{124}I, using the allowed and the 1^{st} forbidden approximations for decay cascades

We can see differences of about 10% in the shape of β^+ energy spectra and positron range distributions we the 1^{st} forbidden approximation for decay cascades is taken into account in our simulations.

In figure 4.6 (left) we show the $1D$ range distributions $aPSF_{sin}(x)$ for the non-conventional radionuclides studied here. Range distributions for ^{18}F (short range) and for ^{82}Rb (large range) are also included in the figure, as reference. On the right side of the figure, we included the values of the C, k_1 and k_2 parameters obtained from the fitting of the 1D range distributions to the expression 3.4.

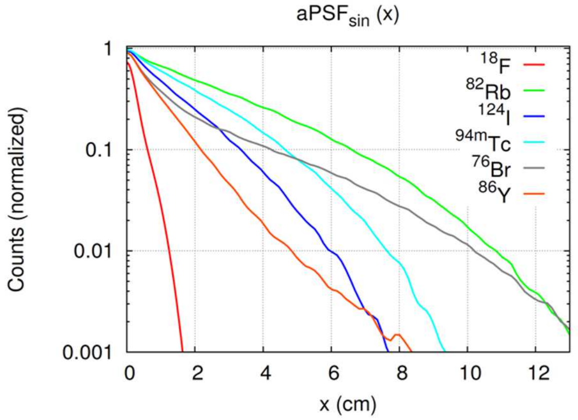

Isotope	Fitting parameters		
	C	k_1 (mm^{-1})	k_2 (mm^{-1})
^{18}F	0.41	25.5	**3.27**
^{82}Rb	0.14	60.5	**0.31**
^{124}I	0.06	3.53	**0.67**
^{94m}Tc	0.02	5.18	**0.48**
^{76}Br	0.62	1.91	**0.32**
^{86}Y	0.19	2.80	**0.95**

Figure 4.6: Left: $aPSF_{sin}(x)$ range distributions for non-conventional radionuclides. Right: Values of C, k_1 and k_2 fitting parameters for these distributions. ^{18}F and ^{82}Rb results are also presented in the figure, as reference.

Alternatively, we show in figure 4.7 the radial range distributions $g_{3D}(r)$ (left) and $G_{3D}(r)$ for the same radionuclides. The fitting parameters of $g_3D(r)$ distributions to the analytic expression in 3.9 are presented in table 4.4, for ^{124}I and ^{94m}Tc radionuclides. In table 4.5 we present the fitting parameters to Eq. 4.5, for ^{76}Br and ^{86}Y radionuclides.

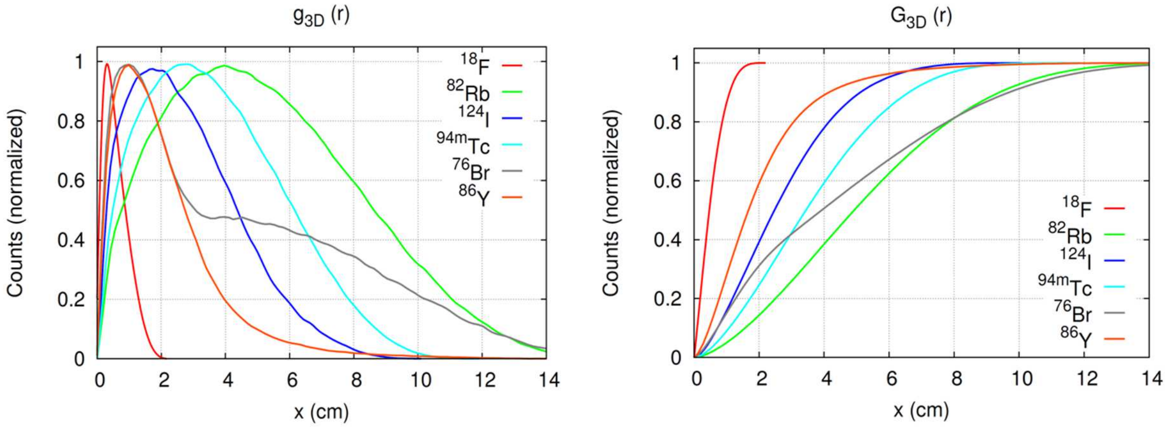

Figure 4.7: $g_{3D}(x)$ (left) and $G_{3D}(r)$ (right) range distributions for non-conventional radionuclides. ^{18}F and ^{82}Rb results are also presented in the figure, as reference.

Radionuclide	**a** (mm^{-1})	r_0 **(mm)**	**n**	r_i **(mm)**
^{124}I	3.07	11.0	4.46	0.36
^{94m}Tc	2.49	11.1	2.72	0.33

Table 4.4: Parameters for the fit of g3D distribution to Eq. 3.9 for ^{124}I and ^{94m}Tc radionuclides.

Radionuclide	$A_1(mm^{-1})$	B_1 **(mm)**	C_1 **(mm)**	A_2	B_2 **(mm)**	C_2 **(mm)**	r_0 **(mm)**	**n**
^{76}Br	9.40	-3.26	7.27	0.52	5.74	35.5	21.8	1.48
^{86}Y	12.5	-3.07	13.1	0.39	6.00	16.9	14.7	0.12

Table 4.5: Parameters for the fit of g3D distribution to Eq. 4.5 for ^{76}Br and ^{86}Y radionuclides.

4.3.2 Statistics of double coincidences

Figure 4.8 shows the evolution in the number of coincidences (trues - black, randoms - red, positron-gamma - green, scatter - dark blue and pile-up - sky blue) with the activity, for: ^{124}I, ^{94m}Tc, ^{76}Br and ^{86}Y radionuclides. The activity of the acquisitions is expressed in MBq.

On the other hand, in figure 4.9 we depict the comparison of the number of coincidences for these non-conventional radionuclides against ^{18}F (no prompt γ photons emitted) results. In the figure we present (from left to right and from top to bottom) the number of total coincidences and the ratio (in percentage) of true, random and positron-gamma coincidences.

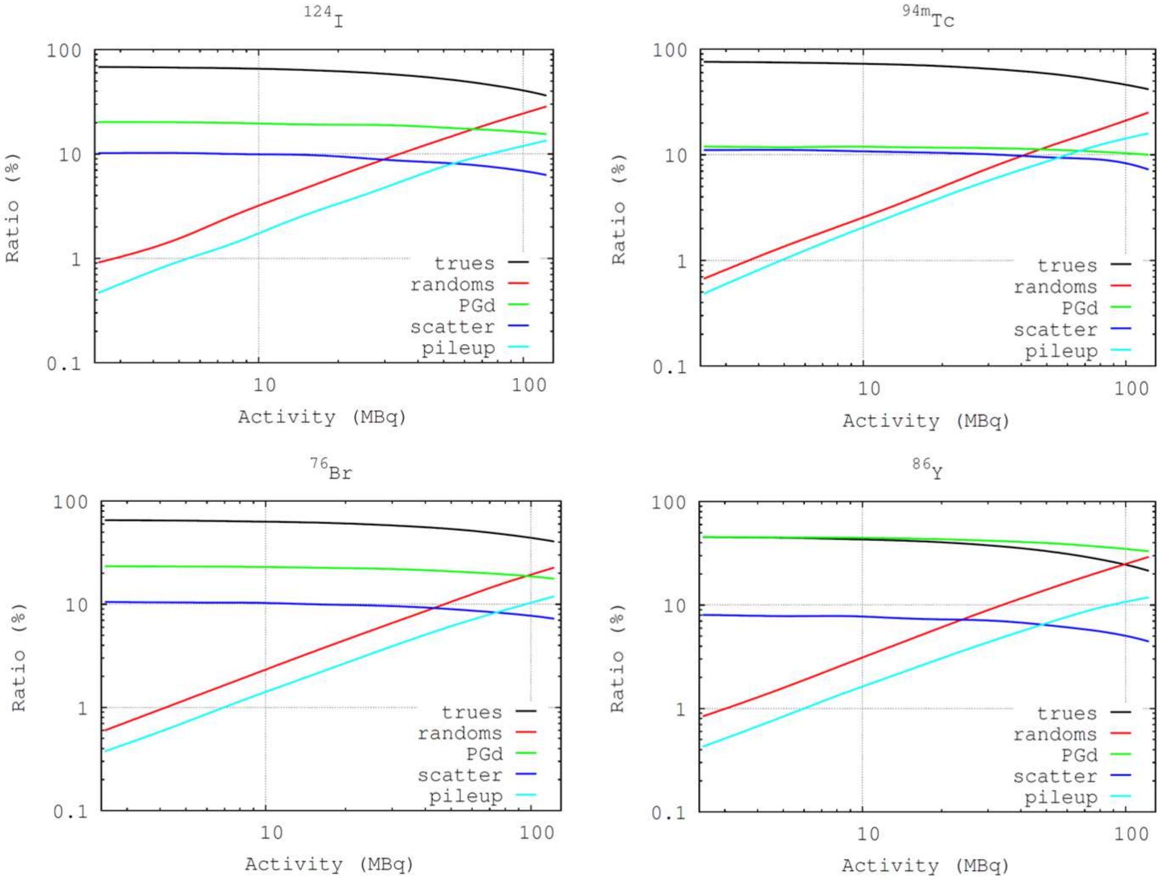

Figure 4.8: Evolution of each type of coincidence with the activity. radionuclides simulated: from left to right and from top to bottom: ^{124}I, ^{94m}Tc, ^{76}Br and ^{86}Y.

4.3.3 Image quality

Figure 4.10 shows the transverse slices, in the capillaries region, for the reconstructed IQ phantom, filled with ^{18}F, ^{68}Ga, ^{124}I and ^{76}Br radionuclides. In this figure we also plotted the profiles through the 3 and 3 mm capillaries of the phantom (bottom side of the picture). In addition, transverse views with hot and cold regions and profiles through these regions are also depicted in the same figure.

Finally, table 4.6 show the measured values for noise, ratio background / uniform, hot / uniform and cold / uniform for the reconstructed IQ phantom.

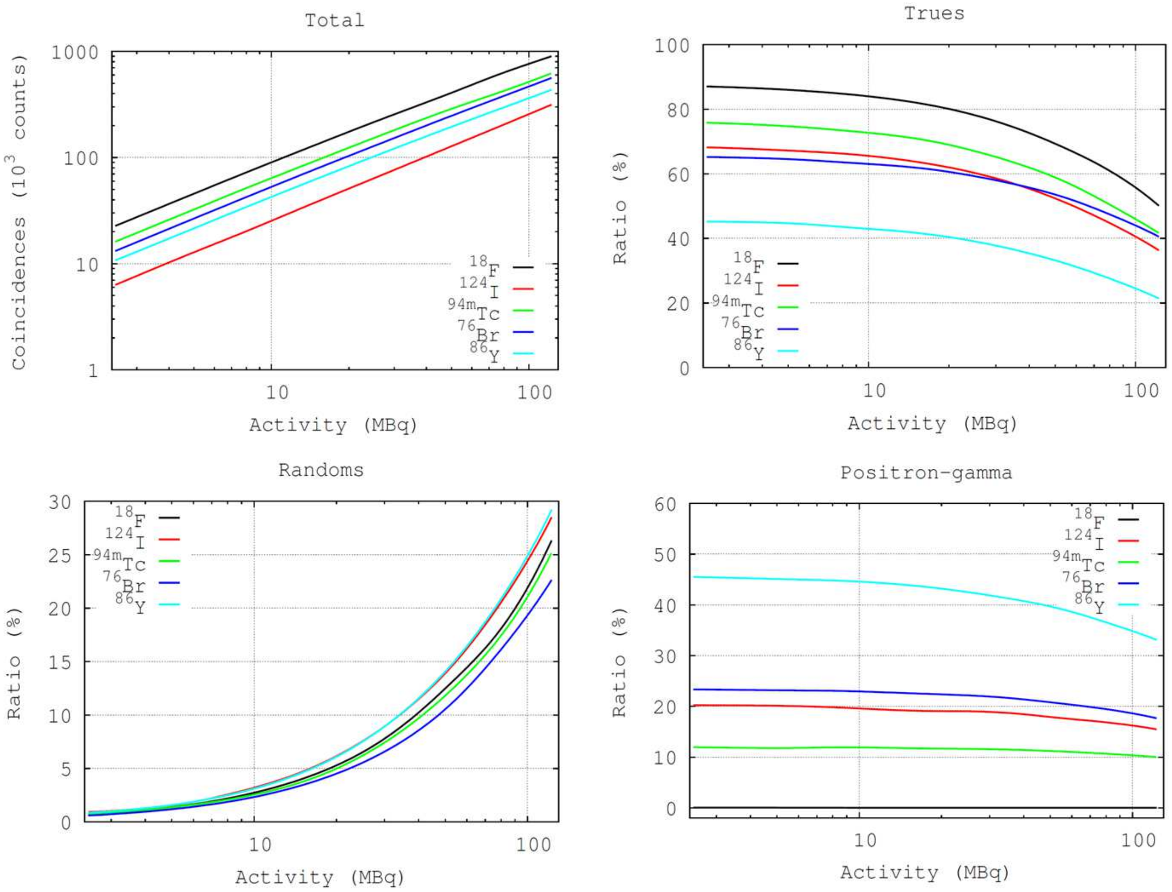

Figure 4.9: Comparison of the number of each type of coincidence for the non-conventional radionuclides against ^{18}F. From left to right and from top to bottom: total coincidences, trues, randoms and positron-gamma ratios.

		Radionuclide			
	Image updates	^{18}**F**	^{68}**Ga**	^{124}**I**	^{76}**Br**
Noise (%)	20	5.34	6.13	6.43	9.26
	60	9.99	10.2	11.1	13.5
	100	11.6	11.8	12.9	15.0
Bckg / Uniform (%)	20	3.49	6.18	8.97	15.2
	60	2.41	5.09	6.08	13.8
	100	2.67	4.74	6.14	12.7
Hot / Uniform	20	4.08	3.38	2.72	2.84
	60	4.01	3.26	2.62	2.73
	100	4.13	3.30	2.65	2.78
Cold / Uniform	20	0.42	0.55	0.56	0.66
	60	0.25	0.44	0.45	0.59
	100	0.22	0.42	0.45	0.58

Table 4.6: Measured values for noise, ratio background / uniform, hot / uniform and cold / uniform for the IQ phantom filled with different radionuclides.

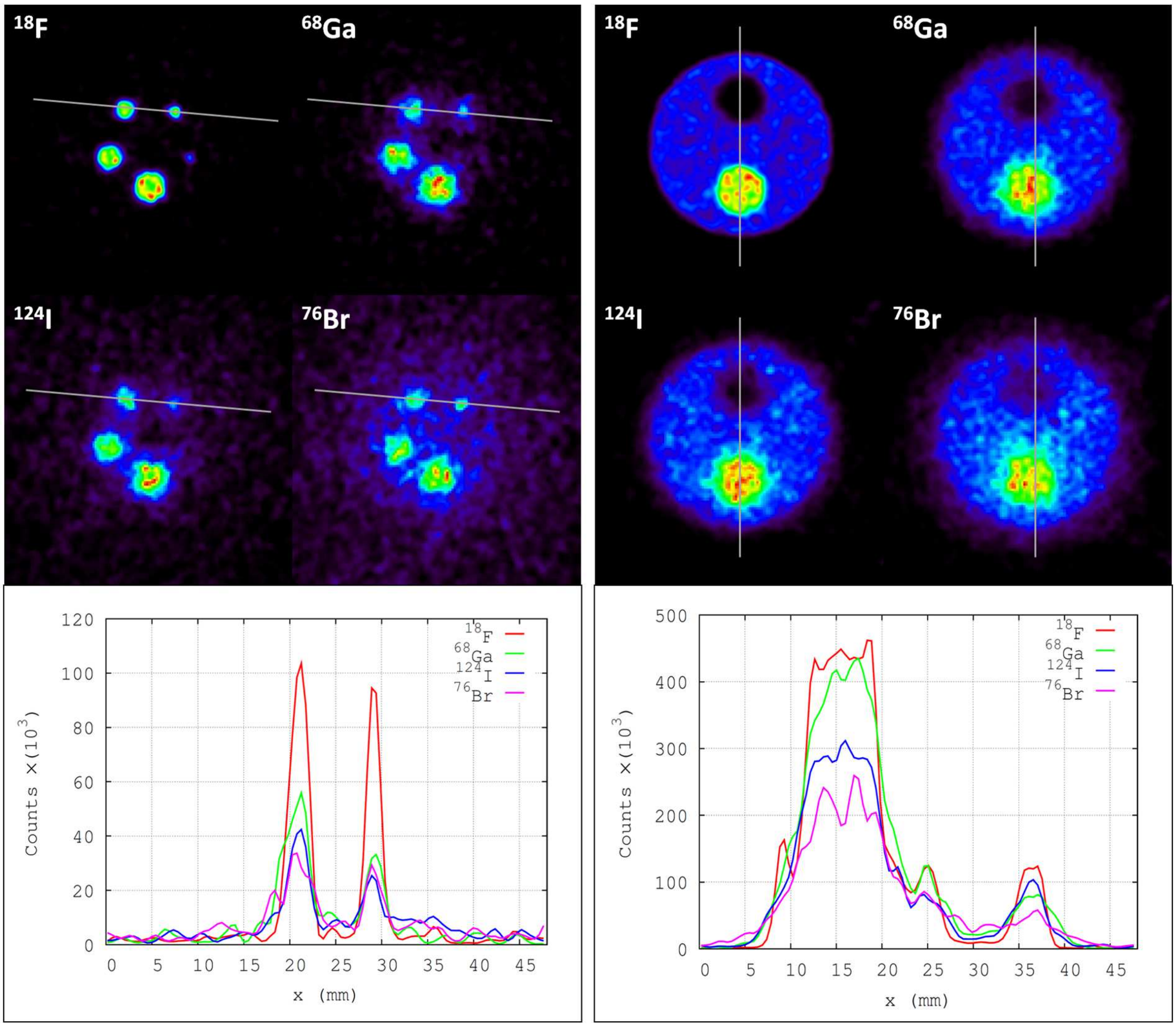

Figure 4.10: Left: Transverse images of the reconstructed IQ phantom, in the region of the capillaries: from left to right and from top to bottom: ^{18}F, ^{68}Ga, ^{124}I and ^{76}Br. Bottom: Profiles through the 3 and 2 mm line sources of the IQ phantom.Right: Transverse images of the reconstructed IQ phantom, with the hot and cold regions included. Bottom: Profiles through the hot and cold regions.

4.4 Discussion and conclusions

In this chapter we studied the feasibility of doing PET imaging with several radionuclides of interest. We focused our study in two parameters which will deteriorate image quality in PET imaging: positron range and prompt γ emissions. Positron range appears as a blurring in the image, and results in a degradation of the spatial resolution of the system. Prompt γ emissions, in the other hand, contribute as a background in the image, which affect the quantitative accuracy, and increase the single event rate producing additional random coincidences.

First, and regarding the positron range, we have seen that many of these non-conventional radionuclides have non-allowed transitions in their decay schemes. Nevertheless, the differences in shape of the energy spectra of emitted positrons for allowed or first-forbidden transitions are relatively small (around 10%), and this also applies for positron range distributions. On the contrary, we have seen a non-negligible dependence on the positron range distributions with the number of positrons emitted, that is, number of decay cascades which involve an emission of a positron. For multiple positron-emitting radionuclides, the expression in Eq. 3.9 does not represent the behaviour of the $g_{3D}(r)$ range distribution, and other analytical expression must be employed.

For the multiple positron-emitting radionuclides (^{76}Br and ^{86}Y in this work) we have chosen Eq. 4.5 as empirical function. This expression has eight fitting parameters, which have been adjusted to the simulated range distribution by means of the genetic algorithm described in **chapter 3**.

In figures 4.8 and 4.9 we have shown the evolution of each type of coincidence with the activity for the non-conventional radionuclides, compared against ^{18}F (no prompt γ emissions) results. One can see that the ratio of positron-gamma coincidences increases with the amount of prompt γ photons emitted in coincidence with the annihilation photons, and the ratio of random coincidences increases with the number of prompt γ emissions not in coincidence. On other hand, the difference observed in the total number of coincidences is due to the different branching ratio for β^+ decay for these radionuclides.

Regarding the image quality that might be achieved with non-conventional radionuclides, we have studied four cases:

- ^{18}F: The standard and most used PET radionuclide. Short positron range and no additional γ emissions.
- ^{68}Ga: Medium-large positron range ($E_{max} = 1900$ keV, table 3.1). No additional γ photons emitted within the energy window (table 4.2).
- ^{124}I: Medium-large positron range ($E_{max} = 2100$ keV, table 4.1). Medium-high amount of prompt γ emissions in coincidence (around 50% respect to β^+ decays, table 4.2).
- ^{76}Br: Large positron range ($E_{max} = 3900$ keV, table 4.1). High amount of prompt γ emissions in coincidence within the energy window (around 130% respect to β^+ decays, table 4.2).

We presented some transverse views of the reconstructed IQ phantoms, filled with these radionuclides, as well as the profiles thought capillaries and hot and cold regions, in figure

4.10. In this figure we can see the degradation in spatial resolution and quantification when radionuclides with large positron range and high amount of prompt γ emissions are employed in the acquisition. In addition, table 4.6 reinforces the statement of higher amount of prompt γ emissions results in poorer quantification. As we can see in this table, for ^{124}I and ^{76}Br radionuclides the background level is higher and the quantification in the hot and cold regions is worse (theoretical values: ratio hot / uniform = 4.0, ratio cold / uniform = 0.0). In table 4.6 we can also see that the noise for these radionuclides is higher, due to the large positron range and the high amount of prompt γ emissions.

In summary, we have presented data that illustrate that: the positron range clearly reduce the spatial resolution of PET images, image noise is largely increased due to the range and the prompt γ emissions, and the quantification accuracy degrades significantly when radionuclides with large positron range and prompt γ emissions are being used. Therefore, and in order to obtain high image quality and quantification accuracy for these radionuclides, positron range and cascade γ rays must be considered under special considerations.

The objective for the following two chapters of this thesis will be to accurately correct for positron range and prompt γ emissions in 3D high resolution preclinical PET imaging, in order to obtain high image quality and quantification accuracy for the radionuclides studied in this chapter.

Chapter 5

CT-based positron range correction

5.1 Introduction

Positron range is a significant factor that limits PET image resolution, independently of other physical effects such as inter-crystal scatter, non-collinearity, apart from the size of the PET detectors and patient motion [Levin and Hoffman, 1999]. On one hand, as we already mentioned in *chapter 3*, for certain radionuclides and tissues, it might be the most important source of resolution degradation. On the other hand, it has been shown that positron physics is becoming one the major factors that may limit the spatial resolution of future PET scanners [Cal-Gonzalez et al., 2009, Blanco, 2006, Levin and Hoffman, 1999].

Accurate system modeling is critical to the success of iterative image reconstruction in emission tomography. A number of studies have shown that accurate modeling of system response matrix can lead to superior image quality [Rahmim et al., 2008, Panin et al., 2006, Stickel and Cherry, 2005, Qi et al., 1998]. In particular, modeling of positron physics, such as positron range and photon non-collinearity, has attracted growing attention in the last years.

In this chapter we present a review of the existent literature about range correction in PET, as well as the development and evaluation of our proposed methods for positron range correction.

5.1.1 Previous work found in the literature

Traditionally, positron range was not a major concern in PET: for lower-energy emitters such as ^{18}F is much lower than the resolutions achievable with old PET scanners. Nevertheless, in a few recent simulation studies positron range has been identified as a limiting factor if the spatial resolution below the millimeter is achieved [Blanco, 2006, Stickel and Cherry, 2005, Lee et al., 2004]. Not only that, for long-ranged radionuclides, as for example ^{82}Rb in cardiac imaging, positron range will impose a great influence on overall system resolution [Rahmim et al., 2008].

The blurring effect of positron range of several medically important isotopes has been measured by physical experiments [Phelps et al., 1975, Cho et al., 1975, Hoffman et al., 1976]. These experiments were of limited accuracy due to the fact that the resolution of the detector was comparable to the positron range to be measured. For this reason, other authors proposed to compute range distributions using analytical formulae [Alessio and MacDonald, 2009, Palmer and Brownell, 1992],or by means of Monte Carlo simulations [Cal-González et al., 2013a, Jødal et al., 2012, Lehnert et al., 2011, Alessio and MacDonald, 2009, Champion and Le Loirec, 2007, Sánchez-Crespo et al., 2004, Levin and Hoffman, 1999, Harrison et al., 1999]. In water medium, the blurring effect ranges from a few tenths of a millimeter for lower-energy emitters to several millimeters for higher-energy emitters.

Several correction approaches have been proposed to remove the blurring caused by positron range. Fourier-deconvolution techniques have been proposed [Derenzo, 1986, Haber et al., 1990]. Nevertheless, these works share the handicap that they do not consider the tissue where the positrons are annihilated, and the corrections are performed considering only water as annihilation medium. This might result in over- or infra-corrected images if the positron annihilations take place in a non-water equivalent tissue, such as lung or bone. Other approaches, which used material-dependent space-invariant isotropic filters, obtained from a CT or MRI anatomical image, have been also proposed to deconvolve the blurring kernel [Kraus et al., 2012, Cal-González et al., 2011b, Cal-Gonzalez et al., 2009]. These approaches are computationally efficient and are valid for phantoms in which the activity is within a homogeneous medium. However, it has been reported that in vivo small animal studies, a non-negligible amount of positrons close to the skin/air boundary can escape from the animal, and therefore violates the space-invariant assumption, and using space-invariant deblurring filters can result in severe artifacts [Bai et al., 2003]. Boundaries between lung/soft tissue and tissue/bone may lead to similar effects for the same reason. These artifacts were also observed, for instance, in clinical ^{124}I PET imaging of thyroid glands close to the trachea [Abdul-Fatah et al., 2009].

To address the presence of inhomogeneous media, space-variant analytic filtering approaches were proposed [Alessio and Kinahan, 2006, Bai et al., 2005, 2003]. Bai and collaborators [Bai et al., 2005, 2003] compensated for variant positron ranges by either A) anisotropically truncating an isotropic point probability density function dependent on tissue type, or B) performing successive convolution operations of tissue dependent range kernels to determine range models across tissue boundaries. On the other hand, [Alessio and MacDonald, 2009] performed an average of the fitting parameters (of distribution $aPSF_{sin}(x)$, see *chapter 3*) of annihilation densities for the originating voxel and the target voxel. These filters are a fast and robust method for implementing a positron range correction, but due to the complexity of positron migration at irregular interfaces, developing such filters is usually difficult and not always accurate.

An alternative to analytic models, is using Monte Carlo simulations, which are tools able to model complex structures of biological tissues, as long as sufficient physical details about the attenuation media are provided. However, MC simulations are also associated with excessively long computation time. To solve this problem, [Fu and Qi, 2010] have proposed the development of a MC based positron range model and incorporate it into a factorized system matrix to be used in high-resolution MAP image reconstruction [Fu and Qi, 2010]. Alternatively, [Kraus et al., 2012] developed MC-based correction kernels for positron range in presence of magnetic fields.

5.1.2 Our approach to positron range correction in PET imaging

In this chapter we present the positron range correction we developed for PET imaging, and show test results with the preclinical Argus PET/CT scanner [Wang et al., 2006]. We introduced an analytical expression for the positron range blurring kernel, from fits to MC simulations of positron range, following the expressions on Eqs. 3.9 and 4.5. This kernel is unfolded during the reconstruction procedure. The unfolding procedure can take into account the tissue in which the positron is annihilated, obtained for instance from a CT image. A scaling by the electron density of the material is employed to obtain the positron range blurring kernel (or positron range contribution to the PSF) at each material.

In order of increasing complexity, different approaches to positron range correction have been implemented and evaluated in this chapter:

- A) Uniform range correction: Non-tissue dependent, uniform correction for all voxels, assuming water as the media on which positrons travel and annihilate. This is a fast and easy procedure to implement, and does not need a CT image. It is useful to estimate to which extent image can be improved when positron range correction is taken into account, particularly in phantom studies. Of course this algorithm is not completely realistic and can be improved, as we will show next.
- B) Tissue-dependent correction with homogeneous, isotropic kernel: the blurring kernel that is applied depends on the voxel in which it is applied, that is, the blurring kernel is taken from the material where the positron is emitted, irrespectively of the surrounding media. The blurring is homogeneous and isotropic. This correction needs the co-registration of the CT image and it is expected to work well everywhere except near tissue boundaries.
- C) Tissue-dependent and spatially-variant correction: the blurring kernel takes into account the voxel in which it will be applied, that is, the material at which the positron is emitted, and will take fully into account the different materials that the positron travels by until it annihilates. This approach should be realistic enough even when the activity is distributed at extreme tissue boundaries.

5.2 Scaling of positron range distributions in different materials

Positron range distributions for most common radionuclides used in PET were computed using Monte Carlo simulations with PeneloPET (see *chapters 3 and 4*) and the radial integrated range distribution ($g_{3D}(r)$) was fitted using equation 3.9 (for ^{18}F, ^{11}C, ^{13}N, ^{15}O, ^{68}Ga, ^{82}Rb, ^{124}I and ^{94m}Tc radionuclides) and equation 4.5 (for ^{76}Br and ^{86}Y radionuclides). These analytic range profiles were introduced into the 3D-OSEM image reconstruction software FIRST [Herraiz et al., 2006] and employed to blur the image either in the forward projection or in the forward and backward projections.

The fitting parameters for the analytic $g_{3D}(r)$ distributions were obtained using water as annihilation medium. In this section we studied if different range profiles can be scaled taking into account the density of materials to a universal profile (for a detailed discussion see [Cal-González et al., 2013a]).

To obtain material-independent profiles, a scaling by the density of material was performed. A similar method of scaling with the tissue density was recently presented by [Jødal et al., 2012]. In this work we have chosen the scaling with the electronic density of material, because the relationship between relative electron density and positron range is expected to be almost linear. The scaling was performed using the expression:

$$R_{scaled} = R \cdot \frac{\rho_e}{\rho_e^{water}} \tag{5.1}$$

where R is the unscaled distance traveled by the positron, ρ_e is the electronic density of the material and ρ_e^{water} is the electronic density of water.

Figure 5.1 shows tissue-scaled $aPSF_{sin}(x)$ and $g_{3D}(r)$ distributions for ^{18}F radionuclide. The universal curves, computed as the mean of the different scaled curves, are also shown in the figure. We expect to obtain similar results for other radionuclides.

Using these universal curves, one can easily calculate the positron range distribution for any other tissue solving the equation 5.1 for R .

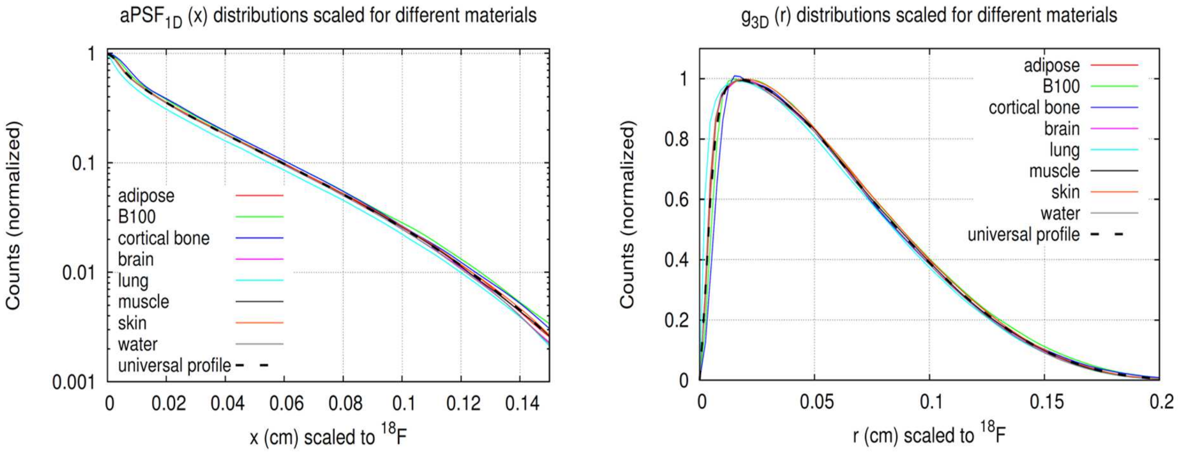

Figure 5.1: Scaled $aPSF_{sin}(x)$ and $g_{3D}(r)$ distributions for ^{18}F in different tissues.

Table 5.1 shows mean and maximum ranges obtained from PeneloPET for the ^{18}F radionuclide placed in different materials. These mean ranges are compared with the ones obtained using the universal curves and applying the corresponding scaling factor for each tissue from equation 5.1.

In table 5.1 one can see that the mean and maximum positron ranges derived from the universal profiles, for different materials, are very similar to the ones obtained with PeneloPET, with discrepancies smaller than 4% in all cases. This allows to use an universal positron range curve, derived from simulations in water, and introducing tissue-scaling to compute the blurring kernel for other biological tissues, without the need of computing the positron range distribution, paving the way for fast algorithms to correct images for positron range during reconstruction.

		R_{mean} (mm)		R_{max} (mm)	
Radionuclide	**Material**	**PeneloPET**	**Univ. distrib. and scaling**	**PeneloPET**	**Univ. distrib. and scaling**
^{18}F	Adipose tissue	0.62	0.62 (-0.1%)	2.30	2.35 (2.2%)
	B100 bone eq. plastic	0.41	0.40 (-2.9%)	1.55	1.49 (-3.9%)
	Cortical bone	0.32	0.31 (-2.2%)	1.21	1.17 (-3.3%)
	Muscle	0.55	0.55 (0.2%)	2.06	2.08 (1.0%)
	Lung	1.85	1.91 (3.6%)	7.41	7.20 (-2.8%)
	Skin	0.52	0.52 (-0.5%)	2.00	1.96 (-2.0%)
	Water	0.57	0.57 (1.2%)	2.16	2.16 (0.0%)

Table 5.1: Comparison of PeneloPET mean and maximum positron ranges with the universally scaled prediction for different tissues (differences in percentage are also shown).

5.3 Positron range correction

In this section we describe the positron range corrected OSEM algorithm (PR-OSEM) that have been implemented in this work.

Positron range correction can be introduced into the iterative image reconstruction in two different ways:

- Introducing the effect of positron range in the System Response Matrix (SRM). This can be done by using a system model where positron range is factored out, so that different positron range blurring can be used, by means of a realistic simulation that includes all the main physical effects into account [Herraiz et al., 2006] or by obtaining the SRM from point source measurements [Panin et al., 2006].
- Using the positron range profiles obtained from Monte Carlo simulations as an additional blurring applied to the image. In this case, the SRM should not incorporate any positron range effects.

In this work we have chosen the second option, because analytic range profiles are available and it is possible to introduce the blurring as a function of the material properties of the object in which positrons are annihilated, by using the scaling approach previously described.

5.3.1 Tissue-dependent positron range correction

The SRM was simulated with PeneloPET [España et al., 2009] without positron range effects, but considering all other physical effects like non-colinearity or inter-crystal scatter. Following a similar approach as in [Tsyganov et al., 2005] the tissue-dependent spatially-invariant positron range corrected OSEM (PR-OSEM) algorithm reads:

$$x'_j = x_j \frac{\sum_i A_{ij} \left(\frac{y_i}{\sum_j A_{ij} \tilde{\mathrm{x}}_j} \right)}{\sum_i A_{ij}} \tag{5.2}$$

where $\tilde{\mathrm{x}}_j$ is the object blurred by positron range that is forward projected. $\tilde{\mathrm{x}}_j$ is obtained by the convolution of the initial object with a blurring function corresponding to the $g_{3D}(r)$ range profile of the emitter present at voxel j and the tissue in that voxel:

$$\tilde{\mathrm{x}}_j = x_j \otimes g_{3D}^{(j)} = \frac{\sum_{j'} x_{j'} g_{3D}^{(jj')}(r_{eq}^{jj'})}{\sum_{j'} g_{3D}^{(jj')}(r_{eq}^{jj'})} \tag{5.3}$$

where the convolution is performed though all the j' neighboring voxels of j, $x_{j'}$ is the activity of the initial image (before convolution) in voxel j' and $g_{3D}^{(jj')}(r_{eq}^{jj'})$ is the value of the g_{3D} analytic function, with origin in j, at voxel j'. $r_{eq}^{jj'}$ is the distance from voxel j to voxel j', scaled to equivalent distance in water using as reference the tissue in voxel j. $r_{eq}^{jj'}$ is given by:

$$r_{eq}^{jj'} = r^{jj'} \cdot \rho_j \tag{5.4}$$

where $r^{jj'}$ is the geometrical distance between voxels j and j' and ρ_j is the density in voxel j.

The factor $\sum_{j'} g_{3D}^{(jj')}(r_{eq}^{jj'})$ in equation 5.3 is included in order to normalize the number of counts after the convolution operation; that is, the number of counts in the image, after convolution, must be the same than the counts that we had before convolution.

The properties of the object that we use to compute the tissue-dependent blurring kernel in each voxel are obtained from the co-registration and segmentation of a CT image. The CT segmentation was performed using three different tissues: water ($\rho_e = 1.0$ g $\cdot cm^{-3}$), cortical bone ($\rho_e = 1.64$ g $\cdot cm^{-3}$) and lung ($\rho_e = 0.29$ g $\cdot cm^{-3}$). Where ρ_e is the electronic density, previously reported in table 3.2 (*chapter 3*).

As it can be noticed, a miss-matched projector / backprojector pair is used in Eq. 5.2. Indeed, positron range blurring is only applied in the forward projection operation. This approach has been used in several works [Zeng et al., 1991, Zeng and Gullberg, 2000, Cal-Gonzalez et al., 2009], and it is shown that good reconstructed images can be attained with a full modeling of blurring effects during the projection step, whereas a simplified modeling is employed into the backprojector [Cal-Gonzalez et al., 2009]. We have also seen that using a detailed range blurring kernel in the backprojector has only the effect of reduce the convergence speed of the iterative algorithm [Cal-González et al., 2011b].

5.3.2 Spatially-variant positron range correction

In non-homogenous tissues, accurate positron range modeling requires using anisotropic kernels, which ideally would be derived from Monte Carlo simulations for each tissue distribution. This can be computationally very intensive. Thus, a primary challenge in determining the range effect in non-homogenous media is how to model the range across boundaries in an efficient way.

In this work we propose a simple, but effective, method to correct for positron range in heterogeneous media (see figure 5.2A). First, we compute a segmentation of the CT image (as it was previously mentioned), and using this segmentation we find the boundaries between tissues.

For each voxel (j) of the image, we determine whether there is any boundary close to that voxel (at a distance smaller than the kernel size, scaled to the actual material of the voxel, used to blur the image). If not, then the voxel is marked so that any emission from it would be blurred with a homogeneous kernel (as in the previous section) adequate to the material. Otherwise, the voxel is marked to compute the blurring kernel in a realistic way, taking into account the different densities of all materials surrounding the voxel. To this end, for each target voxel (j') of the blurring kernel we obtain the densities of the voxels associated with the line connecting the originating voxel j and the target voxel j' (see figure 5.2A).

The water-equivalent distance between j and j' is computed scaling by the mean density of all the voxels associated with the line connecting the originating voxel (j) and the target voxel (j'). This mean density (ρ_w) is calculated using the expression:

$$\rho_m = \sum_{n=j}^{n=j'} \rho_e^{(n)}/N \tag{5.5}$$

where N is the total number of voxels associated with the line connecting j and j' and $\rho_e^{(n)}$ is the electronic density of each voxel.

The water-equivalent distance ($r_{eq}^{jj'}$) between j and j' is given by:

$$r_{eq}^{jj'} = r^{jj'} \cdot \rho_m \tag{5.6}$$

where $r^{j,j'}$ is the geometrical distance between voxels j and j' and ρ_w is the mean density along the voxels associated with the line connecting j and j'.

Using this procedure, we obtain a convolution kernel $g_{3D}^{(j)}$ for each voxel j. This kernel may be homogeneous, if there is not any tissue-boundary within the spatial extent of the kernel, or inhomogeneous if there are tissue boundaries within the kernel volume.

Finally, the convolution for each voxel j is computed using expression 5.3 and the convolution kernel obtained for the corresponding voxel.

In figure 5.2B we represent the homogeneous and spatially-variant blurring kernels for a case in which the activity is located near to a air cylinder (see section 5.4 for more details).

5.3.3 Stability of CT-based positron range correction

We also studied the effect in the quality of the reconstructed images of using different shapes for positron range profiles. We performed a comparison of the range-corrected reconstructed images using the correct positron range blurring, and using erroneous range profiles, corresponding to a maximum energy of positrons that is ±10% and ±50% of the energy of correct profile. This comparison would allow us to assess what is the accuracy needed in the positron blurring determination, as positron ranges are still not very well determined for high-energy positrons (see *chapter 3*).

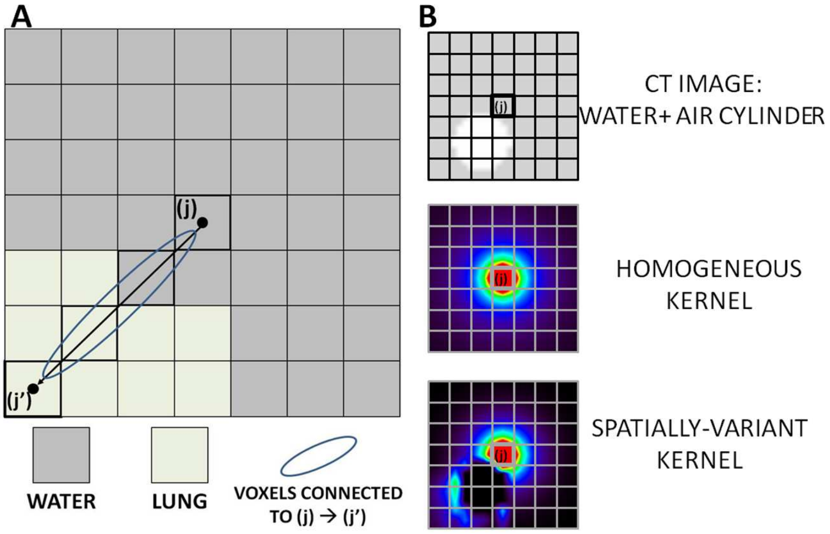

Figure 5.2: A: Schematic procedure to obtain the spatially-variant blurring kernel in non-homogeneous media. B: Comparison between the homogeneous and the spatially-variant blurring kernels for a case in which the activity is located close to a boundary water-air (see section 5.4)

5.4 Simulations and real acquisitions

In this section we describe the simulated and real acquisitions that we have used to evaluate our reconstruction algorithms with positron range correction.

5.4.1 Simulated phantoms

Activity in homogeneous media

Acquisitions of a NEMA NU-4 2008 IQ phantom [NEMA-NU-4, 2008] filled with ^{18}F(short range) or with ^{68}Ga (medium-large range) have been simulated in this work (a brief description of this phantom can be found in *appendix 1*). The simulations were chosen to represent acquisitions with the ARGUS small animal PET scanner [Wang et al., 2006]. The simulated acquisitions have been reconstructed with FIRST, our 3D PR-OSEM procedure [Herraiz et al., 2006], with and without positron range modeling [Cal-González et al., 2011b]. Reconstruction parameters have been set as follows:

- Reconstruction method: FIRST, based on 3D OSEM and a realistic system response matrix.
- 200 image updates (20 iterations with 10 subsets each of them). A high number of iterations are chosen in order to have many intermediate images to asses image quality evolution.
- Energy window: 400 - 700 keV.
- Number of voxels in the image: 175 × 175 × 61 voxels.

- Voxel size: $0.389 \times 0.389 \times 0.775\ mm^3$.

For all simulations with the NEMA IQ phantom, the initial activity was around 25 MBq and the number of coincidences accumulated in the acquisitions was above 100 million counts.

In order to measure the quality of our reconstructed images, we compared the spatial resolution and recovery coefficient [Lee et al., 2004] (RC) variation against noise of the image.

Spatial resolution has been estimated as the average FWHM of Gaussian fits to derivatives of radial profiles across several line sources of the IQ. Alternatively, RC has been calculated from the number of counts obtained in the reconstruction for a Region of Interest (ROI) drawn inside the 3 mm in diameter line source, divided by the true number of counts in this ROI. Finally, noise in the image has been estimated as the ratio of the standard deviation of counts in each voxel in a cylindrical ROI of 20 mm radius and 10 mm length, taken in the uniform region of the scanner, and the total counts in this ROI.

Activity concentrated in different tissues

In order to evaluate the tissue-dependent positron range correction we have simulated acquisitions of ^{18}F and ^{68}Ga line sources placed within different media.

- **Water - bone phantom (figure 5.3):** A water cylinder of 5 cm of diameter and 5 cm length, centered in the FOV, was simulated. It contains a 1 cm off-centered rod of bone material, 1 cm of diameter and the same length as the cylinder. Two line sources with low activity and 1 mm of diameter were simulated, placed at (1, 0, 0) cm inside water, and at (-1, 0, 0) cm inside bone, respectively. The reconstruction was performed with FIRST and 100 image updates (2 iterations of 50 subsets each of them).

- **Water - lung phantom (figure 5.3):** In this case we simulated a water cylinder, with 6 cm of diameter and 6 cm of length, located at the center of the FOV. Within this cylinder we simulated a lung cylinder, 1.5 cm off-centered, with 2 cm of diameter and the same length than the water cylinder. Two low activity line sources were simulated, one of them placed at (1.5,0,0) cm, inside water; and the other one placed at (-1.5,0,0) cm, at the center of the lung cylinder. As in the previous case, the reconstruction was performed with FIRST and 100 image updates (2 iterations of 50 subsets each of them).

The initial activity was 2 MBq in both acquisitions, the energy window: 400 - 700 keV, and the number of coincidences accumulated in the acquisitions was 20 million coincidences.

Activity close to tissue boundaries

To evaluate the performance of our positron range correction algorithms when the activity is located close to a boundary between different tissues, we simulated the following phantom (figure 5.3):

A 3.2 cm diameter water cylinder (5 cm length) placed at the center of the FOV. Within this water cylinder we also simulated an air cylinder, 4 mm diameter and the same length, 3 mm off-centered. The activity is confined in a 1 cm length ^{124}I line source, with a diameter of 2 mm and placed at the center of the FOV. Thus, the ^{124}I line source is situated just at the boundary between water and air. The initial activity for this line source was 2 MBq, and the number of simulated detected coincidences was 40 million counts. We set the energy window to 400 - 700 keV.

The motivation of this study was to evaluate PET imaging of rats thyroid gland with ^{124}I radionuclide [Emanuelsson, 2006, Kanai et al., 2012]. In these cases, if the activity is placed close to the trachea, positrons can cross it and annihilate at the opposite side of the trachea. Therefore, if positron range is not properly corrected, artifacts may appear in thyroid imaging with ^{124}I. Similar artifacts were reported in clinical studies [Abdul-Fatah et al., 2009].

In our study, we simulated the air-filled trachea as a 4 mm diameter air cylinder ([Cassidy et al., 2001] reported an average tracheal diameter of 3.25 ± 0.19 mm for rats), and the ^{124}I activity distribution as a line source of 2 mm diameter and 1 cm length.

The reconstruction parameters in this case have been the same than in the previous studied phantoms. The reconstruction was performed with FIRST and 100 image updates (2 iterations and 50 subsets per iteration).

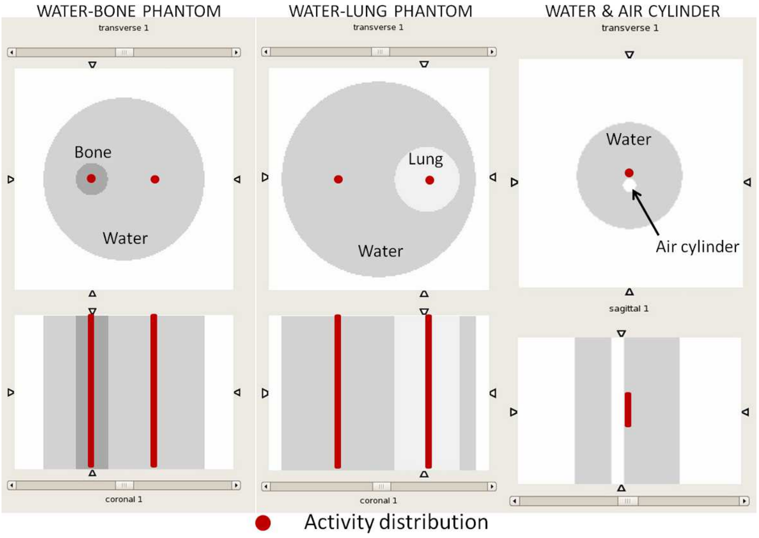

Figure 5.3: Schematic representation of the phantoms simulated to evaluate the performance of the positron range algorithms developed in this work.

5.4.2 Derenzo phantom acquisition

Finally, we studied the performance of our reconstruction algorithm with positron range correction in a real acquisition of a micro-Derenzo IQ phantom filled with ^{68}Ga (a brief description of this phantom can be found in *appendix 1*). In this case, we set the energy window to 400 - 700 keV, the initial activity was about 100 MBq and the number of counts accumulated in the acquisitions was 40 million.

5.5 Results and discussion

In this section we present and discuss the main results obtained in this work. We have chosen ^{68}Ga or ^{124}I as the radionuclides for the majority of the tests, as they are commercially available, used in many PET studies [Hoffend et al., 2005, Breeman and Verbruggen, 2007, Bailey et al., 2005, Pentlow et al., 1991, Herzog et al., 2002, Belov et al., 2011] and they both have a large positron range compared to the resolution of the scanner. We also obtained similar results for other radionuclides.

5.5.1 Positron range correction in water

Figure 5.4 (left) shows the reconstructed images of the simulated acquisitions in the Argus scanner using the NEMA IQ phantom filled with ^{68}Ga radionuclide, with and without positron range correction. In both cases, 10% noise (measured in uniform regions) images are compared. On the right side of the figure we plot the activity profiles though the 2 and 3 mm capillaries of the phantom, again with and without positron range correction.

In addition, figure 5.5 shows the resolution-noise and RC-noise curves, obtained for the 3 mm rod of the NEMA IQ phantom, filled with ^{18}F (short range) and ^{68}Ga (medium-large range) radionuclides, reconstructed with 3D PR-OSEM with and without range corrections. Images were reconstructed using 20 iterations of 10 subsets storing the image obtained after each iteration.

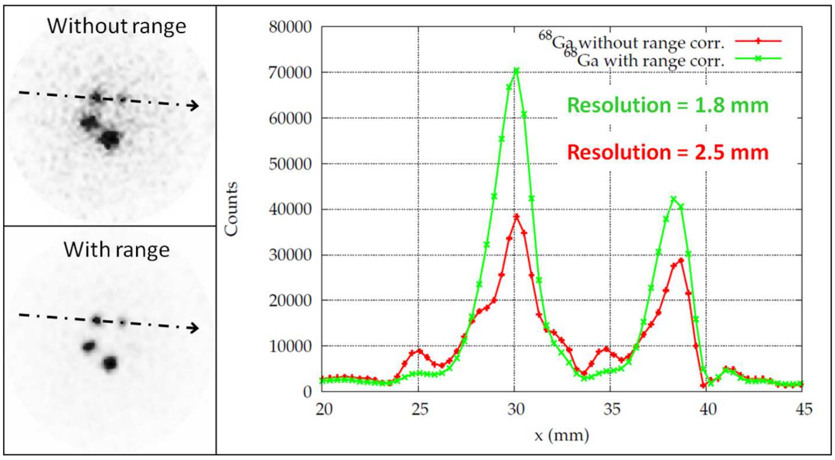

Figure 5.4: Left: IQ phantom filled with ^{68}Ga and reconstructed with 3D PR-OSEM. Without and with range corrections. 10% noise images are compared. Right: count line profiles along the 2 and 3 mm rods (arrow in the images) are shown.

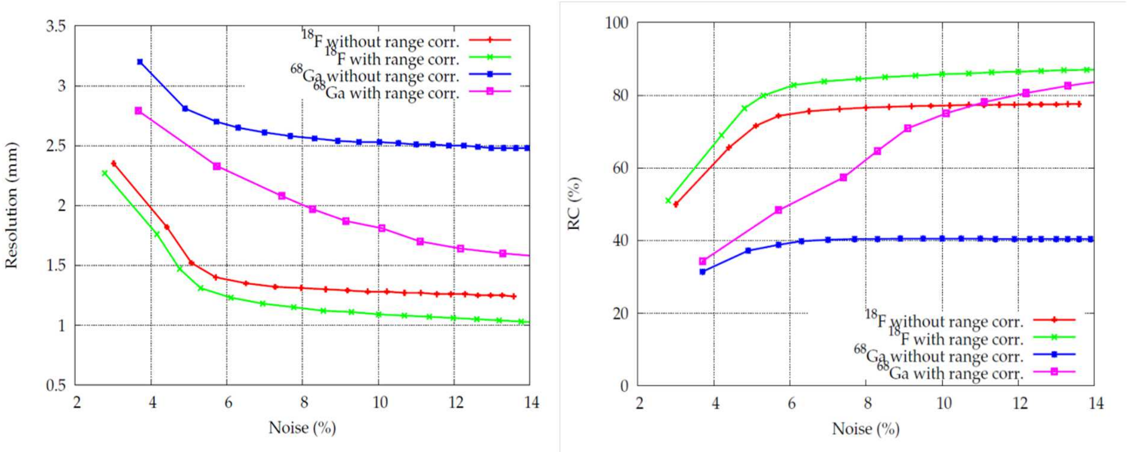

Figure 5.5: Left: Resolution - noise curves obtained for the IQ phantom filled with^{18}F or with ^{68}Ga and reconstructed using 3D PR-OSEM with and without range corrections. Right: RC-noise curves for the same reconstructions. Each point corresponds to 10 image updates.

Figures 5.4 and 5.5 suggest that a significant improvement in image quality (resolution and RC for a given noise level) is achieved when we use a positron range correction during the reconstruction, especially for higher energy isotopes.

For radionuclides that emit positron with relatively low-energy, such as ^{18}F, using positron range correction during reconstruction allow us to achieve a spatial resolution of almost 1 mm (see figure 5.5), while the spatial resolution achieved without range correction was 1.2 mm. The improvement in RC when positron range is modeled in the reconstruction is about 10%. On the other hand, for medium-large range radionuclides, as for example ^{68}Ga, the improvement in spatial resolution and RC values is very significant (spatial resolution: 1.6 mm with range correction and 2.5 mm without it; RC values with range correction, on the other hand, are twice than the ones obtained without range correction).

As it was commented, the use of the positron blurring during backprojection just delay the appearance of high resolution details in the image. Apart from this, the resolution versus noise curves are nearly identical [Cal-González et al., 2011b] when positron range blurring is included in both projection and back-projection or only in the projection stage.

Stability of range correction

In figure 5.6 we show a comparison between the results obtained with the 3D PR-OSEM reconstruction which takes into account the correct positron range blurring, that is, the same range employed during the PeneloPET simulation, and reconstructions with erroneous positron range profiles, corresponding to a maximum energy of positrons that is ±10% and ±50% of the maximum energy of correct profile. In addition, we also plot, at the bottom of the figure, the transaxial views of these reconstructed IQ images (in the region of the rods) with different positron range blurring.

The results obtained suggest that the use of erroneous positron range profiles with an error of ±50% has a significant effect in the quality of the reconstructed images. Comparing images at the same noise level, under-corrected images (-50% curves), have worse resolution and RC values. On the other hand, although resolution and RC seems to be better in over-corrected images, inspection of the images shows that they have large ringing artifacts and produce too narrow line sources, narrower than the actual line sources. This is due to the over-correction for range blurring. On the other hand, for range corrections that are ±10% of the ones employed in the simulation, the resolution-noise or RC-noise curves are very similar to the ones obtained where the correct positron range is employed. This means that positron range profiles should be known with a 10% of accuracy in order to obtain good quality images.

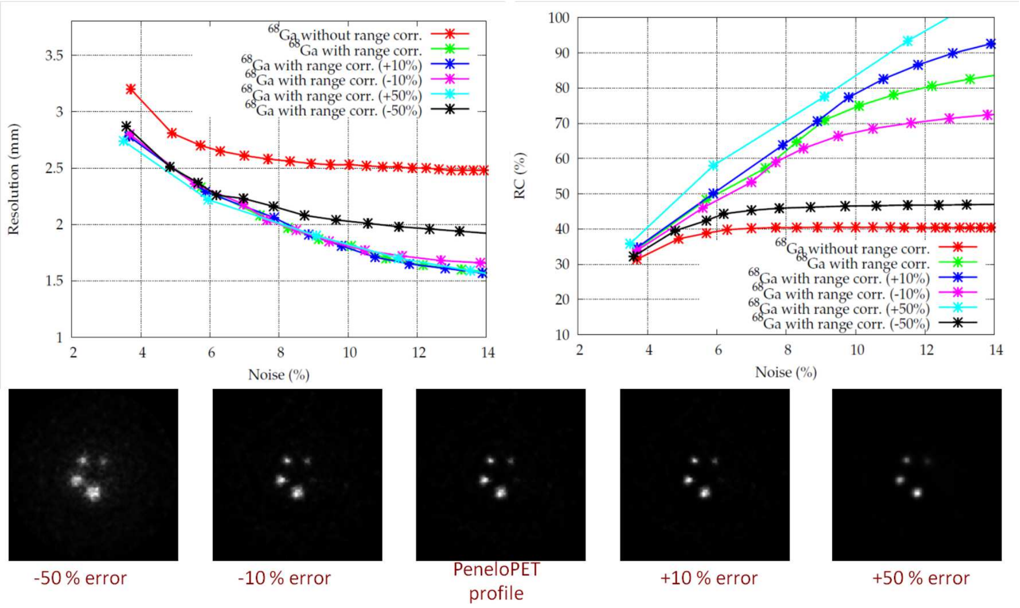

Figure 5.6: Resolution-noise (left) and RC-noise (right) curves obtained for the 3 mm rod IQ phantom filled with ^{68}Ga and reconstructed using range corrections with different levels of blurring. Points correspond to 10 updates of the image. Bottom: transaxial views of the five capillaries of the NEMA IQ phantom.

5.5.2 Range correction for different tissues

Figure 5.7 shows the images reconstructed of the simulated bone - water (left) and water - lung (right) phantoms, filled both of them with ^{68}Ga.

In addition, we show in table 5.2 the Full Width at Tenth Maximum (FWTM) values for the ^{18}F and ^{68}Ga reconstructed line sources, in bone, water and lung, after the 3D PR-OSEM reconstruction with and without positron range corrections. Most of the positron range effects have been removed, making the FWTM obtained for ^{68}Ga and ^{18}F much more similar.

In the first case, without range correction, the reconstructed size of the ^{68}Ga line source in water is larger than in bone, which causes a visible difference in the respective heights of the activity profiles in bone and water. Similar results are obtained for water and lung, but in this case the spatial extent of the source is larger in lung. If we perform uniform positron range correction (taken the positron range profile in water), the line source placed into the bone region is over-corrected and shows in a too high peak of the activity profiles. Alternatively, the line source placed in lung tissue is infra-corrected and it still shows a too blurry aspect. Finally, when tissue-dependent positron range is modeled into the reconstruction (right), similar apparent size for the line sources and identical height of the activity profiles are obtained for water and bone. However, although with tissue-dependent correction the results in lung are better than the ones obtained with uniform correction, we can see that the recovery of activity is not as good as in water or bone tissues.

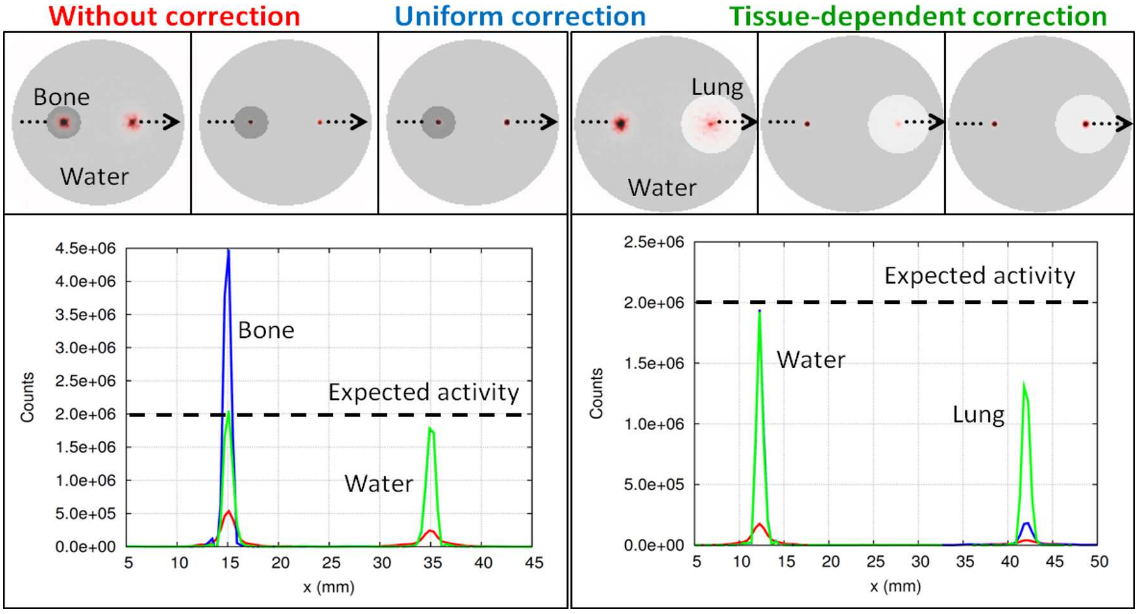

Figure 5.7: Density map of the simulated phantoms along with the images of ^{68}Ga line sources in bone, water and lung after 3D PR-OSEM reconstruction. Images and profiles are compared at 10% noise.

		FWTM of reconstructed line sources (mm)		
Radionuclide	**Annihilation tissue**	**Without range correction**	**Uniform correction**	**Tissue-dependent correction**
	Cortical bone	1.66	1.21	1.37
^{18}**F**	Water	1.70	1.38	1.38
	Lung	2.34	1.95	1.40
	Cortical bone	2.86	1.75	1.86
^{68}**Ga**	Water	3.53	1.90	1.90
	Lung	5.14	3.24	2.24

Table 5.2: FWTM values (in mm) for ^{18}F and ^{68}Ga line sources placed in water, cortical bone and lung tissues, and reconstructed with and without range correction.

5.5.3 Range correction close to tissue-boundaries

Finally, we present in figure 5.8 the results obtained for the simulated 1 cm ^{124}I line source placed close to a water-air boundary. In this case, a portion of the positrons emitted by the line source may escape from the source area, cross the 4 mm air cylinder, and annihilate at the opposite wall of this cylinder, thereby falsely suggesting activity at that location if positron range effects are not appropriately corrected during reconstruction.

In the top part of figure 5.8 we plot the transaxial views of the reconstructed line source, without range correction (left), with spatially-invariant(center) and with spatially-variant (right) range correction. At the bottom we depict the profiles though the line source and the air cylinder. We can see an artifact at the opposite side of the air cylinder if positron range effect is not properly corrected. When spatially-variant blurring kernel is employed in the reconstruction, the above mentioned artifact almost dissapears.

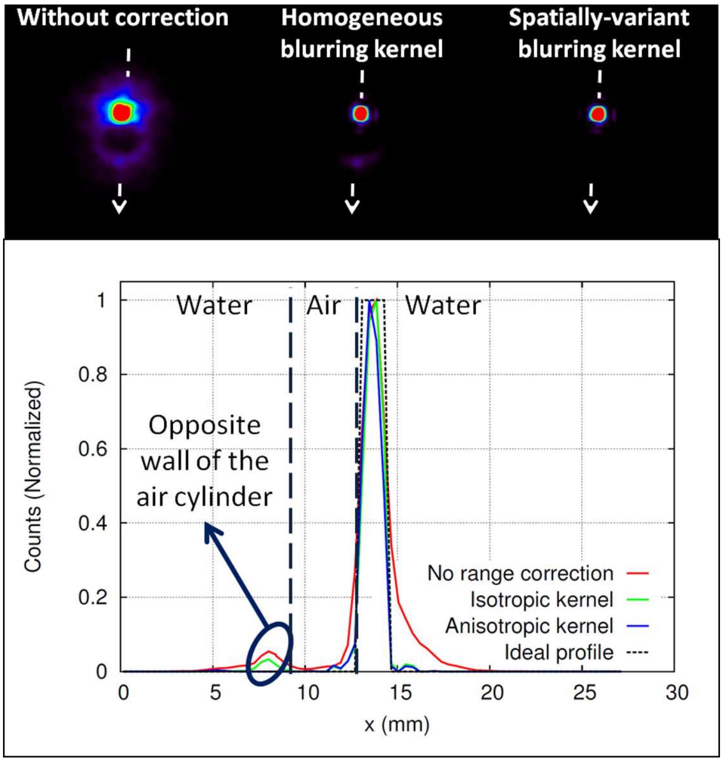

Figure 5.8: Top: transverse views of the line source reconstructed with the PR-OSEM procedure without range correction (left), spatially-invariant and spatially-variant positron range corrections. Bottom: Activity profiles though the source and the air cylinder for the three reconstructed images.

5.5.4 Real phantoms acquisitions

Figure 5.9 shows the reconstructed images of the real acquisition of the Derenzo phantom with (panel B) and without (panel A) positron range modeling in the reconstruction algorithm. In addition, we also plot the CT image (panel C), which was used to obtain the tissue and compute the corresponding blurring kernel in each voxel, and the activity profiles though 4.0 and 3.2 mm line sources (panel D).

In figure 5.9 we can see a significant improvement of the image quality when positron range is corrected during reconstruction. In this case, we can distinguish capillaries up to 1.6 mm in the image obtained with positron range correction. In addition, the signal-to-noise ratio is higher when positron range is modeled in the reconstruction.

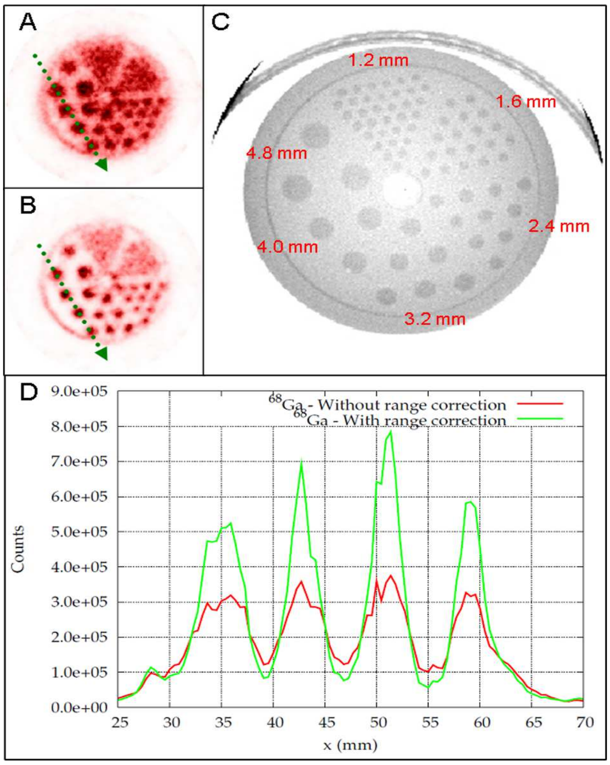

Figure 5.9: A: Reconstruction of a real acquisition of a hot Derenzo phantom without range correction. B: Reconstruction with range correction. C: CT image for this phantom. D: Activity profiles

5.6 Conclusions

From this work on positron-range correction in PET we can conclude that:

- It is possible to improve significantly the quality of the reconstructed images when positron range corrections are taken into account, rendering range corrected images for medium-large positron range radionuclides, like ^{68}Ga or ^{124}I, practical and useful. For instance, with ^{68}Ga, a spatial resolution of around 1.6 mm can be obtained with range correction versus 2.5 mm without it.

- The use of erroneous positron range profiles (±50% of error) has a significant effect in the quality of reconstructed images: infra-corrected images with lower RC and resolution values or not valid over-corrected images, with large ringing artifacts and too narrow line sources. On the other hand, for the scanner and radionuclide reviewed here, a ±10% difference in the positron range employed for acquisition simulation and image reconstruction has a negligible effect in the reconstructed images.

- The use of tissue-dependent positron range correction yields better image quality when several tissues are present within the FOV, giving a similar apparent size and peak height of activity profiles for line sources placed in different tissues.

- We could implement a relatively fast and efficient tissue-dependent and spatially-variant positron range correction, which yields artifact-free reconstructed images in all cases, while the other methods fail when the radioactive source is placed close to tissue-boundaries or in a heterogeneous media.

Chapter 6

Improved quantification for small volumes of interest in PET

6.1 Introduction and motivation

In tomographic imaging, there are several causes of quantitative inaccuracy [Erlandsson et al., 2012, Soret et al., 2007, Barrett and Myers, 2004]. For example: the sampling phenomena due to the continuous-to-discrete mapping from the object to the image, the aperture effects (blurring), the random and scatter coincidence events and the background due to positron-gamma events in non-pure emitters. Another cause of quantitative inaccuracy (related to the limited spatial resolution) is the partial volume effect (PVE), which can be defined as the loss in apparent activity that occurs when an object partially occupies the sensitive volume of the imaging instrument (in space or time) [Hutton and Lau, 1998].

The main PVE in emission tomography corresponds to spill-over of counts (cross-contamination) between different image regions due to the point-spread function (PSF) of the system. The PVE effect, when focusing on one region in which the activity concentration needs to be quantified, can be often viewed as the combined result of two related effects: spill-in (counts from the surrounding media that falls in the region of interest) and spill-out (counts from the region of interest which falls in the surrounding media). Other type of PVE is the sampling effect related to the voxel size of the images, which has as a consequence that each individual voxel can in principle contain two or more tissue types. This can occur at the boundary between regions of different tissue-types, in such a way that a voxel with mixed tissue in principle could be split into a few sub-regions, each with a single tissue type. This type of PVE is also known as the tissue-fraction effect [Erlandsson et al., 2012].

As PVE is directly related to the spatial resolution of the system, it is expected that this effect will be very important when imaging with large positron range radionuclides, such as ^{68}Ga or ^{124}I, and must be treated with special consideration.

The use of iterative reconstruction algorithms such as Maximum Likelihood Expectation Maximization (MLEM) method [Shepp and Vardi, 1982], or an accelerated variant of MLEM, the Ordered Subsets Expectation Maximization (OSEM) [Hudson and Larkin, 1994], which incorporate accurate models of all contributions to image blurring should, in principle, compensate to a large extent for PVE. Unfortunately, the noise amplification and edge artifacts seen when using a large number of iterations (required for a substancial PVE correction) can outweigh the improvement brought about by accurate modelling.

As summarized by [Soret et al., 2007] and by [Erlandsson et al., 2012], many different approaches have been proposed to compensate for partial-volume and spillover effects in nuclear medicine. These techniques can be divided in two different categories: post-reconstruction and within-reconstruction methods.

Among the proposed post-reconstruction methods, one can find in the literature the region-based methods, such as the recovery-coefficient correction [Hoffman et al., 1979] or the geometric transfer-matrix (GTM) method [Rousset et al., 1998], which is more appropriate to use in conjunction with non-linear iterative reconstruction algorithms [Du et al., 2005]. Other post-reconstruction corrections consist of voxel-based methods, as for example, image deconvolution [Teo et al., 2007].

Proposed within-reconstruction method are for example Carson´ s region-based MLEM [Carson, 1986], as well as Bayesian approaches which incorporate region-dependent penalties [Baete et al., 2004].

In this work, we implemented and evaluated the local projection method (LPA) proposed by Moore and collaborators [Moore et al., 2012, Southekal et al., 2012] to compensate for both partial-volume and spillover effects in PET imaging. The method takes advantage of a higher resolution image co-registered with the PET data, so that a high resolution segmentation of typically a few tissues within a small volume of interest centered on the lesion that needs to be quantified can be possible. This additional information can be used to obtain improved activity estimates for each tissue within the small volume of interest (VOI), simply asking for consistency of the raw projection data acquired by the scanner and the high resolution segmentation. The approach requires an accurate model of the scanning system, and in principle can be implemented during iterative reconstruction of the PET images.

In previous works, the evaluation of the LPA method for a multiple-pinhole microSPECT system [Moore et al., 2012] and for a clinical SPECT system [Southekal et al., 2012] was performed. In this chapter we will discuss the implementation and evaluation of this method [Cal-González et al., 2013c] also when it is applied along with the positron range correction described in last chaper, for the preclinical Argus PET/CT scanner [Wang et al., 2006] and ^{18}F, ^{68}Ga and ^{124}I radionuclides. We also evaluate the results obtained when the LPA results (estimated mean activity for each tissue within the VOI) are incorporated during the reconstruction algorithm as a prior.

6.2 Methods

Simulated and real acquisitions for the preclinical ARGUS PET/CT scanner were reconstructed with our iterative PR-OSEM procedure [Cal-González et al., 2011b, Herraiz et al., 2006], modified to incorporate the local-projection algorithm (LPA) that uses the same system model as the one employed for the reconstructions.

In this section we discuss the implementation of the LPA in our reconstruction procedure, both as a post-processing step performed on the images after reconstruction or as a new reconstruction algorithm (LPA reconstruction) which uses the LPA results as prior. We also discuss the background subtraction performed in order to correct for scatter and positron-gamma (in non-pure emitters) coincidence events and to obtain better quantification results. Finally, we present the simulated and real acquisitions used to evaluate the LPA results.

6.2.1 LPA post-processing

We will consider a reconstructed image with a detected lesion (for instance a tumor that shows a high uptake of the administered FDG radiotracer administered). Our goal is to improve the quantification of the activity concentration in that lesion by introducing information from a high resolution segmentation, and also by removing background activity from neighboring tissues. The lesion will be surrounded by one or more different tissues. The tissues would be identified in the high resolution image, and in the method the activity concentration in every different tissue will be represented by the average value inside each tissue.

We have J different tissue compartments, including the lesion of interest, within a small volume of interest (VOI) delineated in the object as shown in figure 6.1 (for J=2). The remaining object outside the VOI is considered as a global background.

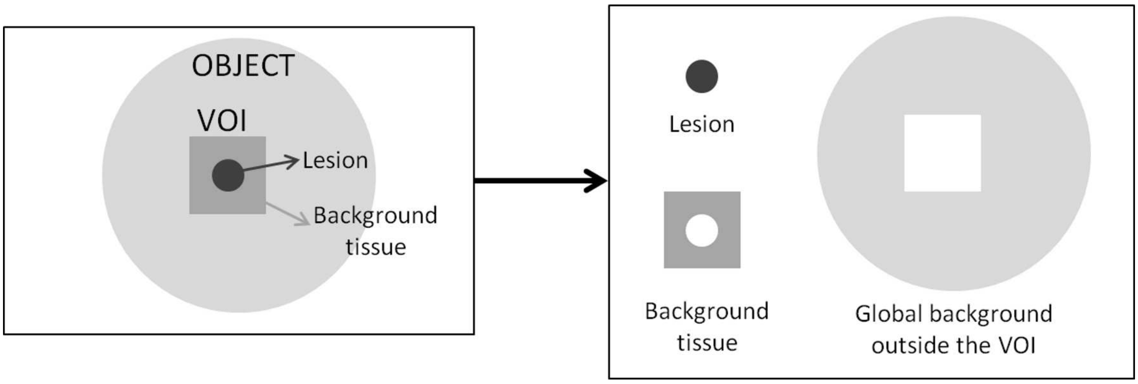

Figure 6.1: Illustration of image model. The gray box represents the VOI, which includes the lesion of interest and a soft-tissue background. The two segmented compartments are forward projected to obtain $P_j = 1$ and $P_j = 2$, while $g_{out}^{(k)}$ is obtained by forward projecting across the reconstructed image at iteration k, with all voxels within the VOI set to zero. This approach is easily extensible to J $>$ 2 compartments.

If we have a precise segmentation of organs and tissues, we can take advantage of this information and improve PET quantification based on [Cal-González et al., 2013c]:

- It is reasonable to assume that voxels belonging to the same tissue have a more similar activity than voxels belonging to other tissues.

- Voxels from different tissues would be represented by in principle different average values of activity within the VOI.

- We can also estimate the PET counts inside the VOI coming from the region of the image outside the VOI.

With these assumptions, the measured emission projection counts λ measured, can be modeled as the sum of the projection counts from each of the J-segmented tissue compartments (with unit-activity concentration), after being scaled by their corresponding activity, plus the counts coming from the global background outside the VOI, as shown in equation 6.1:

$$\lambda_i = \sum_{j=1}^{J} A_j \cdot P_{ij} + g_{out,i}^{(k)} \tag{6.1}$$

Where the activity within the J compartments is represented by an average value inside the compartment.

The activity concentration values A_j can be determined by fitting the measured projection data to the model in equation 6.1. Taking into account that the joint likelihood of measuring a whole projection data set is given by the product of the Poisson probability density function for each measured projection ray, the vector A can be determined by maximizing the log likelihood for the expected value λ_i:

$$\sum_{j'=1}^{J} A_{j'}^{(k)} \left[\sum_i \frac{P_{ij'} P_{ij}}{\lambda_i^{(k)}} \right] = \sum_i \frac{P_{ij}(n_i - g_{out,i}^{(k)})}{\lambda_i^{(k)}}; \qquad j = 1 \to J \tag{6.2}$$

Note that the equations in 6.2 are not, strictly speaking, linear in A_j because the $\lambda_i^{(k)}$ in the denominators also depend on the A_j. Thus they cannot be solved in a exact way. Instead, an iterative solution for these equations will be sought. Indeed, we will solve the equations in 6.2 for the A_j activities by using the following iterative procedure (not to be confused with the iterative reconstruction algorithm):

- **Step 1:** We compute all the matrix elements:

$$H_{jj'}^{(k)} = \sum_i \frac{P_{ij'} P_{ij}}{\lambda_i^{(k)}} \tag{6.3}$$

$$D_j^{(k)} = \sum_i \frac{P_{ij}(n_i - g_{out,i}^{(k)})}{\lambda_i^{(k)}} \tag{6.4}$$

  For the first iteration of the procedure, we can approximate the $\lambda_i^{(k)}$ estimation by the corresponding measured projection data values, this is: $\lambda_i^{(k)} \sim n_i$. After each iteration, we will update these $\lambda_i^{(k)}$ values with the most recently computed estimation of A_j.

- **Step 2:** From the matrix elements calculated previously, we estimate the J values of tissue-activity by inverting the matrix H to solve equation 6.2, obtaining:

$$A_j^{(k)} = \sum_{j'=1}^{J} \left[H_{jj'}^{(k)} \right]^{-1} D_{j'}^{(k)} \qquad (6.5)$$

- **Step 3:** The procedure above is repeated from step 1 using a new estimation of $A_j^{(k)}$ activities to compute new elements of matrices H and D, and after that, improved estimation of the $A_j^{(k)}$ in step 2. This step is repeated until the estimation change by less than a very small amount in a single iteration (typically less than 0.1%).

The convergence of the LPA iterative procedure employed to solve equations is very fast (just 2 or 3 iterations are enough), however, we used 10 iterations in all our studies.

The system response matrix employed to produce the projections was the same as the one one used in the iterative reconstruction procedure for the image. It included non-collinearity effects plus photon penetration in the detectors with full consideration of intra and inter-crystal scatter. Positron range effects had been already considered and corrected during the image reconstruction with the PR-OSEM procedure, as it is discussed in *chapter 5*.

6.2.2 LPA reconstruction

Removing the partial volume effects in a volume of interest with the proposed local projection algorithm can be not only implemented as a post-processing step on reconstructed images (as described in the previous section), but it can be used to feed back the activity values deduced into the image itself, during the image reconstruction as well (LPA reconstruction, or LPAR, method). In this case, the local projection algorithm is applied to the images obtained after each iteration. Using this algorithm, activity estimation in each tissue within the VOI is computed, and the activity in the reconstructed images is substituted by the tissue-activity obtained using the LPA processing (i.e. corrected by PVE), and these more accurate activities are used as a prior in the following iterations.

Following the mentioned procedure we expect to obtain better quantification values in the different tissues inside the VOI, for the reconstructed images. A schematic view of this procedure is presented in figure 6.2.

As we can see in figure 6.2, in this procedure we first compute the system matrix values (P_{ij}) for the tissue j within the VOI (0). This operation is performed only once just before the first iteration of the PR-OSEM iterative reconstruction. Later, after each iteration of the PR-OSEM algorithm (1), we compute the global background $g_{out,i}^{(k)}$ that comes to inside the VOI from outside (2) and the LPA activities for each tissue within the VOI (3). Finally, and using the mask obtained from the segmentation of the CT image, we substitute the activity in each voxel within the VOI for the tissue-activities obtained by means of the LPA (4) and continue with a new iteration of the PR-OSEM procedure (5).

Of course, we can also apply the LPA as a post-processing step on the images already reconstructed with the LPAR method. The assumption here is that any remaining PVE can be further corrected. Therefore, in this work we evaluate several methods to improve the quantification in a given VOI:

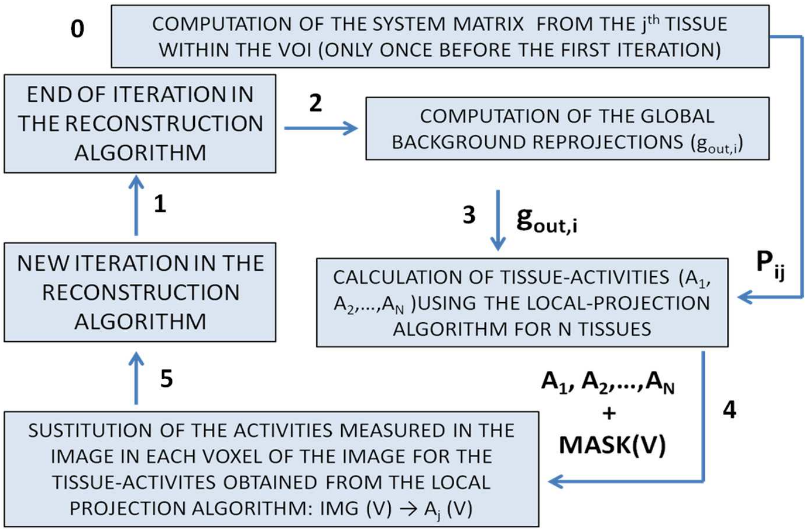

Figure 6.2: Illustration of the procedure employed to improve the quantification of the reconstructed image within the VOI using the activities computed with the LPA processing.

- **IMG:** Quantification obtained from the image reconstructed using the standard PR-OSEM iterative reconstruction.
- **LPA:** Quantification obtained using the LPA post-processing from the images reconstructed using the standard PR-OSEM procedure.
- **LPAR:** Quantification obtained from the image reconstructed using the LPA reconstruction
- **LPAR + LPA:** Quantification obtained using the LPA post-processing from the image reconstructed using the LPA reconstruction.

6.2.3 Background subtraction

A background subtraction must be performed during image reconstruction in order to obtain the better possible quantification within the VOI. Background counts may arise from different sources, such as for example: scattered events, random coincidences or positron-gamma events (coincidence event between one annihilation photon and one additional prompt gamma emitted by the radionuclide) when imaging with non-pure emitters. This background subtraction is of great importance when imaging with non-pure emitters (^{124}I or ^{76}Br, for instance) because the prompt gamma rays emitted by the radionuclide will contribute to increase the background level of the image.

Several methods have been proposed in the literature to correct for scatter and random coincidence events in PET [Cherry et al., 2003]. The background due to prompt gamma emissions have been also studied and corrected by several authors [Lubberink and Herzog, 2011, Liu and

Laforest, 2009, Laforest and Liu, 2008]. In this work we followed a straightforward but accurate method to estimate the background counts in our acquisitions:

- First, we obtain the reconstructed image without any background subtraction. Using the CT information, we set to zero the activity values in all voxels where there is no material, because no activity distribution should be present there. The activity in the rest of the voxels are calibrated to represent Bq/cc.
- We perform a Monte Carlo simulation with the same settings of the acquisition using the image obtained in the previous step as the activity source distribution for the simulation.
- We store the scattered, random and positron-gamma counts in the LOR histogram obtained from the MC simulation.
- Finally, we can subtract the MC-estimated background from the data or include it during the reconstruction procedure. The resulting images in both cases are very similar (although not identical).

This simple method is valid if we assume that the distribution of scattered, random and positron-gamma events is very smooth across the FOV of the system and the amount of these events is relatively small in comparison with the true coincidences, so that the initial estimate of activity can be used reasonably in the MC simulation of the backgrounds. These assumptions are usually granted and indeed, in the acquisitions studied in this work they are correct, because the activity is relatively small in all cases (small amount of randoms) and the amount of scattered events is around 10% (for the energy window of 400-700 keV). For the non-pure emitter studied here (^{124}I), the amount of positron-gamma events at the activity simulated is about 20% of the total coincidences (see figure 4.8). In case these assumptions should be removed, this procedure can be applied iteratively, that is, using the reconstructed activity distribution once the background counts are estimated from the first MC simulation as input for a second MC simulation employed to compute a better approach to the background counts.

6.2.4 Simulation and acquisition settings

Simulated acquisitions

Acquisitions of the NEMA NU4 IQ phantom [NEMA-NU-4, 2008] filled with ^{18}F, ^{68}Ga or ^{124}I radionuclides were simulated with the PeneloPET MC code (see *chapter 2* and [España et al., 2009]). In these simulated acquisitions, the five capillaries and the cylindrical cavity were filled with a uniform activity concentration of 10^6 Bq/mL (background). One of the two small cavities was filled with an activity concentration 4 times higher than that of the background (hot region), and the other small cavity was not filled, so no activity should be present there (cold region). Attenuation, scatter and randoms were included in the simulation. The main parameters set to this simulated acquisitions have been:
- Energy window: 400 - 700 keV
- Theoretical hot/uniform ratio: 4.0
- Theoretical cold/uniform ratio: 0.0

- Attenuation correction: No
- Background subtraction: Yes
- Iterative reconstruction: 5 iterations, 20 subsets per iteration.
- Voxels in the image: 175 × 175 × 61 voxels
- Voxel size: 0.3886 × 0.3886 × 0.775 mm^3

In order to evaluate the performance of the LPA method, the quantification in hot and cold regions of the simulated IQ phantoms has been studied. The LPA post-processing results have been compared with those obtained directly from the reconstructed image.

Acquisitions of real phantoms

In addition, several acquisitions of a phantom (made from gels) with several hot and cold lesions (diameters around 4 mm) were performed in the Brigham and Women´ s Hospital (Boston, MA). The settings for these acquisitions were:

- Energy window: 250 - 700 keV
- Theoretical hot/uniform ratio: 4.25
- Theoretical cold/uniform ratio: 0.0
- Attenuation correction: Yes
- Background subtraction: Yes
- Iterative reconstruction: 5 iterations, 20 subsets per iteration.
- Voxels in the image: 175 × 175 × 61 voxels
- Voxel size: 0.3886 × 0.3886 × 0.775 mm^3

As in the previous cases, the evaluation of the LPA post-processing results were performed by comparing the LPA results with those obtained directly from the reconstructed image.

6.3 Results and discussion

6.3.1 Simulated NEMA IQ phantom (^{18}F)

Figure 6.3 shows the transverse and sagittal views of the simulated NEMA IQ phantom, filled with ^{18}F and reconstructed with the PR-OSEM procedure using 5 iterations and 20 subsets per iteration. In addition, we show on the images the masks employed to delimitate the hot and cold regions.

In figure 6.4 we plot the evolution of the hot/uniform and cold/uniform ratio activities with the number of iterations, for the four quantification methods studied in this work (IMG and LPAR in red, LPA and LPAR + LPA in blue). In the upper part of the figure we plot a transverse view of the reconstructed image; using the standard PR-OSEM reconstruction with positron range correction (left), LPA reconstruction using the LPA values for the HOT region as prior (center) and LPA reconstruction using LPA values for the COLD region (right).

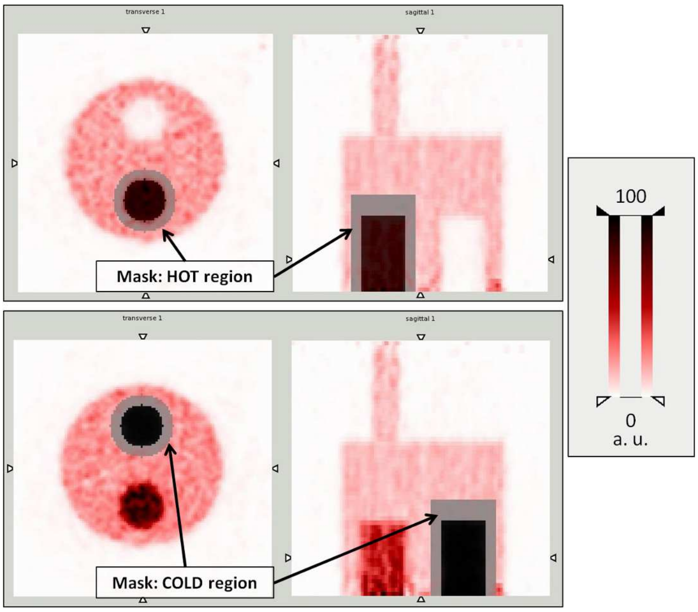

Figure 6.3: Transverse and sagittal views of the reconstructed IQ phantom (simulated acquisition) filled with ^{18}F, 5 iterations and 20 subsets. The masks for the hot and cold regions are depicted in the figure.

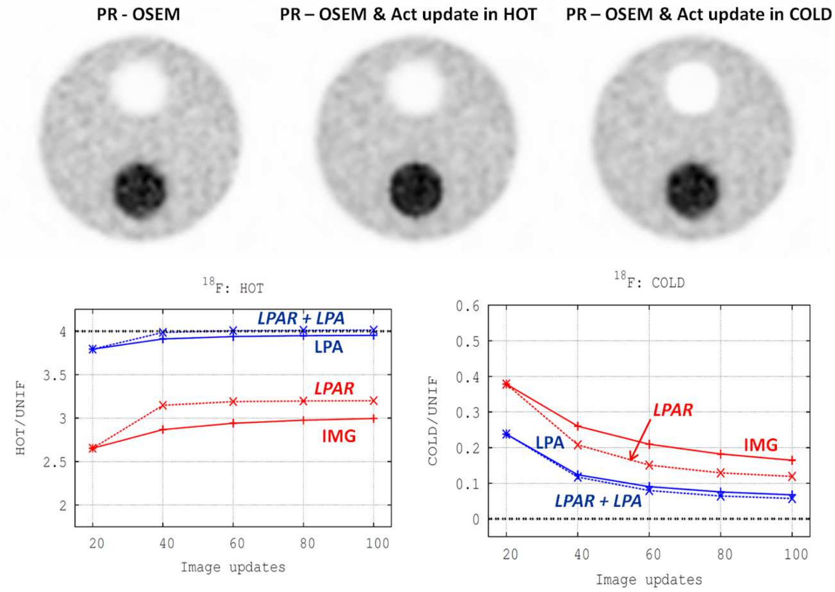

Figure 6.4: Top: Reconstructed images of the IQ phantom: left: PR-OSEM, center: LPA reconstruction using LPA values from hot VOI, right: LPA reconstruction using LPA values from cold VOI. Bottom: hot/uniform and cold/uniform ratio activities.

As we can see in figure 6.4, the quantification in both hot and cold regions improves significantly when LPA post-processing is applied. We can also see that the use of LPA activities during image reconstruction (LPAR) improves the quantification, within the VOI, obtained both from the image and from the LPA post-processing.

For example, regarding the quantification within the VOI which includes the hot region, the ratio hot/uniform (within the VOI) obtained from the image is about 3.0, while the same ratio from the LPA post-processing improves up to 3.9 (the theoretical value is 4.0). In addition, the quantification is even better when LPAR is used (ratio of 3.2 from the image and 4.0 from the LPA post-processing).

On the other hand, and regarding the quantification within the VOI which includes the cold region, similar results are obtained. The cold vs uniform ratio values are 0.16 from the standard PR-OSEM image and 0.12 from the image obtained by means of the LPAR. In this case, the quantification obtained from the LPA post-processing is about 0.06 (we should keep in mind that the theoretical value for this case should be 0.0).

The effect of using LPA post-processing after LPAR is a slightly improvement in the quantification of the lesion of interest. This improvement is more significant for cold lesions.

6.3.2 Results for acquisitions of real phantoms

In this section we present the results obtained for the phantom acquisitions performed at Brigham and Women´ s Hospital (Boston, MA). Figure 6.5 shows the reconstructed images of the phantom and the three hot and cold lesions considered.

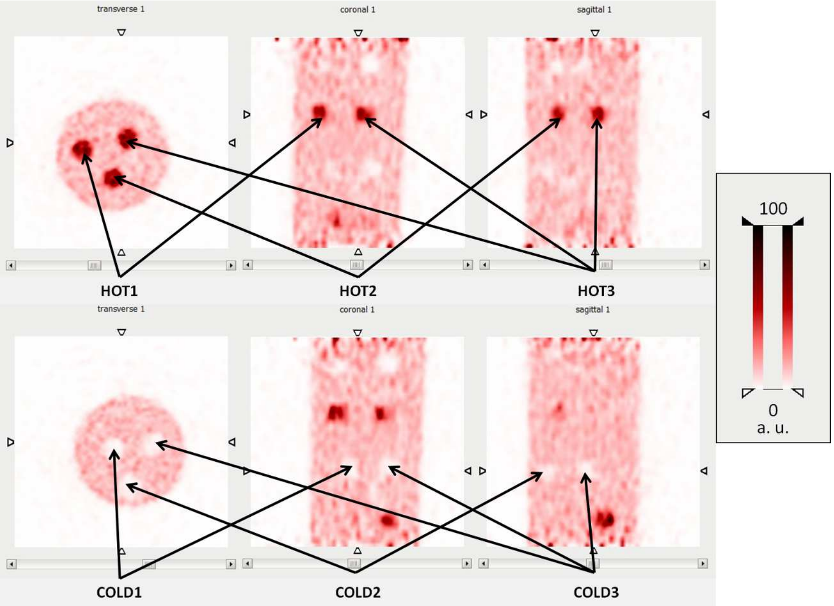

Figure 6.5: Transverse, coronal and sagittal views of the reconstructed phantom filled with ^{18}F, 5 iterations and 20 subsets. The three hot and cold regions analyzed in this work are depicted in the figure. The transverse and axial FOVs of these images are 68 and 47 mm respectively

In addition, we show in figure 6.6 the reconstructed images of the phantom, using the standard PR-OSEM procedure (left) and the LPA reconstruction with LPA values of the HOT1 mask and with LPA values of the COLD1 mask. In the same figure we also plot the evolution of the hot/uniform and cold/uniform ratio activities for each lesion. As in the previous subsection, we plot the results obtained with the four quantification methods: IMG and LPAR in red, LPA and LPAR + LPA in blue.

For the real acquisitions, we can see (figure 6.6) a significant improvement in the quantification when LPA post-processing or LPAR are employed, for all the hot and cold lesions analyzed. We can also see (figure 6.6) better lesion delimitation and quantification when the LPA activities (for the tissues within the VOI) are used during reconstruction.

Regarding the quantification of hot lesions, the mean hot-uniform ratio values obtained from the images are about 2.9 and 3.0 for the LPAR. With the LPA post-processing we obtained a significant improvement, with hot /uniform ratios above 4.0 in all cases (the theoretical estimated value is 4.25).

For the cold lesions, the quantification also improves when LPA post-processing is used. We obtained cold-uniform ratios very close to the theoretical value (0.0) with the LPA post-processing. The ratios obtained from the image are of about 0.4 in all cases. If LPA activities are used during reconstruction we obtained a improvement up to 0.3 approximately.

6.3.3 Results with ^{68}Ga and ^{124}I radionuclides

In this section we analyze the performance of the LPA post-processing and LPA-reconstruction method for simulated acquisitions of the NEMA IQ phantom filled with ^{68}Ga (with a large positron range and no additional prompt-gamma emissions) and with ^{124}I (with a large positron range and additional prompt-gamma emissions) radionuclides.

The masks employed for the hot and cold regions were the same than the ones that we used in the simulated acquisitions with ^{18}F (see figure 6.3).

Figures 6.7 and 6.8 show the evolution of the hot/uniform and cold/uniform ratio activities with the number of iterations, for the four quantification methods studied in this work (IMG and LPAR in red, LPA and LPAR+LPA in blue), when applied to the acquisitions with ^{68}Ga (figure 6.7) and with ^{124}I (figure 6.8). In the upper part of the figures we plot the images reconstructed using the standard PR-OSEM method (i.e. with positron range correction) (left), LPA reconstruction using the LPA values for the HOT region (center) and LPA reconstruction using LPA values for the COLD region (right).

As it was the case for the common radioisotopes, for these non-standard radionuclides we observed a significant improvement in the quantification of hot and cold regions when the LPA post-processing or reconstruction were applied (see figures 6.7 and 6.8). However, for these long positron range radionuclides, we were not able to achieve the theoretical values for hot/uniform and cold/uniform ratios (4.0 and 0.0 respectively). As one can see in the figures, maximum values of hot/uniform ratios of about 3.3 are achieved using LPA post-processing, while from the image we obtained 2.5 (standard PR-OSEM reconstruction) and 2.9 (LPA reconstruction). We obtained similar results for cold regions, giving cold/uniform ratios of about 0.2 with LPA post-processing, 0.3 from the image (PR-OSEM reconstruction) and 0.25 from the LPA reconstruction.

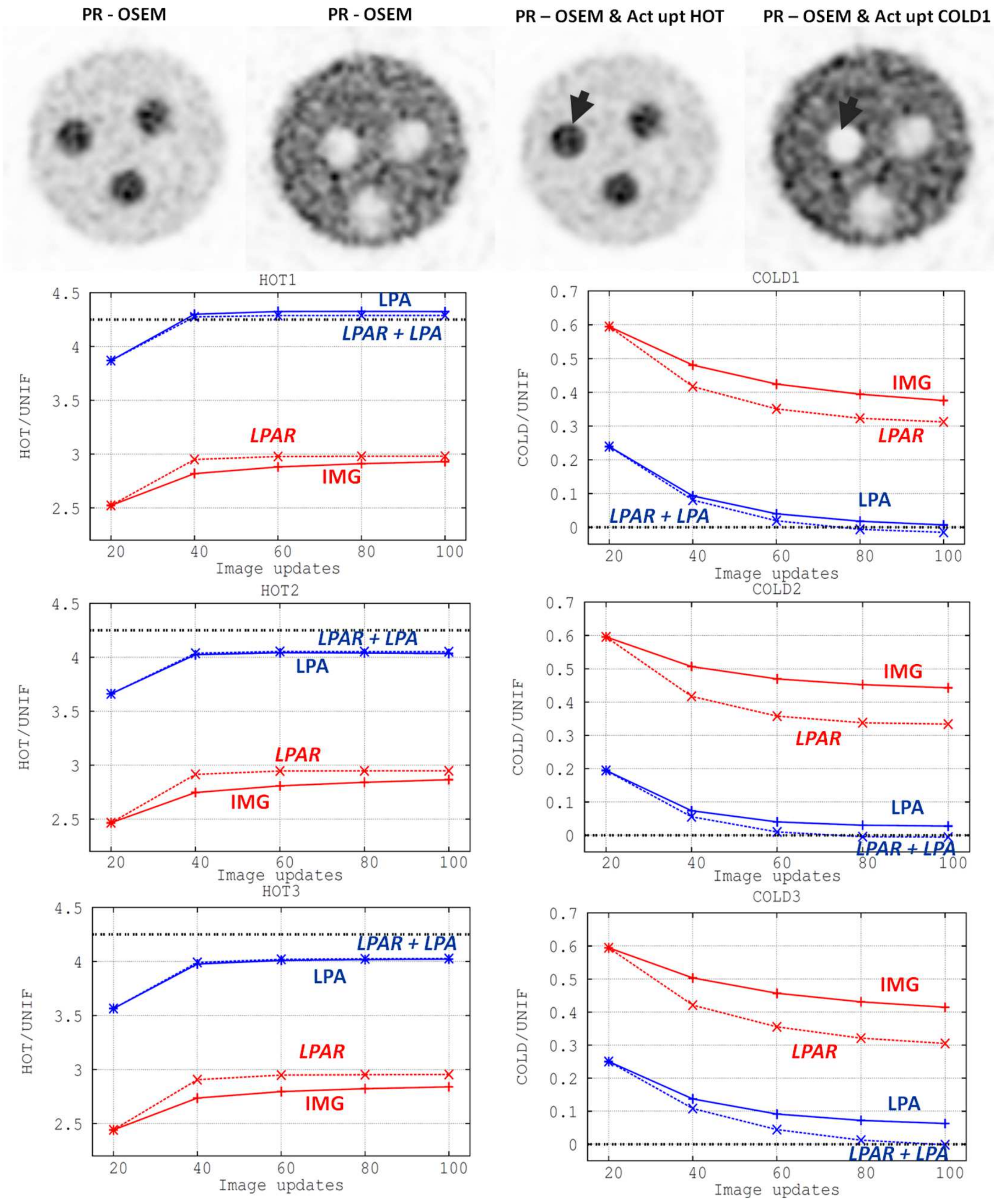

Figure 6.6: Top: Transverse views of the reconstructed phantom. From left to right: PR-OSEM reconstruction (2 views), LPA reconstruction using LPA values from HOT1 region and from COLD1 region. Hot/uniform and cold/uniform ratio activities for each lesion studied in this work.

Note that the hot/uniform and cold/uniform ratios given here are not directly comparables with the ones we presented in table 4.6 (*chapter 4*). This is because the ratios obtained here were computed using the tissues within the local VOI analyzed, and the quantification of the uniform region in table 4.6 was computed in a different VOI. A fast review to the reconstructed images (figures 6.7, 6.8 and 4.10 in *chapter 4*) show us that the PR-OSEM images (with positron range correction and background subtraction) obtained for these radionuclides are of better quality (better spatial resolution and quantitative accuracy) than the ones that we obtained in *chapter 4*, without positron range correction and without background subtraction.

In addition, we can see (figures 6.7 and 6.8) a significant improvement (better lesion of interest delimitation and quantification within the chosen VOI) when LPA activities are used during reconstruction.

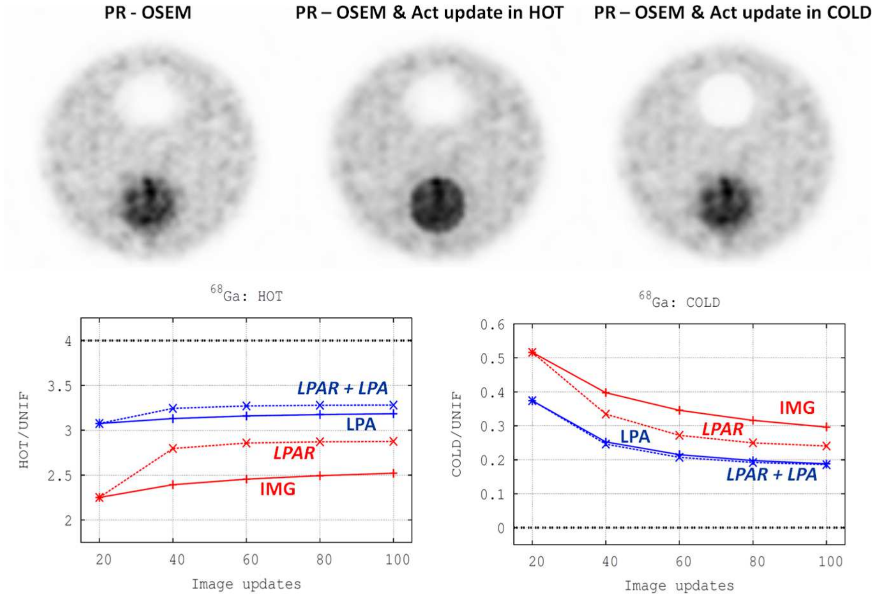

Figure 6.7: Top: Reconstructed images of the simulated IQ phantom filled with ^{68}Ga: left: PR-OSEM, center: LPA reconstruction using LPA values from HOT region, right: LPA reconstruction using LPA values from COLD region. Bottom: hot/uniform and cold/uniform ratio activities.

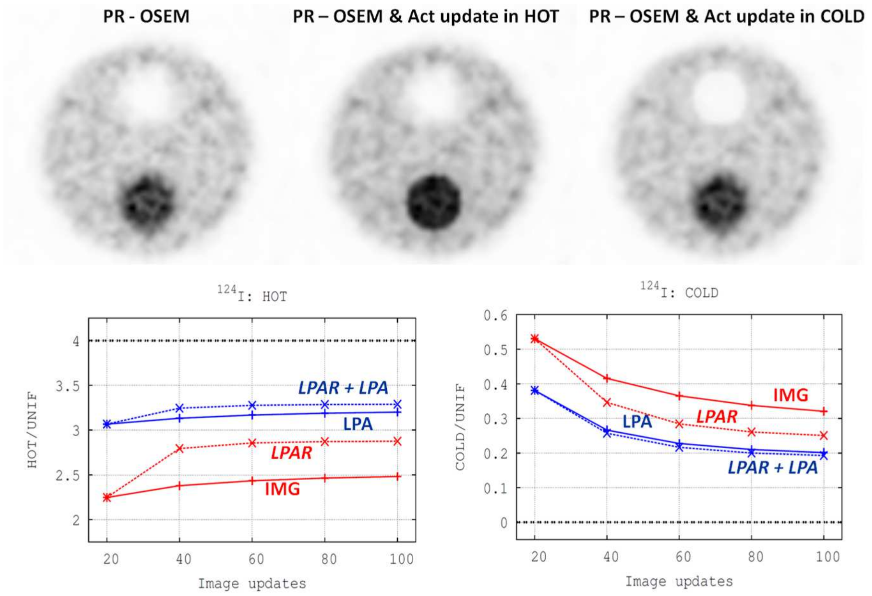

Figure 6.8: Top: Reconstructed images of the simulated IQ phantom filled with ^{124}I: left: PR-OSEM, center: LPA reconstruction using LPA values from HOT region, right: LPA reconstruction using LPA values from COLD region. Bottom: hot/uniform and cold/uniform ratio activities.

6.4 Summary and conclusions

For the NEMA IQ simulations and phantom acquisitions with the standard ^{18}F radionuclide, quantification improved significantly when the LPA post-processing or LPA reconstruction were used, giving hot/uniform and cold/uniform ratios much closer to the theoretical ones that the ones obtained from the images reconstructed with the PR-OSEM procedure.

On the other hand, for the simulated acquisitions with the ^{68}Ga and ^{124}I radionuclides, we observed also a significant improvement in the quantification within small volumes of interest when the LPA were applied as a post-processing method or during the reconstruction. We also noted that better images of local VOIs (with better identification of the lesion of interest) might be obtained when LPA values are employed during reconstruction. For these radionuclides, although the images are not as good as the ones obtained with ^{18}F, using positron range correction and LPA reconstruction we can obtain acceptable images, with good spatial resolution and quantitative accuracy.

In the case of large positron range radionuclides, the loss of quantitative accuracy is probably due to the spatial extent of annihilations caused by the positron range, which is not completely recovered by the positron range correction algorithm. For these cases, we expect to obtain better LPA quantification using bigger VOIs for each lesion of interest, in order to recover the effects of spill-in and spill-out in the VOI.

For ^{68}Ga and ^{124}I acquisitions we have seen a significant improvement in the quantification in the images of the lesions of interest when positron range correction and background substraction are applied during image reconstruction. This improvement is enhanced when LPAR method is employed. For example, for ^{124}I, the hot-to-background ratio is 2.0 in the reconstructed image (5 iterations, 20 subsets) without positron range correction and background substraction. When these corrections are applied during reconstruction, the above mentioned ratio is 2.5. Finally, if we reconstruct the image using the LPAR method, the hot-to-background ratio is 2.9.

Generally speaking, for hot lesions we obtained similar results using the LPA post-processing in images reconstructed with the PR-OSEM and with the LPAR methods. A slightly better quantification for cold lesions was obtained using LPA post-processing in images reconstructed using the LPAR method.

In summary, in this chapter we proposed and evaluated a method to improve the quantification within small volumes of interest. The LPA procedure may be applied as a post-reconstruction method (LPA) or as a within-reconstruction method (LPAR). This algorithm is easy to implement and flexible enough to be used in other preclinical or clinical scanners, provided that an accurate System Response Matrix is available for the scanner under consideration. The running time of the LPA method is the needed time to perform a whole projection from the image space to the data space. In a single 3 GHz CPU it takes around 15 minutes. This procedure can be easily accelerated running it simultaneously in several CPUs.

The conclusions of this chapter are the following:

- Quantification was significantly improved by using LPA, which provided more accurate ratios of lesion-to-background activity concentration for both hot and cold lesions.
- Using activities obtained with the LPA during the reconstruction improves the quantification in the VOI, especially in cold regions.
- Better results are obtained using more accurate delimitations of the lesions and with scatter and random counts considered in the model of the system employed for the reconstruction.

Chapter 7

Simulation of triple coincidences in PET

7.1 Introduction

Currently, PET scanners are designed to detect and record double coincidences [Levellen, 2008, Zanzonico, 2004, Badawi et al., 2000], which correspond to two independent events recorded almost simultaneously within a narrow time coincidence window (between 2 and 5 ns). Typically, these detections correspond to the two gamma-rays emitted in opposite directions resulting from the annihilation of a positron emitted by the radionuclide present in the subject under study with a surrounding electron. Therefore, triple coincidences in standard PET scanners are either discarded (with an important loss of sensitivity) or processed as a set of double coincidences (which introduce spurious background to the acquisition, due to the fact that only one of the possible LORs defined by a triple event might have useful information).

There are several situations in which triple-event coincidences may occur (Figure 7.1):

- **Inter-Detector Scatter (IDS) coincidences:** in which at least one of the annihilation gamma-rays deposit its energy in several detectors ([Clerk-Lamalice et al., 2012, Wagadarikar et al., 2012, Gu et al., 2010]) and each of these interactions is registered as a separated event by the scanner. It is important to distinguish this type of events from intra-detector scatter events, in which the several interactions occur in the same detector module and therefore they are processed effectively as one single interaction.

- **Random triple coincidences:** R_{T1} - Three detected events coming from two independent decays. R_{T2} - Three detected events coming from three different decays.

- **Positron-gamma coincidences** ($\beta^+\gamma$): When non-pure positron emitters like ^{124}I, ^{86}Y or ^{76}Br are used, the one or more gamma rays emitted per decay can be detected in coincidence with the annihilation gamma rays [Belov et al., 2011, Koehler et al., 2010, Surti et al., 2009]. The half-life of the intermediate excited states in the daughter nuclei are usually very short (inferior to 100 ps) and of the same order than the life time of the positrons in tissue, therefore they are detected in coincidence with the annihilation photons. Nevertheless, some exceptions, with a non-negligible half-life of the intermediate excited states, have been reported in the literature, as for example in the ^{89}Zr radionuclide [Singh, 2013].

- Finally, when the positron annihilates via formation of Positronium in the triplet state ($^3S_1$, ortho-positronium), the **disintegration of the ortho-positronium** may result into the emission of three gamma-rays, which can also create triple-coincidences [Harpen, 2004]. However, due to the large half-life of the ortho-positronium state, most annihilation in tissue result in two-gamma ray emissions, and the probability for this process is very low [Harpen, 2004]. Therefore it has not been considered in this work.

IDS, R_{T1} and R_{T2} events may occur both for pure and non-pure emitters, while $\beta^+\gamma$ events only take place for non-pure β^+ radionuclides. Of course, more than 3 coincidences are also possible. For instance the annihilation gamma rays from 2 decays can produce 4 events detected in coincidence (random quadruple). However, the sensitivity for these >3 events is usually very low and it has not been considered in this work.

Useful information may be obtained from IDS, R_{T1} and $\beta^+\gamma$ coincidences, since in these cases at least one of the possible LORs corresponds to the line along which the annihilation occurred. On the other hand, R_{T2} coincidences, in which the three singles comes from three independent decays, does not provide useful information and must be discarded.

To select the right LOR among the possible ones defined by a triple coincidence; that is, the one along which the positron annihilation took place, several methods have been proposed in the literature. For instance, IDS events can be sorted applying Compton kinematics and the information of the energy deposited in each event [Rafecas et al., 2003]. Alternatively, in [Lage et al., 2013], the authors proposed a method for recovering IDS and R_{T1} coincidences which do not require energy information. The idea behind that method consists of using the distribution of double coincidences as a reference to assign a probability for each of the possible LORs associated with the triple coincidence. Finally, iterative reconstruction schemes in which the two possible LORs of the triple coincidence are considered have also been proposed [Parot et al., 2013].

On the other hand, for non-pure emitters, the procedure to distinguish the useful LOR between the possible LORs of the multiple coincidences depends on the energy of the extra gamma ray. If the prompt gamma ray emitted has an energy significantly higher to 511 keV and it is detected with an energy high enough to be distinguishable from annihilation gamma-rays, the useful LOR will be easily identified. However, if the extra gamma ray has a similar energy to the annihilation gamma rays (for instance with ^{76}Br or ^{124}I radionuclides), it cannot be easily distinguishable and therefore the procedure to choose the useful LOR might be similar to the one used for the IDS events [Lage et al., 2013].

Triple coincidences in PET are starting to be of interest in the field because of the above mentioned recent works which have shown the possibility of using them to unlock new applications. For example, they may be used to differentiate standard positron emitters from positron-gamma emitters that may enable dual-tracer PET [Parot et al., 2013, Andreyev et al., 2012, Andreyev and Celler, 2011, Sitek et al., 2011]. On the other hand, IDS or R_{T1} triple coincidences can be used for increasing the photon sensitivity of PET scanners [Lage et al., 2013,

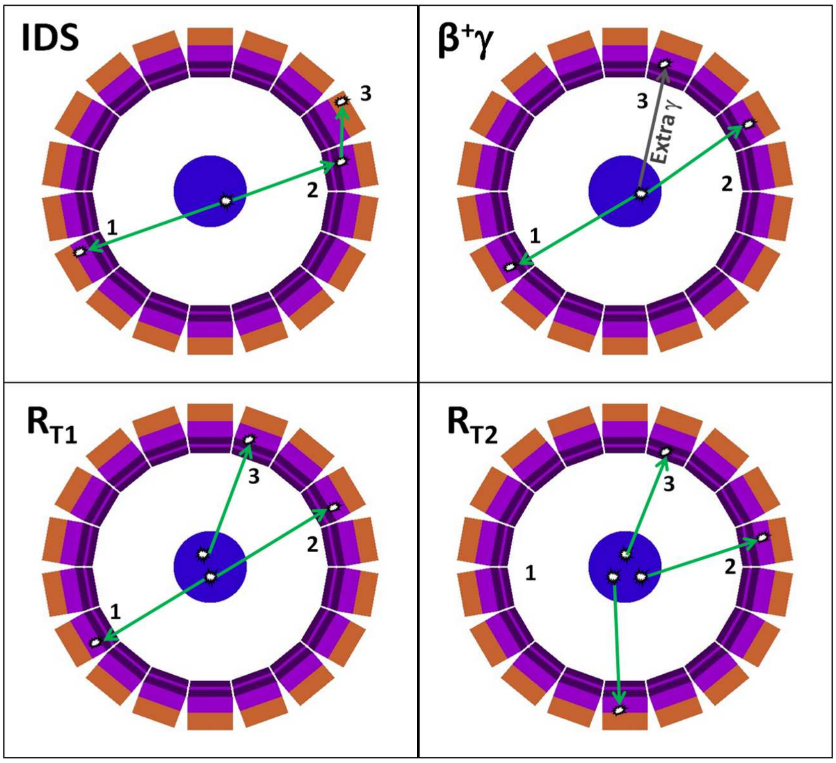

Figure 7.1: Different types of multiple coincidences that may occur in PET acquisitions. IDS: Inter-Detector Scatter coincidences. $\beta^+\gamma$: detection in coincidence of one extra gamma-ray emitted by a non-pure β^+ radionuclide with the two annihilation photons. R_{T1}: random event from two decays, R_{T2}: random coincidence from three different decays. IDS, R_{T1} and R_{T2} coincidences may occur both for pure and non-pure β^+ emitters, while $\beta^+\gamma$ events only take place for non-pure β^+ radionuclides.

Clerk-Lamalice et al., 2012, Gillam et al., 2012, Levin, 2008, Rafecas et al., 2003], thus enabling reduction in acquisition times and dose to the patient. In a similar way, when using positron-gamma emitters, detection of triple coincidences hold also the potential to improve sensitivity [Lin et al., 2012].

In order to evaluate the relevance of triple coincidences in PET scanners in each of these situations and to evaluate the optimal settings of the scanner to make use of them, it is useful to have a complete and accurate model of the emission and detection of the radiation. Monte Carlo (MC) simulations, as we have previously seen, are commonly used for this task [Buvat and Lazaro, 2006], because they allow tracking all possible emissions and interactions. Nevertheless, as triple coincidences are not usually considered in PET acquisitions, these MC simulators may require some modifications in the code and additional tools to analyze the simulated results.

7.1.1 Objectives

The goal of this work was to include in our simulation software (PeneloPET, see *chapter 2* and [España et al., 2009]) the possibility of studying triple coincidences and to validate this tool to study triple coincidences in many different PET scanners with several radionuclides of interest. In order to achieve the proposed goal [Cal-González et al., 2013b] we followed these steps:

- We implemented a framework to simulate and analyze triple coincidences in PET imaging.
- In order to validate our simulation we compared simulated results against experimental measurements obtained with a modified acquisition software on the Argus preclinical scanner [Wang et al., 2006], capable of acquire, store and analyze multiple coincidences.
- Once validated, we used our simulator to evaluate the amount and characteristics of the triple coincidences that could be detected in other scenarios with the Argus scanner.
- We also evaluated the amount and characteristics of triple coincidences in two clinical scanners: the Siemens Biograph TPTV scanner [Jakoby et al., 2009] and the GE Discovery-690 [Bettinardi et al., 2011].

7.2 Methods

7.2.1 Simulated scanners

Argus preclinical scanner

The geometry and acquisition parameters of the Argus PET/CT preclinical scanner are described in the *chapter 2* of this thesis. Therefore, here we will focus on the modifications performed on the acquisition system of this scanner, required to allow the processing of triple coincidence events.

The acquisition software of the small-animal PET/CT scanner Argus [Wang et al., 2006] was adapted so that it provides list-mode data files with the information of all the detected single events in coincidence. Each single event in the file contains a time-stamp which allows the identification of coincidences from two, three or more events falling within a defined time window. This file was processed to create two data sets, one for double coincidences and another one with triple coincidences. In this work, coincidences of more than three events, being significantly less likely than triple coincidences, were not considered. In order to be classified as valid coincidences, and consequently recorded, coincidence events have to be within a user-specified energy window and a predefined timing window.

The average energy and timing resolution for 511 keV photons were measured experimentally [Lage et al., 2013] for this scanner, obtaining a good agreement for the reported values in the literature [Wang et al., 2006]: the average timing resolution was 1.24 ns (FWHM, front-front coincidence events) and the energy resolution was 25 % ± 3.5% in the LYSO layer and 29% ± 3.9% in the GSO layer. Similar values for energy and timing resolution have been used in the simulations.

As the timing resolution depends on the layer of crystal where the pair of events are detected (front layer = LYSO, back layer = GSO), the timing window used in the experimental measurements was: 5 ns for the coincidences between front and front layers, 7 ns for front-back layers and 10 ns for back-back layers. For the simulations we used the coincidence time window for the front - front layers in all cases. In addition, we also used an effective dead time for singles of 2000 ns [España et al., 2009]. We obtained this effective value by fitting to the experimental data the double coincidences NECR curve.

Clinical scanners

Appart from the preclinical scanner, two clinical scanners have been also considered in this study: the Biograph TruePoint TrueV (B-TPTV) [Jakoby et al., 2009] and the GE Discovery-690 [Bettinardi et al., 2011].

The B-TPTV scanner consist of four rings, each one with 48 detector blocks of 5.4 cm × 5.4 cm in cross-section. Each block comprises a 13 × 13 matrix of 4 × 4 × 20 mm^3 LSO scintillator crystals coupled to 4 photomultiplier tubes. Data are acquired with a 4.5 ns coincidence time window and an energy window of 425 - 650 keV. The axial field of view (FOV) of this scanner is equal to 21.8 cm, while the transaxial FOV with 25 detectors in coincidence is 68.4 cm. It operates only in 3-dimensional mode (3D) with an axial coincidence acceptance of ±38 planes.

In our simulations of the Biograph TPTV scanner, we used all the published values for geometries and energy and timing windows. The dead time was computed as an effective value obtained by fitting the simulated peak of the NECR curve to the experimental one reported in the literature [Jakoby et al., 2009]. The dead time was computed as an effective value of 50 ns.

The other clinical scanner considered in this work is the GE Discovery-690 [Bettinardi et al., 2011]. It consists of 13824 LYSO crystals with dimensions of 4.2 × 6.3 × 25 mm^3 arranged in blocks of 54 (9 × 6) crystals coupled to a single squared photomultiplier tube with 4 anodes. The energy window is 425 - 650 keV and the coincidence time window is 4.9 ns. The axial and transaxial FOV are respectively 15.7 and 70 cm. As the Biograph TPTV scanner, the Discovery-690 operates only in 3D mode with an axial coincidence acceptance of ±23 planes. These values were used in all the simulations performed for the Discovery scanner.

The effective dead time for this scanner (100 ps) was also computed by fitting the simulated peak of the NECR curve to the experimental value reported in the literature [Bettinardi et al., 2011].

7.2.2 Validation of the new version of PeneloPET

The validation of the new version of our simulation tool for double coincidences was performed by computing the sensitivity, scatter fraction and NEC curve with our simulator, and comparing these values with the experimental ones obtained for the Argus scanner and with the values reported in the literature for the clinical scanners.

On the other hand, to validate the performance the simulation toolkit for triple coincidences we compared the output of the simulator with real measurements obtained with pure and positron-gamma emitters in the Argus scanner. As a figure of merit we have used the ratio of triple to double coincidences measured in acquisitions with different radionuclides. his value provides a quick estimate of the importance of relative importance of triple coincidences in each particular case. We also compared energy spectra for double and triple coincidences.

Analysis of experimental and simulated data

To analyze the output data from the Argus scanner, an analysis software (*list2sin* code [Parot et al., 2013] - V. Parot, E. Lage and J. Herraiz - mPET project, M+Vision Consortium) reads the singles list mode data acquired with the scanner and classify it into double, triple and multiple (more than 3 singles) coincidences. For this work, a similar program was developed to sort the singles list mode data obtained from simulations.

With the above mentioned software, the user can choose the timing window (for each combination of layers front-front, front-back and back-back layers) and the energy window for double and triple coincidences.

The energy windows considered for measured and simulated data were set as follows:

- For double coincidences (EW_D): 400 - 700 keV for the Argus scanner and 425 - 650 keV for the Biograph and Discovery scanners.

On the other hand, the optimal energy windows for triple coincidences (EW_T) depends on the type of triple coincidence considered:

- IDS coincidences (EW_{T-IDS}): the energy of one single event and the sum of the other two events (the ones that had scatter in a detector) should be within the EW_D.
- $\beta^+\gamma$ coincidences ($EW_{T-\beta\gamma}$) for positron-gamma emitters: Two single events should be within the EW_D and the third single event should be above a threshold selected according the energy of the prompt gamma ray. This threshold may be the upper limit of the EW_D if the extra gamma rays emitted have energy much higher than 511 keV (^{22}Na, ^{82}Rb or ^{94m}Tc radionuclides) or the lower limit of the EW_D if the extra gamma rays have energy similar to annihilation photons (^{124}I, ^{86}Y or ^{76}Br).
- RT coincidences (EW_{T-RT}): All the three single events are chosen to be within the EW_D.

Note that more than one type of triple coincidences might be within a given energy window. For example, in a non-pure emitter such as ^{124}I within the EW_{T-RT} window we can find R_T events as well as $\beta^+\gamma$ triple events that we cannot be directly differentiated in the experimental data but can be differentiated in the simulation output.

As mentioned before, coincidences of four or more events, being around one order of magnitude less likely, were not considered in this work.

Argus preclinical scanner: Measurements and simulations

Sensitivity, scatter fraction and noise equivalent count rate (NECR) curve were measured following the NEMA protocol for preclinical scanners ([NEMA-NU-4, 2008]). In order to evaluate the amount of triple coincidences in PET acquisitions, we have performed several acquisitions of an Image Quality phantom (IQ) according to NEMA protocol ([NEMA-NU-4, 2008]) filled with different radionuclides.

To evaluate the sensitivity of the scanner, we have measured and simulated the acquisition of a ^{22}Na point source placed at the center of the FOV. In this case, No object was used in the simulation (only the ^{22}Na disk and the bed of the scanner), in order to avoid attenuation and scatter effects.

To obtain the scatter fraction and the NECR curve we used a mouse phantom. We measured and simulated acquisitions using as an object a polyethylene cylinder with a diameter of 2.5 cm and a total length of 7 cm, which was positioned in the isocenter of the FOV of the scanner. As source we used a thin capillary tube filled with the radionuclide of interest, the capillary was inserted axially into the cylinder through a hole located 1 cm below the central phantom axis.

The validation of our simulation tool for triple coincidences in the preclinical Argus scanner was performed by means of experimental and simulated acquisitions of the NEMA IQ phantom ([NEMA-NU-4, 2008]). The radionuclides used for the validation of the code have been: ^{18}F (pure emitter), ^{22}Na, ^{124}I and ^{76}Br (positron-gamma emitters), and the figures of merit evaluated have been:

- Averaged energy spectra for singles in all LYSO and GSO scintillator crystals and for double and triple coincidences.
- Statistics of triple coincidences within each of the considered energy windows for triples (ratio triples versus doubles within EW_D).
- Variation of triple coincidences with the activity at the optimal energy window to detect IDS or $\beta^+\gamma$ triple events ($EW_{T-\beta\gamma}$) in ^{124}I.

Using our simulation tool, we also estimated the amount of each type of triple coincidence (IDS, $\beta^+\gamma$ or R_T) obtained within each energy window for triples.

In addition, we also evaluated, by means of MC simulations, the statistics of triple events within different energy windows for the following radionuclides: ^{68}Ga, ^{82}Rb, ^{94m}Tc and ^{86}Y. The activity simulated for these radionuclides has been 95 μCi.

PeneloPET simulations of clinical scanners

To validate our simulation tool in double coincidence mode for clinical scanners, we simulated the sensitivity, scatter fraction and Noise Equivalent Count Rate (NECR) curve of the aforementioned scanners following the NEMA protocol for clinical scanners [NEMA-NU-2, 2007]. Afterwards we compared the results of our simulation with the experimental values for these figures of merit reported by [Jakoby et al., 2009] for the Biograph TPTV and from [Bettinardi et al., 2011] for the Discovery-690.

The sensitivity was measured with the simulation of a line source (70 cm length) placed at the center of the FOV.

To obtain the scatter fraction and NECR curve, we simulated acquisitions of a 70 cm long and 20 cm diameter polyethylene cylinder positioned in the isocenter of the FOV of the scanner.

A thin capillary tube was filled with the isotope of interest and inserted axially into the cylinder hole, located 4.5 cm below the central phantom axis.

The radionuclides studied in this case have been ^{18}F, ^{82}Rb, ^{124}I and ^{86}Y. We have simulated the energy spectra and the statistics of triple coincidences using different energy windows for the two clinical scanners.

First, the energy spectra have been obtained with a simulation of a point source in air (without object) placed in the center of the FOV.

Later, we also studied the ratio triples / doubles for different energy windows. In this case we simulated the acquisition of a line source placed at the center of the FOV and filled with one of the following radionuclides: ^{18}F, ^{82}Rb, ^{124}I and ^{86}Y. The activity of the line source in these simulations was 10 MBq in all cases. The chosen energy windows for triple coincidences have been the ones corresponding to IDS coincidences (EW_{T-IDS}, one single and the sum of the other two within EW_D), R_T coincidences (EW_{T-RT}, the three singles within the EW_D) and to $\beta^+\gamma$ coincidences for the positron-gamma emitters ($EW_{T-\beta\gamma}$, two singles within the EW_D and the third single above the lower energy of the EW_D).

Uncertainties in simulated and experimental data

Many different factors may affect the accuracy of the results, both for measured and simulated data. In our simulations, sources of error may arise from unknown details of the geometry and acquisition parameters, as well as from the neglected decay cascades and prompt gamma emissions.

For the experiments, to the usual sources of error (positioning of the source, energy and timing resolution, etc), we also have to take into account the effect of contaminants in the acquisitions, which may affect the quantitative results.

In this work, we estimated a systematic uncertainty of 5%, both for measured and simulated data. The statistical uncertainties have been computed as the square root of the number of events in each energy window for double and for triple coincidences.

The total uncertainty is the quadratic sum of the statistical error and the 5% of estimated systematic error.

7.3 Results

In this section the main results obtained in this work are described. First we present the validation of the new version of PeneloPET [España et al., 2009] for double coincidences in the preclinical and clinical scanners. Later, the results for the validation of the detection of triple coincidences in the Argus scanner are shown, and some cases with different situations and radionuclides were studied. Finally, we present the results obtained for triple coincidences in the clinical scanners.

7.3.1 Validation of the new version of PeneloPET for double coincidences

Table 7.1 shows the experimental and simulated sensitivities for different energy windows in the Argus PET/CT scanner, while in table 7.2 we report the sensitivities for the clinical scanners.

Table 7.3, on the other hand, shows the scatter fraction and the value of the peak of the NEC curve for the scanners studied in this work.

	Sensitivity (%)	
Energy window (keV)	**Simulated**	**Experimental**
100 - 700	5.7 ± 0.3	5.4 ± 0.3
250 - 700	3.33 ± 0.17	3.34 ± 0.17
400 - 700	2.09 ± 0.11	2.06 ± 0.11

Table 7.1: Experimental and simulated sensitivity values for the Argus PET/CT preclinical scanner.

		Sensitivity at the center (%)	
Scanner	**Energy window (keV)**	**Simulated**	**Experimental**
Biograph TPTV	425 - 650	0.82 ± 0.04	0.81 ± 0.04
Discovery-690	425 - 650	0.74 ± 0.04	0.74 ± 0.04

Table 7.2: Sensitivity for the Biograph TPTV and Discovery-690 clinical scanners. Experimental values were obtained from [Jakoby et al., 2009] (Biograph) and [Bettinardi et al., 2011] (Discovery).

	NEC [kcps] @ [kBq / mL]		Scatter fraction (%)	
Scanner	**Simulated**	**Experimental**	**Simulated**	**Experimental**
Argus (mouse phantom)	(91 ± 5 @ 75 ± 4) × 10	(86 ± 4 @ 65 ± 3) × 10	13.5 ± 0.7	13.9 ± 0.7
Biograph TPTV	159 ± 8 @ 33 ± 2	161 ± 8 @ 31 ± 2	33.0 ± 1.7	32.5 ± 1.7
Discovery-690	136 ± 7 @ 35 ± 2	139 ± 7 @ 29 ± 2	35.0 ± 1.8	37.0 ± 1.9

Table 7.3: Values for NEC peak and SF for the Argus preclinical scanner and the Biograph TPTV and Discovery-690 clinical scanners. Experimental values for clinical the scanners were again obtained from [Jakoby et al., 2009] (Biograph) and [Bettinardi et al., 2011] (Discovery).

7.3.2 Triple coincidences in the Argus scanner

In this section we present the validation of our simulation tool for triple coincidences.

Energy spectra for double and triple coincidences

Figure 7.2 shows the comparison of the simulated and measured energy spectra, for all coincidence singles in the LYSO and GSO layers (left) and after they have been divided into double and triple coincidences (right).

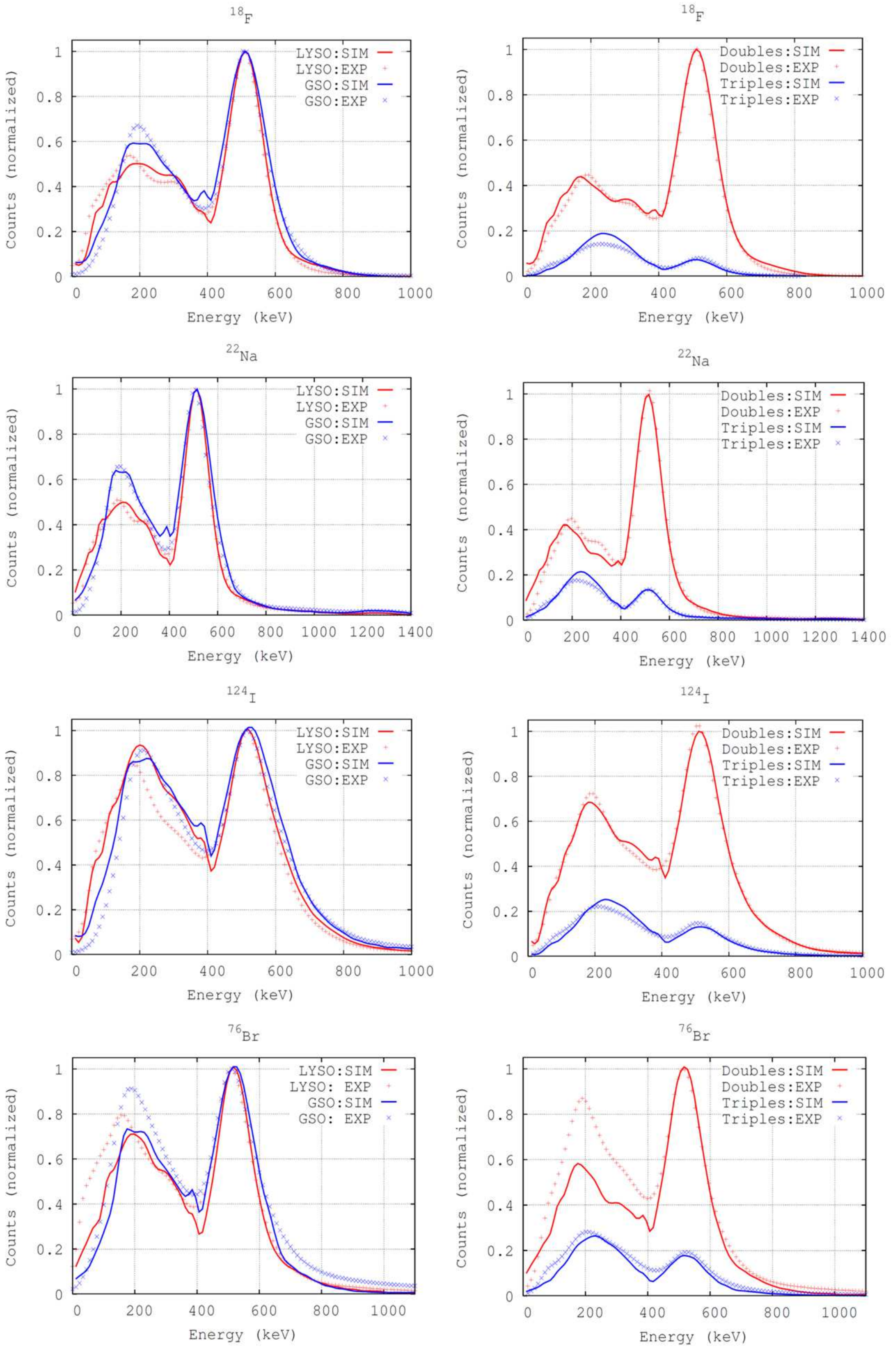

Figure 7.2: Simulated (solid lines) and measured (points) energy spectra for the Argus scanner. Radionuclides from top to bottom are ^{18}F, ^{22}Na, ^{124}Iand ^{76}Br.

As previously explained in the methods section, we obtained the energy spectra for ^{18}F (pure emitter), ^{22}Na, ^{124}I and ^{76}Br (positron-gamma emitters). On the left side of the figure we show the energy spectra for coincidence singles interacting in the LYSO (red) and GSO (blue) layers, respectively. On the right side, we show the energy spectra for double (red) and triple (blue) coincidences. We normalized the spectra for LYSO and GSO to a maximum value of 1, both for simulated and measured results. Spectra of double and triple coincidences have been scaled to a value of 1 in the photopeak energy (511 keV) for double coincidences.

In table 7.4 we show the measured and simulated energy resolution (FWHM in %) at the 511 keV photopeak of the LYSO and GSO averaged energy spectra obtained for each radionuclide. As we can see in figure 7.2 and table 7.4, the fitting obtained for the simulated energy spectra to the measured ones are very accurate in the majority of the cases.

	Energy resolution @ 511 keV (%) (Measured / **Simulated**)			
	^{18}F	^{22}Na	^{124}I	^{76}Br
LYSO	(25.5 / **25.3**) ± 1.3	(26.2 / **25.8**) ± 1.3	(34.0 / **35.0**) ± 1.8	(30.6 / **29.2**) ± 1.5
GSO	(28.2 / **29.9**) ± 1.5	(28.3 / **30.1**) ± 1.5	(37.2 / **38.1**) ± 1.9	(34.9 / **33.9**) ± 1.8

Table 7.4: Measured and simulated energy resolution @ 511 keV for LYSO and GSO scintillator crystals in the Argus scanner; for ^{18}F, ^{22}Na, ^{124}I and ^{76}Br.

Statistics of triple coincidences

Table 7.5 presents the ratio of triple coincidences (in each energy window for triples) versus the double coincidence events within the energy window for doubles, and the simulated amount of each type of triple coincidence (IDS, $\beta^+\gamma$ or R_T) in each energy window for triples.

As in the previous subsection, we found a good agreement between simulations and measured results in the majority of the cases.

Relative abundance of triple coincidences as a function of the activity within the FOV

We present in figure 7.3 the comparison between triples-to-doubles ratio for a pure emitter (^{18}F) and a non-pure emitter (^{124}I).

In addition, figure 7.4 shows the dependence of the statistics for each type of triple coincidence with the total activity in the acquisition of an IQ phantom, for a pure emitter: ^{18}F (top) and a positron-gamma emitter: ^{124}I (bottom). The energy windows used for triples were: EW_{T-IDS} (left) and $EW_{T-\beta\gamma}$ for ^{124}I (right).

In the aforementioned figures we show that the random triple coincidences increases with the activity within the FOV as expected. Non-significative influence of activity was found for IDS and $\beta^+\gamma$ events.

Energy window	**Type of coincidence**	**^{18}F (92 μCi)**	**^{22}Na (3.5 μCi)**	**^{124}I (212 μCi)**	**^{76}Br (105 μCi)**
EW_D **(D)** **(kcps)**	**Doubles EXP**	**31.3 ± 1.7**	**2.37 ± 0.17**	**20.1 ± 1.1**	**16.2 ± 0.9**
	Prompts (%)	99.4	99.5	98.8	98.7
	Randoms (%)	0.6	0.5	1.2	1.3
	Doubles SIM	**31.7 ± 1.8**	**2.45 ± 0.17**	**20.0 ± 1.1**	**16.1 ± 0.9**
	Trues (%)	87.5	87.7	67.5	64.9
	Sc (%)	11.5	6.4	10.0	10.7
	$\beta^+\gamma$ (%)	0.0	5.8	20.0	23.2
	R_D (%)	1.0	0.1	2.5	1.2
EW_{T-IDS} (%)	**T / D exp**	**17.0 ± 1.1**	**18.8 ± 1.8**	**23.7 ± 1.5**	**30.7 ± 2.0**
	T / D sim	**19.0 ± 1.3**	**19.9 ± 2.2**	**23.0 ± 1.7**	**24.4 ± 1.8**
	IDS	18.4 ± 1.2	17.7 ± 1.7	15.5 ± 1.1	16.1 ± 1.1
	$\beta^+\gamma$	<0.01	2.2 ± 0.4	6.2 ± 0.5	7.8 ± 0.6
	R_{T1}	0.38 ± 0.05	<0.01	0.67 ± 0.09	0.34 ± 0.05
	R_{T2}	0.18 ± 0.03	<0.01	0.59 ± 0.08	0.21 ± 0.05
EW_{T-RT} (%)	**T / D exp**	**0.59 ± 0.07**	**1.3 ± 0.3**	**2.3 ± 0.3**	**3.1 ± 0.3**
	T / D sim	**0.32 ± 0.05**	**1.6 ± 0.3**	**2.4 ± 0.3**	**4.0 ± 0.4**
	$\beta^+\gamma$	<0.01	1.6 ± 0.3	2.0 ± 0.2	3.8 ± 0.3
	R_{T1}	0.31 ± 0.05	<0.01	0.38 ± 0.08	0.16 ± 0.04
	R_{T2}	<0.01	<0.01	0.04 ± 0.02	0.024 ± 0.015
$EW_{T-\beta\gamma}$ (**^{22}Na**) (%)	**T / D exp**	**0.06 ± 0.02**	**2.4 ± 0.4**	**0.83 ± 0.11**	**1.8 ± 0.2**
	T / D sim	**0.030 ± 0.011**	**2.7 ± 0.5**	**0.69 ± 0.11**	**0.85 ± 0.13**
	$\beta^+\gamma$	<0.01	2.7 ± 0.5	0.56 ± 0.08	0.79 ± 0.11
	R_{T1}	0.030 ± 0.011	<0.01	0.14 ± 0.03	0.06 ± 0.02
	R_{T2}	<0.01	<0.01	<0.01	<0.01
$EW_{T-\beta\gamma}$ (**^{124}I,^{76}Br**) (%)	**T / D exp**	**0.64 ± 0.08**	**3.7 ± 0.6**	**3.0 ± 0.3**	**4.8 ± 0.4**
	T / D sim	**0.35 ± 0.05**	**4.3 ± 0.7**	**3.1 ± 0.3**	**4.7 ± 0.4**
	$\beta^+\gamma$	<0.01	4.3 ± 0.6	2.5 ± 0.2	4.5 ± 0.4
	R_{T1}	0.35 ± 0.05	0.012 ± 0.010	0.50 ± 0.08	0.21 ± 0.05
	R_{T2}	<0.01	<0.01	0.04 ± 0.02	<0.01

Table 7.5: Statistics of double and triple coincidences in the Argus scanner, for ^{18}F, ^{22}Na, ^{124}I and ^{76}Br radionuclides.

Evaluation of triple coincidences for other radionuclides

Table 7.6 shows the ratio of triple coincidences (using the different energy windows for triples) versus the double coincidence events within the energy window for doubles. This table also shows simulated results for each type of triple coincidence (IDS, $\beta^+\gamma$ or R_T) obtained for each energy window for triples. Triples versus doubles events ratio for each energy window for triples are presented in bold, while ratios for each type of triple coincidences are presented in regular typesetting. The differences observed in table 7.6 between the studied radionuclides are due to the different amount of prompt gamma emissions in these emitters.

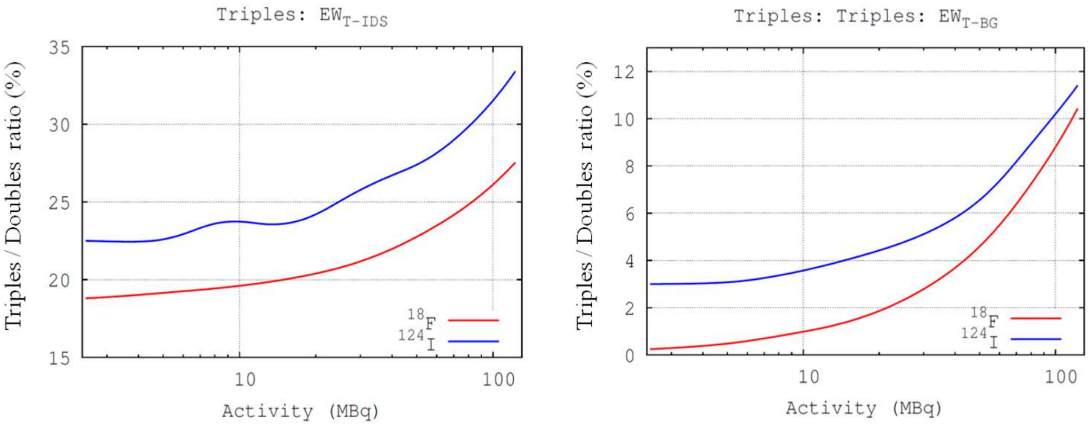

Figure 7.3: Simulated values for the triples / doubles ratio in the EW_{T-IDS} (left) and $EW_{T-\beta\gamma}$ (right) energy windows for triples. Results for ^{18}F (red) and ^{124}I (blue) radionuclides.

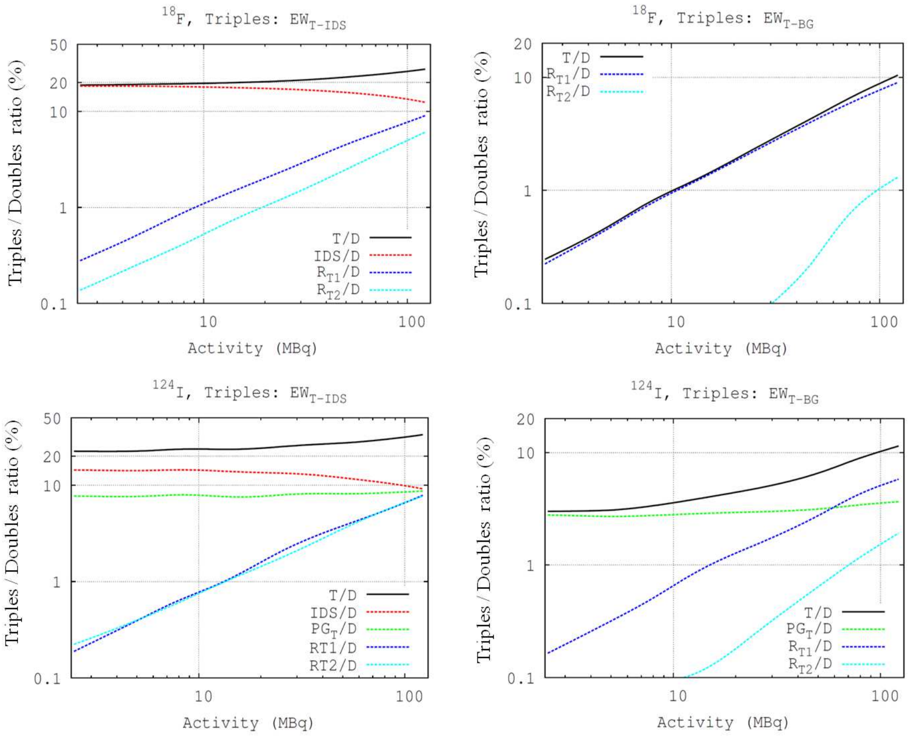

Figure 7.4: Simulated triples to doubles ratio in the Argus scanner for each type of triple coincidence as a function of the activity in the IQ acquisition. Simulated results for ^{18}F (top) and ^{124}I (bottom).

Energy window	**Type of coincidence**	**^{68}Ga**	**^{82}Rb**	**^{94m}Tc**	**^{86}Y**
EW_D	**Doubles (kcps)**	**29.3 ± 1.6**	**29.8 ± 1.7**	**22.3 ± 1.2**	**15.0 ± 0.8**
	Trues (%)	87.4	85.6	76.2	45.6
	Sc (%)	11.5	11.6	11.1	8.0
	$\beta^+\gamma$ (%)	0.2	1.9	11.7	45.2
	R_D (%)	0.9	0.9	0.9	1.2
EW_{T-IDS} (%)	**T / D**	**18.9 ± 1.2**	**19.9 ± 1.4**	**25.1 ± 1.8**	**36 ± 2**
	IDS	18.3 ± 1.1	18.0 ± 1.1	16.0 ± 1.1	12.6 ± 0.9
	$\beta^+\gamma$	0.11 ± 0.02	1.33 ± 0.13	8.4 ± 0.6	22.1 ± 1.5
	R_{T1}	0.34 ± 0.05	0.38 ± 0.06	0.46 ± 0.07	0.60 ± 0.09
	R_{T2}	0.16 ± 0.03	0.20 ± 0.04	0.29 ± 0.05	0.49 ± 0.08
EW_{T-RT} (%)	**T / D**	**0.30 ± 0.05**	**0.56 ± 0.09**	**2.1 ± 0.2**	**5.3 ± 0.5**
	$\beta^+\gamma$	0.036 ± 0.012	0.27 ± 0.04	1.9 ± 0.2	5.0 ± 0.4
	R_{T1}	0.26 ± 0.04	0.29 ± 0.05	0.21 ± 0.04	0.19 ± 0.05
	R_{T2}	<0.01	<0.01	0.023 ± 0.011	0.06 ± 0.02
$EW_{T-\beta\gamma}$ (**^{68}Ga,^{82}Rb,^{94m}Tc**) (%)	**T / D**	**0.06 ± 0.02**	**0.50 ± 0.08**	**3.3 ± 0.3**	**6.4 ± 0.6**
	$\beta^+\gamma$	0.036 ± 0.012	0.43 ± 0.06	3.0 ± 0.3	6.1 ± 0.5
	R_{T1}	0.028 ± 0.010	0.060 ± 0.017	0.16 ± 0.04	0.24 ± 0.05
	R_{T2}	<0.01	<0.01	0.041 ± 0.016	0.10 ± 0.03
$EW_{T-\beta\gamma}$ (**^{86}Y**) (%)	**T / D**	**0.37 ± 0.06**	**1.06 ± 0.14**	**5.4 ± 0.5**	**11.7 ± 0.9**
	$\beta^+\gamma$	0.07 ± 0.02	0.70 ± 0.08	4.9 ± 0.4	11.1 ± 0.8
	R_{T1}	0.30 ± 0.04	0.35 ± 0.05	0.37 ± 0.06	0.43 ± 0.08
	R_{T2}	<0.01	<0.01	0.06 ± 0.02	0.16 ± 0.04

Table 7.6: Statistics of double and triple coincidences in the Argus scanner, for ^{68}Ga, ^{82}Rb, ^{94m}Tc and ^{86}Y radionuclides. The simulated activity was 95 μCi in all cases

7.3.3 Simulation of triple coincidences in clinical scanners

In this section we used our simulator to evaluate the statistics of triple coincidences in two clinical scanners: the Biograph TPTV from Siemens and the Discovery-690, from GE.

In figure 7.5 we depict the simulated energy spectra for double and triple coincidences in the Biograph and Discovery scanners. The radionuclides simulated have been, from left to right and from top to bottom: ^{18}F, ^{82}Rb, ^{124}I and ^{86}Y. These spectra have been scaled to a value of 1 in the photopeak energy (511 keV) for double coincidences. As we can see in the figure, clinical scanners show better energy spectra than the preclinical Argus scanner, with better energy resolution and higher efficiency at large energies.

Table 7.7 shows the ratio of triple / double coincidence events within three different energy windows for triples, in the Biograph TPTV and Discovery-690 scanners. The ratios of triples / doubles for each triples energy window are presented in bold. The results presented in table 7.7 suggest that, for clinical scanners, the number of IDS events is smaller than the value obtained for the preclinical Argus system, due to the bigger size of detectors in clinical scanners. We also see that the influence of prompt gamma emissions in the amount of triple events is much more significant in clinical systems.

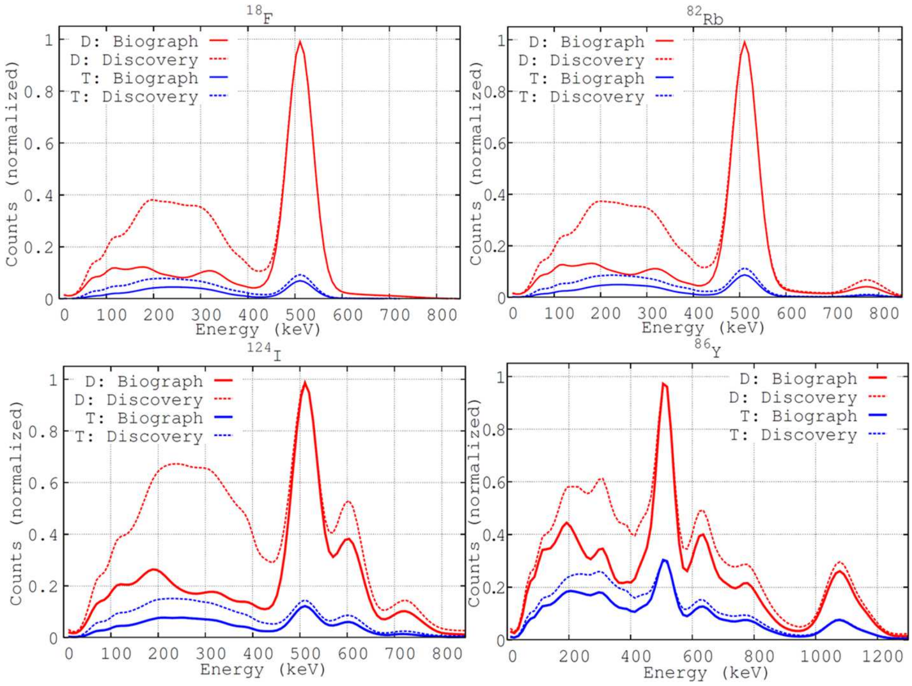

Figure 7.5: Simulated energy spectra for double (red) and triple (blue) coincidences in the Biograph TPTV (solid lines) and the Discovery-690 (dashed lines) clinical scanners.

7.4 Discussion

The feasibility of using triple coincidences in a PET study in an effective way will depend on several factors, like the radionuclide employed (pure or non-pure emitter and abundance of extra-gammas emitted per decay), the geometry and modularity of the scanner where the acquisition is performed (which affect to a large extent the amount of IDS events), the energy window used for the triple coincidences, as well as the amount of activity used in the acquisition (which affect the amount of triple random coincidences detected).

7.4.1 Argus scanner

Regarding the validation of the simulation tool, we can observe good agreement between simulated results and measured data, with deviations from each other smaller than 10%, both for energy spectra (figure 7.2 and table 7.4) and for triple-to-doubles ratios (table 7.5), in most cases. Actually, the agreement is excellent for ^{18}F, ^{22}Na and ^{124}I radionuclides. In the case of ^{76}Br, our simulation results do not fit well the experimental results. Large discrepancies have been found for the energy spectra obtained with this radionuclide. We attribute these discrepancies to the presence of long-life contaminants during the experiments with ^{76}Br. These contaminants would have been created during the production of ^{76}Br, and were not taken into account in our simulations.

		Biograph TPTV / Discovery-690			
E window	**Coinc.**	^{18}**F**	^{82}**Rb**	^{124}**I**	^{86}**Y**
EW_D	**Doubles (kcps)**	**19.6 (1.0) / 17.4 (0.9)**	**18.8 (0.9) / 17.3 (0.9)**	**7.3 (0.4) / 9.1 (0.5)**	**13.7 (0.7) / 23.2 (1.2)**
	Trues (%)	54.1 / 52.5	51.2 / 48.0	30.2 / 19.9	14.7 / 6.9
	Sc (%)	39.6 / 37.8	38.9 / 36.3	28.9 / 22.9	19.5 / 12.3
	$\beta^+\gamma$ (%)	0.0 / 0.0	3.9 / 7.1	34.9 / 51.1	61.7 / 77.8
	R_D (%)	6.3 / 9.7	6.0 / 8.6	6.0 / 6.1	4.1 / 3.0
EW_{T-IDS} **(%)**	**T / D**	**13.8 (0.7) / 21.6 (1.1)**	**17.7 (0.9) / 27.3 (1.4)**	**25.6 (1.4) / 33.1 (1.8)**	**77 (4) / 67 (3)**
	IDS	9.8 (0.5) / 17.1 (0.9)	9.4 (0.5) / 15.6 (0.8)	5.5 (0.4) / 6.5 (0.4)	3.1 (0.2) / 2.26 (0.15)
	$\beta^+\gamma$	<0.01 / <0.01	4.1 (0.3) / 7.2 (0.4)	16.3 (0.9) / 23.4 (1.3)	66 (3) / 61 (3)
	R_{T1}	2.81 (0.19) / 3.8 (0.2)	2.91 (0.19) / 3.8 (0.2)	2.3 (0.2) / 2.6 (0.2)	4.9 (0.3) / 3.9 (0.2)
	R_{T2}	1.19 (0.10) / 0.68 (0.07)	1.34 (0.11) / 0.73 (0.08)	1.58 (0.17) / 0.56 (0.08)	2.8 (0.2) / 0.46 (0.05)
EW_{T-RT} **(%)**	**T / D**	**0.60 (0.06) / 0.42 (0.05)**	**0.91 (0.08) / 0.70 (0.07)**	**2.4 (0.2) / 1.86 (0.17)**	**5.4 (0.3) / 5.0 (0.3)**
	$\beta^+\gamma$	<0.01 / <0.01	0.30 (0.04) / 0.28 (0.04)	1.95 (0.19) / 1.57 (0.15)	4.8 (0.3) / 4.7 (0.3)
	R_{T1}	0.60 (0.06) / 0.41 (0.05)	0.57 (0.06) / 0.40 (0.05)	0.33 (0.06) / 0.27 (0.06)	0.39 (0.06) / 0.31 (0.04)
	R_{T2}	<0.01 / <0.01	<0.01 / <0.01	0.09 (0.04) / 0.014 (0.012)	0.18 (0.04) / 0.041 (0.013)
$EW_{T-\beta\gamma}$ **(%)**	**T / D**	**0.70 (0.07) / 0.45 (0.06)**	**1.72 (0.13) / 1.43 (0.12)**	**4.1 (0.3) / 4.5 (0.3)**	**18.7 (1.0) / 16.4 (0.9)**
	$\beta^+\gamma$	<0.01 / <0.01	0.95 (0.09) / 0.87 (0.08)	3.3 (0.3) / 3.9 (0.3)	16.7 (0.9) / 15.1 (0.8)
	R_{T1}	0.69 (0.07) / 0.44 (0.06)	0.69 (0.07) / 0.53 (0.06)	0.60 (0.10) / 0.57 (0.08)	1.24 (0.11) / 1.11 (0.09)
	R_{T2} / D	<0.01 / <0.01	0.08 (0.02) / 0.026 (0.012)	0.21 (0.06) / 0.05 (0.03)	0.72 (0.08) / 0.13 (0.03)

Table 7.7: Simulated values of double and triple coincidences for ^{18}F, ^{82}Rb, ^{124}I and ^{86}Y radionuclides in the Biograph TPTV and Discovery-690 clinical scanners. The simulated activity was 10 MBq in all cases. The uncertainties for these estimations are shown in brackets.

In table 7.5 we also show the simulated triples-to-doubles ratios for each type of triple coincidence in each EW_T. For example, if we look for IDS coincidences (EW_{T-IDS}), we have to take into account that for non-pure emitters we will have a non-negligible amount of $\beta^+\gamma$ triple events (about 1/3 of the triples within the energy window). Alternatively, if we want to use $\beta^+\gamma$ events to differentiate standard positron emitters from positron-gamma emitters in dual-tracer PET imaging, the optimal energy window for the third single event should lie above 400 keV (lower energy of the EW_D) and it would be advisable to use low activities in the acquisition, in order to avoid R_T events.

In figure 7.4 (left) we can see the triples-to-doubles ratio for each type of triple event within $EW_T - IDS$. For activities below 50 MBq, IDS events dominate. However, if the activity is higher than 50 MBq, R_T triple events become significant, and for activities above 100 MBq, they may be higher than IDS events. Note that for non-pure emitters (^{124}I in the figure), one third of the triple coincidences within EW_{T-IDS} are $\beta^+\gamma$ events. On the right part of figure 7.4 we can see the evolution of triples-to-doubles ratio with the activity for each type of triple event within EW_{T-RT}. In this case, for pure emitters (^{18}F) R_{T1} triple events are predominant at all activities; while for non-pure emitters we have majority of $\beta^+\gamma$ events at low activities (below 50 MBq) and majority of R_{T1} events for high activities (above 60-70 MBq).

Once validated, we used our code to evaluate triple coincidences in different scenarios for the preclinical Argus scanner.

First, we studied the performance of the Argus scanner acquiring triple coincidences for other radionuclides of interest: ^{68}Ga, ^{82}Rb, ^{94m}Tc and ^{86}Y. ^{68}Ga has only 1 % per decay of extra gamma emissions in coincidence with annihilation photons and in practical terms it can be considered as a pure emitter. ^{82}Rb, with 12% of additional gamma emissions per decay, is a non-pure emitter with low ratio of gamma emissions. On the other hand, ^{94m}Tc and ^{86}Y are non-pure emitters with a very high ratio of additional gamma radiation emissions (1 and 5 extra photons per positron emission, respectively). For these radionuclides, we can see (table 7.6) that the proportion of $\beta^+\gamma$ events increases with the amount of additional gamma emissions.

7.4.2 Clinical scanners

Alternatively, we also evaluated the amount and type of triple coincidences that would be recorded by current clinical scanners.

We simulated the energy spectra of these radionuclides for double and triple coincidences in the Biograph TPTV and the Discovery-690 scanners (figure 7.5). As expected from the larger scintillator crystal size in the clinical scanners we found better spectra than in the preclinical scanner (figure 7.5), with better energy resolution and better identification of emission peaks for the gammas emitted in non-pure radionuclides. For example, for ^{82}Rb we can clearly see a gamma emission peak at 775 keV. For ^{124}I, we found two gamma peaks at 603 and 720 keV; and for ^{86}Y one can easily see three gamma peaks, at 620, 775 and 1075 keV respectively. The energy spectra obtained for the Biograph scanner present a higher photopeak to Compton ratio than the ones obtained for the Discovery scanner. This is probably due to the difference in crystal shape and block size between both scanners.

We also see a higher efficiency for high energy events (energy above the photopeak) for the Discovery scanner, due to the crystals are larger in this scanner. As a consequence of this we expect to have a higher amount of $\beta^+\gamma$ triple coincidences in the Discovery scanner.

Table 7.7 present triple coincidences results obtained with our simulation tool, for the Biograph TPTV and Discovery-690 scanners. As in the preclinical scanner, triples-to-doubles ratios are presented for different EW_T. For both scanners, we find a significant amount of triple coincidences. The ratio of triples IDS versus doubles events is around 10% for the Biograph TPTV scanner and 17% for the Discovery-690 scanner. This indicates a large potential for sensitivity increase taking advantage of IDS events ([Lage et al., 2013]).

For these clinical scanners we also found a significant amount of triple coincidences within EW_{T-RT} window (three singles within the energy window for doubles), specially for non-pure emitters (around 2% in ^{124}I and 5% in ^{86}Y for both scanners). As the majority of triple events within this energy window, for non-pure emitters at low activities, are $\beta^+\gamma$ coincidences, we can predict a potential use of these events to separate non-pure and pure emitters in multiple isotope imaging, as it has been described in [Parot et al., 2013]. Additionally, we can improve the triples-to-doubles ratio for $\beta^+\gamma$ events by using an optimal energy window for triple coincidences. As we can see in table 7.7, this ratio might be improved up to 4% in ^{124}I and 15% in ^{86}Y, by using triple coincidences within $EW_{T-\beta\gamma}$: two singles within EW_D and the third single above the lower energy of EW_D.

7.5 Conclusions

The conclusions from this chapter are thus the following:

- Agreement between simulated and real data was very good (discrepancies below 10% in most cases) for most radionuclides, both in the energy spectra and in the triples-to-doubles ratio.
- IDS coincidences constitute a significant contribution in all the situations studied. In the Argus preclinical scanner, these events represent a (measured (simulated)) of 17(19)% for ^{18}F and 24(23)% for ^{124}I. This ratio of IDS events translates into an increase of sensitivity by about the same amount ([Lage et al., 2013]).
- Simulations predict ratios of IDS vs. double coincidences in clinical scanners of about 10% (Biograph TPTV) and 17% (Discovery-690) for pure or almost pure emitters, using the appropriate energy window.
- The ratio between $\beta^+\gamma$ and double coincidences for non-pure emitters depends on the amount of extra gammas emitted. For ^{124}I, this ratio may be up to 2.5% for the Argus scanner and up to 4% for clinical scanners (using the proper energy window). For a radionuclide with higher amount of extra gammas emitted, as ^{86}Y, this ratio may be higher than 10% in clinical scanners (within the proper energy window).
- On the other hand, using EW_{T-RT} for triple coincidences (the three single events should be within the same energy window used for doubles), a potential triples-$\beta^+\gamma$ versus doubles ratio of 2% for ^{124}I might be obtained.
- These results show the benefits of using Monte Carlo simulations with a validated code for evaluating the potential of triple coincidences in different scenarios and cases under study.

Conclusions of this thesis

The main contributions and conclusions of the thesis are summarized in this chapter.

Positron range modeling and correction in PET

In this thesis we used PeneloPET [España et al., 2009] to model positron range for different radionuclides in several biological tissues (chapter 3): $aPSF_{sin}(x)$, $aPSF_{img}(x)$, $g_{3D}(r)$, $g_{2D}(r)$, $G_{3D}(r)$ and $G_{2D}(r)$ distributions for each radionuclide-tissue combination have been determined and PeneloPET estimations have been compared with previous results found in the literature. We also proposed the use of a new framework based on a genetic algorithm that fits the $g_{3D}(r)$ distribution to any other positron range distribution (chapter 3). This study of positron range for several isotopes and materials paved the way the methods for correcting positron range during image reconstruction that have been developed and evaluated in chapter 5: uniform (non-tissue dependent) range correction taken water as reference media; tissue-dependent correction with homogeneous kernel, and finally tissue-dependent and spatially variant correction.

The conclusions of this part of the thesis are:

- Our simulated results were consistent with previous literature, except for the case of [Champion and Le Loirec, 2007], which included Positronium formation in their model. There is currently insufficient experimental data available to disentangle the importance of Positronium formation.
- The approaches proposed in this thesis to correct for positron range in 3D PET image reconstruction improved significantly the quality of the reconstructed images, rendering range corrected images for medium-large range radionuclides practical and useful.
- An efficient algorithm for a realistic tissue-dependent and spatially variant positron range correction kernels was implemented. We have verified that this algorithm, when employed to correct positron range effects during image reconstruction, yields artifact-free and better quality images when several tissues are present within the FOV and there is activity distributed near tissue boundary.

Modeling of prompt-gamma emissions

We have extended (chapter 4) PeneloPET to simulate accurately the decay cascades for the $\beta^+\gamma$ radionuclides studied in this thesis (see table 1.1).

We also studied the image quality of non-conventional radionuclides acquisitions, and the effect of prompt-gamma emissions in the properties of the reconstructed images. We have seen that the additional gamma emissions result in a smooth background in the image, which may be estimated by means of Monte Carlo simulations and introduced into the iterative reconstruction as a background contribution, in a similar way to the scatter counts.

Therefore:

- We have seen that the quantification accuracy of PET images with non-pure emitters is significantly degraded due to the presence of additional gamma emissions, which may be detected in coincidence with an annihilation photon.

- Modeling the background due to prompt-gamma emissions and introducing it in our iterative reconstruction, we have found that the quantitative accuracy of the image may be significantly improved.

Correction of partial volume and spillover effects

In chapter 6 of this thesis, we have discussed the implementation and evaluation of the local projection algorithm (LPA) [Moore et al., 2012] to compensate for partial volume and spillover effects. We use as test-bench the Argus PET/CT scanner [Wang et al., 2006]. We also evaluated the results obtained when the LPA estimations are incorporated into the reconstruction algorithm as a prior.

The above described evaluations have been performed both for pure (^{18}F) and non-pure emitters (^{68}Ga, ^{124}I). Positron range correction and background subtraction were also introduced into the reconstruction procedure, in order to obtain the best possible images for medium and large positron range non-pure emitters studied here (^{68}Ga, ^{124}I).

Simulated phantoms and real acquisitions have been used to study the partial volume and spillover corrections with the methods introduced in this thesis.

The main conclusions that we have obtained can be summarized as follows:

- Quantification was significantly improved by using LPA, providing more accurate ratios of lesion-to-background activity concentration for hot and cold regions, and both for pure and non-pure emitters.

- The use of the activities estimated with the LPA during reconstruction improves the quantification within the volume of interest (VOI), specially for cold regions.

Simulation of triple coincidences

Finally, in chapter 7 of this thesis we have included in our simulation software (PeneloPET [España et al., 2009]) the possibility of triple coincidences. We also have implemented a framework to analyze triple events.

We validated our simulation tool by comparing our simulated estimations against measurements performed in a modified acquisition software on the Argus PET/CT scanner [Wang et al., 2006], capable of acquiring, storing and analyzing triple coincidence events.

Once validated, we have used our simulator to evaluate the feasibility of using triple coincidences in other scenarios for the preclinical Argus scanner [Wang et al., 2006] and for two clinical scanners: the Siemens Biograph TPTV [Jakoby et al., 2009] and the GE Discovery-690 [Bettinardi et al., 2011].

The conclusions for this last part of the thesis are:

- Agreement between simulated and experimental results was very good, with discrepancies below 10% in most cases, both for energy spectra and for triples-to-doubles ratio.
- The simulations were used to determine that inter detector scatter (IDS) events are significant in all the situations studied. In the Argus preclinical scanner, these events represent a (measured (simulated)) of 17(19)% for ^{18}F and 24(23)% for ^{124}I. This ratio of IDS events translates into an increase of sensitivity by about the same amount [Lage et al., 2013]. For clinical scanners these ratios are about 10% (Biograph) and 17% (Discovery).
- The ratio between $\beta^+\gamma$ events and double coincidences for non-pure emitters depends on the amount of extra gammas emitted. For ^{124}I, this ratio may be up to 2.5% for the Argus scanner and up to 4% for clinical scanners (using the proper energy window).

Final conclusion

As a summarizing conclusion, with this thesis we have shown that Monte Carlo simulations may guide the modelling and correction of the main effects which compromise the image quality in PET imaging, including the case of non-conventional radionuclides. The use of this information obtained and/or validated with the help of MC simulations, during image reconstruction, allows to improve the quality of PET images from emitters whose properties are not optimal for PET (large positron range, emission of prompt gammas, etc.).

Bibliography

S. B. Abdul-Fatah, M. Zamburlini, S. G. E. A. Halders, B. Brans, G. J. J. Teule, and G. J. Kemerink. Identification of a Shine-Through Artifact in the Trachea with 124I PET/CT. *J Nucl Med*, 50:909–911, 2009.

D. Abriola and A. A. Sonzogni. Nuclear data sheets for A = 94. *Nuclear Data Sheets*, 107(9): 2423–2578, 2006.

K. M. Abushab. *Simulation and image reconstruction of clinical TOF-PET scanners.* PhD thesis, Universidad Complutense de Madrid, 2013.

K. M. Abushab, J. L. Herraiz, E. Vicente, S. España, J. J. Vaquero, B. W. Jakoby, and J. M. Udías. PeneloPET simulations of the Biograph ToF clinical PET scanner. In *IEEE NSS-MIC Conference Record*, pages 4420–4428, 2011.

S. Agostinelli. GEANT4 - a simulation toolkit. *Nucl. Inst. Meth. in Phys. Res. A*, 506:250–303, 2003.

A. Alessio and P. E. Kinahan. *Nuclear Medicine*, chapter PET image reconstruction. Elsevier, 2006.

A. Alessio and L. MacDonald. Spatially Variant Positron Range Modeling Derived from CT for PET Image Reconstruction. In *IEEE NSS-MIC Conference Record*, pages 2912–2915, 2009.

T. M. Alvarez-Diez, R. deKemp, R. Beanlands, and J. Vincent. Manufacture of strontium-82 / rubidium-82 generators and quality control of rubidium-82 chloride for myocardial perfusion imaging in patients using positron emission tomography. *Applied Radiation and Isotopes*, 50: 1015–1023, 1999.

P. Andreo. Monte Carlo techniques in medical radiation physics. *Phys. Med. Biol.*, 36:861, 1991.

P. Andreo and A. Brahme. Restricted energy-loss straggling and multiple scattering of electrons in mixed Monte Carlo procedures. *Rad. Res.*, 100:16–29, 1984.

A. Andreyev and A. Celler. Dual-isotope PET using positron-gamma emitters. *Phys. Med. Biol.*, 56:4539–4556, 2011.

A. Andreyev, A. Sitek, and A. Celler. EM Reconstruction of Dual Isotope PET with Staggered Injections and Prompt Gamma Positron Emitters. In *IEEE NSS MIC Conf. Record*, pages 4420–4428, 2012.

H. O. Anger. Scintillation Camera and Multiplane Tomographic Scanner. *Kaku Igaku*, 62: 125–148, 1969.

P. Arce, P. Rato, M. Cañadas, and J. I. Lagares. GAMOS: A Geant4-based easy and flexible framework for nuclear medicine applications. In *IEEE NSS-MIC Conference Record*, pages 3162–3168, 2008.

S. Asai, S. Orito, and N. Shinohara. New measurement of the orthopositronium decay rate. *Phys. Lett. B*, 357:475–480, 1995.

R. D. Badawi and P. K. Marsden. Developments in component-based normalization for 3D PET. *Phys. Med. Biol.*, 44:571–594, 1999.

R. D. Badawi, S. G. Kohlmyer, R. L. Harrison, S. D. Vannoy, and T. K. Lewellen. The effect of camera geometry on singles flux, scatter fraction and trues and randoms sensitivity for cylindrical 3D PET: a simulation study. *IEEE Trans. Nucl. Sci.*, 47:1228–1232, 2000.

K. Baete, J. Nuyts, W. Paesschen, P. Suetens, and P. Dupont. Anatomical-based FDG-PET reconstruction for the detection of hypo-metabolic regions in epilepsy. *IEEE Trans. Med. Imag.*, 23:510–519, 2004.

B. Bai, A. Ruangma, R. Laforest, Y. C. Tai, and R. M. Leahy. Positron range modeling for statistical PET image reconstruction. In *IEEE NSS-MIC Conference Record*, pages 2501–2505, 2003.

B. Bai, R. Laforest, A. M. Smith, and R. M. Leahy. Evaluation of MAP image reconstruction with positron range modeling for 3D PET. In *IEEE NSS-MIC Conference Record*, pages 2686–2689, 2005.

D. L. Bailey, J. S. Karp, and S. Surti. *Positron Emission Tomography: Basic Science and Clinical Practice*, chapter Physics and instrumentation in PET. Springer, 2003.

D. L. Bailey, D. Townsend, P. E. Valk, and M. N. Maisey. *Positron emission tomography: basic sciences*. Springer, 2005.

W. C. Barker, L. P. Szajek, S. L. Green, and R. E. Carson. Improved quantification for Tc-94m PET imaging. *IEEE Trans Nucl Sci*, 48(3):739–742, 2001.

J. Baró, J. Sempau, J. M. Fernández-Varea, and F. Salvat. PENELOPE: An algorithm for Monte Carlo simulation of the penetration and energy loss of electrons and positrons in matter. *Nucl. Inst. Meth. in Phys. Res. B*, 100:31–46, 1995.

O. Barret, T. A. Carpenter, J. C. Clark, R. E. Ansorge, and T. D. Fryer. Monte Carlo simulation and scatter correction of the GE Advance PET scanner with SimSET and Geant4. *Phys. Med. Biol.*, 50:4823–4840, 2005.

H. H. Barrett and K. J. Myers. *Foundations of Image Science*. Wiley, 2004.

V. V. Belov, A. A. Bonab, A. J. Fischman, M. Heartlein, P. Calias, and M. I. Papisov. Iodine-124 as a label for pharmacological PET imaging. *Molecular Pharmaceutics*, 8:736–747, 2011.

B. Bendriem and D. Townsend. *The Theory and Practice of 3D PET*. Kluwer Academic Publishers, 1998.

M. Bergström, L. Lu, K. J. Fasth, F. Wui, E. Bergstroem-Pettermann, V. Tolmachev, E. Hedberg, A. Cheng, and B. Langstrom. In vitro and animal validation of bromine-76-bromodeoxyuridine as a proliferation marker. *J. Nucl. Med.*, 39:1273–1279, 1998.

S. Berko and F. L. Hereford. Experimental studies of positron interactions in solids and liquids. *Rev. Mod. Phys.*, 28:299–307, 1956.

V. Bettinardi, E. Pagani, M. C. Gilardi, S. Alenius, K. Thielemans, M. Teras, and F. Fazio. Implementation and evaluation of a 3D one-step late reconstruction algorithm for 3D positron emission tomography brain studies using median root prior. *Eur. J. Nucl. Med. Mol. Imaging*, 29:7–18, 2002.

V. Bettinardi, L. Presotto, E. Rapisarda, M. Pichio, L. Gianolli, and M. C. Gilardi. Physical Performance of the new hybrid PET/CT Discovery-690. *Med. Phys.*, 38(10):5394–5411, 2011.

A. F. Bielajew and W. O. Rogers. *Monte Carlo Transport of Electrons and Photons*, chapter Variance-reduction techniques. Plenum, 1989.

A. F. Bielajew and F. Salvat. Improved electron transport mechanics in the PENELOPE Monte-Carlo model. *Nucl. Inst. Meth. in Phys. Res. B*, 173:332–343, 2001.

J. Biemond, R. Lagendijk, and R. Mersereau. Iterative methods for image deblurring. In *IEEE NSS-MIC Conference Record*, pages 856–883, 1990.

A. Blanco. Positron Range Effects on the Spatial Resolution of RPC-PET. In *IEEE NSS-MIC Conference Record*, pages 2570–2573, 2006.

A. Braem, M. Chamizo-Llatas, E. Chesi, J. G. Correia, F. Garibaldi, C. Joram, S. Mathot, E. Nappi, M. Ribeiro da Silva, F. Schoenahl, J. Séguinot, P. Weilhammer, and H. Zaidi. Feasibility of a novel design of high resolution parallax-free Compton enhanced PET scanner dedicated to brain research. *Phys. Med. Biol.*, 49:2547–2562, 2004.

S. J. Brawley, S. Armitage, J. Beale, D. E. Leslie, A. I. Williams, and G. Laricchia. Electron-like scattering of positronium. *Science*, 330:789, 2010a.

S. J. Brawley, A. I. Williams, M. Shipman, and G. Laricchia. Resonant scattering of positronium in collision with CO2. *Phys. Rev. Lett.*, 105:263401, 2010b.

W. A. P. Breeman and A. M. Verbruggen. The 68Ge/68Ga generator has high potential, but when can we use 68Ga-labelled tracers in clinical routine? *Eur. J. Nucl. Med. Mol. Imaging*, 34:978–981, 2007.

J. F. Briesmeister. *MNCP 4 A Monte Carlo N-Particle Transport System.* Los Alamos, New Mexico: Los Alamos National Laboratory, 1993.

D. E. Burdette, S. Y. Sakurai, T. R. Henry, D. A. Ross, P. B. Penell, K. A. Frey, J. C. Sackellares, and R. L. Albin. Temporal lobe central benzodiazepine binding in unilateral mesial temporal lobe epilepsy. *Neurology*, 45(5):934–941, 1995.

I. Buvat and D. Lazaro. Monte Carlo simulations in emission tomography and GATE: An overview. *Nucl. Instrum. Meths. Phys. Res. A*, 569:323–329, 2006.

C. L. Byme. Likelihood maximization for list-mode emission tomographyc image reconstruction. *IEEE Trans. Med. Imaging*, 20:1084–1092, 2001.

J. Cabello, J. E. Gillam, and M. Rafecas. High Performance 3D PET Reconstruction Using Spherical Basis Functions on a Polar Grid. *International Journal of Biomedical Imaging*, 2012:1–11, 2012.

J. Cal-Gonzalez, J. L. Herraiz, S. España, M. Desco, J. J. Vaquero, and J. M. Udias. Positron range effects in high resolution 3D PET imaging. In *IEEE NSS-MIC Conference Record*, pages 2788–2791, 2009.

J. Cal-González, J. L. Herraiz, S. España, P. M. G. Corzo, M. Desco, J. J. Vaquero, and J. M. Udías. Validation of PeneloPET Positron Range Estimations. In *IEEE NSS-MIC Conference Record*, pages 2396–2399, 2010.

J. Cal-González, J. L. Herraiz, S. España, P. M. G. Corzo, and J. M. Udías. A General Framework to study Positron Range Distributions. In *IEEE NSS-MIC Conference Record*, pages 2733–2737, 2011a.

J. Cal-González, J. L. Herraiz, S. España, E. Vicente, E. Herranz, M. Desco, J. J. Vaquero, and J. M. Udías. Study of CT-based positron range correction in high resolution 3D PET Imaging. *Nucl. Inst. Meth. in Phys. Res. A*, 648:S172–S175, 2011b.

J. Cal-González, J. L. Herraiz, S. España, and J. M. Udias. Scaling of Positron Range Distributions in Biological Materials. In *International Scientific Meeting on Nuclear Physics: La Rábida 2012*, pages 169–171, 2012.

J. Cal-González, J. L. Herraiz, S. España, P. M. G. Corzo, M. Desco, J. J. Vaquero, and J. M. Udías. Positron Range Estimations with PeneloPET. *Phys. Med. Biol.*, 58:5127–5152, 2013a.

J. Cal-González, E. Herranz, E. Vicente, J. M. Udías, S. R. Dave, V. Parot, E. Lage, and J. L. Herraiz. Simulation of Triple Coincidences in PET. In *IEEE NSS MIC Conf. Record*, pages –, 2013b.

J. Cal-González, S. C. Moore, M.-A. Park, J. L. Herraiz, J. J. Vaquero, M. Desco, and J. M. Udías. Projection-Based tissue activity estimation of PET images. presented at: IEEE NSS-MIC 2013, 2013c.

R. E. Carson. A maximum-likelihood method for region-of-interest evaluation in emision tomography. *J. Comput. Assist. Tomogr.*, 10:654–663, 1986.

M. Casey, H. Gadagkar, and D. F. Newport. A component based method for normalisation in volume PET. In *3rd International Meeting on Fully Three-Dimensional Image Reconstruction in Radiology and Nuclear Medicine*, page 67, 1995.

M. E. Casey and R. Nutt. A Multicrystal Two Dimensional BGO Detector System for Positron Emission Tomography. *IEEE Trans. Nuc. Sci.*, 33:460–463, 1986.

K. J. Cassidy, J. L. Bull, M. R. Glucksberg, C. A. Dawson, S. T. Haworth, R. Hirschl, N. Gavriely, and J. B. Grotberg. A rat lung model of instilled liquid transport in the pulmonary airways. *J. Appl. Physiol.*, 90:1955–1967, 2001.

P. Castellaz, A. Siegle, and H. Stoll. Positron age-momentum correlation (AMOC) measurements on organic liquids. *J. Nucl. Radiochem. Sci.*, 3:R1–R7, 2002.

C. Champion and C. Le Loirec. Positron follow-up in liquid water: I. A new Monte Carlo track-sctructure code. *Phys. Med. Biol.*, 51:1707–1723, 2006.

C. Champion and C. Le Loirec. Positron follow-up in liquid water: II. spatial and energetic study for the most important radioisotopes used in PET. *Phys. Med. Biol.*, 52:6605–6625, 2007.

S. R. Cherry, J. A. Sorenson, and M. E. Phelps. *Physics in Nuclear Medicine.* Saunders, 2003.

Z. H. Cho, J. K. Chan, L. Ericksson, M. Singh, S. Graham, N. S. Macdonald, and Y. Yano. Positron Ranges Obtained From Biomedically Important Positron-Emitting Radionuclides. *J. Nucl. Med.*, 16:1174–1176, 1975.

N. L. Christensen, B. E. Hammer, B. G. Heil, and K. Fetterly. Positron emission tomography within a magnetic field using photomultiplier tubes and lightguides. *Phys. Med. Biol.*, 40:691, 1999.

I. F. Ciernik, E. Dizendorf, B. G. Baumert, B. Reiner, C. Burger, and J. B. Davis. Radiation treatment planning with an integrated positron emission and computer tomography (PET/CT): A feasibility study. *International Journal of Radiation Oncology, Biology, Physics*, 57(3):853, 2003.

R. Clackdoyle, F. Noo, J. Guo, and J. A. Roberts. Quantitative Reconstruction From Truncated Projections in Classical Tomography. *IEEE Trans. Nucl. Sci.*, 51:2570–2578, 2004.

J. Clerk-Lamalice, M. Bergeron, C. Thibaudeau, R. Fontaine, and R. Lecomte. Evaluation of Easily Implementable Inter-Crystal Scatter Recovery Schemes in High-Resolution PET Imaging. In *IEEE NSS MIC Conf. Record*, pages 2196–2199, 2012.

B. E. Cooke, A. C. Evans, E. O. Fanthome, R. Alarie, and A. M. Sendyk. Performance figure and images from the Therascan 3128 positron emission tomograph. *IEEE Trans. Nucl. Sci.*, 31:640–644, 1984.

P. M. G. Corzo, J. Cal-González, E. Picado, S. España, J. L. Herraiz, E. Herranz, E. Vicente, J. M. Udías, J. J. Vaquero, A. Muñoz Martin, and L. M. Fraile. Measurement of Activity Produced by Low Energy Proton Beam in Metals Using off-Line PET Imaging. In *IEEE NSS-MIC 2011 Conference Record*, pages 3514–3517, 2011.

H. Daniel. Shapes of Beta-Ray Spectra. *Reviews of Modern Physics*, 40(3):659–672, 1968.

M. E. Daube-Witherspoon and G. Muehllehner. An Iterative Image Space Reconstruction Algorithm Suitable for Volume ECT. *IEEE Trans. Med. Imaging*, 5(2):61–66, 1986.

M. E. Daube-Witherspoon and G. Muehllehner. Treatment of axial data in three-dimensional PET. *J. Nucl. Med.*, 28:1717–1724, 1987.

S. DeBenedetti, C. E. Cowan, W. R. Konneker, and H. Primakoff. On the angular distribution of two-photon annihilation radiation. *Physical Review*, 77:205–212, 1950.

M. Defrise and P. E. Kinahan. *The Theory and Practice of 3D PET*, chapter Data acquisition and image reconstruction for 3D PET. Kluwer Academic Publishers, 1998.

M. Defrise, P. E. Kinahan, D. Townsend, C. Michel, M. Sibomana, and D. F. Newport. Exact and approximate rebinning algorithms for 3D PET data. *IEEE Trans. Med. Imaging*, 16: 145–158, 1997.

M. Defrise, F. Noo, R. Clackdoyle, and H. Kudo. Truncated Hilbert transform and image reconstruction from limited tomographic data. *Inverse Problems*, 22:1037–1052, 2006.

C. Degenhardt, G. Prescher, T. Frach, A. Thon, R. de Gruyter, A. Schmitz, and R. Ballizany. The digital silicon photomultiplier. A novel sensor for the detection of scintillation light. In *IEEE NSS-MIC Conference Record*, pages 2383–2386, 2009.

R. A. deKemp and C. Nahmias. Attenuation correction in PET using single photon transmission measurement. *Med. Phys.*, 21:771–778, 1995.

A. Dempster, N. Laird, and D. Rubin. Maximum likelihood from incomplete data via the EM algorithm. *Journal of the Royal Statistical Society*, 39:1–38, 1977.

S. Derenzo. Measurement of annihilation point spread distribution for medically important positron emitters. In *5th Int. Conf. of Positron Annihilation*, pages 819–823, 1979.

S. E. Derenzo. Mathematical Removal of Positron Range Blurring in High Resolution Tomography. *IEEE Trans. Nucl. Sci.*, 33:565–569, 1986.

S. E. Derenzo, H. Zaklad, and T. F. Budinger. Analytical study of a high resolution positron ring detector system for transaxial reconstruction tomography. *J. Nucl. Med.*, 16(12):1166–1173, 1975.

S. E. Derenzo, W. W. Moses, R. H. Huesman, and F. B. Budinger. PET 93. In *ICS*, page 1030, 1993.

Y. Du, E. C. Frey, W. T. Wang, C. Tocharoenchai, W. H. Baird, and B. M. W. Tsui. Combination of MCNP and SimSET for Monte Carlo simulation of SPECT with medium- and high-energy photons. *IEEE Trans. Nucl. Sci.*, 49:668–674, 2002.

Y. Du, B. M. W. Tsui, and E. C. Frey. Partial volume effect compensation for quantitative brain SPECT imaging. *IEEE Trans. Med. Imag.*, 24:969–976, 2005.

S. Dupont, F. Semah, C. Loch, V. Strijckmans, M. Baulac, and S. Y. In vivo imaging of muscarinic cholinergic receptors in temporal lobe epilepsy with a new PET tracer: [76Br]4-bromodexetimide. *J NuclMed*, 40(6):935–941, 1999.

M. Emanuelsson. Development of an animal in vivo 124I-MicroPET/MicroCAT imaging model of the thyroid. Master's thesis, Lund University, 2006.

K. L. Erdman. The angular correlation of annihilation radiation. *Physical Society*, pages 304–311, 1955.

L. Eriksson, K. Wienhard, and M. Dahlbom. A simple data loss model for positron camera systems. *IEEE Trans. Nucl. Sci.*, 41:1566–1570, 1994.

K. Erlandsson, I. Buvat, H. Pretorius, B. A. Thomas, and B. F. Hutton. A review of partial volume correction techniques for emission tomography and their applications in neurology, cardiology and oncology. *Phys. Med. Biol.*, 57:R119–R159, 2012.

S. España. *Simulaciones avanzadas aplicadas al diseño de escáneres y mejora de la calidad de imagen en tomografía por emisión de positrones.* PhD thesis, Universidad Complutense de Madrid, 2009.

S. España, J. L. Herraiz, E. Vicente, J. J. Vaquero, M. Desco, and J. M. Udías. PeneloPET, a Monte Carlo PET simulation tool based on PENELOPE: features and validation. *Phys. Med. Biol.*, 54:1723–1742, 2009.

S. España, L. M. Fraile, J. L. Herraiz, J. M. Udías, M. Desco, and J. J. Vaquero. Performance evaluation of SiPM photodetectors for PET imaging in the presence of magnetic fields. *Nucl. Inst. Meth. in Phys. Res. A*, 613:308–316, 2010.

R. D. Evans. *The Atomic Nucleus.* McGraw-Hill, 1972.

F. H. Fahey. Data acquisition in PET imaging. *J. Nucl. Med. Technol.*, 30:39–49, 2002.

E. Fermi. Versuch einer Theorie der β-Strahlen. I. *Z. Physik*, 88:161–177, 1934.

C. Fernández-Ramirez, E. Moya de Guerra, A. Udías, and J. M. Udías. Properties of nucleon resonances by means of a genetic algorithm. *Physical Review C*, 77:065212, 2008.

J. M. Fernández-Varea, R. Mayol, J. Baró, and F. Salvat. On the theory and simulation of multiple elastic scattering of electrons. *Nucl. Inst. Meth. in Phys. Res. B*, 73:447–473, 1993.

L. Fu and J. Qi. A residual correction method for high-resolution PET reconstruction with application to on-the-fly Monte Carlo based model of positron range. *Med. Phys.*, 37:704–714, 2010.

O. Gardelle, U. Roelcke, P. Vontobel, N. E. A. Crompton, I. Guenther, P. Blauenstein, A. P. Schubiger, H. Blattmann, J. E. Ryser, K. L. Leenders, and B. Kaser-Hotz. [Br-76]bromodeoxyuridine PET in tumor-bearing animals. *Nuclear Medicine and Biology*, 28(1): 51–57, 2001.

J. E. Gillam, P. Solevi, J. F. Oliver, and M. Rafecas. Inclusion of inter crystal scatter data in PET. In *9th IEEE International Symposium on Biomedical Imaging (ISBI)*, pages 62–65, 2012.

A. L. Goertzen, J. Y. Suk, and C. J. Thompson. Imaging of weak-source distributions in LSO-based small-animal PET scanners. *J Nucl Med.*, 48(10):1692–8, 2007.

A. L. Goertzen, Q. Bao, M. Bergeron, E. Blankemeyer, S. Blinder, M. Cañadas, A. F. Chatziioannou, K. Dinelle, E. Elhami, H.-S. Jans, E. Lage, R. Lecomte, V. Sossi, S. Surti, Y.-C. Tai, J. J. Vaquero, E. Vicente, D. A. Williams, and R. Laforest. NEMA NU 4-2008 Comparison of Preclinical PET Imaging Systems. *J. Nucl. Med.*, 53(8):1–10, 2012.

N. B. Gove and M. J. Martin. Log-f tables for beta decay. *Nuclear Data Tables*, 10:205, 1971.

P. J. Green. Bayesian reconstructions from emission tomography data using a modified EM algorithm. *IEEE Trans. Med. Imaging*, 9:84–93, 1990.

W. Gropp, E. Lusk, and A. Skjellum. Using MPI: portable parallel programming with the message-passing interface. Technical report, MIT Press, 1999.

Y. Gu, G. Pratx, F. W. Y. Lau, and C. S. Levin. Effects of multiple-interaction photon events in a high-resolution PET system that uses 3-D positioning detectors. *Med Phys*, 37:5494–5508, 2010.

P. Guerra, W. Gonzalez, M. J. Ledesma-Carbayo, J. Cal-González, E. Herranz, J. M. Udías, A. Lallena, and A. Santos. Monte Carlo Based Dose Estimation in Intraoperative Radiotherapy. In *IEEE NSS-MIC Conference Record*, pages 3069–3072, 2010.

S. F. Haber, S. E. Derenzo, and D. Uber. Application of mathematical removal of positron range blurring in positron emission tomography. *IEEE Trans. Nucl. Sci.*, 37:1293–1299, 1990.

M. D. Harpen. Positronium: Review of symmetry, conserved quantities and decay for the radiological physicist. *Med. Phys.*, 31(1):57–61, 2004.

R. L. Harrison, S. D. Vannoy, D. R. Haynor, S. B. Gillispie, M. S. Kaplan, and T. K. Lewellen. Preliminary Experience With The Photon History Generator Module Of A Public domain Simulation System For Emission Tomography. In *IEEE NSS-MIC Conference Record*, pages 1154–1158, 1993.

R. L. Harrison, M. S. Kaplan, S. D. Vannoy, and T. K. Lewellen. Positron range and coincidence non-collinearity in SimSET. In *IEEE NSS-MIC Conference Record*, pages 1265–1268, 1999.

R. A. Hawkins, Y. Choi, S.-C. Huang, C. K. Hoh, M. Dahlbom, C. Schiepers, N. Satyamurthy, J. R. Barrio, and M. E. Phelps. Evaluation of the Skeletal Kinetics of Fluorine-18-Fluoride Ion with PET. *J. Nucl. Med.*, 33(5):633–642, 1992.

P. Hellman, H. Ahlstrom, M. Bergstrom, A. Sundin, B. Langstrom, G. Weterberg, and C. Julin. Positron emission tomography with ^{11}C-methionine in hyperparathyroidism. *Surgery*, 116(6): 974–981, 1994.

R. E. Henkin, D. Bova, G. L. Dillehay, and S. M. Karesh. *Nuclear Medicine.* Elsevier Health Sciences, 2006.

G. T. Herman. *Image reconstruction from projections.* Academic Press, 1980.

J. L. Herraiz. Técnicas avanzadas de reconstrucción de imagen nuclear PET, X-CT y SPECT. Master's thesis, Universidad Complutense de Madrid, 2008.

J. L. Herraiz, S. España, J. J. Vaquero, M. Desco, and J. M. Udías. FIRST: Fast Iterative Reconstruction Software for (PET) tomography. *Phys. Med. Biol.*, 51:4547–4565, 2006.

J. L. Herraiz, S. España, E. Vicente, J. J. Vaquero, M. Desco, and J. M. Udias. Noise and physical limits to maximum resolution of PET images. *Nucl. Inst. Meth. in Phys. Res. A*, 580: 934–937, 2007.

J. L. Herraiz, S. España, R. Cabido, A. S. Montemayor, M. Desco, J. J. Vaquero, and J. M. Udías. GPU-Based Fast Iterative Reconstruction of Fully 3-D PET Sinograms. *IEEE Trans. Nucl. Sci.*, 58:2257–2263, 2011a.

J. L. Herraiz, S. España, J. Cal-González, J. J. Vaquero, M. Desco, and J. M. Udías. Fully 3D GPU PET reconstruction. *Nucl. Instrum. Meths. Phys. Res. A*, 648:S169–S171, 2011b.

E. Herranz, J. L. Herraiz, J. Cal-González, P. M. G. Corzo, P. Guerra, and J. M. Udias. Iterative Reconstruction of Whole Accelerator Phase Spaces for Intraoperative Radiation Therapy (IORT). In *IEEE NSS-MIC 2011 Conference Record*, pages 2644–2646, 2011.

E. Herranz, J. L. Herraiz, P. Guerra, J. Cal-González, M. Perez-Liva, R. Rodriguez, C. Illana, M. Ledesma, J. Calama, and J. M. Udías. Iterative Determination of Clinical Beam Phase Space From Dose Measurements. *International Journal of Radiation Oncology * Biology * Physics*, 84(3):S869, 2012a.

E. Herranz, J. L. Herraiz, P. Ibáñez, M. Pérez-Liva, R. Puebla, J. Cal-González, P. Guerra, R. Rodriguez, C. Illana, and J. M. Udias. Phase space determination of electron beam for intraoperative radiation therapy from measured dose data. presented at: Third European Workshop on Monte Carlo Treatment Planning (EW-MCTP), 2012b.

E. Herranz, J. L. Herraiz, P. Ibáñez, M. Pérez-Liva, R. Puebla, J. Cal-González, P. Guerra, R. Rodriguez, C. Illana, and J. M. Udías. Phase space determination from measured dose data for intraoperative electron radiation therapy. Submitted to: Phys. Med. Biol. (Dec 2013), 2013.

P. Herrero, J. Markham, M. E. Shelton, and S. R. Bergmann. Implementation and evaluation of a two-compartment model for quantification of myocardial perfusion with rubidium-82 and positron emission tomography. *Circ Res*, pages 496–507, 1992.

H. Herzog, F. Rosch, G. Stocklin, C. Lueders, S. M. Qaim, and L. E. Feinendegen. Measurement of pharmacokinetics of yttrium-86 radiopharmaceuticals with PET and radiation dose calculation of analogous yttrium-90 radiotherapeutics. *J Nucl Med*, 34(12):2222–2226, 1993.

H. Herzog, L. Tellmann, S. M. Qaim, S. Spellerberg, A. Schmid, and H. H. Coenen. PET quantitation and imaging of the non-pure positron emitting iodine isotope I-124. *Appl Radiat Isot*, 56(5):673–679, 2002.

H. Herzog, H. Iida, C. Weirich, L. Tellmann, J. Kaffanke, S. Spellerberg, L. Caldeira, E. R. Kops, and N. J. Shah. Influence from high and ultra-high magnetic field on positron range measured with a 9.4T MR-BrainPET. In *IEEE NSS-MIC Conference Record*, pages 3410–3413, 2010.

J. Hoffend, W. Mier, J. Schuhmacher, K. Schmidt, A. Dimitrakopoulou-Strauss, L. G. Strauss, M. Eisenhut, R. Kinscherf, and U. Haberkorn. Gallium-68-DOTA-Albumin as a PET Blood-Pool Marker: Experimental Evaluation in vivo. *Nucl. Med. Biol.*, 32:287–292, 2005.

E. J. Hoffman, M. E. Phelps, N. A. Mullani, S. C. Higgins, and M. M. Ter-Pogossian. Design and performance characteristics of a whole-body positron transaxial tomograph. *J. Nucl. Med.*, 17:493–502, 1976.

E. J. Hoffman, S. C. Huang, and E. Phelps. Quantitation in positron emission computed tomography, 1: Effect of object size. *J. Comput. Assist. Tomogr.*, 3:299–308, 1979.

E. J. Hoffman, M. E. Phelps, and S. C. Huang. Performance evaluation of a positron tomograph designed for brain imaging. *J. Nucl. Med.*, 24:245–257, 1983.

E. J. Hoffman, R. M. Guerrero, G. Germano, W. M. Digby, and M. Dahlbom. PET system calibrations and corrections for quantitative and spatially accurate images. *IEEE Trans. Nucl. Sci.*, 36:1108–1112, 1989.

C. K. Hoh. Clinical use of FDG PET. *Nuclear Medicine and Biology*, 34:737–742, 2007.

I. K. Hong, S. T. Chung, H. K. Kim, Y. B. Kim, Y. D. Son, and Z. H. Cho. Ultra Fast Symmetry and SIMD-Based Projection-Backprojection (SSP) Algorithm for 3-D PET Image Reconstruction. *IEEE Trans. Med. Imaging*, 26:789–803, 2007.

S.-C. Huang, C. S. Hoffman, M. E. Phelps, and D. E. Kuhl. Quantitation in positron emission computed-tomography: 2. effects if inaccurate attenuation correction. *J. Comput. Assit.Tomogr.*, 3:804–814, 1979.

S.-C. Huang, R. E. Carson, E. J. Hoffman, J. Carson, N. MacDonald, J. R. Barrio, and M. E. Phelps. Quantitative measurement of local cerebral blood flow in humans by positron emission tomography and ^{15}O-water. *J. Cereb. Blood Flow Metabol.*, 3(2):141–153, 1983.

H. M. Hudson and R. S. Larkin. Accelerated image reconstruction using ordered subsets of projection data. *IEEE Trans. Med. Imaging*, 13:601–609, 1994.

B. F. Hutton and Y. H. Lau. Application of distance-dependent resolution compensation and post-reconstruction filtering for myocardial SPECT. *Phys. Med. Biol.*, 43:1679–1993, 1998.

ICRP. Report of the Task Group on Reference Man. ICRP Publication 23, 1975.

ICRU. Tissue Substitutes in Radiation Dosimetry and Measurement. ICRU Report 44, 1989.

A. A. Isola, A. Ziegler, T. Koehler, W. J. Niessen, and M. Grass. Motion-compensated iterative cone-beam CT image reconstruction with adapted blobs as basis functions. *Phys. Med. Biol.*, 53:6777–6797, 2008.

A. H. Jacobs, A. Winkler, M. G. Castro, and P. Lowenstein. Human gene therapy and imaging in neurological diseases. *Eur J Nucl Med Mol Imaging*, 32:S358–S383, 2005.

B. W. Jakoby, M. Y. Bercier, C. C. Watson, B. Bendriem, and D. W. Townsend. Performance characteristics of a new LSO PET/CT scanner with extended axial field of view and PSF reconstruction. *IEEE Trans. Nucl. Sci.*, 56:633–639, 2009.

F. James. Monte Carlo theory and practice. *Rep. Prog. Phys.*, 43:1145–1189, 1980.

S. Jan, G. Santin, D. Strul, S. Staelens, K. Assié, D. Autret, and S. Avner. GATE: a simulation toolkit for PET and SPECT. *Phys. Med. Biol.*, 49:4543–4561, 2004.

L. Jødal, C. Le Loirec, and C. Champion. Positron range in PET imaging: an alternative approach for assessing and correcting the blurring. *Phys. Med. Biol.*, 57:3931–3943, 2012.

C. A. Johnson and A. Sofer. In *7th Symp. on the Frontiers of Massively Parallel Computation (Los Alamitos, CA: IEEE Computer Society Press)*, pages 126–137, 1999.

C. A. Johnson, J. Seidel, R. E. Carson, W. R. Gandler, A. Sofer, M. V. Green, and M. E. Daube-Witherspoon. Evaluation of 3D reconstruction algorithms for a small animal PET camera. *IEEE Trans. Nucl. Sci.*, 44:1303–1308, 1997.

M. D. Jones and R. Yao. Parallel programming for OSEM reconstruction with MPI, OpenMP, and hybrid MPI-OpenMP. In *IEEE NSS-MIC Conference Record*, pages 3036–3042, 2004.

J. Joung, R. S. Miyaoka, and T. K. Lewellen. cMiCE: a high resolution animal PET using continuous LSO with a statistics based positioning scheme. In *IEEE NSS-MIC Conference Record*, pages 1137–1141, 2001.

M. S. Judenhofer, H. F. Wehrl, et al. Simultaneous PET-MRI: A new approach for functional and morphological imaging. *Nature Medicine*, 14:459–465, 2008.

D. J. Kadrmas. LOR-OSEM: statistical PET reconstruction from raw line-of-response histograms. *Phys. Med. Biol.*, 49:4731–4744, 2004.

A. C. Kak and M. Slaney. *Principles of Computerized Tomographic Imaging.* Society for Industrial Mathematics, 1988.

M. H. Kalos and P. A. Whitlock. *Monte Carlo Methods, vol. 1.* Wiley, 1986.

Y. Kanai, N. Takahashi, T. Watabe, H. Watabe, S. Yamamoto, E. Shimosegawa, A. Shinohara, K. Nakai, and J. Hatazawa. Rat thyroid gland imaging with 124I using semiconductor PET scanner and PET-MR. *J. Nucl. Med.*, 53 (Supplement 1):1221, 2012.

I. Kanno, A. A. Lammertsma, J. D. Heather, J. M. Gibbs, C. G. Rhodes, J. C. Clark, and T. Jones. Measurements of cerebral blood flow using bolus inhalation of $C_{15}O_2$ and positron emission tomography: description of the method and comparison with $C_{15}O_2$ continuous inhalation method. *J. Cereb. Blood Flow Metabol.*, 4(2):224–234, 1984.

J. S. Karp, G. Muehllehner, H. Qu, and X. H. Yan. Singles transmission in volume-imaging PET with a 137Cs source. *Phys. Med. Biol.*, 40:929–944, 1995.

J. Katakura and Z. D. Wu. Nuclear data sheets for A = 124. *Nuclear Data Sheets*, 109(7): 1655–1877, 2008.

L. Katz and A. S. Penfold. Range-energy relations for electrons and the determination of beta-ray end-point energies by absorption. *Rev. Mod. Phys.*, 24:28–44, 1952.

P. E. Kinahan and J. G. Rogers. Analytic 3D image reconstruction using all detected events. *IEEE Trans. Nucl. Sci.*, 36:964–968, 1989.

P. E. Kinahan, D. W. Townsend, T. Beyer, and D. Sashin. Attenuation correction for a combined 3D PET/CT scanner. *Med. Phys.*, 25:2046–2053, 1998.

G. F. Knoll. *Radiation Detection and Measurements.* Wiley, 2000.

L. Koehler, K. Gagnon, S. McQuarrie, and F. Wuest. Iodine-124: A Promising Positron Emitter for Organic PET Chemistry. *Molecules*, 15:2686–2718, 2010.

W. J. Koh, K. S. Bergman, J. S. Rasey, L. M. Peterson, M. L. Evans, M. M. Graham, J. R. Grierson, K. L. Lindsley, T. K. Lewellen, K. A. Krohn, and T. W. Griffin. Evaluation of oxygenation status during fractionated radiotherapy in human non-small cell cancers using 18F-Fluoromisonidazole positron emission tomography. *Int. J. Radiat. Oncol. Biol. Phys.*, 33(2):391–398, 1995.

K. S. Krane. *Introductory Nuclear Physics.* Wiley, 1987.

R. Kraus, G. Delso, and S. I. Ziegler. Simulation Study of Tissue-Specific Positron Range Correction for the New Biograph mMR Whole-Body PET/MR System. *IEEE Trans. Nucl. Sci.*, 59:1900–1909, 2012.

W. G. Kuhle, G. Porenta, S. C. Huang, D. Buxton, S. S. Gambhir, H. Hansen, M. E. Phelps, and H. R. Schelbert. Quantification of regional myocardial blood flow using ^{13}N ammonia and reoriented dynamic positron emission tomographic imaging. *Circulation*, 86(3):1004–1017, 1992.

R. Laforest and X. Liu. Image quality with non-standard nuclides in PET. *Q J Nucl Med Mol Imaging*, 52:151–158, 2008.

R. Laforest, D. J. Rowland, and M. J. Welch. MicroPET imaging with non-conventional isotopes. *IEEE Trans Nucl Sci*, 49(5):2119–2126, 2002.

E. Lage, V. Parot, S. R. Dave, J. M. Udias, S. C. Moore, A. Sitek, M.-A. Park, J. J. Vaquero, and J. L. Herraiz. Recovery of multi-interaction photon events to improve the performance of PET scanners. presented at: IEEE NSS-MIC 2013, 2013.

D. Lazaro, I. Buvat, G. Loudos, D. Strul, G. Santin, N. Giokaris, and D. Donnarieix. Validation of the GATE Monte Carlo simulation platform for modelling a CsI(Tl) scintillation camera dedicated to small-animal imaging. *Phys. Med. Biol.*, 49:271–285, 2004.

C. Le Loirec and C. Champion. Track structure simulation for positron emitters of medical interest. Part I: The case of the allowed decay isotopes. *Nucl. Inst. Meth. in Phys. Res. A*, 582:644–653, 2007a.

C. Le Loirec and C. Champion. Track structure simulation for positron emitters of physical interest. Part II: The case of the radiometals. *Nucl. Inst. Meth. in Phys. Res. A*, 582:654–664, 2007b.

C. Le Loirec and C. Champion. Track structure simulation for positron emitters of physical interest. Part III: The case of the non-standard radionuclides. *Nucl. Inst. Meth. in Phys. Res. A*, 582:665–672, 2007c.

R. Leahy and J. Qi. Statistical Approaches in Quantitative PET. In *Statistics and Computing*, 2000.

R. Lecomte. Novel detector technology for clinical PET. *Eur J. Nucl. Med. Mol. Imaging*, 36: S69–S85, 2009.

R. Lecomte, D. Schmitt, A. W. Lightstone, and R. J. McIntyre. Performance characteristics of BGO-silicon avalanche photodiode detectors for PET. *IEEE Trans. Nucl. Sci.*, 32(1):482–486, 1985.

K. Lee, P. E. Kinahan, R. S. Miyaoka, J.-S. Kim, and T. K. Lewellen. Impact of system design parameters on image figures of merit for a mouse PET scanner. *IEEE Trans. Nucl. Sci.*, 51(1): 27–33, 2004.

W. Lehnert, M. C. Gregoire, A. Reilhac, and S. R. Meikle. Analytical positron range modelling in heterogeneous media for PET Monte Carlo simulation. *Phys. Med. Biol.*, 56:3313–3335, 2011.

C. W. Lerche, J. M. Benlloch, F. Sanchez, N. Pavon, B. Escat, E. N. Gimenez, M. Fernandez, I. Torres, M. Gimenez, A. Sebastia, and J. Martinez. Depth of γ-ray interaction within continuous crystals from the width of its scintillation light-distribution. *IEEE Trans. Nuc. Sci.*, 52:560–572, 2005.

T. K. Levellen. Recent developments in PET detector technology. *Phys. Med. Biol.*, 53:R287–R317, 2008.

C. S. Levin. New Imaging Technologies to Enhance the Molecular Sensitivity of Positron Emission Tomography. *Proceedings of the IEEE*, 96:439–467, 2008.

C. S. Levin and E. J. Hoffman. Calculation of positron range and its effect on the fundamental limit of positron emission tomography system spatial resolution. *Phys. Med. Biol.*, 44:781–799, 1999.

C. S. Levin, A. M. K. Foudray, and F. Habte. Impact of high energy resolution detectors on the performance of a PET system dedicated to breast cancer imaging. *Physica Medica*, 21:28–34, 2006.

T. K. Lewellen, C. M. Laymon, R. S. Miyaoka, L. Ki Sung, and P. E. Kinahan. Design of a Firewire based data acquisition system for use in animal PET scanners. In *IEEE NSS-MIC Conference Record*, pages 1974–1978, 2001.

R. M. Lewitt and S. Matej. Overview of methods for image reconstruction from projections in emission computed tomography. In *Proceedings IEEE*, pages 1588–1611, 2003.

R. M. Lewitt, G. Muehllehner, and J. S. Karpt. Three-dimensional image reconstruction for PET by multi-slice rebinning and axial image filtering. *Phys. Med. Biol.*, 39:321–339, 1994.

A. Lilja and K. Bergstrom. Dynamic study of supratentorial gliomas with methyl-11C-L-methionine and positron emission tomography. *A J N R*, 6:605–614, 1985.

H. Lin, K. Chuang, S. Chen, C. Chiang, C. Lin, and M. Jan. Recycling of triple coincidences for non-pure positron emitters in microPET imaging. *Eur J Nucl Med Mol Imaging*, 39:S155–S303, 2012.

J. S. Liow and S. C. Strother. Practical trade-offs between noise, resolution, quantitation and number of iterations for maximum likelihood reconstructions. *IEEE Trans. Med. Imaging*, 10: 563–567, 1991.

X. Liu and R. Laforest. Quantitative small animal PET imaging with non-conventional nuclides. *Nuclear Medicine and Biology*, 36:551–559, 2009.

M. Ljungberg, S.-E. Strand, and M. A. King. *Monte Carlo Calculations in Nuclear Medicine.* IOP, 1998.

A. Lövqvist, A. Sundin, A. Roberto, H. Ahlström, J. Carlsson, and H. Lundqvist. Comparative PET imaging of experimental tumors with bromine-76-labeled antibodies, fluorine-18-fluorodeoxyglucose, and carbon-11-methionine. *J Nucl Med*, 38:1029–1035, 1997.

A. Lövqvist, H. Lundqvist, M. Lubberink, V. Tolmachev, J. Carlsson, and A. Sundin. Kinetics of [76]Br-labeled anti-CEA antibodies in pigs; aspects of dosimetry and PET imaging properties. *Med Phys*, 26(2):249–258, 1999.

A. Lövqvist, J. L. Humm, A. Sheikh, R. D. Finn, J. Koziorowski, S. Ruan, K. S. Pentlow, A. Jungbluth, S. Welt, F. T. Lee, M. W. Brechbiel, and S. M. Larson. PET imaging of (86)Y-labeled anti-Lewis Y monoclonal antibodies in a nude mouse model: comparison between (86)Y and (111)In radiolabels. *J Nucl Med.*, 42(8):1281–1287, 2001.

M. Lubberink and H. Herzog. Quantitative imaging of ^{124}I and ^{86}Y with PET. *Eur J Nucl Med Mol Imaging*, 38(Suppl 1):S10–S18, 2011.

M. Lubberink, H. Schneider, M. Bergstromm, and H. Lundqvist. Quantitative imaging and correction for cascade gamma radiation of 76Br with 2D and 3D PET. *Phys Med Biol*, 47(19): 3519, 2002.

M. MacManus, U. Nestle, K. E. Rosenzweig, I. Carrio, C. Messa, O. Belohlavek, M. Danna, T. Inoue, E. Deniaud-Alexandre, S. Schipani, N. Watanabe, M. Dondi, and B. Jeremic. Use of PET and PET/CT for radiation therapy planning: Iaea expert report 2006-2007. *Radiother. Oncol.*, 91:85–94, 2009.

B. A. Mair, R. B. Carrol, and J. M. M. Anderson. Filter banks and the EM algorithm. In *IEEE NSS-MIC Conference Record*, pages 2–9, 1996.

R. C. Marshall, J. H. Tillisch, M. E. Phelps, S.-C. Huang, R. Carson, E. Henze, and H. R. Schelbert. Identification and differentiation of resting myocardial ischemia and infarction in man with positron computed tomography, 18F-labelled fluorodeoxyglucose and N-13 ammonia. *Circulation*, 67(4):766–778, 1983.

S. Matej and R. M. Lewitt. Practical considerations for 3-D image reconstruction using spherically symmetric volume elements. *IEEE Trans. Med. Imaging*, 15:68–78, 1996.

B. M. Mazoyer, M. S. Roos, and R. H. Huesman. Dead time correction and counting statistics for positron tomography. *Phys. Med. Biol.*, 30:385–399, 1985.

C. L. Melcher. Scintillation crystals for PET. *J. Nucl. Med.*, 41:1051–1055, 2000.

MICAD. Molecular imaging and contrast agent database. http://www.ncbi.nlm.nih.gov/books/NBK5330/, 2013.

C. Michel, M. Schmand, X. Liu, M. Sibomana, S. Vollmar, C. Knoss, M. Lercher, C. Watson, D. Newport, M. Casey, M. Defrise, K. Wienhard, and W. D. Heiss. Reconstruction strategies for the HRRT. In *IEEE NSS-MIC Conference Record*, volume 2, pages 15/207–15/212 vol.2, 2000.

S. C. Moore, S. Southekal, S. J. McQuaid, M. F. Kijewski, and S. P. Mueller. Improved regional activity quantitation in nuclear medicine using a new approach to correct for tissue partial volume and crosstalk effects. *IEEE Trans. Med. Imag.*, 31:405–416, 2012.

W. W. Moses. Time of Flight in PET Revisited. *IEEE Trans. Nucl. Sci.*, 50:1325–1330, 2003.

A. Muñoz, J. M. Pérez, G. García, and F. Blanco. An approach to Monte Carlo simulation of low-energy electron and photon interactions in air. *Nucl. Inst. Meth. in Phys. Res. A*, 536: 176–189, 2005.

H. Murayama, H. Ishibashi, and T. Omura. Depth encoding multicrystal detectors for PET. *IEEE Trans. Nucl. Sci.*, 45:1152–1157, 1998.

C. Nanni, L. Fantini, S. Nicolini, and S. Fanti. Non FDG PET. *Clinical Radiology*, 65:536–548, 2010.

F. Natterer and F. Wübbeling. *Mathematical Methods in Image Reconstruction.* SIAM, 2001.

NEMA-NU-2. Performance Measurements of Positron Emission Tomographs. Technical report, National Electrical Manufacturers Association, 2007.

NEMA-NU-4. Performance Measurements for Small Animal Positron Emission Tomographs. Technical report, National Electrical Manufacturers Association, 2008.

NIST. Photon cross section database. http://physics.nist.gov/PhysRefData/Xcom/Text/, 2012.

NNDC. National nuclear data center. http://www.nndc.bnl.gov/, 2011.

NVIDIA. CUDA Programming Guide v.2.5.0 (Online). http://developer.nvidia.com/object/gpu_programming_guide.html, 2010.

B. Olaizola, L. M. Fraile, H. Mach, A. Aprahamian, J. A. Briz, J. Cal-González, D. Ghita, U. Koster, W. Kurcewicz, S. R. Lesher, D. Pauwels, E. Picado, A. Poves, D. Radulov, G. S. Simpson, and J. M. Udías. β^- decay of ^{65}Mn to ^{65}Fe. *Physical Review C*, 88:044306, 2013.

J. F. Oliver and M. Rafecas. Revisiting the singles rate method for modeling accidental coincidences in PET. In *IEEE NSS-MIC Conference Record*, pages 4288–4291, 2008.

J. M. Ollinger and J. A. Fessler. Positron-emission tomography. *Signal Processing Magazine*, 14: 43–55, 1997.

M. R. Palmer and G. L. Brownell. Annihilation density distribution calculations for medically important positron emitters. *IEEE Trans. Med. Imaging*, 11:373–378, 1992.

M. R. Palmer, X. Zhu, and J. A. Parker. Modeling and Simulation of Positron Range Effects for High Resolution PET Imaging. *IEEE Trans. Nucl. Sci.*, 52:1391–1395, 2005.

V. Panettieri, B. Wennberg, G. Gagliardi, M. A. Duch, M. Ginjaume, and I. Lax. SBRT of lung tumours: Monte Carlo simulation with PENELOPE of dose distributions including respiratory motion and comparison with different treatment planning systems. *Phys. Med. Biol.*, 52:4265–4281, 2007.

V. Y. Panin, F. Kehren, C. Michel, and M. Casey. Fully 3D PET reconstruction with system matrix derived from point source measurements. *IEEE Trans. Med. Imaging*, 25(7):907–921, 2006.

V. Parot, J. L. Herraiz, S. R. Dave, J. M. Udias, S. C. Moore, M.-A. Park, J. J. Vaquero, and E. Lage. A new approach for multiplexed PET imaging. presented at: IEEE NSS-MIC 2013, 2013.

L. Parra and H. H. Barrett. List-mode likelihood: EM algorithm and image quality estimation demonstrated on 2D PET. *IEEE Trans. Med. Imaging*, 17:228–235, 1998.

M. Partridge, A. Spinelli, W. Ryder, and C. Hindorf. The effect of β^+ energy on performance of a small animal PET camera. *Nucl. Inst. Meth. in Phys. Res. A*, 568:933–936, 2006.

A. P. Patro and P. Sen. Parapositronium lifetime. *J.Phys. A: Gen. Phys.*, 4:856–858, 1971.

H. Peng. *Investigation of new approaches to combined positron emission tomography and magnetic resonance imaging systems.* PhD thesis, University of Western Ontario, 2006.

K. S. Pentlow, M. C. Graham, R. M. Lambrecht, N. K. V. Cheung, and S. M. Larson. Quantitative imaging of I-124 using positron emission tomography with applications to radioimmunodiagnosis and radioimmunotherapy. *Med Phys*, 18(3):357–366, 1991.

M. E. Phelps, E. J. Hoffman, and S. Huang. Effects of Positron Range on Spatial Resolution. *J. Nucl. Med.*, 16:649–652, 1975.

B. J. Pichler, B. K. Swann, J. Rochelle, R. E. Nutt, S. R. Cherry, and S. B. Siegel. Lutetium oxyorthosilicate block detector readout by avalanche photodiode arrays for high resolution animal PET. *Phys. Med. Biol.*, 49:4305–4319, 2004.

A. D. Poularikas. *The Transforms and Applications Handbook.* CRC Press LLC, 2000.

P. Powsner and E. Powsner. *Essential Nuclear Medicine Physics.* Blackwell Publishing, 2006.

W. H. Press. *Numerical Recipes in C, The Art of Scientific Computing.* University Press, 1992.

J. Qi and R. M. Leahy. Iterative reconstruction techniques in emission computed tomography. *Phys. Med. Biol.*, 51:R541–R578, 2006.

J. Qi, S. R. Leahy, R M and. Cherry, A. Chatziioannou, and T. H. Farquhar. High-resolution 3D Bayesian image reconstruction using the microPET small-animal scanner. *Phys. Med. Biol.*, 46:2597–2605, 1998.

M. Rafecas, G. Böning, B. J. Pichler, E. Lorenz, M. Schwaiger, and S. I. Ziegler. Inter-crystal scatter in a dual layer, high resolution LSO-APD positron emission tomograph. *Phys Med Biol*, 48:821–848, 2003.

M. Rafecas, B. Mosler, M. Dietz, M. Pgl, A. Stamatakis, M. P. McElroy, and S. I. Ziegler. Use of a Monte Carlo based probability matrix for 3D iterative reconstruction of MADPET-II data. *IEEE Trans. Nucl. Sci.*, 51:2597–2605, 2004.

A. Rahmim, J. Tang, M. A. Lodge, S. Lashkari, M. R. Ay, R. Lautamäki, B. M. W. Tsui, and F. M. Bengel. Analytic system matrix resolution modeling in PET: An application to Rb-82 cardiac imaging. *Phys. Med. Biol.*, 53:5947–5965, 2008.

M. E. Raichle. Positron emission tomography. *Ann. Rev. Neurosci.*, 6:249–267, 1983.

E. Rapisarda, V. Bettinardi, K. Thielemans, and M. C. Gilardi. Image-based point spread function implementation in a fully 3D OSEM reconstruction algorithm for PET. *Phys. Med. Biol.*, 55:4131–4151, 2010.

A. J. Reader and H. Zaidi. Advances in PET Image Reconstruction. *PET Clin.*, 2:173–190, 2007.

S. N. Reske, N. M. Blumstein, B. Neumaier, H.-W. Gottfried, F. Finsterbusch, D. Kocot, P. Moller, G. Glatting, and S. Perner. Imaging Prostate Cancer with ^{11}C-Choline PET/CT. *J. Nucl. Med.*, 47:1249–1254, 2006.

P. Rodrigues, A. Trindade, and J. Varela. Clear-PEM system counting rates: a Monte Carlo study . *J. Instrumentation*, 2:1–14, 2007.

D. W. O. Rogers. Low energy electron transport with EGS. *Nucl. Inst. Meth. in Phys. Res. A*, 227:535–548, 1984.

O. G. Rousset, Y. Ma, and A. C. Evans. Correction for partial volume effects in PET: Principle and validation. *J. Nucl. Med.*, 39:904–911, 1998.

V. Rufini, M. L. Calcagni, and R. P. Baum. Imaging of neuroendocrine tumors. *Semin. Nucl. Med.*, 36:228–247, 2007.

G. B. Saha. *Basics of PET Imaging.* Springer, 2005.

G. B. Saha. *Basics of PET Imaging: Physics, Chemistry, and Regulations.* Springer, 2010.

F. Salvat and J. M. Fernández-Varea. Semiempirical cross sections for the simulation of the energy loss of electrons and positrons in matter. *Nucl. Inst. Meth. in Phys. Res. B*, 63:255–269, 1992.

F. Salvat, D. Fernandez-varea, and J. Sempau. PENELOPE-2008: A code system for Monte Carlo simulation of electron and photon transport. Documentation of PENELOPE 2008 code, 2008.

A. Sánchez-Crespo, P. Andreo, and S. A. Laarson. Positron flight in human tissues and its influence on PET image spatial resolution. *Eur. J. Nucl. Med. Mol. Imaging*, 31:44–51, 2004.

D. R. Schaart, H. T. Van Dam, S. Seifert, R. Vinke, P. Dendooven, H. Löhner, and F. J. Beekman. A novel, SiPM-array-based, monolithic scintillator detector for PET. *Phys. Med. Biol.*, 54: 3501–3512, 2009.

D. W. Schneider, T. Heitner, B. Alicke, D. R. Light, K. McLean, N. Satozawa, G. Parry, J. Yoo, J. S. Lewis, and R. Parry. In vivo biodistribution, PET imaging, and tumor accumulation of 86Y- and 111In-antimindin/RG-1, engineered antibody fragments in LNCaP tumor-bearing nude mice. *J Nucl Med.*, 50(3):435–443, 2009.

U. Schneider, E. Pedroni, and A. Lomax. The calibration of CT Hounsfield units for radiotherapy treatment planning. *Phys. Med. Biol.*, 41:111–124, 1996.

J. Seidel, J. J. Vaquero, S. Siegel, W. R. Gandler, and M. V. Green. Accuracy of a Three-Layer Phoswich PET Detector Module. *IEEE Trans. Nucl. Sci.*, 46:485–490, 1999.

J. Sempau and P. Andreo. Configuration of the electron transport algorithm of PENELOPE to simulate ion chambers. *Phys. Med. Biol.*, 51:3533–3548, 2006.

L. Shepp and Y. Vardi. Maximum Likelihood Reconstruction for Emission Tomography. *IEEE Trans. Med. Imaging*, MI-1:113–122, 1982.

B. Singh. Nuclear data sheets update for A = 76. *Nuclear Data Sheets*, 74(1):63–164, 1995.

B. Singh. Nuclear data sheets for A = 86. *Nuclear Data Sheets*, 94(1):1–130, 2001.

B. Singh. Nuclear Data Sheets for A = 89. *Nuclear Data Sheets*, 114(1):1–208, 2013.

A. Sitek, A. Andreyev, and A. Celler. Reconstruction of Dual Isotope PET Using Expectation Maximization (EM) Algorithm. In *IEEE NSS MIC Conf. Record*, pages 4323–4326, 2011.

E. T. P. Slijpen and F. J. Beekman. Comparison of post-filtering and filtering between iterations for SPECT reconstruction. *IEEE Trans. Nucl. Sci.*, 46:2233–2238, 1999.

D. L. Snyder, M. I. Miller, L. J. Thomas, and D. G. Politte. Noise and edge artifacts in maximum-likelihood reconstruction for emission tomography. *IEEE Trans. Nucl. Sci.*, MI-6:228–238, 1987.

M. Soret, S. L. Bacharach, and I. Buvat. Partial-volume effect in PET tumor imaging. *J. Nucl. Med.*, 48:932–945, 2007.

G. Soultanidis, N. Karakatsanis, G. Nikiforidis, and G. Loudos. Study of the effect of magnetic field in positron range using GATE simulation toolkit. *J. Phys.: Conf. Ser.*, 317:012021, 2011.

S. Southekal, S. J. McQuaid, M. F. Kijewski, and S. C. Moore. Evaluation of a method for projection-based tissue-activity estimation within small volumes of interest. *Phys. Med. Biol.*, 57:685–701, 2012.

V. C. Spanoudaki and C. S. Levin. Photo-Detectors for Time of Flight Positron Emission Tomography (ToF-PET). *Sensors*, 10:10484–10505, 2010.

C. W. Stearns, D. A. Chesler, J. E. Kirsch, and G. L. Brownell. Quantitative Imaging with the MGH Analog Ring Positron Tomograph. *IEEE Trans. Nucl. Sci.*, 32:898–901, 1985.

J. R. Stickel and S. R. Cherry. High-resolution PET detector design: Modeling components of intrinsic spatial resolution. *Phys. Med. Biol.*, 50:179–195, 2005.

S. C. Strother, M. E. Casey, and E. J. Hoffman. Measuring PET scanner sensitivity: relating count rates to image signal-to-noise ratios using noise-equivalent counts. *IEEE Trans. Nucl. Sci.*, 37:783–788, 1990.

S. Surti, R. Scheuermann, and J. S. Karp. Correction Technique for Cascade Gammas in I-124 Imaging on a Fully-3D, Time-of-Flight PET Scanner. *IEEE Trans. Nucl. Sci.*, 56:653–660, 2009.

B. K. Teo, Y. Seo, S. L. Bacharach, J. A. Carrasquillo, S. K. Libutti, H. Shukla, B. H. Hasegawa, R. A. Hawkins, and B. L. Franc. Partial volume correction in PET: Validation of an iterative post reconstruction method with phantom and patient data. *J. Nucl. Med.*, 48:802–810, 2007.

M. M. Ter-Pogossian. Positron emission tomography (PET). *J. Med. Syst.*, 6:569–577, 1982.

C. J. Thomson, J. Moreno-Cantu, and Y. Picard. PETSIM: Monte Carlo simulation of all sensitivity and resolution parameters of cylindrical positron imaging systems. *Phys. Med. Biol.*, 37:731–749, 1992.

D. W. Townsend, T. Beyer, and T. M. Blodgett. PET/CT scanners: A hardware approach to image fusion. *Semin. Nucl. Med.*, 33(3):193, 2003.

E. N. Tsyganov et al. *Small-Animal SPECT Imaging*, chapter Reconstruction Algortithm with Resolution Deconvolution in a Small-Animal PET Imager. Springer, New York, 2005.

P. E. Valk, D. Delbeke, and D. L. Bailey. *Positron emission tomography: clinical practice.* Springer, 2003.

S. Vallabhajosula, L. Solnes, and B. Vallabhajosula. A Broad Overview of Positron Emission Tomography Radiopharmaceuticals and Clinical Applications: What Is New? *Seminars in Nuclear Medicine*, 65:246–264, 2011.

J. J. Vaquero, J. J. Sánchez, J. M. Udías, J. Cal-González, and M. Desco. MRI compatibility of position-sensitive photomultiplier depth-of-interaction PET detectors modules for in-line multimodality preclinical studies. *Nucl. Inst. Meth. in Phys. Res. A*, 702:83–87, 2012.

E. Vicente. *Caracterización, mejora y diseño de escáneres PET preclínicos.* PhD thesis, Universidad Complutense de Madrid, 2012.

E. Vicente, M. Soto-Montenegro, S. España, J. L. Herraiz, E. Herranz, J. J. Vaquero, M. Desco, and J. M. Udías. Influence of random, pile-up and scatter corrections in the quantification properties of small-animal PET scanners. In *IEEE NSS-MIC Conference Record*, pages 3964–3968, 2007.

E. Vicente, J. L. Herraiz, M. Cañadas, J. Cal-González, S. España, M. Desco, J. J. Vaquero, and J. M. Udías. Validation of NEMA NU4-2008 Scatter Fraction estimation with 18F and 68Ga for the ARGUS small-animal. In *IEEE NSS-MIC Conference Record*, pages 3553–3557, 2010.

E. Vicente, J. L. Herraiz, S. España, E. Herranz, M. Desco, J. J. Vaquero, and J. M. Udías. Improved effective dead-time correction for PET scanners: Application to small-animal PET. *Phys. Med. Biol.*, 58:2059–2072, 2013.

A. A. Wagadarikar, A. Ivan, S. Dolinsky, and D. L. McDaniel. Sensitivity improvement of time-of-flight (TOF)-PET detector through recovery of Compton Scattered Annihilation Photons. In *IEEE NSS MIC Conf. Record*, pages 4323–4326, 2012.

S. Walrand, F. Jamar, I. Mathieu, J. De Camps, M. Lonneux, and M. Sibomana. Quantitation in PET using isotopes emitting prompt single gammas: application to yttrium-86. *Eur J Nucl Med Mol Imag*, 30(3):354–361, 2003.

G. Wang and J. Qi. Penalized likelihood PET image reconstruction using patch-based edge-preserving regularization. *IEEE Trans. Med. Imaging*, 31(12):2194–2204, 2012.

Y. Wang, J. Seidel, W. M. B. Tsui, J. J. Vaquero, and M. G. Pomper. Performance Evaluation of the GE Healthcare eXplore VISTA Dual-Ring Small-Animal PET Scanner. *J. Nucl. Med.*, 47:1891–1900, 2006.

O. Warburg. *The metabolism of tumors.* New York: Richard Smith, 1931.

C. C. Watson. New, Faster, Image-Based Scatter Correction for 3D PET. *IEEE Trans. Nucl. Sci.*, 47(4):1587–1594, 2000.

P. P. Webb, R. J. McIntyre, and J. Conradi. Properties of avalanche photodiodes. *RCA Rev*, 35(2):234–278, 1974.

M. N. Wernick and J. N. Aarsvold. *Emission tomography: the fundamentals of PET and SPECT.* Elsevier Academic Press, 2004.

C. I. Westbrook, D. W. Gidley, R. S. Conti, and A. Rich. New precision measurement of the orthopositronium decay rate: A discrepancy with theory. *Phys. Rev. Lett.*, 58:1328–1331, 1987.

C. I. Westbrook, D. W. Gidley, R. S. Conti, and A. Rich. Precision measurement of the orthopositronium vacuum decay rate using the gas technique. *Phys. Rev. A*, 40:5489, 1989.

L. I. Wiebe. PET radiopharmaceuticals for metabolic imaging in oncology. *International Congress Series*, 1264:53–76, 2004.

A. Wirrwar, H. Vosberg, H. Herzog, H. Halling, S. Weber, and H. W. Muller-Gartner. 4.5 Tesla magnetic field reduces range of high-energy positrons-Potential implications for positron emission tomography. *IEEE Trans. Nucl. Sci.*, 44:184–189, 1997.

C. S. Wu and S. A. Moskowski. *Beta Decay.* Interscience, 1966.

S. Yamamoto, M. Amano, S. Miura, H. Iida, and I. Kanno. Deadtime correction method using random coincidence for PET. *J. Nucl. Med.*, 27:1925–1928, 1986.

S. Yamamoto, H. Horii, M. Hurutani, K. Matsumoto, and M. Senda. Investigation of single, random and true counts from natural radioactivity in LSO-based clinical PET. *Ann. Nucl. Med.*, 19(2):109–114, 2005.

K. Yoshinaga, B. J. W. Chow, K. Williams, L. Chen, R. A. deKemp, L. Garrard, A. L. Szeto, M. Aung, R. A. Davies, T. D. Ruddy, and R. S. B. Beanlands. What is the prognostic value of myocardial perfusion imaging using rubidium-82 positron emission tomography? *J. Am. Coll. Cardiol.*, 48(5):1029–1039, 2006.

H. Zaidi. Relevance of accurate Monte Carlo modeling in nuclear medical imaging. *Med. Phys.*, 26:574–608, 1999.

H. Zaidi. *Quantitative Analysis in Nuclear Medicine Imaging*, chapter Monte Carlo modeling in nuclear medicine imaging. Kluwer Academic Publishers, 2006.

H. Zaidi and A. Del Guerra. An outlook on future design of hybrid PET/MRI systems. *Med. Phys.*, 38(10):5667–5689, 2011.

H. Zaidi and G. Sgouros. *Therapeutic applications of Monte Carlo calculations in nuclear medicine*. Institute of Physics Pub., 2003.

P. Zanzonico. Positron emission tomography: A review of basic principles, scanner design and performance, and current systems. *Seminars in Nuclear Medicine*, 34:87–111, 2004.

P. Zanzonico and S. Heller. *Clinical Nuclear Medicine*, chapter Physics, instrumentation, and radiation protection. Springer, 2007.

G. L. Zeng and G. Y. Gullberg. Unmatched projector/backprojector pairs in an iterative reconstruction algorithm. *IEEE Trans.Med. Imaging*, 19:548–555, 2000.

G. L. Zeng, G. Y. Gullberg, B. M. W. Tsui, and J. A. Terry. Three-dimensional iterative reconstruction algorithms with attenuation and geometric point response correction. *IEEE Trans. Nucl. Sci.*, 38:693–702, 1991.

X. Zhu and G. El Fakhri. Monte Carlo modeling of cascade gamma rays in ^{86}Y PET imaging: preliminary results. *Phys. Med. Biol.*, 54:4181–4193, 2009.

I. G. Zubal and C. R. Harell. Voxel-based Monte Carlo calculations of nuclear medicine images and applied variance reduction techniques. *Image Vis. Comput.*, 10:342–348, 1992.

Appendix A

Description of the phantoms

A.1 NEMA NU-4 IQ phantom

The NEMA NU-4 IQ phantom [NEMA-NU-4, 2008] is made from PMMA (polymethyl methacrylate) and offers a large fillable cylindrical cavity with 30 mm diameter and 30 mm length. This large chamber houses two smaller cavities with 8 mm diameter, 15 mm length (see figure A.1, left). The second half of the cylinder houses five smaller cavities with diameters of 1, 2, 3, 4, and 5 mm, respectively, radially aligned around the phantom length axis (see figure A.1, right) and provides an interconnection to the first half cavity.

This phantom is used to obtain the recovery coefficients for studying the resolution and noise properties of the images, and the spill over ratios, in order to study the efficiency of scatter correction methods.

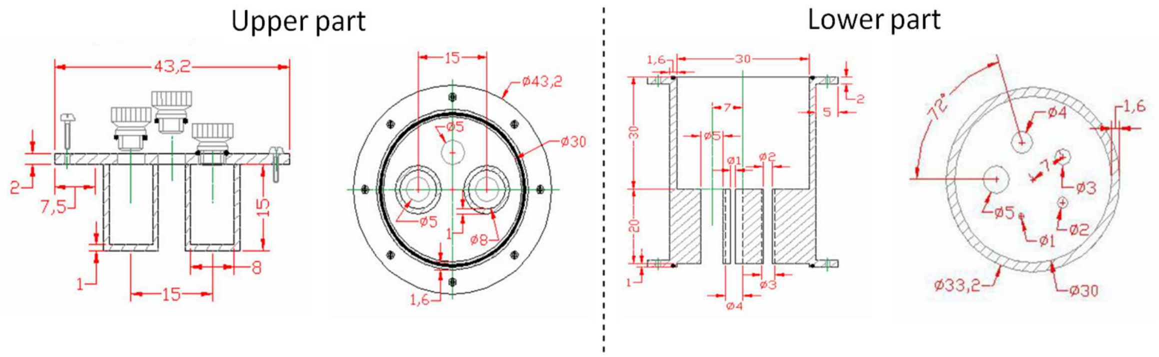

Figure A.1: Coronal and transverse views of the two parts of the NEMA NU 4 IQ phantom.

A.2 Derenzo phantom

This phantom consists of five sectors (figure A.2), each one containing radioactive rods with various diameters (1.2, 1.5, 2.0, 2.5, and 3.0 mm), the distance between sources being twice their diameter. The sources were distributed within a disk of diameter 36 mm.

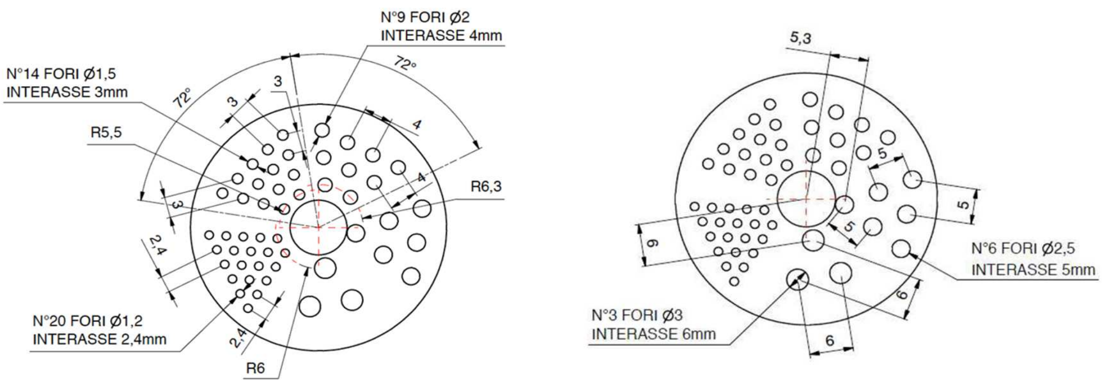

Figure A.2: Schematic view of the Derenzo-like phantom.

Appendix B

Publications derived from this thesis

B.1 Published articles

1. J. Cal-González, J. L. Herraiz, S. España, P. M. G. Corzo, M. Desco, J. J. Vaquero, and J. M. Udías. Positron Range Estimations with PeneloPET. *Phys. Med. Biol.*, 58:5127–5152, 2013a
2. B. Olaizola, L. M. Fraile, H. Mach, A. Aprahamian, J. A. Briz, J. Cal-González, D. Ghita, U. Koster, W. Kurcewicz, S. R. Lesher, D. Pauwels, E. Picado, A. Poves, D. Radulov, G. S. Simpson, and J. M. Udías. β^- decay of ^{65}Mn to ^{65}Fe. *Physical Review C*, 88:044306, 2013
3. J. J. Vaquero, J. J. Sánchez, J. M. Udías, J. Cal-González, and M. Desco. MRI compatibility of position-sensitive photomultiplier depth-of-interaction PET detectors modules for in-line multimodality preclinical studies. *Nucl. Inst. Meth. in Phys. Res. A*, 702:83–87, 2012
4. J. Cal-González, J. L. Herraiz, S. España, E. Vicente, E. Herranz, M. Desco, J. J. Vaquero, and J. M. Udías. Study of CT-based positron range correction in high resolution 3D PET Imaging. *Nucl. Inst. Meth. in Phys. Res. A*, 648:S172–S175, 2011b
5. J. L. Herraiz, S. España, J. Cal-González, J. J. Vaquero, M. Desco, and J. M. Udías. Fully 3D GPU PET reconstruction. *Nucl. Instrum. Meths. Phys. Res. A*, 648:S169–S171, 2011b

B.2 Articles submitted for publication

1. E. Herranz, J. L. Herraiz, P. Ibáñez, M. Pérez-Liva, R. Puebla, J. Cal-González, P. Guerra, R. Rodriguez, C. Illana, and J. M. Udías. Phase space determination from measured dose data for intraoperative electron radiation therapy. Submitted to: Phys. Med. Biol. (Dec 2013), 2013

B.3 International conference proceedings

1. J. Cal-González, E. Herranz, E. Vicente, J. M. Udías, S. R. Dave, V. Parot, E. Lage, and J. L. Herraiz. Simulation of Triple Coincidences in PET. In *IEEE NSS MIC Conf. Record*,

pages –, 2013b

2. J. Cal-González, S. C. Moore, M.-A. Park, J. L. Herraiz, J. J. Vaquero, M. Desco, and J. M. Udías. Projection-Based tissue activity estimation of PET images. presented at: IEEE NSS-MIC 2013, 2013c
3. J. Cal-González, J. L. Herraiz, S. España, and J. M. Udias. Scaling of Positron Range Distributions in Biological Materials. In *International Scientific Meeting on Nuclear Physics: La Rábida 2012*, pages 169–171, 2012
4. E. Herranz, J. L. Herraiz, P. Guerra, J. Cal-González, M. Perez-Liva, R. Rodriguez, C. Illana, M. Ledesma, J. Calama, and J. M. Udías. Iterative Determination of Clinical Beam Phase Space From Dose Measurements. *International Journal of Radiation Oncology * Biology * Physics*, 84(3):S869, 2012a
5. E. Herranz, J. L. Herraiz, P. Ibáñez, M. Pérez-Liva, R. Puebla, J. Cal-González, P. Guerra, R. Rodriguez, C. Illana, and J. M. Udias. Phase space determination of electron beam for intraoperative radiation therapy from measured dose data. presented at: Third European Workshop on Monte Carlo Treatment Planning (EW-MCTP), 2012b
6. J. Cal-González, J. L. Herraiz, S. España, P. M. G. Corzo, and J. M. Udías. A General Framework to study Positron Range Distributions. In *IEEE NSS-MIC Conference Record*, pages 2733–2737, 2011a
7. P. M. G. Corzo, J. Cal-González, E. Picado, S. España, J. L. Herraiz, E. Herranz, E. Vicente, J. M. Udías, J. J. Vaquero, A. Muñoz Martin, and L. M. Fraile. Measurement of Activity Produced by Low Energy Proton Beam in Metals Using off-Line PET Imaging. In *IEEE NSS-MIC 2011 Conference Record*, pages 3514–3517, 2011
8. E. Herranz, J. L. Herraiz, J. Cal-González, P. M. G. Corzo, P. Guerra, and J. M. Udias. Iterative Reconstruction of Whole Accelerator Phase Spaces for Intraoperative Radiation Therapy (IORT). In *IEEE NSS-MIC 2011 Conference Record*, pages 2644–2646, 2011
9. J. Cal-González, J. L. Herraiz, S. España, P. M. G. Corzo, M. Desco, J. J. Vaquero, and J. M. Udías. Validation of PeneloPET Positron Range Estimations. In *IEEE NSS-MIC Conference Record*, pages 2396–2399, 2010
10. E. Vicente, J. L. Herraiz, M. Cañadas, J. Cal-González, S. España, M. Desco, J. J. Vaquero, and J. M. Udías. Validation of NEMA NU4-2008 Scatter Fraction estimation with 18F and 68Ga for the ARGUS small-animal. In *IEEE NSS-MIC Conference Record*, pages 3553–3557, 2010
11. P. Guerra, W. Gonzalez, M. J. Ledesma-Carbayo, J. Cal-González, E. Herranz, J. M. Udías, A. Lallena, and A. Santos. Monte Carlo Based Dose Estimation in Intraoperative Radiotherapy. In *IEEE NSS-MIC Conference Record*, pages 3069–3072, 2010
12. J. Cal-Gonzalez, J. L. Herraiz, S. España, M. Desco, J. J. Vaquero, and J. M. Udias. Positron range effects in high resolution 3D PET imaging. In *IEEE NSS-MIC Conference Record*, pages 2788–2791, 2009

Appendix C

Resumen en castellano

C.1 Introducción y objetivos

La Tomografía por Emisión de Positrones (PET, de sus siglas en inglés: Positron Emission Tomography) es una técnica de Medicina Nuclear no invasiva que permite la visualización *in vivo* de múltiples fenómenos biológicos y bioquímicos [Bailey et al., 2005]. Gracias a que la PET es capaz de visualizar estos procesos a un nivel molecular, se puede usar en múltiples aplicaciones, entre las que cabe destacar el diagnóstico y seguimiento del paciente, la investigación farmacológica, el estudio de enfermedades humanas en modelos de laboratorio y la caracterización de la expresión genética.

Desde el desarrollo de los primeros escáneres PET, la tomografía por emisión de positrones se ha establecido como una técnica de uso rutinario en oncología, cardiología y neurología. Por otro lado, con la extensión de esta técnica a la investigación preclínica, se han desarrollado los escáneres PET para pequeños animales, como por ejemplo ratones y ratas, con una resolución espacial muy alta, del orden del milímetro [Goertzen et al., 2012].

Por otro lado, durante las últimas décadas se han propuesto varios radioisótopos de interés para imagen PET (ver tabla C.1), como por ejemplo: ^{68}Ga, ^{82}Rb, ^{124}I, ^{94m}Tc, ^{76}Br y ^{86}Y. También se ha desarrollado una gran cantidad de radiofármacos basados en estos radioisótopos [MICAD, 2013].

Radioisótopo	**Vida media**	**Mecanismo de producción**	**Intensidad β^+ (%)**
^{18}F	109.8 min	Ciclotron	96.7
^{11}C	20.5 min	Ciclotron	99.8
^{13}N	10.0 min	Ciclotron	99.8
^{15}O	2.0 min	Ciclotron	99.9
^{68}Ga	67.7 min	Generador (de ^{68}Ge)	89.1
^{82}Rb	1.3 min	Generador (de ^{82}Sr)	95.4
^{124}I	4.2 dás	Ciclotron	22.7
^{64}Cu	12.8 horas	Ciclotron	17.6
^{76}Br	16.2 horas	Ciclotron	55.0
^{94m}Tc	52.0 min	Ciclotron	70.2
^{86}Y	14.7 horas	Ciclotron	31.9

Table C.1: Radionúclidos de interés en imagen PET (adaptado de [Bailey et al., 2005]).

La utilización de estos nuevos radionúclidos plantea importantes cuestiones acerca de su utilización como emisores PET y la calidad de imagen (resolución espacial, cuantificación, contraste, etc) alcanzable con ellos, especialmente en los casos de imagen preclínica con escáneres PET de alta resolución. Esto es debido principalmente a dos factores:

- **Energía de los positrones emitidos:** Muchos de estos radioisótopos, en su proceso de decaimiento β^+, emiten positrones de alta energía [Laforest et al., 2002], que interactuan con los electrones del medio en su trayectoria, hasta que se aniquilan con un electrón despúes de haber recorrido una determinada distancia, conocida como **rango del positrón**. A mayor energía, mayor es el rango. El efecto del rango es un emborronamiento en la imagen reconstruida y constituye una importante limitación a la resolución espacial alcanzable por el sistema [Levin and Hoffman, 1999], en especial para PET preclínico con radionúclidos que emiten positrones de alta energía.

- **Emisión de fotones gamma adicionales:** Otra característica de estos radioisótopos es la emisión, durante el proceso de decaimiento, de fotones gamma adicionales a los positrones emitidos por el núcleo [Lubberink and Herzog, 2011]. Estos fotones gamma se pueden emitir en coincidencia con los positrones (en la misma cascada de decaimiento) o en diferentes cascadas. Esto tiene como consecuencia que aumente el número de coincidencias espúreas (entre fotones de aniquilación y fotones adicionales), creando un fondo adicional en la imagen que compromete las propiedades de cuantificación.

En esta tesis se estudia, mediante simulaciones Monte Carlo, el efecto del rango del positrón y de la emisiones gamma adicionales en la calidad de imagen alcanzable en sistemas PET de pequeños animales. Hemos modificado nuestro simulador PET (PeneloPET [España et al., 2009]) para incluir un modelado preciso de las emisiones β^+ y gamma de los radionúclidos estudiados. También hemos implementado y validado varios métodos para corregir el efecto del rango del positrón durante el proceso de reconstrucción de la imagen. Otro estudio que se ha llevado a cabo en esta tesis es la mejora de cuantificación PET en pequeños volúmenes de interés. Por último, también hemos implementado una herramienta de simulación y análisis de coincidencias triples en PET.

Los objetivos que se persiguen en esta tesis son por lo tanto los siguientes:

- Obtener distribuciones de rango del positrón para diferentes radioisótopos en varios tejidos biológicos. Validar las simulaciones realizadas con PeneloPET con otros resultados encontrados en la literatura, tanto experimentales como simulaciones con otros códigos.

- Implementar y evaluar diferentes métodos para corregir el efecto del rango del positrón durante la reconstrucción de imagen.

- Modificar nuestro código de simulación Monte Carlo para incluir un modelo preciso de las cascadas de decaimiento y las emisiones β^+ y gamma de los nuevos radionúclidos estudiados en esta tesis.

- Implementar y evaluar un método para mejorar la cuantificación PET en volúmenes de interés, tanto para emisores puros (^{18}F) como no puros (^{124}I).

- Finalmente, incluir en nuestra herramienta de simulación la posibilidad de simular y analizar coincidencias triples, y estudiar la cantidad de los diferentes tipos de coincidencias triples en varias situaciones de interés, tanto en escáneres preclínicos como clínicos.

Cabe mencionar que las herramientas desarrolladas en esta tesis no son exclusivas para un escáner en particular, sino que han sido diseñadas para ser flexibles y adaptables a diferentes arquitecturas, tanto para escáneres PET preclínicos como clínicos. Sin embargo, en esta tesis presentamos la implementación y evaluación de la mayor parte de estas herramientas para el escáner preclínico Argus PET / CT [Wang et al., 2006], debido a que se tiene acceso a datos reales adquiridos con este escáner y un profundo conocimiento del mismo.

C.2 Materiales

Escáner Argus PET / CT

Argus [Wang et al., 2006] es el nombre comercial de un escáner PET/CT para pequeños animales comercializado por la empresa SUINSA Sedecal. Este escáner es el que se ha usado para evaluar las herramientas desarrolladas en esta tesis.

El subsistema PET de este escáner consta de 36 bloques detectores dispuestos en dos anillos con 18 detectores cada uno de ellos. Cada bloque detector dispone de un array de 13 x 13 cristales LYSO+GSO, dispuestos en dos capas (lo que se conoce como *phoswich*) de 7 y 8 mm respectivamente. El tamaño de los cristales es de 1.45 × 1.45 mm^2, y cada cristal está separado por una fina capa de reflector de 0.1 mm de espesor. A cada bloque detector se le acopla un fotomultiplicador multiánodo Hamamatsu R8520-00-C12 [Wang et al., 2006], de 6(X) + 6(Y) ánodos.

Este escáner incorpora, además del subsistema PET, un sistema CT completamente funcional, compuesto por un tubo de rayos X de micro-foco y un detector plano con tecnología CMOS y detector de CsI.

Simulación Monte Carlo: PeneloPET

La herramienta de simulación Monte Carlo que se ha empleado en esta tesis ha sido el código PeneloPET [España et al., 2009]. PeneloPET es un entorno de simulación Monte Carlo para la tomografía por emisión de positrones. Para la simulación de la física de la interacción radiación-materia se ha utilizado el simulador Penelope [Salvat et al., 2008]. La aplicación hace uso de las subrutinas de Penelope y además consta de subrutinas propias que se encargan de simular el resto de procesos de emisión y detección.

El paquete de simulación PeneloPET contiene dos módulos principales. El primero se ocupa de la simulación de la física del sistema y las comunicaciones PeneloPET - PENELOPE. Este módulo incluye las subrutinas involucradas en la emisión y detección de la radiación. El segundo módulo se encarga de procesar los datos acquiridos en los detectores y simular la electrónica del sistema. En este segundo bloque no hay involucrada ninguna subrutina de PENELOPE.

Reconstrucción iterativa 3D: FIRST

Las reconstrucciones iterativas realizadas en esta tesis (para adquisiciones reales o simuladas en el escáner Argus PET/CT) se han realizado con el código FIRST [Herraiz et al., 2006]. Este es un código de reconstrucción 3D basado en el algoritmo OSEM [Hudson and Larkin, 1994], implementado por nuestro grupo (GFN, Universidad Complutense de Madrid), que usa una matriz de respuesta del sistema (SRM) comprimida con las propiedades físicas del escáner.

C.3 Principales resultados

C.3.1 Simulación de rango del positrón

En esta tesis hemos estudiado el rango del positrón para diferentes materiales e isótopos, mediante el código Monte Carlo PeneloPET [España et al., 2009]. Esta simulación calcula las trayectorias de los positrones desde que son emitidos hasta que se aniquilan, para después computar la distribución de las coordenadas de aniquilación de los mismos, obteniendo diferentes perfiles del rango del positrón para cada radioisótopo en cada medio.

Las distribuciones de rango calculadas han sido: las proyecciones en una dimensión de los puntos de aniquilación ($aPSF_{sin}(x)$ y $aPSF_{img}(x)$), las distribuciones radiales 3D: integrada en ángulos ($g_{3D}(r)$) y acumulada ($G_{3D}(r)$), y las distribuciones radiales 2D ($g_{2D}(r)$ y $G_{2D}(r)$). Se han comparado los resultados obtenidos con PeneloPET con otros resultados de la literatura, tanto de simulaciones como de medidas experimentales (ver figura C.1 y tabla C.2), obteniendo por lo general buena concordancia (discrepancias por debajo del 10% en la mayor parte de los casos). El único caso en donde hemos visto discrepancias importantes ha sido al comparar con los resultados de [Champion and Le Loirec, 2007]. Esto es debido a que [Champion and Le Loirec, 2007] incluyeron en su modelo la posibilidad de formación de Positronio. A día de hoy, no existen medidas experimentales suficientes para determinar la influencia de la formación de Positronio en el rango del positrón.

	R_{mean} en agua (mm)				R_{max} en agua (mm)		
Radioisótopo	**PeneloPET**	**Otras simulaciones**	**Eq. 3.10**	**Experimentos**	**PeneloPET**	**Otras simulaciones**	**Eq. 3.11**
^{18}F	0.57	0.66[1] / 0.6[2] / 0.6[3]	0.64[4]	0.54[5] / 0.9[6]	2.16	2.63[1]	2.27[4]
^{11}C	1.02	1.13[1] / 1.1[2] / 1.1[3]	1.03[4]	0.92[5] / 1.095[6]	3.67	4.54[1]	3.91[4]
^{13}N	1.40	1.73[1] / 1.5[2] / 1.5[3]	1.32[4]	1.39[6]	4.88	5.75[1]	5.16[4]
^{15}O	2.34	2.96[1] / 2.5[2] / 2.5[3]	2.01[4]	1.785[6]	7.92	9.13[1]	8.02[4]
^{68}Ga	2.69	3.56[1] / 2.9[2]	2.24[4]	2.8[5] / 1.975[6]	9.06	10.3[1]	8.84[4]
^{82}Rb	5.33	7.49[1] / 5.9[2]	4.29[4]	6.1[5] / 2.9[6]	16.5	18.6[1]	16.1[4]

Table C.2: Comparación de rango medio en agua, obtenido con PeneloPET, frente a los valores obtenidos por [Champion and Le Loirec, 2007] (1), [Partridge et al., 2006] (2), [Bailey et al., 2003] (3) y con los valores experimentales de [Derenzo et al., 1993] (5) y [Cho et al., 1975] (6). También se muestra la comparación del rango máximo con [Champion and Le Loirec, 2007] (1) y las estimaciones semi-empíricas de [Evans, 1972] (4).

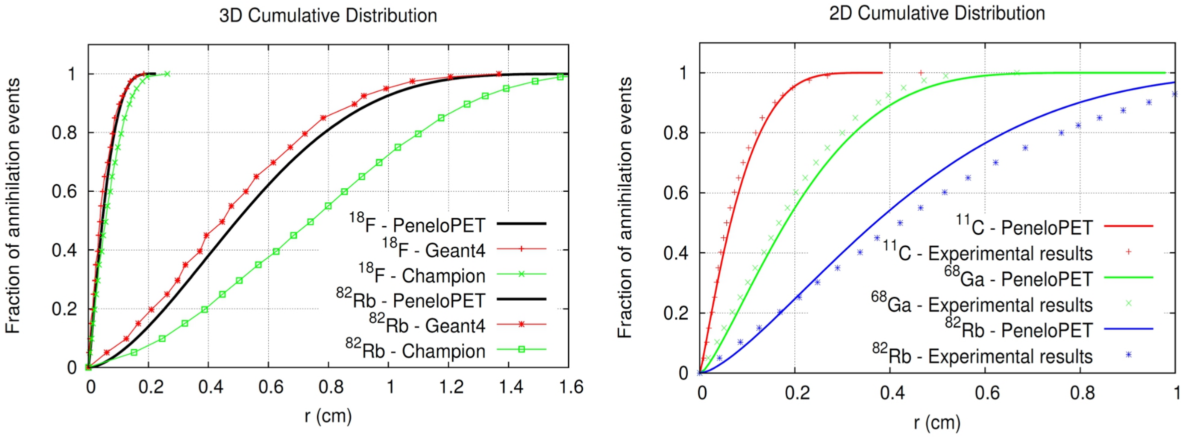

Figure C.1: Izquierda: Distribuciones acumuladas $3D$ obtenidas mediante simulaciones con PeneloPET, GEANT4 [Blanco, 2006] y [Champion and Le Loirec, 2007], para ^{18}F y ^{82}Rb en agua. Derecha: Distribuciones $G_{2D}(r)$ obtenidas con PeneloPET y medidas por [Derenzo, 1979], para ^{11}C, ^{68}Ga y ^{82}Rb en agua.

C.3.2 Simulación de emisiones gamma adicionales en PET

En esta tesis hemos modificado nuestro código de simulación Monte Carlo (PeneloPET) para incluir un modelo preciso de las cascadas de decaimiento y las emisiones β^+ y gamma de varios emisores no-puros de interés en PET. Los radionúclidos estudiados han sido (en orden de menor a mayor cantidad de emisiones gamma adicionales en relación con los positrones emitidos): ^{68}Ga, ^{82}Rb, ^{124}I, ^{22}Na, ^{94m}Tc, ^{76}Br y ^{86}Y. La cantidad de fotones gamma emitidos (en coincidencia y no en coincidencia con emisión de positrón) para cada radionúclido y su distribución energética se muestra en la tabla C.3.

				Emisiones γ: En coinc. / No en coinc. (% por decaimiento)			
Radioisótopo	**Intensidad β^+ (%)**	**CE (%)**	**γ de ann. (%)**	**$<$ 400 keV**	**400 - 650 keV**	**$>$ 650 keV**	**Total**
^{22}Na	90.4	9.6	180.8	0.0 / 0.0	0.0 / 0.0	90.4 / 9.5	90.4 / 9.5
^{68}Ga	88.9	11.1	177.8	0.0 / 0.0	0.0 / 0.0	1.2 / 2.2	1.2 / 2.2
^{82}Rb	95.4	4.6	190.9	0.0 / 0.0	0.0 / 0.0	13.1 / 2.6	13.1 / 2.6
^{94m}Tc	70.2	29.8	140.3	0.0 / 0.0	0.0 / 0.0	70.2 / 37.1	70.2 / 37.1
^{124}I	22.7	77.3	45.0	0.0 / 0.0	11.9 / 43.0	0.5 / 27.7	12.4 / 70.7
^{76}Br	55.0	45.0	109.0	0.0 / 0.0	71.8 / 2.4	34.8 / 25.6	106.6 / 28.0
^{86}Y	31.9	68.1	64.0	3.2 / 5.0	37.9 / 33.9	133.3 / 61.0	174.4 / 99.9

Table C.3: Distribución de energia de los fotones gamma adicionales emitidos por los radioisótopos de interés estudiados en esta tesis.

La nueva versión de PeneloPET, implementada en este trabajo, simula el esquema de desintegración del radionuclido, y genera historias para cada cascada de desintegración del mismo, teniendo en cuenta la probabilidad de cada cascada. Se han considerado todas las cascadas de desintegración con probabilidad de ocurrencia mayor que un 1%. Del mismo modo, en nuestro simulador también hemos considerado todas aquellas emisiones gamma con probabilidad mayor que el 1% [Cal-González et al., 2013b].

Con el nuevo simulador se ha estudiado la calidad de imagen alcanzable con los radionúclidos de interés evaluados en este trabajo. Como se ha mencionado anteriormente, para estos radioisótopos hay dos factores que van a limitar la calidad de imagen alcanzable: el rango del positrón, que afecta a la resolución espacial y aumenta el efecto de volumen parcial; y las emisiones gamma adicionales, que afectan a la cuantificación en la imagen.

En la figura C.2 se muestran las reconstrucciones del maniquí NEMA IQ [NEMA-NU-4, 2008], rellenado con ^{18}F (emisor puro, positrones de baja energía), ^{68}Ga (emisor casi puro, positrones de energía medio-alta), ^{124}I (emisor no puro con emisión moderada de fotones gamma adicionales, positrones de energía medio-alta) y ^{76}Br (emisor no puro con alta emisión de fotones gamma, positrones de alta energía). Se puede ver como la resolución y contraste en la imagen se degrada de forma muy significativa debido al rango del positrón y a las emisiones gamma de estos radionúclidos.

C.3.3 Corrección del rango del positrón

En esta tesis se ha estudiado como corregir el efecto del rango del positrón en la reconstrucción de imagen. Introduciendo los perfiles del rango del positrón obtenidos con PeneloPET en el algoritmo de reconstrucción FIRST [Herraiz et al., 2006], y empleándolos para emborronar la imagen antes de la proyección, se corrige el efecto de emborronamiento producido por el rango. Este emborronamiento podrá ser modificado en función de la densidad del material en el cual el positrón se aniquila, la cual se obtiene a partir del corregistro y segmentación de una imagen CT [Cal-González et al., 2011b].

Para llevar esta correción a cabo, empleamos una fórmula analítica para la distribución $g_{3D}(r)$, que viene dada por:

$$g_{3D}(r) \approx C\left[(ar+1)\left(1-\frac{r}{r_0}\right)^n - \frac{\epsilon}{r^n}\right] \tag{C.1}$$

Para radionúclidos con emisión de solo uno o dos positrones en su decaimiento: ^{18}F, ^{11}C, ^{13}N, ^{15}O, ^{68}Ga, ^{82}Rb, ^{94m}Tc y ^{124}I. a, r_0, n y $\epsilon(\epsilon << 1)$ son los parámetros de ajuste para cada radionúclido (ver tablas 3.7 y 4.4).

$$g_{3D}(r) \approx C\left[A_1 \cdot r \cdot e^{-\frac{(r-B_1)^2}{C_1}} + A_2 \cdot e^{-\frac{(r-B_2)^2}{C_2}}\right]\left[1-\left(\frac{r}{r_0}\right)^2\right] \tag{C.2}$$

Para radionúclidos con emisión de varios positrones en su decaimiento: ^{76}Br y ^{86}Y. En este caso los parámetros de ajuste son: A_1, B_1, C_1, A_2, B_2, C_2, r_0 y n, y sus valores se pueden consultar en la tabla 4.5.

En este trabajo se han implementado y evaluado tres métodos de corrección de rango. El primero, y más sencillo, es una correción uniforme independiente del medio de aniquilación, tomando agua como material de referencia. También hemos evaluado una corrección dependiente del material con kernel homogéneo (es decir, que no tiene en cuenta si hay medios heterogéneos o cambios de medio cerca del voxel donde se aplica la corrección), y otra corrección dependiente del material y con kernel inhomogéneo.

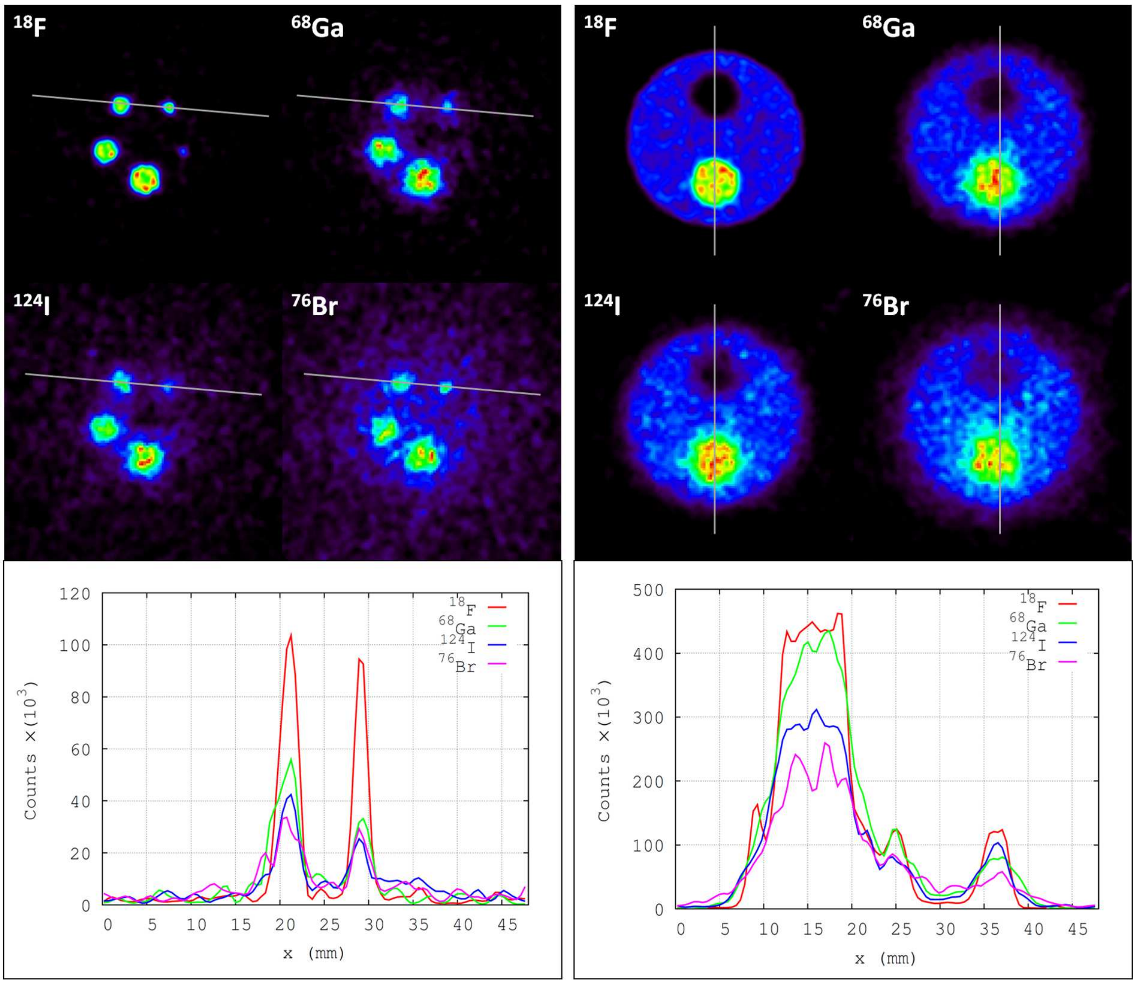

Figure C.2: Izquierda: Imágenes transversales del maniquí IQ, en la región de los capilares: de izquierda a derecha y de arriba a abajo: ^{18}F, ^{68}Ga, ^{124}I and ^{76}Br. Debajo de las imágenes se muestran los perfiles a traves de los capilares de 2 y 3 mm. Derecha: Imágenes del maniquí IQ en la región de las cavidades *hot* (con alta actividad) y *cold* (sin actividad). En la parte inferior se muestran los perfiles a través de los regiones *hot* y *cold*.

Los resultados obtenidos con corrección uniforme en agua se pueden observar en la figura C.3, donde se muestra la resolución y los valores RC obtenidos en la simulación del maniquí NEMA IQ [NEMA-NU-4, 2008] relleno con ^{18}F y con ^{68}Ga. En la tabla C.4 vemos la comparación entre corrección uniforme y dependiente del material cuando tenemos la actividad localizada en diferentes medios (agua, hueso cortical y pulmón), con los valores del FWTM (anchura a un décimo de altura) obtenidos de la reconstrucción de capilares de ^{18}F y ^{68}Ga, con corrección de rango y sin ella. Finalmente, también hemos evaluado los algoritmos implementados en un caso en el que la actividad está situada muy próxima a una frontera agua-aire (por ejemplo, actividad de ^{124}I en el tiroides, situada muy cerca de la traquea). La comparación entre la corrección con kernel homogéneo y con kernel inhomogéneo se muestra en la figura C.4.

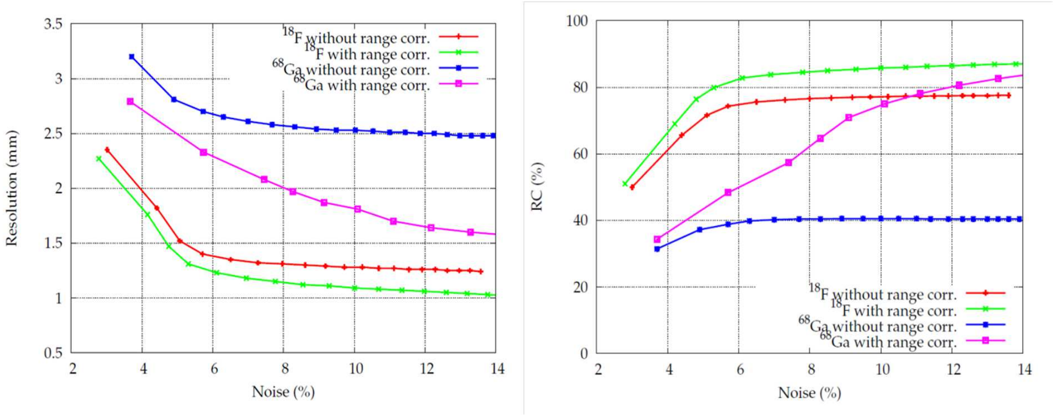

Figure C.3: Curvas resolución - ruido (izquierda) y RC - ruido (derecha) para ^{18}F y ^{68}Ga. Cada punto de las curvas corresponde a 10 actualizaciones de la imagen.

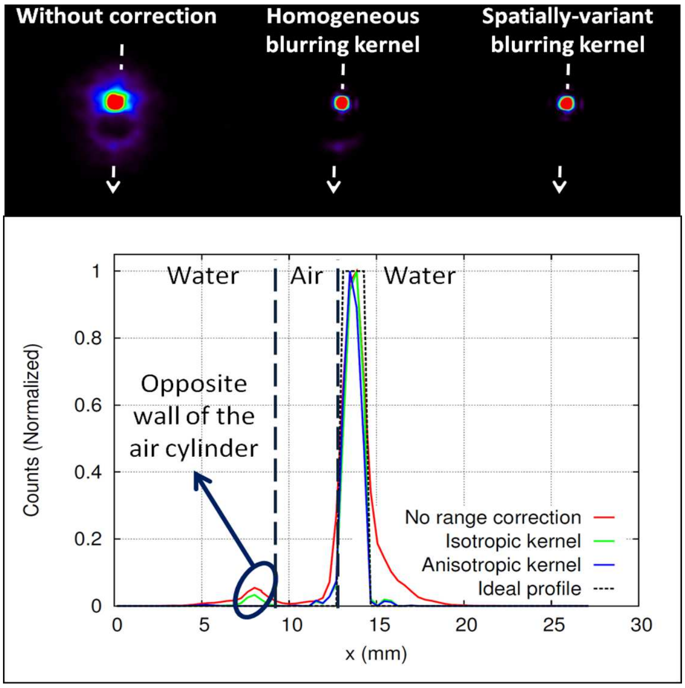

Figure C.4: Arriba: Vista transversal del capilar reconstruido con PR-OSEM, sin corrección de rango (izquierda), corrección con kernel homogéneo (centro) y con kernel inhomogéneo (derecha). Debajo: Perfil de actividad a través del capilar de ^{124}I y el cilindro de aire, para las tres reconstrucciones.

		FWTM de los capilares reconstruidos (mm)		
Radioisótopo	**Medio de aniquilación**	**Sin corrección de rango**	**Corrección uniforme**	**Corrección dependiente del material**
^{18}**F**	Hueso cortical	1.66	1.21	1.37
	Agua	1.70	1.38	1.38
	Pulmón	2.34	1.95	1.40
^{68}**Ga**	Hueso cortical	2.86	1.75	1.86
	Agua	3.53	1.90	1.90
	Pulmón	5.14	3.24	2.24

Table C.4: FWTM (en mm) para ^{18}F y ^{68}Ga en hueso cortical, agua y pulmón tras la reconstrucción.

C.3.4 Mejora de cuantificación en pequeños volúmenes de interés

En esta tesis se ha implementado y evaluado el método de *cuantificación mediante proyección local (LPA)*, propuesto previamente por S. C. Moore y colaboradores [Moore et al., 2012, Southekal et al., 2012], para corregir los efectos de volumen parcial (pérdida de actividad en una región de interés debido a la resolución espacial del sistema) y de *spillover* (cuentas de fuera de la región de interés que caen dentro de la misma o viceversa) en PET.

Este método requiere la segmentación del volumen que se desea cuantificar en 2 a 4 tejidos. Dicha segmentación se obtiene a partir de la imagen CT. La actividad correspondiente a cada tejido dentro del volumen de interés (VOI) se calcula mediante el ajuste del modelo del sistema a los datos proyectados. El método propuesto se ha implementado y validado para el escáner de pequeños animales Argus PET / CT.

En este trabajo se ha evaluado la cuantificación en pequeños volúmenes de interés de la imagen reconstruida del maniquí NEMA IQ [NEMA-NU-4, 2008], obtenida mediante los siguientes métodos: cuantificación directamente de la imágen reconstruida (IMG), cuantificación LPA después de la reconstrucción (LPA), cuantificación en la imagen usando los resultados del LPA en la reconstrucción como prior (LPAR) y cuantificación LPA en la imagen reconstruida usando los resultados del LPA como prior (LPAR + LPA). Dicha evaluación se ha realizado para acquisiciones con ^{18}F, ^{68}Ga y ^{124}I.

El fondo debido a cuentas de *scatter*, *randoms* y gammas adicionales (en ^{124}I) se ha estimado mediante simulaciones Monte Carlo e incorporado en la reconstrucción para corregir estos efectos. También se ha incluido corrección por rango del positrón en estas reconstrucciones.

En la figura C.5 se muestra comparación de los cuatro métodos de cuantificación, en la region caliente y en la region fría, para la reconstrucción del IQ relleno con ^{18}F. También se muestran las imágenes reconstruidas de modo usual y usando los valores de actividad del LPA durante la reconstrucción. En la figura C.6 se muestran los mismos resultados, pero en este caso para el IQ relleno con ^{124}I.

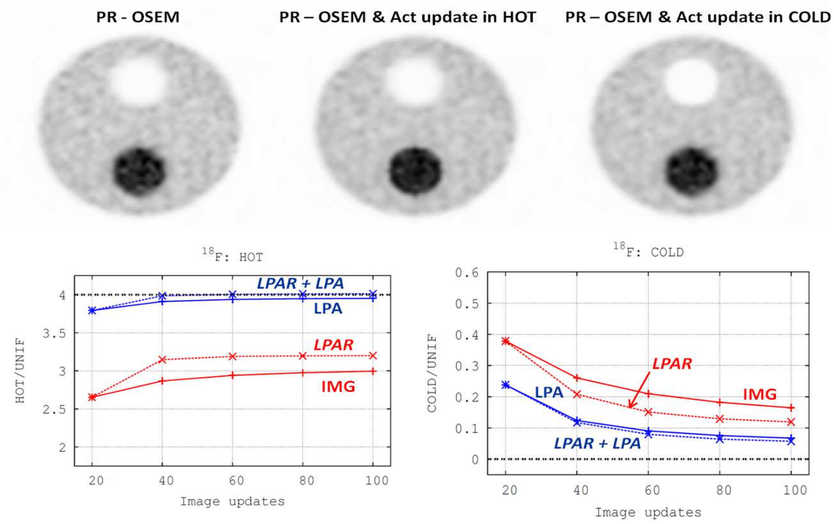

Figure C.5: Arriba: Imágenes reconstruidas del IQ (^{18}F) - izquierda: PR-OSEM, centro: reconstrucción LPA usando actividades LPA de la zona HOT, derecha: reconstrucción LPA usando actividades LPA de la zona COLD. Abajo: Evolución de los ratios HOT/uniform y COLD/uniform.

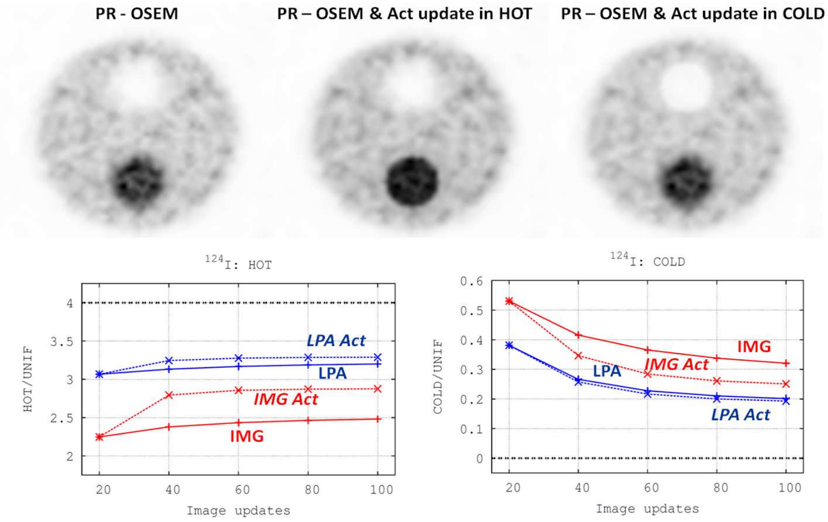

Figure C.6: Arriba: Imágenes reconstruidas del IQ (^{124}I) - izquierda: PR-OSEM, centro: reconstrucción LPA usando actividades LPA de la zona HOT, derecha: reconstrucción LPA usando actividades LPA de la zona COLD. Abajo: Evolución de los ratios HOT/uniforme y COLD/uniforme.

C.3.5 Simulación de coincidencias triples en PET

Por último, se ha incluido en nuestra herramienta de simulación la posibilidad de simular y analizar coincidencias triples en PET, y se ha validado nuestro simulador contra datos reales adquiridos en una versión del escáner Argus PET/CT, modificado para adquirir y procesar este tipo de coincidencias. También se ha evaluado la presencia de coincidencias triples en dos escáneres clínicos: el Biograph TPTV [Jakoby et al., 2009] y el Discovery-690 [Bettinardi et al., 2011].

Las coincidencias triples se pueden producir por diferentes razones, dando diferentes tipos de evento triple:

- IDS: Cuando uno de los fotones deposita su energía en dos detectores.

- R_T: Eventos triples *random*. Detección de 3 singles provenientes de dos desintegraciones (R_{T1}) o de tres desintegraciones (R_{T2}).

- $\beta^+\gamma$: Coincidencias triples entre dos fotones de aniquilación y un gamma adicional (en emisores no puros).

Las coincidencias triples IDS, R_{T1} y R_{T2} pueden ocurrir tanto para emisores puros como para emisores no puros. Por el contrario, las $\beta^+\gamma$ sólo pueden ocurrir cuando se ultilizan radionúclidos con emisión de fotones gamma adicionales.

Las coincidencias triples tienen aplicaciones de gran interés en PET, por ejemplo: se pueden usar las coincidencias IDS para aumentar la sensibilidad del sistema [Lage et al., 2013] o las $\beta^+\gamma$ para diferenciar emisores puros de no puros al hacer imagen multi-isótopo [Parot et al., 2013].

La ventana de energía más apropiada para cada tipo de evento viene dada por la naturaleza física del mismo. Por ejemplo, para eventos IDS, la condición de ventana de energía será: un single en la misma ventana que las coincidencias dobles (en este trabajo 400 - 700 keV), y la suma de los otros dos singles en la misma ventana. Para eventos R_T, la condición es: los tres singles dentro de la ventana de dobles. Por último, para eventos $\beta^+\gamma$, dos singles deben de estar en la ventana de dobles, y el tercero en otra ventana de energía que vendrá dada por la distribución energética de los fotones gamma adicionales emitidos por el radionúclido considerado. Por ejemplo, para ^{22}Na, el tercer single deberá de estar por encima de 700 keV, mientras que para ^{124}I, deberá estar por encima de 400 keV.

En la tabla C.5 se muestran las estadísticas de coincidencias dobles y triples para diferentes ventanas de energía, en adquisiciones en el escáner Argus de un maniquí IQ relleno con diferentes radioisótopos. Las ventanas de energía son las que se han detallado anteriormente, y las estadísticas de triples se presentan como el ratio entre triples / dobles (en la ventana de energía correspondiente). En la tabla también se muestran los valores experimentales obtenidos.

Finalmente, en la tabla C.6 se muestran las mismas estadísticas de triples, pero en este caso para los escáneres clínicos Biograph TPTV y Discovery-690. En esta tabla solo se muestran las estimaciones obtenidas con nuestro simulador.

Ventana de energía	**Tipo de coincidencia**	**^{18}F (92 μCi)**	**^{22}Na (3.5 μCi)**	**^{124}I (212 μCi)**	**^{76}Br (105 μCi)**
EW_D **(D)** **(kcps)**	**Doubles EXP**	**31.3 ± 1.7**	**2.37 ± 0.17**	**20.1 ± 1.1**	**16.2 ± 0.9**
	Prompts (%)	99.4	99.5	98.8	98.7
	Randoms (%)	0.6	0.5	1.2	1.3
	Doubles SIM	**31.7 ± 1.8**	**2.45 ± 0.17**	**20.0 ± 1.1**	**16.1 ± 0.9**
	Trues (%)	87.5	87.7	67.5	64.9
	Sc (%)	11.5	6.4	10.0	10.7
	$\beta^+\gamma$ (%)	0.0	5.8	20.0	23.2
	R_D (%)	1.0	0.1	2.5	1.2
EW_{T-IDS} (%)	**T / D exp**	**17.0 ± 1.1**	**18.8 ± 1.8**	**23.7 ± 1.5**	**30.7 ± 2.0**
	T / D sim	**19.0 ± 1.3**	**19.9 ± 2.2**	**23.0 ± 1.7**	**24.4 ± 1.8**
	IDS	18.4 ± 1.2	17.7 ± 1.7	15.5 ± 1.1	16.1 ± 1.1
	$\beta^+\gamma$	<0.01	2.2 ± 0.4	6.2 ± 0.5	7.8 ± 0.6
	R_{T1}	0.38 ± 0.05	<0.01	0.67 ± 0.09	0.34 ± 0.05
	R_{T2}	0.18 ± 0.03	<0.01	0.59 ± 0.08	0.21 ± 0.05
EW_{T-RT} (%)	**T / D exp**	**0.59 ± 0.07**	**1.3 ± 0.3**	**2.3 ± 0.3**	**3.1 ± 0.3**
	T / D sim	**0.32 ± 0.05**	**1.6 ± 0.3**	**2.4 ± 0.3**	**4.0 ± 0.4**
	$\beta^+\gamma$	<0.01	1.6 ± 0.3	2.0 ± 0.2	3.8 ± 0.3
	R_{T1}	0.31 ± 0.05	<0.01	0.38 ± 0.08	0.16 ± 0.04
	R_{T2}	<0.01	<0.01	0.04 ± 0.02	0.024 ± 0.015
$EW_{T-\beta\gamma}$ (**^{22}Na**) (%)	**T / D exp**	**0.06 ± 0.02**	**2.4 ± 0.4**	**0.83 ± 0.11**	**1.8 ± 0.2**
	T / D sim	**0.030 ± 0.011**	**2.7 ± 0.5**	**0.69 ± 0.11**	**0.85 ± 0.13**
	$\beta^+\gamma$	<0.01	2.7 ± 0.5	0.56 ± 0.08	0.79 ± 0.11
	R_{T1}	0.030 ± 0.011	<0.01	0.14 ± 0.03	0.06 ± 0.02
	R_{T2}	<0.01	<0.01	<0.01	<0.01
$EW_{T-\beta\gamma}$ (**^{124}I,^{76}Br**) (%)	**T / D exp**	**0.64 ± 0.08**	**3.7 ± 0.6**	**3.0 ± 0.3**	**4.8 ± 0.4**
	T / D sim	**0.35 ± 0.05**	**4.3 ± 0.7**	**3.1 ± 0.3**	**4.7 ± 0.4**
	$\beta^+\gamma$	<0.01	4.3 ± 0.6	2.5 ± 0.2	4.5 ± 0.4
	R_{T1}	0.35 ± 0.05	0.012 ± 0.010	0.50 ± 0.08	0.21 ± 0.05
	R_{T2}	<0.01	<0.01	0.04 ± 0.02	<0.01

Table C.5: Estadísticas de coincidencias dobles y triples en el escáner Argus PET / CT, para ^{18}F, ^{22}Na, ^{124}I y ^{76}Br.

		Biograph TPTV / Discovery-690			
Ventana de energía	**Coinc.**	**^{18}F**	**^{82}Rb**	**^{124}I**	**^{86}Y**
EW_D	**Doubles (kcps)**	**19.6 (1.0) / 17.4 (0.9)**	**18.8 (0.9) / 17.3 (0.9)**	**7.3 (0.4) / 9.1 (0.5)**	**13.7 (0.7) / 23.2 (1.2)**
	Trues (%)	54.1 / 52.5	51.2 / 48.0	30.2 / 19.9	14.7 / 6.9
	Sc (%)	39.6 / 37.8	38.9 / 36.3	28.9 / 22.9	19.5 / 12.3
	$\beta^+\gamma$ (%)	0.0 / 0.0	3.9 / 7.1	34.9 / 51.1	61.7 / 77.8
	R_D (%)	6.3 / 9.7	6.0 / 8.6	6.0 / 6.1	4.1 / 3.0
EW_{T-IDS} (%)	**T / D**	**13.8 (0.7) / 21.6 (1.1)**	**17.7 (0.9) / 27.3 (1.4)**	**25.6 (1.4) / 33.1 (1.8)**	**77 (4) / 67 (3)**
	IDS	9.8 (0.5) / 17.1 (0.9)	9.4 (0.5) / 15.6 (0.8)	5.5 (0.4) / 6.5 (0.4)	3.1 (0.2) / 2.26 (0.15)
	$\beta^+\gamma$	<0.01 / <0.01	4.1 (0.3) / 7.2 (0.4)	16.3 (0.9) / 23.4 (1.3)	66 (3) / 61 (3)
	R_{T1}	2.81 (0.19) / 3.8 (0.2)	2.91 (0.19) / 3.8 (0.2)	2.3 (0.2) / 2.6 (0.2)	4.9 (0.3) / 3.9 (0.2)
	R_{T2}	1.19 (0.10) / 0.68 (0.07)	1.34 (0.11) / 0.73 (0.08)	1.58 (0.17) / 0.56 (0.08)	2.8 (0.2) / 0.46 (0.05)
EW_{T-RT} (%)	**T / D**	**0.60 (0.06) / 0.42 (0.05)**	**0.91 (0.08) / 0.70 (0.07)**	**2.4 (0.2) / 1.86 (0.17)**	**5.4 (0.3) / 5.0 (0.3)**
	$\beta^+\gamma$	<0.01 / <0.01	0.30 (0.04) / 0.28 (0.04)	1.95 (0.19) / 1.57 (0.15)	4.8 (0.3) / 4.7 (0.3)
	R_{T1}	0.60 (0.06) / 0.41 (0.05)	0.57 (0.06) / 0.40 (0.05)	0.33 (0.06) / 0.27 (0.06)	0.39 (0.06) / 0.31 (0.04)
	R_{T2}	<0.01 / <0.01	<0.01 / <0.01	0.09 (0.04) / 0.014 (0.012)	0.18 (0.04) / 0.041 (0.013)
$EW_{T-\beta\gamma}$ (%)	**T / D**	**0.70 (0.07) / 0.45 (0.06)**	**1.72 (0.13) / 1.43 (0.12)**	**4.1 (0.3) / 4.5 (0.3)**	**18.7 (1.0) / 16.4 (0.9)**
	$\beta^+\gamma$	<0.01 / <0.01	0.95 (0.09) / 0.87 (0.08)	3.3 (0.3) / 3.9 (0.3)	16.7 (0.9) / 15.1 (0.8)
	R_{T1}	0.69 (0.07) / 0.44 (0.06)	0.69 (0.07) / 0.53 (0.06)	0.60 (0.10) / 0.57 (0.08)	1.24 (0.11) / 1.11 (0.09)
	R_{T2} / D	<0.01 / <0.01	0.08 (0.02) / 0.026 (0.012)	0.21 (0.06) / 0.05 (0.03)	0.72 (0.08) / 0.13 (0.03)

Table C.6: Estadísticas de coincidencias dobles y triples en escáneres clínicos, para ^{18}F, ^{82}Rb, ^{124}I y ^{86}Y. Las incertidumbres para estos valores están expresadas entre paréntesis.

C.4 Conclusiones y contribuciones de esta tesis

Simulación y corrección de rango del positrón

En esta tesis hemos estudiado, mediante el simulador PeneloPET [España et al., 2009], las distribuciones de rango de positrón para diferentes isótopos y materiales. Hemos comparado las distribuciones obtenidas con PeneloPET con otros resultados de la literatura. También se ha desarrollado una herramienta, basada en un algoritmo genético, que permite convertir una distribución de rango en cualquier otra.

Por otro lado, se han implementado y evaluado varios métodos de corrección de rango en nuestro código de reconstrucción FIRST.

Las conclusiones de esta parte de la tesis son:

- Las estimaciones de rango de PeneloPET son consistentes con otros resultados de la literatura (discrepancias por debajo del 10% en la mayor parte de los casos). Excepto en el caso de [Champion and Le Loirec, 2007], donde se considera la formación del Positronio.
- Los métodos propuestos para corregir el efecto del rango del positrón funcionan de forma eficaz, dando imágenes de calidad para isótopos en los que el efecto del rango es significativo.
- El uso de kernel dependiente del material e inhomogeneo permite obtener imágenes de calidad cuando la actividad está localizada en diferentes tejidos.

Emisiones gamma adicionales

Se ha modificado el código PeneloPET para incluir un modelado preciso de las cascadas de decaimiento en isótopos con emisión de gammas adicionales.

- Se ha comprobado que la cuantificación PET empeora con la cantidad de fotones gamma adicionales emitidos por el radionúclido.
- Hemos visto que modelando (mediante simulaciones Monte Carlo) la distribución de las coincidencias espúreas debidas a gammas adicionales e introduciendo esta información en la reconstrucción, junto a la corrección de rango del positrón, se puede mejorar la cuantificación en la imagen PET.

Corrección de volumen parcial y spillover

Se ha implementado y evaluado un algoritmo de corrección de los efectos de volumen parcial y *spillover* para mejorar la cuantificación de lesiones en pequeños volúmenes de interés. El método propuesto se ha evaluado tanto con simulaciones como con adquisiciones reales, y para un emisor estándar (^{18}F, emisor puro y poco rango) y dos emisores de interés con emisiones gamma adicionales y rango del positrón significativos (^{68}Ga y ^{124}I). Las conclusiones de esta parte son:

- En todos los casos estudiados, la cuantificación mejora notablemente cuando se usa el método LPA de corrección de volumen parcial y *spillover*, tanto para regiones calientes como para regiones frías.

- El uso de las actividades obtenidas usando el método LPA durante la reconstrucción mejora notablemente la cuantificación y la delimitación de las lesiones de interés en la imagen.

Simulación de coincidencias triples

Se ha incluido en nuestro paquete de simulación (PeneloPET, [España et al., 2009]) la posibilidad de simular y analizar coincidencias triples. Se ha validado nuestra herramienta de simulación y análisis de triples frente a datos adquiridos en el escáner Argus, y se ha empleado esta herramienta para estimar el impacto de las coincidencias triples en dos escáneres clínicos (Biograph TPTV y Discovery-690). Las principales conclusiones de este trabajo son:

- Se ha obtenido un buen acuerdo entre datos simulados y datos experimentales en el escáner Argus, con discrepancias por debajo del 10% en la mayoría de los casos.
- Hemos visto una cantidad significativa de triples IDS en todos los casos estudiados. El ratio IDS / dobles en emisores puros ha sido en torno al 18% en el Argus, 10% en el Biograph y 17% para el Discovery.
- Para eventos $\beta^+\gamma$ el ratio triples / dobles para ^{124}I es del 2.5% en el Argus y hasta el 4% en escáneres clínicos (usando la ventana de energía adecuada).

Conclusión final de la tesis

En resumen, en esta tesis se muestra como el uso de simulaciones Monte Carlo realistas nos puede guiar para modelar y corregir los parámetros que afectan de un modo más significativo a la calidad de imagen PET, cuando se usan radioisótopos no convencionales en PET, permitiendo la obtención de imágenes de calidad incluso cuando se usan emisores cuyas propiedades no son óptimas para PET (alta energía de emisión de los positrones, emisión de fotones gamma adicionales, etc).